

2013

# Engineering aperiodic spiral order for photonic-plasmonic device applications

---

<https://hdl.handle.net/2144/11068>

*Downloaded from DSpace Repository, DSpace Institution's institutional repository*

BOSTON UNIVERSITY  
COLLEGE OF ENGINEERING

Dissertation

**ENGINEERING APERIODIC SPIRAL ORDER FOR PHOTONIC-PLASMONIC  
DEVICE APPLICATIONS**

by

**JACOB TIMOTHY TREVINO**

B.S., Susquehanna University, 2002  
M.S., Case Western Reserve University, 2006

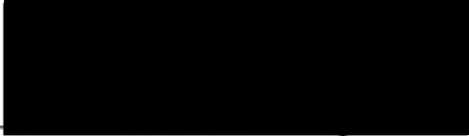
Submitted in partial fulfillment of the  
requirements for the degree of  
Doctor of Philosophy

2013


© 2013 by  
JACOB TIMOTHY TREVINO  
All rights reserved except for section 6.1 and 8.1 ©  
2011 ACS Publications, sections 6.2, 7.1, 8.2, and 8.3  
© 2012 Optical Society of America, and section 7.3 ©  
2013 IOP Publishing

Approved by

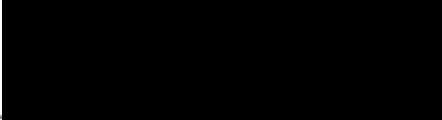
First Reader

  
Luca Dal Negro, Ph.D.  
Associate Professor of Electrical and Computer Engineering

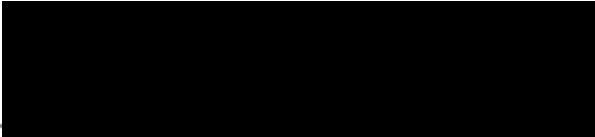
Second Reader

  
Anna Swan, Ph.D.  
Associate Professor of Electrical and Computer Engineering

Third Reader

  
Siddharth Ramachandran, Ph.D.  
Associate Professor of Electrical and Computer Engineering

Fourth Reader

  
Enrico Bellotti, Ph.D.  
Professor of Electrical and Computer Engineering



*Dedicated to*

My Wife and Family

## Acknowledgements

I would like to thank my advisor, Professor Luca Dal Negro, for his extensive help, advice, feedback and encouragement over the past four years, without which this thesis would not be possible. Additionally, I would like to thank the Air Force Office of Scientific Research, which has provided funding for me throughout the majority of my time at Boston University under the program *Deterministic Aperiodic Structures for On-chip Nanophotonic and Nanoplasmonic Device Applications* (Award # FA9550-10-1-0019).

I would also like to thank the members of the Nanomaterials and Nanostructure Optics group at Boston University who all contributed in various manners to this thesis. In particular: Nate Lawrence, Dr. Gary Walsh, Dr. Emanuele Pecora, Dr. Carlo Forestiere, Dr. Sylvanus Lee, Dr. Antonio Capretti, Dr. Alyssa Pasquale, Dr. Selcuk Yerci, Dr. Svetlana Boriskina, Travis Rich, Dr. Ashwin Gopinath, Dr. Rui Li, Dr. Salvatore Minissale, Dianmin Lin, Alex Handin, Giuliana Di Martino, Tom Murphy, and Yu Wang. There have also been several research collaborators who been an absolute pleasure to work with over the years including Professors Hui Cao (Yale University), Giovanni Miano (Complesso Universitario di Monte S. Angelo), Anna Fontcuberta i Morral (École Polytechnique Fédérale de Lausanne), Alexander Sergienko (Boston University), Fiorenzo Omenetto (Tufts University), Francesco Priolo (Università di Catania), Diederik Wiersma and Francesca Intonti (European Laboratory for Non-linear Spectroscopy).

Finally, I would like to thank all of my friends and family for their support over the last four years. A special thanks to my wonderful parents, Usbaldo and Debbie Trevino, who sacrificed in so many ways throughout my entire life to provide every opportunity for me to pursue my aspirations. To my sister Meagan for keeping me grounded, my Uncle Jeremy for believing in me no matter what I choose to do, and my Grandmother Virginia for her constant prayers and love, thank you all so much. You are all a constant source of inspiration. Finally, I cannot thank my amazing wife Kelly Trevino enough, for her never ending love, patience, inspiration and support. You were my rock in this turbulent time of graduate school and I could not have done it without you.

**ENGINEERING APERIODIC SPIRAL ORDER FOR PHOTONIC-PLASMONIC  
DEVICE APPLICATIONS**

**JACOB TIMOTHY TREVINO**

Boston University, College of Engineering, 2013

Major Professor: Luca Dal Negro, Ph.D., Associate Professor of Electrical and Computer Engineering and of Materials Science and Engineering

**ABSTRACT**

Deterministic arrays of metal (i.e., Au) nanoparticles and dielectric nanopillars (i.e., Si and SiN) arranged in aperiodic spiral geometries (Vogel's spirals) are proposed as a novel platform for engineering enhanced photonic-plasmonic coupling and increased light-matter interaction over broad frequency and angular spectra for planar optical devices. Vogel's spirals lack both translational and orientational symmetry in real space, while displaying continuous circular symmetry (i.e., rotational symmetry of infinite order) in reciprocal Fourier space. The novel regime of "circular multiple light scattering" in finite-size deterministic structures will be investigated. The distinctive geometrical structure of Vogel spirals will be studied by a multifractal analysis, Fourier-Bessel decomposition, and Delaunay tessellation methods, leading to spiral structure optimization for novel localized optical states with broadband fluctuations in their photonic mode density. Experimentally, a number of designed passive and active spiral structures will be fabricated and characterized using dark-field optical spectroscopy, ellipsometry, and Fourier space imaging. Polarization-insensitive planar omnidirectional diffraction will be demonstrated and engineered over a large and controllable range of

frequencies. Device applications to enhanced LEDs, novel lasers, and thin-film solar cells with enhanced absorption will be specifically targeted. Additionally, using Vogel spirals we investigate the direct (i.e. free space) generation of optical vortices, with well-defined and controllable values of orbital angular momentum, paving the way to the engineering and control of novel types of phase discontinuities (i.e., phase dislocation loops) in compact, chip-scale optical devices. Finally, we report on the design, modeling, and experimental demonstration of array-enhanced nanoantennas for polarization-controlled multispectral nanofocusing, nanoantennas for resonant near-field optical concentration of radiation to individual nanowires, and aperiodic double resonance surface enhanced Raman scattering substrates.

## Table of Contents

<b>1</b>	<b>Introduction .....</b>	<b>1</b>
1.1	Motivation.....	1
1.2	Outline.....	3
<b>2</b>	<b>Theoretical Background .....</b>	<b>6</b>
2.1	Electrodynamics.....	6
2.2	Electromagnetic Waves in Metals .....	9
2.2.1	Surface plasmon polaritons .....	11
2.2.2	Localized surface plasmons .....	13
2.3	Nanoparticle Coupling and Particle Arrays .....	15
2.3.1	Near-field coupling .....	15
2.3.2	Far-field and Fano-type Coupling.....	18
2.4	Nonlinear Optics .....	21
2.4.1	Nonlinear Media.....	22
2.4.2	Second-harmonic generation.....	23
<b>3</b>	<b>Computational Design Methods.....</b>	<b>26</b>
3.1	Analytical Multiple Scattering.....	26
3.1.1	Generalized Mie Theory.....	27
3.1.2	Coupled Dipole Approximation.....	31
3.2	Finite Element Modeling .....	34

3.3	Finite Difference Time Domain Modeling .....	39
<b>4</b>	<b>Nanofabrication Methods .....</b>	<b>46</b>
4.1	Fabrication of Nanoplasmonic Structures.....	46
4.1.1	Sample Cleaning and Spin-coating .....	47
4.1.2	Electron-Beam Lithography and Development.....	48
4.1.3	Metal Deposition and Lift-off .....	50
4.2	Fabrication of Dielectric Nanopillar Arrays .....	53
4.2.1	RF Sputter Deposition of Nanopillar Materials .....	54
4.2.2	Pillar Metal Mask Fabrication.....	56
4.2.3	Pillar Etching and Metal Removal .....	57
4.3	Photo-detector Device Fabrication .....	60
4.3.1	Fabrication of Optical Absorption Quantification Chip.....	63
<b>5</b>	<b>Deterministic Aperiodic Order .....</b>	<b>65</b>
5.1	Periodic and Quasi-Periodic Order .....	65
5.2	Beyond Quasicrystals: Aperiodic Order and Substitutions .....	70
5.2.1	Rotational Symmetry in Aperiodic Arrays.....	72
5.3	Classification of Aperiodic Structures .....	74
5.4	Conclusion .....	76
<b>6</b>	<b>Engineering Aperiodic Spiral Order .....</b>	<b>78</b>
6.1	Spiral Geometry .....	79

6.1.1	Irrational Spirals and Rational Approximations.....	85
6.1.2	Fourier Hankel Decomposition .....	92
6.2	Orbital Angular Momentum in Scattered Radiation.....	94
6.3	Conclusions.....	100
<b>7</b>	<b>Optical Properties of Dielectric Spirals.....</b>	<b>101</b>
7.1	Engineering Band Gaps and Band Edge Modes.....	101
7.1.1	Density of States and Optical Modes .....	111
7.1.2	Multifractal and scaling properties of Vogel spirals .....	114
7.1.3	Optical Mode Analysis of Vogel spirals .....	122
7.1.4	Band Edge Mode Formation and OAM.....	130
7.2	Dielectric Vogel Spiral Nanopillar Arrays .....	135
7.2.1	Motivation for Lasing in DANS.....	135
7.2.2	Band Gaps in GA-spirals.....	137
7.2.2	Additional Prospects for Lasing in Vogel Spirals .....	147
7.3	Near-field Coupling and Scattering in Dielectric Vogel Spirals .....	151
7.3.1	Experimental Methods .....	152
7.3.2	Results and Discussion.....	154
7.4	Conclusions.....	161
<b>8</b>	<b>Optical Properties of Plasmonic Spirals.....</b>	<b>163</b>



8.1	Plasmonic Vogel Spirals .....	163
8.1.1	Fourier Space Analysis.....	165
8.1.2	Dark-field Scattering Analysis .....	168
8.1.3	Planer Diffraction in Vogel Spirals .....	171
8.1.4	Circular Light Scattering in Vogel Spirals .....	174
8.1.5	Angular Momentum in Plasmonic Vogel Spirals .....	177
8.2	Thin-film Solar Cell Enhancement .....	180
8.2.1	Photovoltaic Principles.....	181
8.2.2	Plasmonics for Thin-film Enhancement.....	183
8.2.2	Plasmon-enhanced Large-Angle Scattering .....	186
8.2.3	Array Parameter Design for Photocurrent Enhancement .....	190
8.2.4	Device Fabrication .....	194
8.2.5	Absorption and Photocurrent Enhancement Results .....	198
8.3	Nonlinear Properties of Plasmonic Vogel Spirals .....	205
8.3.1	Enhanced 2 <sup>nd</sup> Harmonic Generation with Vogel Spiral Arrays ..	205
8.4	Conclusions.....	210
<b>9</b>	<b>Radiation-enhanced Plasmonic Coupling .....</b>	<b>213</b>
9.1	Nanoantennas for Multispectral Nanoscale Focusing.....	213
9.2	Coupling of GaAs Nanowires with Nanoantenna Arrays.....	221

9.2.1	Fabrication and design of antenna coupled GaAs NWs.....	222
9.2.2	Modeling of antenna coupled GaAs NWs.....	225
9.2.3	SH-E Spectroscopy of Antenna Coupled GaAs NWs.....	230
9.3	Conclusion .....	234
<b>10</b>	<b>Aperiodic SERS Substrates .....</b>	<b>236</b>
10.1	Surface Enhanced Raman Scattering .....	236
10.2	Coupled SERS System Design .....	241
10.3	Experimental SERS .....	246
10.3.1	SERS Fabrication and Sample Preparation.....	248
10.3.2	Experimental SERS Measurements .....	251
10.4	Conclusions.....	255
<b>11</b>	<b>Conclusions and Future Prospects.....</b>	<b>257</b>
11.1	Summary of Results .....	257
11.2	Future Prospects.....	259
	<b>Vita.....</b>	<b>284</b>

## List of Tables

Table 4.1: Sputter deposition parameters for a-Si:H, SiN and Er:SiN <sub>x</sub> films.....	56
Table 4.2: Etch recipes for SiN based films using RIE and Si films using an ICP RIE.....	58
Table 5.1: Substitution rules and reciprocal space spectral classification for Fibonacci, Thue-Morse and Rudin-Shapiro sequences. ....	70
Table 6.1: The Listing of irrational angles as well as their corresponding rational approximations ( $p/q$ ). $E/M$ is a measure of the difficulty to approximate the irrational number with a given a set of rational approximates, where $E$ is the absolute difference from the irrational value for a given $p/q$ and $M$ is the Hurwitz bound. ....	90
Table 7.1: Divergence angle structural perturbations of GA-spiral.....	102

## List of Figures

Figure 2.1: The Drude model dielectric function $\epsilon(\omega)$ of the free electron gas (solid line) fitted to the experimentally measured values (red dots) of the dielectric data for gold (Johnson and Christy, 1972). The model breaks down at visible and higher frequencies due to Interband transitions (Maier, 2007).....	10
Figure 2.2: Dispersion of SPP at a dielectric metal interface (solid), the dispersion of light in the dielectric medium (dotted), and the corresponding surface plasmon frequency. The parameters assumed are $\omega_p = 11.9989 \times 10^{15} \text{ s}^{-1}$ (silver) and $\epsilon_1=2.25$ .....	12
Figure 2.3: Diagram illustrating an excited localized surface plasmon by an external electric field (Willets and Van Duyne, 2007).....	13
Figure 2.4: (a) SEM micrograph of nanofabricated array of 88-nm diameter gold nanocylinder pairs with inter-particle separation of 12 nm (inset is a magnified SEM of a dimer pair). Extinction spectra show that the LSPR of the particle pair (b) red-shifts with decreasing gap for polarization along the inter-particle axis. (c) Blue-shifts very slightly with decreasing gap for polarization orthogonal to the inter-particle axis (Jain, Huang and El-Sayed, 2007). .....	17
Figure 2.5: Scattering efficiencies for a chain of 500 cylinders with height of 30 nm and diameter of 130 nm with (A) an incident angle of 0 degrees (normal incidence) and (B) with an incident angle of 30 degrees.....	19
Figure 3.1: Calculated spectra of the efficiency of absorption $Q_{abs}$ (red dashed), scattering $Q_{sca}$ (black dotted), and extinction $Q_{ext}$ (green solid) for gold nanospheres (a) $D = 40 \text{ nm}$ and (b) $D = 80 \text{ nm}$ (Jain et al., 2006). .....	29
Figure 3.2: Scattering efficiency and maximum field enhancement spectra of a dimer of spherical particles of 50 nm radius and with edge-edge distances: (a-b) $d = 10 \text{ nm}$ , (c-d) $d = 25 \text{ nm}$ , and (e-f) $d = 50 \text{ nm}$ calculated with the multi-particle Mie theory and the point dipole method (Forestiere et al., 2013).....	34
Figure 3.3: Example FEM mesh (Comsol 3.5a). Each cylinder is 200 nm in diameter. ....	36
Figure 3.4: (a) The demonstration of the Two-dimensional Yee cell, the basis of the FDTD algorithm. The cell edges are set to be the Magnetic field whereas the center of the cell is set to represent the Electric field. (b)	

Finite difference mesh for Yee ' s FDTD algorithm. Modified figure from (Jin, 2011). .....	40
Figure 3.5: A plane wave incident on the interface between the upper and lower half-spacers.....	44
Figure 4.1: The general process flow of EBL used of the fabrication of metallic nanostructures that are on an insulating substrate (i.e. quartz or fused silica). .....	46
Figure 4.2: The general process flow of EBL used of the fabrication of metallic nanostructures that are on a conductive substrate (i.e. Si, SiN, or metal surfaces).....	47
Figure 4.3: SEM micrographs of Au nanocylinders arrays (30 nm height). (a) Periodic array with particle diameter 215nm and edge to edge separation 15nm. (b) Thue-Morse array with particle diameter 195nm and minimum edge to edge separation of 30 nm. ....	52
Figure 4.4: The complete nanofabrication process flow used in the fabrication of dielectric nanopillar arrays on a transparent glass.....	54
Figure 4.5: SEM micrographs of fabricated nanopillar arrays. (a) 750 nm-tall SiN pillars with 150 nm top diameter (b) 1 $\mu$ m-tall a-Si:H nanopillars with 100nm diameters, (c) 1 $\mu$ m-tall c-Si nanopillars with 100nm diameters (d) c-Si aperiodic nanopillar spiral array with pillars 1 $\mu$ m-tall and 100nm diameters. ....	59
Figure 4.6: Si based Schottky photo-detector fabrication process flow. ....	61
Figure 4.7: SEM micrographs of fabricated nanopillar arrays. (a) 750 nm-tall SiN pillars with 150 nm top diameter.....	62
Figure 4.8: Fabrication process flow for optical absorption quantification chip.....	63
Figure 5.1: (a) Periodic array; (b) random array on periodic lattice; (c) Penrose array; (d) periodic array reciprocal space; (e) random array reciprocal space; (f) Penrose array reciprocal space. ....	67
Figure 5.2: (a) Classification of aperiodic systems according to the spectral measures of their Fourier transform and their Hamiltonian energy spectrum. Reprinted from (Maciá, 2006). ....	69
Figure 5.3: (a) Fibonacci array, $L = 13.4\mu\text{m}$ , generation 7 (b) Thue-Morse array, $L = 12.6\mu\text{m}$ ; (c) Rudin-Shapiro array, $L = 16.4\mu\text{m}$ , generation 6; (d) Fibonacci reciprocal space; (e) Thue-Morse reciprocal space; (f) Rudin-	

Shapiro reciprocal space. In all cases $\Delta = 400$ nm is the minimum center-to-center particle distance.....	71
Figure 5.4: (a) Danzer array, $L = 26.6$ $\mu\text{m}$ , generation 4 (b) Pinwheel array, $L = 16.1$ $\mu\text{m}$ ; (c) Danzer array reciprocal space; (e) Pinwheel array reciprocal space. In all cases $\Delta = 400$ nm is the minimum center-to-center particle distance. ....	73
Figure 5.5: (a) $H(q)$ plot for periodic array, plotting the first 3 Brillouin zones. (b) $H(q)$ plots for Fibonacci, Rudin-Shapiro and Thue-Morse arrays, plotting the first pseudo Brillouin zone. ....	75
Figure 6.1: Examples of spirals in nature: (a) seeds on the head of a sunflower(Image, "Sunflower Head," 2013), (b) nautilus shell (Image, "Nautilus Shell," 2013), (c) cactus leaves (Image, "Catus Leaves," 2013), and (d) spiral galaxy (NASA, 2013).....	78
Figure 6.2: Representations of the first 1000 particles plotted in the (a) GA-spiral ( $\alpha \approx 137.5077^\circ$ ), (b) $\alpha_1$ -spiral ( $\alpha = 137.3^\circ$ ), and (c) $\beta_4$ -spiral ( $\alpha = 137.6^\circ$ ). The calculated discrete Fourier transform of the (d) GA-spiral, (e) $\alpha_1$ -spiral, and (f) $\beta_4$ -spiral, where the plotted region is restricted to the first pseudo-Brillouin zone. $H(q)$ plots for the (g) GA-spiral, (h) $\alpha_1$ -spiral, and (i) $\beta_4$ -spiral.....	80
Figure 6.3: (a) Inverse of the scattering ring radius $v$ in the reciprocal space as a function of the average interparticle spacing for a GA-spiral (black), $\alpha_1$ -spiral (blue) and $\beta_4$ -spiral (red). (b) Calculated average (solid lines) and minimum (dotted lines) edge-to-edge interparticle separation as a function of the scaling factor for the g-spiral (black), $\alpha_1$ -spiral (blue) and $\beta_4$ -spiral (red). All the arrays considered in this analysis contain 8000 particles (Trevino, Cao and Dal Negro, 2011). ....	84
Figure 6.4: (a) The first 9 points of a Vogel spiral generated with $\alpha = 45^\circ$ . (b) First 100 points of Vogel spiral generated with $\alpha = 45^\circ$ (c) First 100 points of Vogel spiral generated with $\alpha = 172.8^\circ$ (Naylor, 2002). ....	85
Figure 6.5: The first 2000 points of the (a) $\pi$ -spiral, (b) $\mu$ -spiral, (c) $\tau$ -spiral, and (d) GA-spiral. ....	90
Figure 6.6: The calculated Fourier space for the (a) $\pi$ -spiral, (b) $\mu$ -spiral, (c) $\tau$ -spiral, and (d) GA-spiral, shown in Figure 6.5.....	92
Figure 6.7: $F(m)$ values calculated by the Fourier Hankel transform of the spiral geometry for the (a) $\pi$ -spiral, (b) $\mu$ -spiral, (c) $\tau$ -spiral, and (d) GA-spiral, shown in Figure 6.5. ....	94

Figure 6.8: Different columns show the beam helical structures, phase fronts, and corresponding intensity distributions (Wikipedia, 2013).	95
Figure 6.9: A simulated random optical field (speckle field), computed as a superposition of 729 plane waves with random phases and amplitudes. (a) Intensity; (b) phase, with inset showing singularities (strength +1 black, -1 white) (Dennis, O'Holleran and Padgett, 2009).	96
Figure 6.10: Fourier-Hankel decomposition of far-field scattered radiation from the (a) $\pi$ -spiral, (b) $\mu$ -spiral, (c) $\tau$ -spiral, and (d) GA-spiral, shown in Figure 6.5.	98
Figure 7.1: Vogel spiral array consisting of 1000 particles, created with a divergence angle of (a) $137.3^\circ$ ( $\alpha_1$ ), (b) $137.3692546^\circ$ ( $\alpha_2$ ), (c) $137.4038819^\circ$ ( $\alpha_3$ ), (d) $137.4731367^\circ$ ( $\alpha_4$ ), (e) $137.5077641^\circ$ (GA), (f) $137.5231367^\circ$ ( $\beta_1$ ), (g) $137.553882^\circ$ ( $\beta_2$ ), (h) $137.5692547^\circ$ ( $\beta_3$ ), (i) $137.6^\circ$ ( $\beta_4$ ).	103
Figure 7.2: Calculated spatial Fourier spectrum of the spiral structures shown in Figure 7.1. The reciprocal space structure of a (a) $\alpha_1$ -spiral, (b) $\alpha_2$ -spiral, (c) $\alpha_3$ -spiral, (d) $\alpha_4$ -spiral, (e) g.a-spiral, (f) $\beta_1$ -spiral (g) $\beta_2$ -spiral, (h) $\beta_3$ -spiral, and (i) $\beta_4$ -spiral are plotted where $\Delta$ represents the average edge-to-edge minimum inter-particle separation.	106
Figure 7.3: Pair correlation function $g(r)$ for spiral arrays with divergence angles between (a) $\alpha_1$ and the golden angle and (b) between the golden angle and $\beta_4$ .	107
Figure 7.4: Statistical distribution of spiral structures shown in Figure 7.1. Values represent the distance between neighboring particles $d$ normalized to the most probable value $d_0$ , obtained by Delaunay triangulation (increasing numerical values from blue to red colors). The Y-axis displays the fraction of $d$ in the total distribution.	109
Figure 7.5: Delaunay triangulation of spiral structures shown in Figure 7.1. The line segments that connect neighboring circles are color-coded by their lengths $d$ . The colors are consistent to those in Figure 7.4.	111
Figure 7.6: LDOS calculated at the center of the each spiral array as a function of normalized frequency for spiral arrays with divergence angles between (a) $\alpha_1$ and the golden angle and (b) between the golden angle and $\beta_4$ .	112
Figure 7.7: Multifractal singularity spectra $f(\alpha)$ of direct space spiral arrays ( $N=1000$ ) with divergence angles between (a) $\alpha_1$ and the golden angle and (b) between the golden angle and $\beta_4$ . Multifractal spectra for spiral	



	LDOS with divergence angles between (c) $\alpha_1$ and the golden angle and (d) between the golden angle and $\beta_4$ .....	119
Figure 7.8:	Quality factors of the air band edge modes for (a) $\alpha_1$ -spiral and (b) GA-spiral and $\beta_4$ -spiral versus normalized frequency.....	124
Figure 7.9:	Spatial distributions of electric field $E_z$ for the first three band edge modes of (a-c) class B in a $\alpha_1$ -spiral, (d-f) class A in a g-spiral and (g-i) class A in a $\beta_4$ -spiral. Spectrally located at $\omega/\omega_0 =$ (a) 0.9248, (b) 0.9290, (c) 0.9376, (d) 1.1629, (e) 1.1638, (f) 1.1657, (g) 1.1781, (h) 1.1900, and (i) 1.2152. ....	125
Figure 7.10:	Spatial distributions of electric field $E_z$ class $D_1$ band edge mode ( $\omega/\omega_0 = 1.053$ normalized as described in Section 3) in a $\alpha_1$ -spiral with (a) 1000 particles, (b) 750 particles and (c) 500 particles. (d) LDOS calculated at the center of $\alpha_1$ -spirals with varying number of particles between $n = 150$ and $n = 1000$ .....	127
Figure 7.11	Spatial distributions of electric field $E_z$ class B band edge mode ( $\omega/\omega_0 = 1.175$ normalized as described in Section 3) in a GA-spiral with (a) 1000 particles, (b) 750 particles and (c) 500 particles. (d) LDOS calculated at the center of GA-spirals with varying number of particles between $n = 150$ and $n = 1000$ .....	128
Figure 7.12:	Spatial distributions of electric field $E_z$ class A band edge mode ( $\omega/\omega_0 = 1.190$ normalized as described in Section 3) in a $\beta_4$ -spiral with (a) 1000 particles, (b) 750 particles and (c) 500 particles. (d) LDOS calculated at the center of $\beta_4$ -spirals with varying number of particles between $n=150$ and $n=1000$ .....	130
Figure 7.13:	(a) LDOS calculated at the center of the golden-angle spiral array as a function of the normalized frequency $d_o/\lambda$ . The regions at the lower and upper band edge where the band edge modes exist are highlighted. (a) Spatial distributions of magnetic field $H_z$ for the first three pairs of band edge modes of class A (Seng Fatt Liew et al., 2011). ....	131
Figure 7.14:	(a) Overlay of the region where class A modes are localized on the color map of the neighboring particles distance of air cylinders revealing class A modes stay mostly inside a ring labeled (ii) and sandwiched between two other rings (i) and (iii). (b) LDOS in the regions (i), (ii) and (iii) (Seng Fatt Liew et al., 2011). ....	132
Figure 7.15:	(a) Magnetic field distribution of mode A1 revealing the field maxima follow a family of 21 parastichies twisting in the CCW direction and another family of 89 parastichies in the CW direction (both are marked by the dashed arrows). (b) FBT of the field distribution in (a). (c)	



Region of the spiral array that contains 90% energy of mode A1. (d) FBT of the structure in (c) (Seng Fatt Liew et al., 2011). .....	133
Figure 7.16: (a) Multiple light scattering with gain. A random collection of microspheres containing laser dye is excited to obtain population inversion. The propagation of the light waves becomes that of an amplified random walk (Wiersma, 2008). (b) The modulus of the electric field for a calculated quasibound state of $nkr_0 \approx 129$ ( $n$ is the index of refraction, $k$ is the real part of the resonant wave vector) and $\epsilon = 0.12$ which is scarred by the triangular periodic orbits shown in the inset. The four points of low incidence angle which should emit strongly are indicated (Rex et al., 2002).....	136
Figure 7.17: Normalized transmission spectra for a-Si:H deposited with different $H_2/Ar$ gas flow ratios. ....	138
Figure 7.18: (a) SEM micrograph of hexagonal array of a-Si:H nanopillars and (b) diagram of ellipsometer reflection measurements taken on nanopillar arrays. ....	139
Figure 7.19: (a) SEM micrograph of hexagonal array of a-Si:H nanopillars and (b) diagram of ellipsometer reflection measurements taken on nanopillar.....	141
Figure 7.20: (a) Emission spectrum of Exciton IR-140 laser dye in PMMA film. (b) Process flow for embedding dye doped PMMA in nanopillar array. ....	143
Figure 7.21: (a) Calculated band diagram for hexagonal with $d = 105$ nm and $a = 200$ nm. (b) Top-down SEM micrograph of fabricated a-Si:H GA-spiral nanopillar array. (c) Angled SEM micrograph of array in (b), displaying pillar sidewall quality. ....	144
Figure 7.22: Measured ellipsometer parameters for a GA-spiral nanopillar array with filling fraction 27.3%: (a) $\tan(\psi)$ measured in air, (b) $\cos(\Delta)$ measured in air, (c) $\tan(\psi)$ measured with PMMA laser dye mixture, and (d) $\cos(\Delta)$ measured with PMMA laser dye mixture. ....	145
Figure 7.23: Measured ellipsometer parameters for a $\beta_4$ -spiral nanopillar array with filling fraction 27.3%: (a) $\tan(\psi)$ measured in air, (b) $\cos(\Delta)$ measured in air, (c) $\tan(\psi)$ measured with PMMA laser dye mixture, and (d) $\cos(\Delta)$ measured with PMMA laser dye mixture. ....	146
Figure 7.24: (a) Dark-field images of $\alpha_1$ -spirals with increasing average center-to-center separations, labeled above each array. (b) Dark-field scattering spectra for $\alpha_1$ -spirals shown in (a). (c) The peak scattering wavelength plotted as a function of average center-to-center spacing for the GA-spiral (black), $\alpha_1$ -spiral (red), and $\beta_4$ -spiral (blue).....	148

Figure 7.25: (a) SEM micrograph of directly EBL written GA-spiral hole array in a 120 nm-thick silk film. (b) AFM image of patterned film in (a). (c) AFM scan of single EBL written and developed hole in (a), showing hole depth through the entire silk film. ....	149
Figure 7.26: 2D FEM LDOS calculation at the center of a GA-spiral array with number of holes $N = 1000$ , $r/a = 0.395$ , index of silk $n_{\text{silk}} = 1.8$ and air holes $n_{\text{air}} = 1$ .....	150
Figure 7.27: (a) SEM micrograph of $\alpha_1$ -spiral nanopillar array with array diameter of 50 $\mu\text{m}$ , pillar diameter of 520 nm, and pillar height of 350 nm. (b) Scanning near-field optical microscope configuration with uncoated near-field probes in transmission geometry, excited with a diode laser ( $\lambda = 1556$ nm). ....	153
Figure 7.28: (a) Near-field optical map of an $\alpha_1$ -spiral with 50 $\mu\text{m}$ diameter excited at $\lambda = 1556$ nm, assembled by connecting multiple near-field scans collected on different $20 \times 20 \mu\text{m}^2$ areas. Outer circle defines the position of outer array edge. (b) Topography map of $\alpha_1$ -spiral acquired simultaneously with the optical data show in Figure 7.28a.....	154
Figure 7.29: Magnified image of the (a) optical near-field and the (b) topography of the $6 \times 6 \mu\text{m}^2$ region highlighted by the white squares in Figs. 7.28(a,b) respectively.....	155
Figure 7.30: (a) Simulated (3D FDTD) electric field intensity distribution of the first 500 nanopillars of an $\alpha_1$ -spiral, excited with a plane wave at $\lambda = 1550$ nm. The electric field is plotted at the top surface of the nanopillars (b) Magnified plot measuring $3.6 \times 3.6 \mu\text{m}^2$ of the region highlighted by orange box in Fig. 4a. The electric field distribution is plotted in the top plane (left) and bottom plane (right) of the nanopillars. The same field distributions of (a,b) are convolved with a Gaussian, characterized by a FWHM of 250 nm, and are plotted in (c,d) respectively.....	156
Figure 7.31: Numerical 3D FDTD calculations of the electric field intensity calculated with detectors placed at (a) 1 $\mu\text{m}$ and (b) 4 $\mu\text{m}$ above the $\alpha_1$ -spiral. $30 \times 30 \mu\text{m}^2$ area SNOM scans collected at a constant height modulus approximately (c) 2 $\mu\text{m}$ and (d) 6 $\mu\text{m}$ away from the sample surface, respectively. ....	158
Figure 8.1: SEM micrographs of (a) GA-spiral, (b) $\beta_4$ -spiral, (c) $\alpha_1$ -spiral Au nanoparticle array. The arrays have 27,778 particles with a diameter of 200nm. SEM micrographs of (d) GA-spiral, (e) $\beta_4$ -spiral, (f) $\alpha_1$ -spiral Au nanoparticle arrays containing 1,000 particles with a diameter of 200nm. (g-i). ....	165

Figure 8.2: Measured Fraunhofer far-field intensity for the (a) GA-spiral, (b) $\alpha_1$ -spiral, (c) $\beta_4$ -spiral Au nanoparticle array. Calculated DFT of the same arrays, cropped down to the approximate reciprocal space area measured the (d) GA-spiral, (e) $\alpha_1$ -spiral, (f) $\beta_4$ -spiral. ....	166
Figure 8.3: Experimentally measured far-field diffraction spectra of a g-spiral (8,000 particles) illuminated by a HeNe laser at 633nm, under different conditions: (a) Un-polarized, (b) circular polarized, (c) linear polarized ( $0^\circ$ ), (d) linear polarized light ( $60^\circ$ ). We observe that the vertical line common to all the diffraction spectra is an experimental artifact introduced by the CCD camera. ....	167
Figure 8.4: Measured dark-field scattering spectra of (a) GA-spiral with average interparticle separations $d$ equal to: 312nm (black, 27,778 particles), 398nm (blue, 20,408 particles), 568nm (red, 12,346 particles). (b) $\beta_4$ -spiral with average interparticle separations $d$ equal to: 220nm (black, 27,778 particles), 290nm (blue, 20,408 particles), 430nm (red, 12,346 particles). (c) GMT calculated scattering efficiency of (c) GA-spiral (1,500 particles) and (d) $\beta_4$ -spiral (1,500 particles) with average interparticle separations matching values in (a) and (b) respectively. ....	169
Figure 8.5: CCD image of light emission from a DCM dye layer (100 nm-thick) deposited onto: (a) homogeneous quartz substrate (b) dye emission from scattered light of $\beta_4$ -spiral (27,778 particles) with laser positioned at the center of the spiral. (c) and (d) dye emission from scattered light of $\beta_4$ -spiral with laser positioned off center of the spiral. The peak emission wavelength was 640 nm and the pump laser wavelength was 480 nm. Samples are pumped with the same power of 30mW. ....	173
Figure 8.6: Dark-field microscopy images of plasmonic spirals on quartz substrates. The samples consist of GA-spirals (a-c), $\alpha_1$ -spirals (d-f) and $\beta_4$ -spirals (g-i) of varying (average) interparticle separations, as follows: (a) 1240 nm, (b) 565 nm, (c) 310 nm, (d) 918 nm, (e) 418 nm, (f) 242 nm, (g) 906 nm, (h) 298 nm, (i) 208 nm. All the nanoparticles are Au nanocylinders of 200 nm diameter and 30nm height. ....	175
Figure 8.7: (a-c) Wavelength filtered (a: 585 nm long pass, (b) 360-460 nm band pass and (c) 490 nm – 560 nm band pass) dark-field images of an $\alpha_1$ -spiral with particle diameter of 200 nm and average separation of 242 nm. (d) dark-field image under white light illumination and unfiltered detection. (e-g) GMT calculated electric field amplitude at (f) 475 nm, (g) 510 nm, (e) 650 nm (h) incoherent sum (intensity addition) of the three scattering profiles e-g. All simulated arrays have 1,500 particles with a diameter of 200 nm. ....	176

Figure 8.8: Analytical GMT simulations of an $\beta_4$ -spiral. Simulation consists of 1500 Au spheres of diameter 200 nm excited with a plane wave $\lambda = 650$ nm. Scattered intensity profiles calculated at (a) 1 $\mu\text{m}$ , (b) 3 $\mu\text{m}$ , and (c) 10 $\mu\text{m}$ from the plane of the array. (d) magnitude of the azimuthal-component of the linear momentum density of the scattered electromagnetic field at 10 $\mu\text{m}$ above (time average Poynting vector normalized to $c^2$ ).....	179
Figure 8.9: (a) The basic scheme of a crystalline Si solar cell. (b) Band diagram of the photovoltaic effect in a p-n junction device, where a photon generates a photon-hole pair which is swept out due to the presence of an electric field.....	182
Figure 8.10: Plasmonic light-trapping schemes for thin-film solar cells. (a) Light trapping by scattering from metal nanoparticles at the surface of the solar cell. (b) Light trapping by the excitation of localized surface plasmons in metal nanoparticles embedded in the semiconductor. (c) Light trapping by the excitation of surface plasmon polaritons at the metal/semiconductor interface.....	185
Figure 8.11: Calculated radiation diagrams as a function of the inclination angle (Theta) for a periodic array with $N=3505$ (a) and a GA-spiral with $N=1810$ (b) for three different wavelengths, namely 480 nm (Blue), 520 nm (Green), and 650 nm (Red). The periodic array has a lattice spacing of 300 nm, the GA-spiral features an averaged minimum inter-particle separation of 420 nm. (The interparticle separations in both cases results from the experimental optimization performed in 8.2.5) .....	189
Figure 8.12: (a) Schematic cross section (not to scale) of the performed FDTD simulations. The red and blue dashed lines indicate the limits of the simulation box where PML boundary conditions and periodic boundary conditions are enforced, respectively. The black dashed lines are the monitors where power fluxes are calculated. (b) Fraction of the incident power absorbed into a periodic array of gold nanocylinders ( $D=100\text{nm}$ , $h=30\text{nm}$ ) and on a 50nm thick Silicon substrate, calculated with FDTD. Predicted absorption enhancement within a 50nm thick Si substrate due to a periodic array of gold nanocylinders ( $D=100\text{nm}$ , $h=30\text{nm}$ ) with respect to the bare substrate (c) and the correspondent integrated enhancement factor (d). .....	192
Figure 8.13: Representative SEM micrographs of a (a) periodic and (b) GA-Spiral array of Au nanoparticles with lattice spacing 300nm and average center to center spacing of 425nm respectively. The cylindrical particle diameters are 100nm, while the entire array geometry has a 100 $\mu\text{m}$ circular diameter.....	195



Figure 8.14: (a) Device cross-section of stack used to quantify absorption enhancement. (b) Experimental reflection measurement configuration used calculate absorption enhancement. Reflection of a broadband white light source was measured by a CCD detector through excitation and collection of a 50x objective (NA = 0.5). (c) Device cross-section of the SOI Schottky photo-detector with plasmonic arrays integrated onto the absorbing surface. (d) Bright-field microscope image of the device with five 100 $\mu\text{m}$ diameter GA-spirals integrated into the active device area. ....	198
Figure 8.15: (a) Experimental absorption enhancement for GA-spirals (solid lines) with average center to center spacing of 120 nm, 425 nm, and 680 nm and periodic arrays (dashed lines) with lattice spacing of 150 nm, 300 nm, and 525 nm. (b) Integrated absorption enhancement ratio for GA-spirals (red, solid) and periodic (black, dashed) arrays of various interparticle spacing. Enhancement ratios are calculated by the ratio of the integrated measure with the nanopatterned device verses the integrated measure without nanopatterning.....	200
Figure 8.16: (a) Periodic array photocurrent spectrum with lattice spacing of 300 nm (solid) and empty neighbor reference cell (dashed). (b) GA-spiral array photocurrent with average center to center spacing of 425 nm (solid) and empty neighbor references cells (dashed). (c) Spectral photocurrent enhancement spectra for GA-spiral arrays (red, $a = 425$ nm) and periodic arrays (black dashed, $a = 300$ nm). (d) Integrated photocurrent enhancement ratio for GA-spiral (red) and periodic (black dashed) arrays of different center to center particle spacing. ....	202
Figure 8.17: SEM micrographs of periodic (a), Fibonacci (b) and GA-spiral (c) arrays of 200nm-diameter cylindrical gold nanoparticles with a particle separation of 60 nm. ....	207
Figure 8.18: (a) Intensity of the collected SHG as a function of interparticle separation for periodic (red squares), Fibonacci (green triangles) and GA-spiral (blue circles) arrays; (a inset) Filling fraction of Au for the arrays following the same coloring scheme. (b) Correlation diagram between SHG and pump collected signals. ....	208
Figure 8.19: Near-field distribution at the pump frequency over periodic (a) and GA-spiral (b) arrays with interparticle separation $L = 60$ nm. Near-field distribution at the fundamental frequency over periodic (c) and GA-spiral (d) arrays with interparticle separation $L = 611$ nm. All the near-field maps are plotted in logscale. ....	210
Figure 9.1: (a) Antenna chain designed for near-field enhancement at 780 nm and near-field calculation of the electric field distribution in the dashed area at that wavelength. (b) Antenna chain designed for near-field	

enhancement at 860 nm and near-field calculation of the electric field distribution in the dashed area at that wavelength. (c) Maximum near-field enhancement spectra in the DBA region for (black) DBA only, (blue) DBA and linear grating optimized for 780 nm (configuration 9.1a), and (red) DBA and linear grating optimized for 860 nm (configuration 9.1b).....	216
Figure 9.2: (a) Optimized multi-wavelength nanoantenna array geometry. (b) Double bow-tie antenna (DBA) at center of antenna array. (c) SEM micrograph of EBL fabricated gold nanoantenna array. (d) Close up SEM micrograph of DBA.....	217
Figure 9.3: (a) Pump ( $\lambda_{\omega} = 760$ nm) power dependence of SH signal ( $\lambda_{2\omega} = 380$ nm) from representative array. (Inset) Diagram of SH-E experimental setup. (b) Experimentally measured SH-E spectra of the antenna arrays as a function of the polarization angle. (c) FDTD calculation of the spatially averaged near-field enhancement of the nanoantenna arrays for plane wave excitation with a polarization angle of $0^\circ$ (red) and $90^\circ$ (black).....	219
Figure 9.4: (a) Schematic of GaAs nanowire coupled to nanoantenna. SEM micrographs of NW coupled nanoantennas with lattice spacing $a = 840$ nm and nanocylinder edge to NW edge distance $d$ of (b) 215 nm, (c) 65 nm, (d) 15 nm, (e) 10 nm.....	224
Figure 9.5: 3D FDTD calculated scattering cross-section for isolated NW and antenna coupled NWs, as labeled in the figure. ....	226
Figure 9.6: Calculated electric near-field distribution of the nanoantenna coupled NW system with $d = 215$ nm, plotted in the horizontal plane of the array (half-way up the cylinder in the z-dir) at $\lambda = 855$ nm. The field is plotted for (a) longitudinal and (b) transverse polarization with respect to the wire, as labeled in the figure by the white arrows. ....	227
Figure 9.7: Calculated electric near-field distribution of the nanoantenna coupled NW system with $d = 90$ nm, plotted in the horizontal plane of the array (half-way up the cylinder in the z-dir). The field is plotted at $\lambda = 735$ nm for (a) longitudinal and (b) transverse excitation and at $\lambda = 1150$ nm for (c) longitudinal and (d) transverse excitation. The magnified region denoted by the dashed box in panel (d) is plotted in panel (e). ....	228
Figure 9.8: Cross-sectional average (red) and maximum (black) electric field enhancement values inside the region of the NW are plotted for the case of (a) isolated NW, (b) isolated dimer pair with $d = 10$ nm, (c) antenna coupled NW with $d = 215$ nm, and (c) antenna coupled NW with $d = 10$	

nm. Insets are electric field cross-sections, plotted at 1165 nm in log-scale for each configuration.....	229
Figure 9.9: (a) Diagram of SH-E experimental setup. (b) Pump ( $\lambda_{\omega} = 760$ nm) power dependence of SH signal ( $\lambda_{2\omega} = 380$ nm) from representative array ( $d = 10$ nm). (c) The peak wavelengths of the measured SHG spectra are plotted as a function of pump wavelength, resulting in a slope of 0.5. ....	232
Figure 9.10: Experimentally measured SH-E spectra from NW only and NW-coupled antennas with $d = 215$ nm, $d = 65$ nm, $d = 15$ nm and $d = 10$ nm, as labeled in the figure.....	233
Figure 10.1: Schematic depiction of (a) fluorescence and (b) Raman scattering energy level pictures and representative spectra. Image modified from (Kneipp et al., 2002). ....	238
Figure 10.2: Schematic of plasmonic double layer coupled SERS substrate. The structure consists of Au nanocylinders arrays fabricated onto a thin SiO <sub>2</sub> spacer on top of a continuous and optically-thick Au film. ....	242
Figure 10.3: Maximum intensity enhancement spectra calculated on the surface of a single Au nanocylinder by 3D FDTD. (a) Calculated for a Au cylinder on a SiO <sub>2</sub> substrate with $d = 130, 150, 175,$ and $200$ nm. (b) Calculated for a Au cylinder ( $d = 150$ nm) on top of a SiO <sub>2</sub> with varying thickness of 20, 30, 40, 50, and 70 nm on top of an optically thick Au layer.....	243
Figure 10.4: Maximum intensity enhancement spectra calculated on the surface of a single Au nanocylinder by 3D FDTD. (a) Calculated for a Au cylinder with $d = 80, 90, 100, 110,$ and $120$ nm on top of a SiO <sub>2</sub> layer $t_{ox} = 10$ nm-thick on top of an optically-thick Au layer. (b) Calculated for a Au cylinder with $d = 100, 120, 130, 140,$ and $150$ nm on top of a SiO <sub>2</sub> layer $t_{ox} = 30$ nm-thick on top of an optically-thick Au layer. ....	244
Figure 10.5: 3D FDTD calculated cross-sectional field plots (log scale) at $\lambda = 785$ nm for the optimized Au nanocylinder (a) on quartz ( $d = 175$ nm) and (b) on a spacer/Au stack with $d = 130$ nm and $t_{ox} = 30$ nm-thick. Polarization orientation as noted in (a). Cross-sections plotted on the same scale shown to the right of (b). ....	245
Figure 10.6: Direct space representations of (a) co-prime array and (b) Galois array. First pseudo-Brillouin zone plotted, as calculated by DFT, for the (c) Co-prime array and (d) Galois array. ....	247
Figure 10.7: SEM micrographs of Au nanocylinder ( $d = 175$ nm) fabricated on a quartz substrate in a (a) Co-prime array, (b) Galois array, (c) Rudin-	

Shapiro array, and (d) Fibonacci array, with minimum edge-to-edge separation of 25 nm for all arrays shown. ....	249
Figure 10.8: SEM micrographs of Au nanocylinder ( $d = 130$ nm) fabricated on a SiO <sub>2</sub> /Au stack with $d = 130$ nm and $t_{ox} = 30$ nm-thick in a (a) Co-prime array, (b) Galois array, (c) Rudin-Shapiro array, and (d) Fibonacci array, with minimum edge-to-edge separation of 25 nm for all arrays shown. ....	249
Figure 10.9: High magnification SEM micrographs of nanocylinders (a) shown in Figure 10.5d and (b) shown in Figure 10.6d. ....	250
Figure 10.10: Experimental stokes SERS spectra of pMA on (a) Fibonacci array of Au nanocylinders on quartz ( $d = 175$ nm ) with minimum inter-particle separations listed in the figure. Experimental stokes SERS spectra of pMA on (b) Fibonacci array of Au nanocylinders on a spacer/Au stack with $d = 130$ nm and $t_{ox} = 30$ nm-thick and with minimum inter-particle separations listed in the figure. ....	252
Figure 10.11: Enhancement factors calculated from experimental data by using Eq. 2 for aperiodic arrays of Au nanocylinders (a) on quartz ( $d = 175$ nm ) and (b) on a SiO <sub>2</sub> /Au stack with $d = 130$ nm and $t_{ox} = 30$ nm-thick. ....	255
Figure 11.1: Proposed modification to the classification of aperiodic systems according to the spectral measures of their Fourier transform and their Hamiltonian energy spectrum (Barber, 2008). ....	260
Figure 11.2: Proposed thin-film solar cell integrated with plasmonic Vogel spiral back reflector. ....	261



## List of Abbreviations

<b>3D</b>	Three Dimensional
<b>Ag</b>	Silver
<b>Al</b>	Aluminum
<b>a-Si:H</b>	Hydrogenated Amorphous Silicon
<b>Au</b>	Gold
<b>BOE</b>	Buffered Oxide Etch
<b>CCP</b>	Capacitive Coupled Plasma
<b>CCW</b>	Counter Clock-Wise
<b>CDA</b>	Coupled Dipole Approximation
<b>Cr</b>	Chrome
<b>CW</b>	Clock-Wise
<b>DA</b>	Deterministic Aperiodic
<b>DANS</b>	Deterministic Aperiodic NanoStructures
<b>DBA</b>	Double Bow-tie Antenna
<b>DCM</b>	Dichloromethane
<b>DFT</b>	Discrete Fourier Transform
<b>DI</b>	De-ionized
<b>EBL</b>	Electron Beam Lithography
<b>Er:SiNx</b>	Erbium doped Silicon Nitride
<b>FDTD</b>	Finite Difference Time Domain
<b>FEM</b>	Finite Element Modeling

<b>FHD</b>	Fourier Hankel Decomposition
<b>GaAs</b>	Gallium Arsenide
<b>GMT</b>	Generalized Mie Theory
<b>ICP</b>	Inductively Coupled Plasma
<b>IPA</b>	Isopropanol
<b>IR</b>	Infrared
<b>ITO</b>	Indium Tin Oxide
<b>LDOS</b>	Local Density of States
<b>LSP</b>	Localized Surface Plasmon
<b>LSPR</b>	Localized Surface Plasmon Resonance
<b>MIBK</b>	Methylisobutyle Ketone
<b>MMA</b>	Methyl Methacryllate
<b>MPB</b>	MIT Photonic-Bands
<b>NIR</b>	Near-Infrared
<b>NW</b>	Nanowire
<b>OAM</b>	Orbital Angular Momentum
<b>PBG</b>	Photonic Band Gap
<b>PDE</b>	Partial Differential Equation
<b>PhC</b>	Photonic Crystal
<b>pMA</b>	Para-Mercaptoaniline
<b>PML</b>	Perfectly Matched Layers
<b>PMMA</b>	Poly Methyl Methacryllate

<b>PV</b>	Photovoltaics
<b>RCWA</b>	Rigorous Coupled-Wave Analysis
<b>RF</b>	Radio Frequency
<b>RIE</b>	Reactive Ion Etch
<b>SC</b>	Standard Clean
<b>SEM</b>	Scanning Electron Microscopy
<b>SERS</b>	Surface Enhance Raman Scattering
<b>SFG</b>	Sum Frequency Generation
<b>SH-E</b>	Second Harmonic Excitation
<b>SHG</b>	Second Harmonic Generation
<b>Si</b>	Silicon
<b>SiN</b>	Silicon Nitride
<b>SNOM</b>	Scanning Near-field Optical Microscopy
<b>SP</b>	Surface Plasmon
<b>SPP</b>	Surface Plasmon Polariton
<b>Ti</b>	Titanium

## **Chapter 1**

### **1 Introduction**

#### 1.1 Motivation

Over the last few decades, the steady progress regarding our ability to fabricate photonic nanostructures has led to a rich variety of different one-, two-, and three-dimensional dielectric and metallic structures. These structures exhibit novel and fascinating optical properties, providing an unprecedented control of light propagation and light-matter interaction. Light-matter interaction has turned into a rapidly growing field, yielding the potential to extend concepts and functionalities of conventional optics down to the nanometer scale. This ability to control at light at sub-wavelength scales provides tremendous opportunities for the creation of new materials, functionalities and device applications. A significant portion of this research has been conducted on the periodic arrangements of dielectric and metallo-dielectric systems; focused on the basic physical principles and potential applications associated with the existence of Bragg scattering. While these structures are relatively simple, numerous new devices have been successfully engineered for enhanced light-matter interaction in specific spectral regions. A second methodology is in the utilization of randomly distributed nanostructures for broadband light-matter enhancement. Electromagnetic phenomena in random media, such as dielectric powders, rough thin films, colloidal aggregates and others, have been intensely studied for the last three decades (Shalaev, 2002). While there are numerous

practical applications utilizing periodic media, few devices based on disordered media have been realized due to their inherent irreproducibility. In order to exploit the desirable properties of randomized nanostructures and have the same engineerability found in periodic arrays, the majority of efforts in this dissertation focus on a class of structures known as Deterministic Aperiodic NanoStructures (DANS).

Recent advancements in the design and fabrication of DANS have provided novel opportunities for the creation and manipulation of complex scattering resonances and nanoscale localized optical fields (Dal Negro and Feng, 2007; Dal Negro, Feng and Gopinath, 2008; Gopinath et al., 2008; Luck, 1989). DANS are inhomogeneous nanostructures in which the refractive index fluctuates over multiple length scales comparable to or smaller than the wavelength of light. These structures are designed by mathematical rules, which interpolate between periodicity and randomness in a tunable fashion (Dal Negro, Feng and Gopinath, 2008; Gopinath et al., 2008; Barber, 2008; Steurer and Sutter-Widmer, 2007). DANS provide unprecedented opportunities to manipulate light states, diffraction diagrams, and optical cross-sections for nanophotonic and nanoplasmonic device technologies (Dal Negro and Boriskina, 2012). Such applications are enabled by DANS as a result of their engineerable complex Fourier space. In particular, their reciprocal Fourier space ranges from a discrete set of  $\delta$ -like Bragg peaks (i.e., pure-point spectrum), such as for periodic and quasiperiodic crystals, to a continuous spectrum (i.e., absence of Bragg peaks), as encountered in amorphous systems (Barber, 2008; Janot, 1997). Moreover, due to a far richer structural complexity compared to periodic, quasiperiodic, and disordered random media, the Fourier space of

DANS can encode non-crystallographic point-symmetries with rotational axes of arbitrary order (Senechal, 1996; Vasconcelos and Albuquerque, 1998).

On the other hand, disordered and amorphous structures are characterized by diffuse Fourier spectra which can support continuous rotational symmetry (Janot, 1997; Florescu, Torquato and Steinhardt, 2009). Only recently, have deterministic structures with infinite-order rotational symmetry in reciprocal space have been constructed, utilizing the Pinwheel tiling. Its diffraction pattern approximates continuous circular symmetry in the limit of an infinite-size structure (Senechal, 1996). This dissertation will focus on a set of unique finite-size particle arrays with continuous rotational symmetry in Fourier space, obtained by engineering aperiodic spiral order. Such arrays are known as Vogel spirals. It will be systematically shown, that Vogel spiral arrays provide a diverse photonic platform for engineering planar diffraction, enhanced light-matter coupling, large photonic band-gaps with unique band-edge modes, and scattered electric fields carrying discrete orbital angular momentum values.

## 1.2 Outline

This thesis will begin with a review of fundamentals of photonics and plasmonics followed by an introduction to the various computational design methods utilized throughout this study. Chapter 4 will describe the various nanofabrication techniques used to fabricate photonic and plasmonic device structures experimentally investigated in this thesis. Chapter 5 will introduce the field of DANS and provide an overview of relevant current and past works. The chapter will conclude by highlighting the need for

additional studies of a unique type of DANC geometry, known as a Vogel Spiral, which will be the central point of Chapter 6. A detailed study of various Vogel spiral geometric properties will be presented with attention to the potential implications on the structure's photonic properties.

Using Vogel spirals as a platform, the novel regime of “circular multiple light scattering” will be investigated. It will be shown both experimentally and theoretically that rotational symmetry in diffused reciprocal space gives rise to polarization-insensitive planar diffraction over a large and controllable range of wavelengths. Chapter 7 presents the optical properties of dielectric Vogel spiral arrays. Studies will be presented on band-gap and band-edge mode engineering, the experimental measurement of band-gaps, discussions on the prospects for lasing in spiral nanopillar arrays, as well a study of near-field coupling in Vogel spiral arrays. Chapter 8 covers the application of the Vogel spiral platform in plasmonic configurations. The unique scattering properties, thin-film solar cell enhancement, second harmonic generation and orbital angular momentum generation will all be discussed in this context.

Chapter 9 departs from the spiral platform to investigate the engineering of radiation-enhanced plasmonic coupling. These efforts focus on photonic-plasmonic coupling for nanoscale focusing applications including, optical biosensing, photo-detection, and nonlinear plasmonics. Additionally, Chapter 10 explores surface enhanced Raman spectroscopy (SERS), utilizing various aperiodic geometries and substrate

configurations. Final conclusions and future prospects are discussed in the last chapter of this dissertation.



## Chapter 2

### 2 Theoretical Background

This chapter summarizes the fundamental concepts of electromagnetic theory pertinent for this thesis. In particular, I will discuss the basic concepts of electrodynamics in matter, propagating and localized surface plasmons, and the physics of nanoparticle coupling both in the near-field and far-field. This section of the thesis is intended to serve only as an introduction to specific electrodynamic properties. For comprehensive treatments of electromagnetics and plasmonics, the reader is encouraged to review the textbooks “Classical Electrodynamics ” by Jackson(Jackson, 1975), “Plasmonics: Fundamentals and Applications” by Stefan Maier (Maier, 2007) and “Principles of Nano-Optics” by Novotny (Novotny and Hecht, 2011).

#### 2.1 Electrodynamics

In describing light-matter interactions, the discussion begins in a classical framework based on Maxwell's equations. In this chapter, the macroscopic Maxwell equations will be presented, utilizing a phenomenological approach. In doing so, the fundamental interactions between charged particles inside the media and electromagnetic fields are not taken into account. This approach is valid since the rapidly varying microscopic fields are averaged over distances much larger than the underlying microstructure (Maier, 2007). In the absence of space charge and currents, we have the macroscopic Maxwell's equations:

$$\nabla \cdot \mathbf{D} = \rho_{ext} \quad (2.1)$$

$$\nabla \cdot \mathbf{B} = 0 \quad (2.2)$$

$$\nabla \times \mathbf{E} = -\frac{\partial \mathbf{B}}{\partial t} \quad (2.3)$$

$$\nabla \times \mathbf{H} = \mathbf{J}_{ext} + \frac{\partial \mathbf{D}}{\partial t} \quad (2.4)$$

The equations relate the four macroscopic fields  $\mathbf{D}$  (dielectric displacement),  $\mathbf{E}$  (electric field),  $\mathbf{H}$  (magnetic field), and  $\mathbf{B}$  (magnetic flux density) with the external charge and current densities  $\rho_{ext}$  and  $\mathbf{J}_{ext}$ . Additionally, the four macroscopic fields can be further associated through the polarization  $\mathbf{P}$  and the magnetization  $\mathbf{M}$  by:

$$\mathbf{D} = \varepsilon_0 \mathbf{E} + \mathbf{P} \quad (2.5)$$

$$\mathbf{H} = \frac{1}{\mu_0} \mathbf{B} - \mathbf{M} \quad (2.6)$$

where  $\varepsilon_0$  is the electric permittivity ( $\sim 8.854 \times 10^{-12}$  F/m) of vacuum and  $\mu_0$  is the magnetic permeability ( $\sim 1.257 \times 10^{-6}$  H/m) of vacuum. In addition, we have the following constitutive relations for linear, isotropic and non-magnetic materials:

$$\mathbf{D} = \varepsilon_0 \varepsilon \mathbf{E} \quad (2.7)$$

$$\mathbf{B} = \mu_0 \mu \mathbf{H} \quad (2.8)$$

$$\mathbf{P} = \varepsilon_0 \chi \mathbf{E} \quad (2.9)$$

$$\mathbf{J} = \sigma \mathbf{E} \quad (2.10)$$

where Equation (2.7) relates the dielectric displacement,  $\mathbf{D}$ , to the electric field,  $\mathbf{E}$ , through the dielectric constant,  $\epsilon$ . Equation (2.8) relates the magnetic induction,  $\mathbf{B}$ , to the magnetic field,  $\mathbf{H}$ , through the permeability,  $\mu$ . Equation (2.9) relates the polarization,  $\mathbf{P}$ , to the electric field,  $\mathbf{E}$ , through the dielectric susceptibility,  $\chi = \epsilon - 1$ . The last linear constitutive relationship defines the internal current density  $\mathbf{J}$  by the electric field and the conductivity  $\sigma$  in Equation (2.10). In these constitutive equations,  $\epsilon = \epsilon_1 + i \epsilon_2$  represents the complex dielectric function of a material. While this representation of the material's optical constants is more explicitly used with Maxwell's equations, an equivalent form of this property is given by the complex index of refraction:  $\tilde{n} = n + i\kappa$ . Here,  $n$  is the ratio of the speed of light in vacuum to the speed of light in the material and  $\kappa$  is the extinction coefficient of light within the material. This representation is more directly related to the experimental observation of light interacting with matter. Depending on the situation, the two equivalent forms are used and are related by:

$$\epsilon_1 = n^2 - \kappa^2 \quad (2.11)$$

$$\epsilon_2 = 2n\kappa \quad (2.12)$$

$$n = \sqrt{\frac{\epsilon_1}{2} + \frac{1}{2}\sqrt{\epsilon_1^2 + \epsilon_2^2}} \quad (2.13)$$

$$\kappa = \frac{\epsilon_2}{2n} \quad (2.14)$$

where  $\kappa$  is related to the absorption coefficient  $\alpha$  of light propagating through the material by  $\alpha = 2\kappa\omega/c$ .

## 2.2 Electromagnetic Waves in Metals

The transport properties of electrons in metals were first successfully described by German physicist Paul Drude in the early 1900's when he applied the kinetic theory of gases to a metal, considered as a gas of electrons (Drude, 1900). The theory, known as the Drude model, assumes the conduction electrons in a metal can be treated as molecules in the kinetic gas theory. Drude proposed that the electrons are moving while the positive ionic background of the metal is immobile. During their flight, the electrons scatter on both the positive background as well as with other electrons. In this model, details of the lattice potential and electron-electron potential interactions are not accounted for; instead the band structure aspects are incorporated into the effective optical mass  $m$  of each electron (Maier, 2007). According to this model, the dielectric function of such a free electron gas can be represented as:

$$\varepsilon(\omega) = 1 - \frac{\omega_p^2}{\omega^2 + i\gamma\omega} \quad (2.15)$$

where  $\omega_p^2 = \frac{ne^2}{\varepsilon_0 m}$  is the *plasma frequency* of the free electron gas,  $\gamma = \frac{1}{\tau}$  is the characteristic collision frequency,  $\tau$  is the relaxation time of the free electron gas,  $n$  is the electron density, and  $e$  the unit charge of the electron. The plasma frequency is a resonance that increases with the electron density  $n$ , since the electric restoring force is proportional to the displaced charge (analogous to the force constant of a spring):  $\omega_p \propto \sqrt{n}$ . These electron gas oscillations in bulk metals are known as *bulk or volume*

*plasmons*. They are classically one-dimensional longitudinal oscillations of a free electron gas in a lattice that has positive ion background of atom nuclei of metal. Because of its longitudinal nature, a volume plasmon cannot be excited by a transverse electromagnetic wave such as a plane wave. This model gives a useful approximation of the dielectric function of a metal, given there are no interband transitions. In noble metals where interband transitions occur at optical frequencies, the model however breaks down. This is clearly demonstrated in Figure 2.1 where the dielectric function of gold is fitted to experimentally measured values (Maier, 2007). A similar breakdown of the model occurs for silver, the other predominately utilized metal in plasmonic studies occurring in the visible and near-infrared.

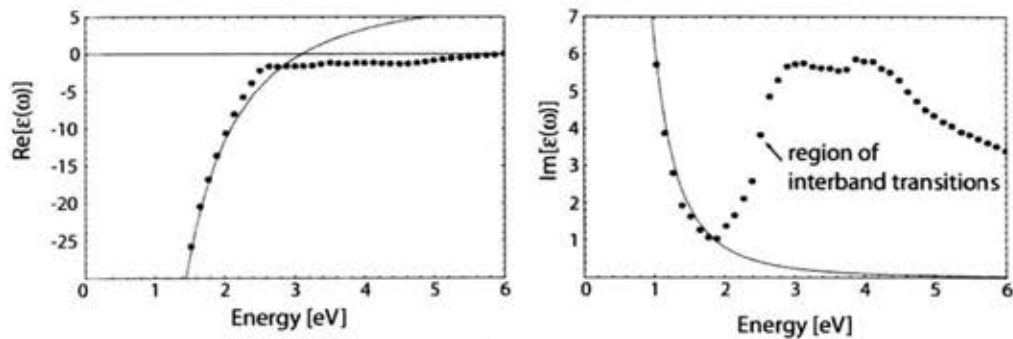


**Figure 2.1:** The Drude model dielectric function  $\epsilon(\omega)$  of the free electron gas (solid line) fitted to the experimentally measured values (red dots) of the dielectric data for gold (Johnson and Christy, 1972). The model breaks down at visible and higher frequencies due to Interband transitions (Maier, 2007).

The issue of interband transitions is addressed by the Drude-Lorentz model, which expresses the permittivity with a series of additive Lorentz-oscillator terms. The frequency depended dielectric function then becomes:

$$\varepsilon(\omega) = \varepsilon_\infty - \frac{\omega_p^2}{\omega(\omega + i\gamma_0)} + \sum_i \frac{A_i}{\omega_i^2 - \omega^2 - i\gamma_i\omega}, \quad (2.16)$$

where  $A_i$ ,  $\gamma_i$  and  $\omega_i$  are constants that depend on the specific interband transition being considered (Maier, 2007). By adding a Lorentzian term to the widely used Drude model, the dispersion curve of gold and silver have been successfully modeled over a wider spectrum possible than with the single Drude model (Vial et al., 2005; Hao and Nordlander, 2007).

### 2.2.1 Surface plasmon polaritons

Surface plasmon polaritons (SPPs) are excited electromagnetic modes that are propagating at the interface of a dielectric and a conductor. The term "polariton" refers to the quasi-particle nature of the SPPs. Generally, a surface plasmon (SP) is an oscillation of conductor's free electron plasma caused by EM interference, for example by light or an energetic electron beam. A SPP is specifically a photon coupled to the plasmon, which is bound to the surface of the metal. SPPs have both a transverse and longitudinal oscillation character. Surface plasmons are obtained from solutions of Laplace's equation for a scalar potential that propagate in a wavelike fashion along a planar dielectric-metal interface, and whose amplitudes decay exponentially with increasing distance from the interface into each medium. They are therefore electrostatic surface waves. One can think of them as related to non-propagating collective vibrations of the electron plasma near the metal surface.

In 1954 Ritchie *et al.* investigated the loss spectra of low energy electron beams in thin metallic films. Energy losses at multiples of  $\hbar\omega_p$  were expected due to bulk plasmon excitation; however energy losses at  $\hbar\omega_p/\sqrt{2}$  were measured instead (Ritchie, 1957). These losses correspond to the plasmon frequency ( $\omega_{sp}$ ) for the SPP:

$$\omega_{sp} = \frac{\omega_p}{\sqrt{1 + \epsilon}} \quad (2.17)$$

where  $\epsilon$  is the relative permittivity of the environment, in this case air where  $\epsilon = 1$ . The corresponding dispersion curve is shown in Fig. 2.2.

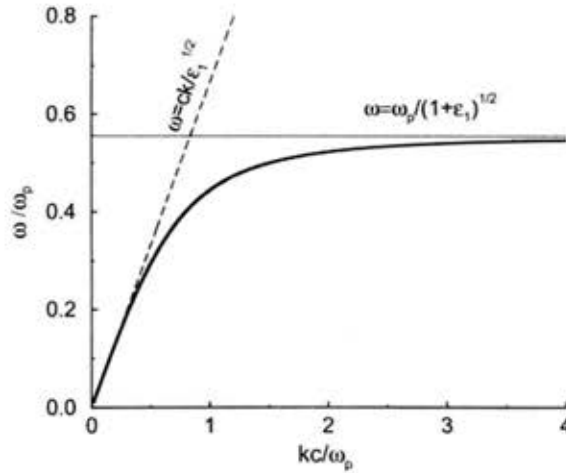


**Figure 2.2:** Dispersion of SPP at a dielectric metal interface (solid), the dispersion of light in the dielectric medium (dotted), and the corresponding surface plasmon frequency. The parameters assumed are  $\omega_p = 11.9989 \times 10^{15} \text{ s}^{-1}$  (silver) and  $\epsilon_1 = 2.25$ .

A key observation of the SPP dispersion curve is that it lies to the right of the dispersion curve of light in the dielectric medium,  $\omega = ck / \epsilon_1^{1/2}$ , the so-called dielectric light line. Consequently, the SPP cannot radiate light into the dielectric medium, and cannot be excited with conventional illumination from the adjacent dielectric.

### 2.2.2 Localized surface plasmons

In contrast to propagating SPPs, I will now present non-propagating excitations of the conduction electrons of metallic nanostructures that are coupled to an electromagnetic field, known as localized surface plasmons (LSPs). Excited LSP oscillations do not propagate on large distances, but only occur within the particle size. Hence, they are called localized surface plasmons and the frequency of these oscillations is the localized surface plasmon resonance (LSPR). A schematic illustration of the excitation of dipolar surface plasmon oscillations is plotted in Figure 2.3. The electric field of an incoming electromagnetic wave induces a polarization of the free electrons with respect to the much heavier ionic core of a nanoparticle. A net charge difference is only felt at the nanoparticle boundaries (surface), which in turn acts as a restoring force. In this way a dipolar oscillation of electrons is created at the localized surface plasmon resonance.

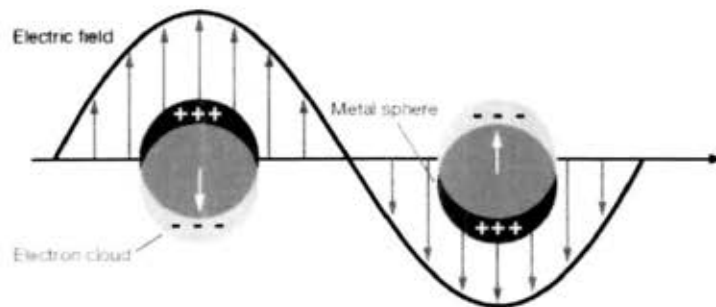


**Figure 2.3:** Diagram illustrating an excited localized surface plasmon by an external electric field (Willets and Van Duyne, 2007).

If metal nanoparticles are considered as spheres, the internal and scattered field can be expanded into spherical vector wave functions, as proposed by Gustav Mie in 1908 (Mie, 1908). The so called Mie solution to Maxwell's equations (also known as the



Lorenz–Mie–Debye solution or Mie scattering) describes the scattering of electromagnetic radiation by a sphere of arbitrary size consisting of a linear, isotropic, and homogeneous material when excited by a monochromatic plane wave (Bohren and Huffman, 1998). Calculations of the Mie solution can be used to find the total scattered and absorbed power, the angular distribution of the scattered field, the near and intermediate-field zones, and the field inside of a particle. The Mie solution is an infinite sum, therefore the method is limited in accuracy only by the number of terms retained. Further details regarding Mie Theory, specifically Generalized Mie theory (GMT), will be presented in Chapter 3 in the context of rigorous semi-analytical calculations of scattered fields and near-fields of particles arrays.

Similar to the surface plasmon, the LSPR is sensitive to changes in the local dielectric environment, size and shape of the particle (Link, Mohamed and El-Sayed, 1999; Noguez, 2007). For particles small compared to local variations of the involved electromagnetic fields, the quasi-static approximation can be utilized to model the material response (Kreibig and Vollmer, 1995). Using this approximation (Brongersma and Kik, 2007), the polarizability of  $\alpha_i$  of a metal nanoparticle in the direction of the  $i$ -axis of an ellipsoid can be expressed as

$$\alpha_i = \frac{4\pi}{3} abc \frac{\epsilon_m - \epsilon_e}{\epsilon_e + A_i(\epsilon_m - \epsilon_e)} \quad (2.18)$$

where  $\epsilon_m$  and  $\epsilon_e$  are the permittivities of the metal and the environment,  $A_i$  is the shape or depolarization constant,  $a$ ,  $b$  and  $c$  are the half axes of the ellipsoid. The value of  $A_i$  is determined by the ratio of the ellipsoid axes lengths and ranges from 0 to 1 (Bohren and

Huffman, 2008). From Equation (2.18), we can see that the nanoparticle plasmon resonance depends strongly on the environment. This implies the resonance of a plasmonic particle in air is different than that in water. Specifically, an environment of higher index of refraction leads to a red-shifted nanoparticle plasmon resonance. The resonance condition of the nanoparticle is full-filled when the denominator of Equation (2.18) is minimized. In the case of the sphere ( $a = b = c, A_i = 1/3$ ) this takes place when the real part of  $\epsilon_m$  is equal to  $-2\epsilon_e$  (Brongersma and Kik, 2007). Such strong sensitivities to changes in the dielectric environment enable several powerful chemical and biological sensing technologies, including surface-enhanced Raman scattering (SERS), surface-enhanced infrared spectroscopy, second harmonic generation, and surface-enhanced fluorescence (Geddes et al., 2004; Haes et al., 2005; Moran et al., 2005).

## 2.3 Nanoparticle Coupling and Particle Arrays

The previous discussion describes isolated individual nanoparticles. When one considers ensembles of particles there are three different regimes that need to be defined, depending on the magnitude of the interparticle distance  $d$  and the nature of the coupling. The following section will describe these three different coupling types known as near-field coupling, far-field coupling and Fano-type coupling.

### 2.3.1 Near-field coupling

When the metal NPs are very close to each other (distances much smaller than the wavelength of the electromagnetic fields,  $d \ll \lambda$ ), the near-fields of the excited plasmon

resonances can overlap (Salerno et al., 2005). The near-field interactions with distance dependence of  $d^{-3}$  dominate and the particle ensemble can be described as an ensemble of point dipoles interacting via their near-field (Maier, 2007). Under these conditions, strong electric field localization is observed between adjacent particles, enhanced by the suppression of scattered radiation into the far-field. In addition to enhanced near-fields, a resonance shift is induced by the close range coupling. By changing the restoring force acting on the free electrons, the resonance is blue-shifted with transverse polarization and red-shifted with longitudinal polarization. This phenomenon is shown clearly by Jain *et al* (Jain, Huang and El-Sayed, 2007) in Figure 2.4, where dimer pairs of gold (Au) nanocylinders (88 nm diameters) have been fabricated on a glass substrate with controllable inter-particle separations ranging from 2 to 212 nm (sample SEM shown in Figure 2.4a). Measured extinction spectra show that the LSPR of the particle pair red-shifts with decreasing gap for polarization along the inter-particle axis (Figure 2.4b). Additionally, the resonance peak blue-shifts very slightly with decreasing gap for polarization orthogonal to the inter-particle axis (Figure 2.4c).

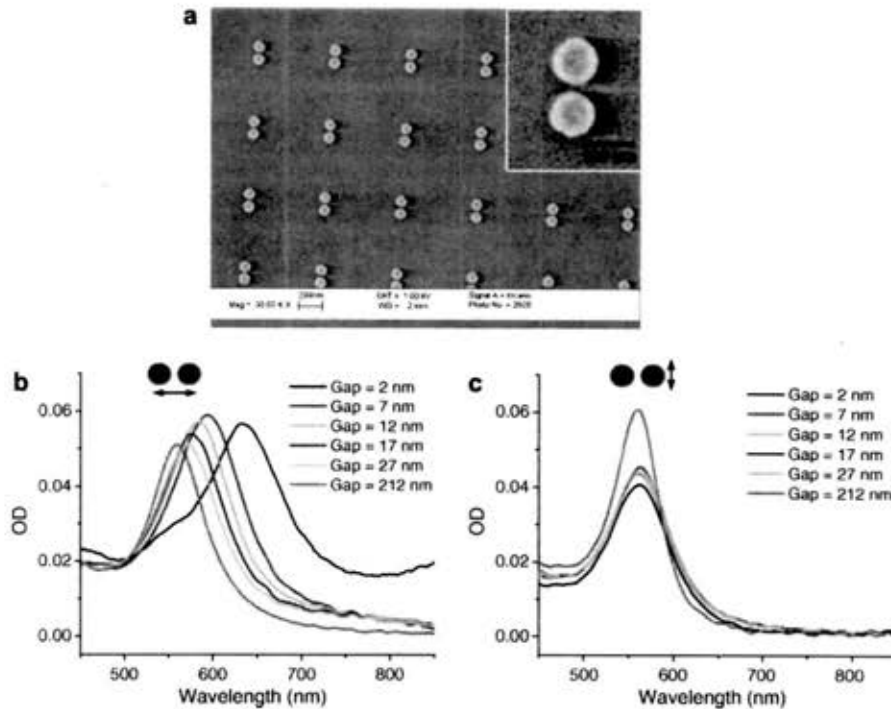


**Figure 2.4:** (a) SEM micrograph of nanofabricated array of 88-nm diameter gold nanocylinder pairs with inter-particle separation of 12 nm (inset is a magnified SEM of a dimer pair). Extinction spectra show that the LSPR of the particle pair (b) red-shifts with decreasing gap for polarization along the inter-particle axis. (c) Blue-shifts very slightly with decreasing gap for polarization orthogonal to the inter-particle axis (Jain, Huang and El-Sayed, 2007).

When the separation of NPs increases enough, the modes will no longer overlap. Then a single NP can be considered as a single dipole and their collective radiation can be seen as fringes of the far-field.

Both SPPs and LSPs facilitate several technologies which require the manipulation and concentration of light on nanoscale, including optical trapping (Novotny, Bian and Xie, 1997), enhanced photodetectors (Ditlbacher et al., 2006), enhanced photovoltaics (Atwater and Polman, 2010), engineering radiative decay (Anger, Bharadwaj and Novotny, 2006), metamaterials (Garcia-Vidal, Martin-Moreno and

Pendry, 2005) and several others. In this section, I have very briefly introduced the several fascinating and enabling properties of plasmonics and the readers are strongly encouraged to review the textbook references (Maier, 2007; Brongersma and Kik, 2007) to fully appreciate the scientific possibilities enabled by this emerging field.

### 2.3.2 Far-field and Fano-type Coupling

A second type of coupling often utilized in photonic and plasmonic arrays is far-field coupling (also known as diffractive or radiative coupling). In this regime, propagating scattered light from one particle can be scattered by another particle located at a distance equal to or greater than the wavelength of the incident light. Such coupling between particles can alter the single particle scattering response in a variety of ways, depending on the distance between particles as well as their geometrical arrangement. Of high interest is the regime where particles are separated by an average distance that is approximately equal to the wavelength of the light that propagates in the surrounding medium. In 1D or 2D ordered grating arrays of such particles, a delocalized surface mode can develop that couples together particles over large distances. Meier *et al* first found that strong dipolar interactions occur when a grating order changes from evanescent to radiative and since has been confirmed experimentally (Meier, Wokaun and Liao, 1985; Lamprecht et al., 2000). Additionally, extinction spectrum has been shown to display narrow features that result from a geometrical resonance associated with a coherent multiple scattering process in periodic arrays (Hicks et al., 2005).

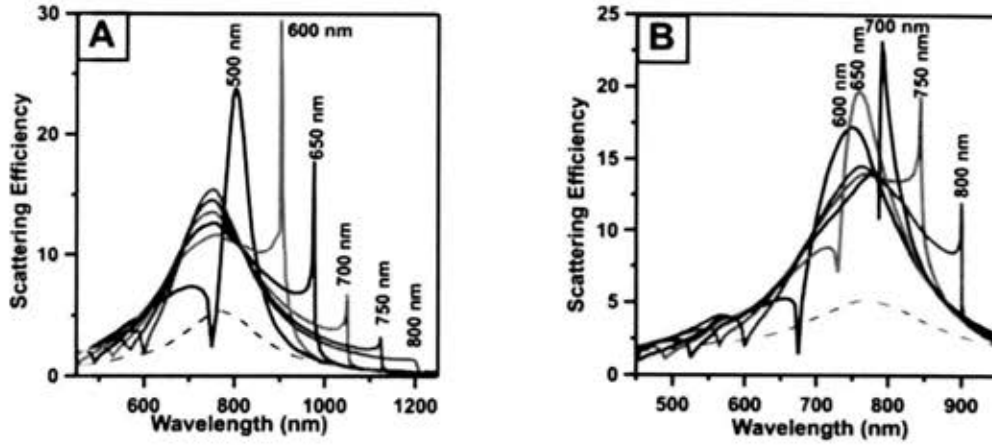


**Figure 2.5:** Scattering efficiencies for a chain of 500 cylinders with height of 30 nm and diameter of 130 nm with (A) an incident angle of 0 degrees (normal incidence) and (B) with an incident angle of 30 degrees.

Figure 2.5 shows scattering efficiencies for chains of 500 Ag nanocylinders with lattice spacings as shown, height of 30nm, and diameter of 130nm, calculated using a discrete dipole approximation (DDA) method (Hicks et al., 2005). The index of refraction of the medium was taken to be 1.5. Figure 2.5a shows the calculations at normal incidence, while Figure 2.5b shows the calculation at an angle  $30^\circ$  off normal. The condition for an evanescent grating mode is given by:

$$\lambda_m = \frac{\Lambda(n_1 \sin(\theta) + n_2)}{m} \quad (2.19)$$

where  $\Lambda$  is the grating constant,  $m$  is the mode order,  $n_1$  is the refractive index of the substrate,  $n_2$  the refractive index of the superstrate, and  $\theta$  is the angle between the incident k-vector and plane normal to the array (Félidj et al., 2005).

One of the most well-known examples of array driven photonic-plasmonic coupling is provided by the Fano-type resonances observed in metal nanoparticle gratings

(Fano, 1941; Luk'yanchuk et al., 2010; Kravets, Schedin and Grigorenko, 2008). In 1961, Ugo Fano discovered what is now known as Fano-resonances while conducting a quantum mechanical study of autoionizing states of atoms (Fano, 1941). The resonance exhibits a distinctive asymmetric shape, which can be modeled as:

$$I \propto \frac{(F\gamma + \omega - \omega_0)^2}{(\omega - \omega_0)^2 + \gamma^2}, \quad (2.20)$$

where  $\omega_0$  and  $\gamma$  are standard parameters that denote the position and width of the resonance, respectively;  $F$  is the so-called Fano parameter, which describes the degree of asymmetry (Luk'yanchuk et al., 2010). The origin of Fano resonances is a result of constructive and destructive interference of a broad spectral line-shape or continuum with a narrow discrete resonance. Recently, the Fano resonance has been observed in a number of nanoscale classical oscillator systems, enabled by plasmonic nanostructures, including diffraction gratings and hole or particle arrays (Mirin, Bao and Nordlander, 2009; Christ et al., 2007; Chen et al., 2009). Additionally, Fano resonances can be induced in plasmonic structures with broken symmetry due to the interaction of narrow resonant dark modes with broad bright modes. The high amount of field localization and associated enhancement results in systems with an exceptionally high sensitivity to local refractive index changes. Such Fano-type coupled systems thus make for a promising platform for ultra-sensitive surface sensing applications (Hao et al., 2009; Yanik et al., 2011). : More recently, Walsh *et al* have systematically investigated the effects of Fano-type coupling between long-range photonic resonances and localized surface plasmons on

the second harmonic generation from periodic arrays of Au nanoparticles (Walsh and Dal Negro, 2013; Walsh, 2013).

Plasmonic-photonic coupling is not limited to periodic geometries, yet by designing arrays with interparticle separations on many length scales, it is possible to engineer several scattering resonances. In fact, this is the case of for random systems, which have been explored for their ability to dramatically enhance near-fields (Wang et al., 2003). While random systems of plasmonic nanoparticles can yielded strong field localization, these systems suffer from a lack of engineerability and fine tuning of optical resonances. One promising solution for engineering disordered systems is found in utilizing deterministic aperiodic arrangements of plasmonic nanoparticles, referred to as Deterministic Aperiodic Nano Structures (DANS) (Dal Negro and Feng, 2007; Gopinath et al., 2008). These plasmonic media are conceived by designing spatial frequencies in aperiodic Fourier space, giving rise to characteristic scattering resonances and localized mode patterns that can enhance the intensity of optical near-fields over planar surfaces and broad frequency spectra (Dal Negro and Boriskina, 2012). This interplay between the two coupling regimes (near-field and radiative) offers a tunable approach to engineer photonic-plasmonic resonances in complex aperiodic media with deterministic order.

## 2.4 Nonlinear Optics

Nonlinear optical effects have an important role in modern photonic functionalities, including control over the frequency spectrum of laser light, generation of ultra-short pulses, all-optical signal processing and ultrafast switching (Boyd, 2008). The



field of nonlinear optics deals with higher order responses of light-matter interaction, which become relevant when the intensity of light is high, i.e. the optical response depends on the field strength. Optical nonlinearities are inherently weak, because they are governed by photon-photon interactions enabled by materials (Kauranen and Zayats, 2012). They are superlinearly dependent on the electromagnetic field and can be strengthened in material environments that provide mechanisms for field enhancement. This superlinearity is where plasmonics can play a significant role, by the fact that strong fields can be locally produced by the plasmons and a strong nonlinear response can be achieved. Nonlinear optics, gives rise to a host of optical phenomena, including second and third harmonic generation, sum frequency generation, the optical Kerr effect, four-wave mixing, and several others. For example, a two-photon absorption or emission process is a third-order nonlinear phenomenon. One particular application is in the use of a two-photon emission microscopy enabling the visualization of plasmonic resonant modes of Au nanoantennas (Ghenuche et al., 2008). Another example is the second order phenomenon of sum frequency generation (SFG). Recently, plasmonic platinum nanoparticles have been used for surface enhanced SFG, detecting of carbon monoxide at ultra-low levels (Baldelli et al., 2000). This discussion will support experimental results later detailed in this thesis, utilizing second harmonic generation (SHG) as a probe of LSP enhanced near-fields.

#### 2.4.1 Nonlinear Media

Up until this point, we have discussed optical waves in linear media where  $\mathbf{P}$  is

related to  $\mathbf{E}$  by Eq. (2.9). This relation permits the modeling of a material's response to an optical field within linear system framework. This results in a system where material properties do not change with the magnitude of  $\mathbf{E}$ . While this consideration tends to be sufficient when relating incident fields at low field strengths, this simplification is not entirely correct. Nonlinear optical effects arise when electronic motion in a strong electromagnetic field cannot be considered harmonic. In reality, when the relationship between  $\mathbf{P}$  and  $\mathbf{E}$  varies from this linear relation, it does so slowly and thus can be expanded in a Taylor series around  $\mathbf{E} = 0$  as:

$$\vec{P} = \epsilon_0 \left[ \chi^{(1)} \vec{E} + \chi^{(2)} \vec{E}^2 + \chi^{(3)} \vec{E}^3 + \dots \right] \equiv \epsilon_0 \chi \vec{E} + \vec{P}_{NL}, \quad (2.21)$$

where  $\chi^{(2)}$  and  $\chi^{(3)}$  are second- and third-order harmonic nonlinear susceptibilities. It is important to note, that in expanding in a Taylor series we are now representing the material polarization in the time domain, where  $\chi^{(1)}$  represents the first order susceptibility  $\chi$  in Eq. (2.9). Also worth noting is that the nonlinear part of the polarization density can be defined as  $\vec{P}_{NL} = \epsilon_0 \chi^{(2)} \vec{E}^2 + \epsilon_0 \chi^{(3)} \vec{E}^3 + \dots$  as an additional contribution to the linear case found in Eq. (2.9).

#### 2.4.2 Second-harmonic generation

The second-order response typically gives rise to wave-mixing effects that lead to frequency conversion, the most common example being SHG, where the incident frequency,  $\omega$ , is converted to its second harmonic,  $2\omega$ . The way the various positive and negative frequencies combine is often described in terms of photon diagrams shown in

Figure 2.4. The solid horizontal lines correspond to the real quantum-mechanical states of the material system and the dashed lines are virtual states where the system resides only instantaneously. The red arrows correspond to the input fields that can drive the material up or down in energy as indicated. The green arrow corresponds to the generated field, which returns the material to the initial state.

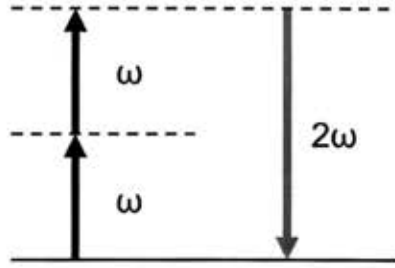


**Figure 2.4:** Photon diagrams for SHG process, with red arrows corresponding to the input driving fields and green arrow corresponding to the generated second harmonic field returning the system to the ground initial state.

In second order, we obtain SHG, sum- and difference-frequency generation, and an electro-optic response; however in this thesis we limit the discussion to SHG only. Let us consider a wave with electric field strength:

$$\vec{E} = \vec{E}_o \exp(-j\omega t) \quad (2.22)$$

The nonlinear polarization density then becomes

$$\vec{P}_{NL} = 2\chi^{(2)}\vec{E}_o\vec{E}_o^* + \chi^{(2)}\vec{E}_o^2 \exp(-2j\omega t), \quad (2.23)$$

which has a two contributions, one at zero frequency and another at the second harmonic of the incident wave ( $2\omega$ ). The second term of this equation ( $\chi^{(2)}\vec{E}_o^2 \exp(-2j\omega t)$ ) is responsible for the SHG, producing radiation at twice the fundamental frequency. It is

important to note, that second order nonlinear susceptibility  $\chi^{(2)}$  can only be nonzero if a material lacks centrosymmetry (Boyd, 2008). This criterion is satisfied in the case of non-centrosymmetric crystals or at the interface between any two media. The latter of which makes it possible to generate second order nonlinear processes with metallic nanoparticles.

## Chapter 3

### 3 Computational Design Methods

A formal solution of rigorous scattering theory for nanoparticles is unfortunately only possible for restricted geometries. There exist analytical solutions for light scattering problems if we expand the electromagnetic potentials and fields to spherical harmonics and limit ourselves to spherical or spheroidal particle shapes. Such techniques can still be very powerful when dealing with particles at the nanoscale, where in some cases spheres approximate the given nanostructures sufficiently well. In reality however, we want to work with arbitrary shaped nanostructures and take advantage of certain structure dependent qualities like the hot spots in the gap regions of bowtie antennas or dimer cylinder pairs. In general a more sophisticated numerical method for solving Maxwell's equations is essential and now available in commercial packages. In this chapter several analytical and commercial numerical methods used in this work are presented in a level relevant to this thesis.

#### 3.1 Analytical Multiple Scattering

Three-dimensional (3D) problems of electromagnetic scattering have long been the subject of intense investigation in various scientific fields such as astronomy, optics, meteorology, photonics and several others. These efforts have led to a development of a large number of analytical tools and modeling techniques for quantitative evaluation of electromagnetic scattering from multiple objects. While several methods exist, we limit

the discussion to those utilized in this thesis, namely the Generalized Mie Theory and the Coupled Dipole Method.

### 3.1.1 Generalized Mie Theory

The solution of Maxwell's equations for spherical particles (or infinitely long cylinders) is named after the physicist Gustav Mie and the expansion for elliptical particles became known as the Mie solution, see Sec. 2.2.2 (Mie, 1908). The Mie solution (often called theory) is an exact solution for the light scattered and absorbed by a spherical particle of arbitrary size, consisting of a linear, isotropic, and homogeneous material when excited by a monochromatic plane wave. A rigorous derivation of Mie's formal solution can be found in (Bohren and Huffman, 2008; Mie, 1908), however we will only present the basic steps here.

The Mie solution can be used to calculate the total scattered and absorbed power, the angular distribution of the scattered field, the near and intermediate-field zones, and the field inside of a particle (Bohren and Huffman, 2008). Let us consider a sphere with radius  $a$  in free space, excited by a monochromatic incident electromagnetic wave of wavelength  $\lambda$ . We introduce a polar coordinate system  $(0, r, \theta, \varphi)$  with origin in the sphere center. In Mie's solution the electric field of the incident plane wave, the scattered wave outside the particle, and inside the particle are shown in equations (3.1), (3.2) and (3.3) respectively as:

$$\mathbf{E}_i = \sum_{n=1}^{\infty} i^n \frac{(2n+1)}{n(n+1)} (c_n M_{o1n}^{(1)} - id_n N_{e1n}^{(1)}) \quad (3.1)$$

$$\mathbf{E}_s = \sum_{n=1}^{\infty} i^n \frac{(2n+1)}{n(n+1)} (ia_n N_{eln}^{(3)} - b_n M_{olin}^{(3)}) \quad (3.2)$$

$$\mathbf{E}_i = \sum_{n=1}^{\infty} i^n \frac{(2n+1)}{n(n+1)} (M_{olin}^{(1)} - iN_{eln}^{(1)}) \quad (3.3)$$

where  $\mathbf{M}$  and  $\mathbf{N}$  are vector spherical harmonics (VSH)

$$\mathbf{M}_{olin}^{(X)} = \begin{pmatrix} 0 \\ \cos(\varphi)\pi_n(\cos\theta)z_n(\rho) \\ -\sin(\varphi)\tau_n(\cos\theta)z_n(\rho) \end{pmatrix} \quad (3.4)$$

$$\mathbf{N}_{eln}^{(X)} = \begin{pmatrix} n(n+1)\cos(\varphi)\sin(\theta)\pi_n(\cos\theta)z(\rho)/\rho \\ \cos(\varphi)\tau_n(\cos\theta)\frac{[\rho z(\rho)]'}{\rho} \\ -\sin(\varphi)\pi_n(\cos\theta)\frac{[\rho z(\rho)]'}{\rho} \end{pmatrix}. \quad (3.5)$$

Additionally,  $z(\rho)$  is  $j_n(\rho)$  if  $(X)=(1)$  or  $h_n^{(1)}(\rho)$  if  $(X)=(3)$ , and  $\pi_n$  and  $\tau_n$  are functions which can be found from a simple recurrence relation (Bohren and Huffman, 2008). The scattered field  $\{a_{mn}, b_{mn}\}$  and the internal field  $\{c_{mn}, d_{mn}\}$  expansion coefficients can be determined in terms of the incident field expansion coefficients  $\{p_{mn}, q_{mn}\}$  and of the Mie coefficients  $\{a_n, b_n, c_n, d_n\}$ . The external Mie coefficients  $a_n$ ,  $b_n$  are

$$a_n = \frac{m\chi_n(mx)\chi_n'(x) - \chi_n(x)\chi_n'(mx)}{m\chi_n(mx)\xi_n'(x) - \xi_n'(x)\chi_n'(mx)} \quad (3.6)$$

$$b_n = \frac{\chi_n(mx)\chi_n'(x) - m\chi_n(x)\chi_n'(mx)}{\chi_n(mx)\xi_n'(x) - m\xi_n'(x)\chi_n'(mx)} \quad (3.7)$$

and the internal Mie coefficient  $c_n$ , and  $d_n$  are

$$c_n = \frac{m\chi_n(mx)\xi_n'(x) - \xi_n(x)\chi_n'(mx)}{m\chi_n(mx)\xi_n'(x) - \xi_n'(x)\chi_n'(mx)} \quad (3.8)$$

$$d_n = \frac{\chi_n(mx)\xi_n'(x) - m\xi_n(x)\chi_n'(mx)}{\chi_n(mx)\xi_n'(x) - m\xi_n'(x)\chi_n'(mx)} \quad (3.9)$$

where  $\chi_n(\rho) = \rho j_n(\rho)$ , and  $\xi_n(\rho) = \rho h_n^{(1)}(\rho)$ , and where  $j_n(\rho)$  and  $h_n^{(1)}(\rho)$  are the spherical Bessel and Hankel functions of first kind. Additionally,  $m$  is the ratio of refractive index of the sphere  $n$  to that of the surrounding medium  $n_m$  and  $x$  is the size parameter given as  $2\pi n_m a / \lambda$  (Bohren and Huffman, 2008). Figure 3.1 shows an example of the calculated spectra of the absorption efficiency  $Q_{abs}$  (red dashed), scattering efficiency  $Q_{sca}$  (black dotted), and extinction efficiency  $Q_{ext}$  (green solid) for Au nanospheres with diameters equal to 40 nm (a) and 80 nm (b).

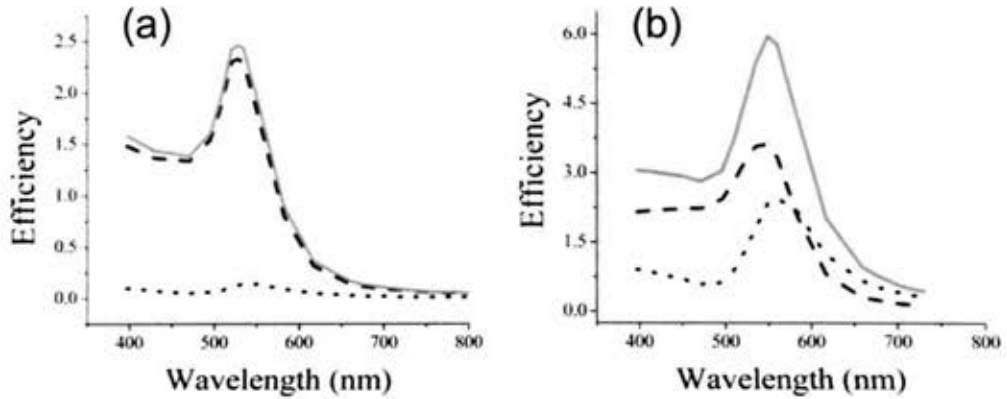


**Figure 3.1:** Calculated spectra of the efficiency of absorption  $Q_{abs}$  (red dashed), scattering  $Q_{sca}$  (black dotted), and extinction  $Q_{ext}$  (green solid) for gold nanospheres (a)  $D = 40$  nm and (b)  $D = 80$  nm (Jain et al., 2006).

The Generalized Mie theory (GMT) now considers the problem of scattering from a number of particles ( $j = 1 \dots L$ ), which have an individual radii ( $a_j$ ) and central



coordinates of  $(x^j, y^j, z^j)$ . The electric field scattered by the  $j^{\text{th}}$  particle can be expressed by using a transformation expressed in terms centered on the  $i^{\text{th}}$  particle. The expression for the scattered electric field then becomes

$$E_s^{ji} = \sum_{n=1}^{\infty} \sum_{m=-n}^n jE_{mn} \left[ a_{mn}^{ji} N_{mn}^{(3)}(k_o r^i, \theta^i \phi^i) + b_{mn}^{ji} M_{mn}^{(3)}(k_o r^i, \theta^i \phi^i) \right], \quad (3.10)$$

where again  $\mathbf{M}$  and  $\mathbf{N}$  are the vector spherical harmonics discussed previously in Eq. (3.4) and Eq. (3.5). The vector addition theorem for vector spherical wave functions enables the transformation of the series expansion coefficients  $a_{mn}^{ji}$  and  $b_{mn}^{ji}$  for the scattered fields of the  $j^{\text{th}}$  particle into an expansion in the local coordinate system  $i^{\text{th}}$  particle. The coefficients  $a_{mn}^{ji}$  and  $b_{mn}^{ji}$  are now defined as

$$a_{mn}^{ji} = \sum_{\nu=1}^{\infty} \sum_{\mu=-\nu}^{\nu} A_{mn,\nu\mu}^{ji} a_{\mu\nu}^{jj} + B_{mn,\nu\mu}^{ji} b_{\mu\nu}^{jj} \quad (3.11)$$

$$b_{mn}^{ji} = \sum_{\nu=1}^{\infty} \sum_{\mu=-\nu}^{\nu} B_{mn,\nu\mu}^{ji} a_{\mu\nu}^{jj} + A_{mn,\nu\mu}^{ji} b_{\mu\nu}^{jj} \quad (3.12)$$

The external field on the  $i^{\text{th}}$  particle can then be expressed as

$$E_s^{ii} = \sum_{n=1}^{\infty} \sum_{m=-n}^n jE_{mn} \left[ c_{mn}^{ji} N_{mn}^{(1)}(k_o r^i, \theta^i \phi^i) + d_{mn}^{ji} M_{mn}^{(1)}(k_o r^i, \theta^i \phi^i) \right] \quad (3.13)$$

In conclusion, the electric field on a particle  $i$  is expressed as the sum of the field contributions from all other particles in the ensemble is given in the reference system  $(0^i, X^i, Y^i, Z^i)$  as

$$E_i^{ii} = \sum_{j=1, j \neq i}^L E_s^{ji} + E_e^{ji}. \quad (3.14)$$

For a comprehensive discussion and derivation of the GMT the author suggests the 1995 paper by Yu-Lin Xu (Xu, 1995).

### 3.1.2 Coupled Dipole Approximation

The Coupled-Dipole Approximation (CDA) was first applied by Purcell and Pennypacker in 1973 to study the scattering by interstellar dust particles (Purcell and Pennypacker, 1973). Today it has been formulated into a powerful method of calculating the near and far-field scattering properties of large ensembles of nanoparticles. Specifically, the formulation being utilized in this thesis considers metallic particles of an array as ellipsoidal particles described by a single electric dipole contribution whose polarizability is a function of the ellipsoidal axis (C. Forestiere et al., 2009). The CDA is particularly suited to efficiently treat large-scale plasmonic systems made of small and well separated nanoparticles, and it has been previously validated against semi-analytical multiple scattering methods (Carlo Forestiere, Giovanni Miano, et al., 2009) used to describe complex nanoparticle arrangements (Carlo Forestiere, Gary F Walsh, et al., 2009).

It is important to first introduce the coordinate system  $(O, x, y, z)$ , where the fundamental directions  $\hat{x}, \hat{y}, \hat{z}$  are chosen to be coincident with the three principal axes of the ellipsoids in such a way that their half lengths  $a_x, a_y, a_z$  verify the inequality  $a_x \leq a_y \leq a_z$ . In this method each ellipsoidal particle is characterized by its permittivity  $\varepsilon = \varepsilon(\omega)$  and volume  $V_0 = 4\pi a_x a_y a_z / 3$ . The electric dipole moment of the  $h^{\text{th}}$  particle is,

$$\mathbf{p}_h = V_0 (\varepsilon - \varepsilon_d) \mathbf{E}_h \quad (3.15)$$

where  $\varepsilon_d$  is the permittivity of the surrounding dielectric, and  $\mathbf{E}_h$  is the local electric field at the particle's location comprising the incident field as well as the field scattered by each particle including the  $h^{\text{th}}$ . The value of the electric field at the  $h^{\text{th}}$  particle center generated by the  $h^{\text{th}}$  particle itself  $\mathbf{E}_{hh}$  is then

$$\mathbf{E}_{hh} = -\frac{1}{V_0 \varepsilon_0} A \mathbf{p}_h \quad (3.16)$$

where  $A = \text{diag}(A_x, A_y, A_z)$  is the diagonal dyad of depolarization coefficients  $A_x, A_y, A_z$  whose expressions can be found in the appendix of (C. Forestiere et al., 2009). The value of the electric field generated by the  $k^{\text{th}}$  particle, with  $h \neq k$ , is

$$\mathbf{E}_{hk} = \frac{1}{4\pi\varepsilon_0} \frac{1}{r_{hk}^3} B_{hk} \mathbf{p}_k \quad (3.17)$$

where  $\mathbf{r}_{hk} = (\mathbf{r}_h - \mathbf{r}_k)$ ,  $r_{hk} = |\mathbf{r}_{hk}|$ ,  $\hat{\mathbf{r}}_{hk} = \mathbf{r}_{hk} / r_{hk}$ ,  $B_{hk}$  is the dyad as defined

$$B_{hk} = 3\hat{\mathbf{r}}_{hk}\hat{\mathbf{r}}_{hk} - I \quad (3.18)$$

and  $I$  is the identity dyad (C. Forestiere et al., 2009). In conclusion, the value of the total electric field at the center of the  $h^{\text{th}}$  particle generated by the entire particle ensemble and the external source is given by

$$\mathbf{E}_h = -\frac{1}{V_0 \varepsilon_0} A \mathbf{p}_h + \frac{1}{4\pi\varepsilon_0} \sum_{k=1}^N \frac{1}{r_{hk}^3} B_{hk} \mathbf{p}_k + \mathbf{E}_{\text{ext}}(\mathbf{r}_h) \quad (3.19)$$

where  $\mathbf{E}_{ext} = \mathbf{E}_{ext}(\mathbf{r})$  is the electric field due to the external sources. By then substituting Eq. (3.19) into Eq. (3.15) the system of linear algebraic equations governing the dipole moments  $(p_1, p_2, \dots, p_N)$  can be obtained as

$$\frac{p_h}{V_0(\epsilon - \epsilon_0)} = -\frac{1}{V_0\epsilon_0} A p_h + \frac{1}{4\pi\epsilon_0} \sum_{k=1}^N \frac{1}{r_{hk}^3} B_{hk} p_k + \mathbf{E}_{ext}(\mathbf{r}_h) \quad (3.20)$$

for  $h=1, 2, \dots, N$  (C. Forestiere et al., 2009). Figure 3.2 plots the scattering efficiency and the maximum field enhancement spectra for a dimer pair of spherical particles with radius 50nm and edge to edge distances of 10 nm, 25 nm and 50 nm calculated with multi-particle Mie theory and the CDA (Forestiere et al., 2013). Notice the agreement between the two techniques. The CDA calculations are computationally less intense than GMT and can be a powerful tool when several particles configured in an array are being investigated.

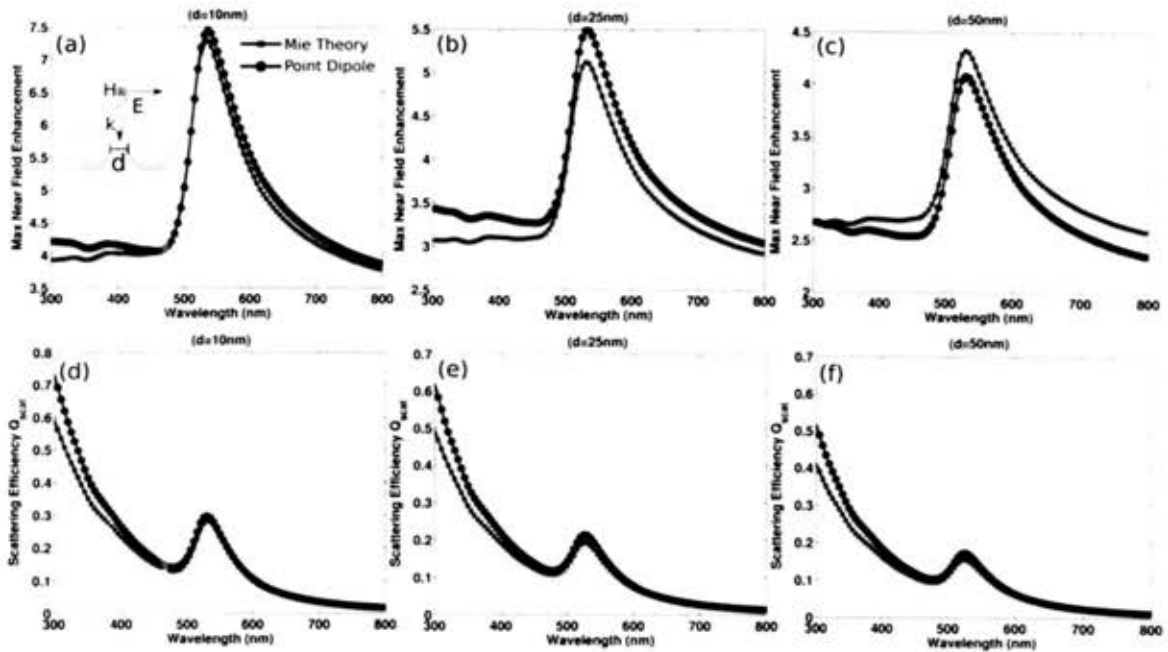


**Figure 3.2:** Scattering efficiency and maximum field enhancement spectra of a dimer of spherical particles of 50 nm radius and with edge-edge distances: (a-b)  $d = 10$  nm, (c-d)  $d = 25$  nm, and (e-f)  $d = 50$  nm calculated with the multi-particle Mie theory and the point dipole method (Forestiere et al., 2013).

## 3.2 Finite Element Modeling

Finite element modeling or the finite element method (FEM) is a numerical technique for finding approximate solutions to boundary value problems, typically through partial differential equation (PDE) solutions. The basic concept in the physical interpretation of the FEM is the subdivision of the mathematical model into disjoint (non-overlapping) components of simple geometry called finite elements or elements for short. The response of each element is expressed in terms of a finite number of degrees of freedom, characterized as the value of an unknown function, or functions, at a set of nodal points.

In electromagnetics, FEM generally approximates the solution to Maxwell's equations in the frequency domain and is hence typically utilized for time-harmonic situations. FEM can be derived using two methods: one using variational analysis and the other using weighted residuals (Davidson, 2005). The variational method finds a variational function whose minimum, maximum and stationary point corresponds to the solution of the PDE subject to the boundary conditions. The weighted residuals method starts with the PDE form of Maxwell's equations and then introduces a "weighted" residual (error). Using Green's theorem, one of the differentials in the PDE is then shifted to weighting functions (Jin and Jin, 2002). This is often referred to in the literature as the "weak" formulation, since the finite element basis functions need only be once differentiable, whereas the wave equation has second-order derivatives. In both cases the unknown field is discretized using an element mesh. Typically, triangular elements are used for surface meshes and tetrahedrons for volumetric meshes, although several other types of elements have been investigated (Jin and Jin, 2002). This discretization or meshing is the main advantage over grid-based methods such as Finite Difference Time Domain (FDTD) (described in the next section). The non-regular FEM mesh can resolve arbitrarily small geometries better than regular rectangular mesh conventionally employed by FDTD and thus leads to a more efficient model (Garg, 2008). The mesh gives details about where each element is, to which material in the simulation domain it associates with, and approximates the geometrical shape of the domain. One drawback resulting from FEM meshes is that they can become very complex for large 3D structures, in some cases taking more computing time to generate a 3D mesh than to run

the simulation. For this reason, all FEM simulations utilized in this thesis are restricted to 2D cases. Figure 3.3 shows a sample FEM mesh for a complex array on nanocylinders ( $d = 200$  nm). Notice the triangular nature of the mesh elements adapting to the curvature of the cylinders.

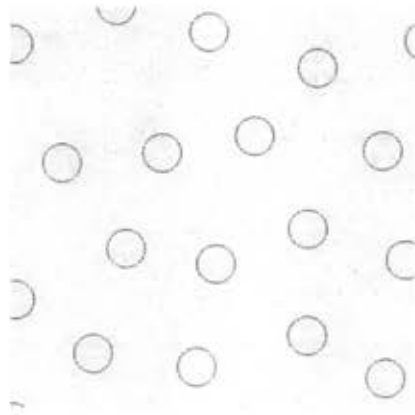


**Figure 3.3:** Example FEM mesh (Comsol 3.5a). Each cylinder is 200 nm in diameter.

FEM analysis of a problem consists of four general steps: meshing the simulation domain so that the simulated material is homogeneous on each element, deriving the governing equation for an element, assembly of all elements into a system of equations, and the solution of the system of equations. The number of elements in a mesh ( $N_e$ ) is directly proportional to the accuracy of the solution; so much detail must be maintained on the meshing order. In meshing nanophotonic structures, a rule of thumb is to choose  $N_e$  so that the maximum element edge length is less than  $\lambda/10$ , where  $\lambda$  is the optical wavelength. Assuming the field distribution of general element  $e$  is  $\varphi^e$ , the distribution throughout the domain is a linear combination of the distribution in each element. The equation describing the total distribution is then:

$$\varphi(x, y) = \sum_{e=1}^{N_e} \varphi^e(x, y) \quad (3.21)$$

The discussion will now follow the "weak" formulation, utilizing weighted residual error in the PDE form of Maxwell's equations as it is the method utilized in the commercial software (COMSOL Multiphysics, vers. 3.5a) employed in this thesis.

The field distribution variable  $\varphi$  for each element is expanded in basis functions  $\psi_i^e$ , which can be either node- or edge-based functions. We will consider the node-based functions for simplicity. Assuming an element  $e$  with  $p$  nodes, the expansion of  $\varphi$  is (Garg, 2008):

$$\varphi^e(x, y) = \sum_{i=1}^p c_i \psi_i^e(x, y), \quad (3.22)$$

where  $c_i$  are unknown complex coefficients and  $\psi_i^e(x, y)$  are the basis functions. By enforcing the governing differential equation for the element using

$$\frac{\partial^2 \varphi^e}{\partial x^2} + \frac{\partial^2 \varphi^e}{\partial y^2} + k^2 \varphi^e = 0, \quad (3.23)$$

the coefficients  $c_i$  can be determined. The differential equation cannot be satisfied fully due to finite memory sizes; however an average satisfaction can be obtained by using the corresponding functional (Garg, 2008):

$$F^e[\varphi^e] = \frac{1}{2} \iint_s \left[ |\nabla \varphi^e|^2 - k^2 (\varphi^e)^2 \right] dx dy \quad (3.24)$$

The expansion in Eq. (3.22) can now be substituted into Eq. (3.24) resulting in a matrix of the form



$$[F^e] = [A^e][\varphi^e] \quad (3.25)$$

where  $[A^e]$  is the elemental matrix and  $[\varphi^e]$  is the nodal vector. The assembly of the matrices is achieved by summing the set of equation for each element, resulting in

$$\sum_{e=1}^{N_e} [A^e][\varphi^e] = \sum_{e=1}^{N_e} [F^e] \quad (3.26)$$

or written in system matrix form:

$$[A][\varphi] = [F] \quad (3.27)$$

The matrix is then solved to determine the unknown vector  $\varphi$  of potentials at the nodes.

There are several methods for solving the equations to determine the unknown vector including the Ritz, Galerkin and others.

Additionally, numerical models using the FEM must be bounded and infinite half spaces of models should be replaced with finite domains or absorbing boundary conditions. The perfectly matched layer (PML) is the most utilized absorbing boundary conditions for truncating the computational domain and is the technique applied in this thesis for all FEM calculations. PMLs are anisotropic artificial media whose parameters are designed for a method of complex coordinate-stretching, in order to attenuate the waves travelling through them exponentially through the width of the layer. The PML technique provides good performance for a wide range of incidence angles and is not particularly sensitive to the shape of the wave fronts. The PML formulation can be deduced from Maxwell's equations by introducing a complex-valued coordinate transformation under the additional requirement that the wave impedance should remain unaffected. PML layers are typically set to absorb the component of the field that is

normal to the boundary. After that component is removed, the parallel component is taken care of by the terminating boundary condition. Hence, different formulations are necessary for spherical coordinates or for when the boundary is not straight.

The details of the PML formulation will not be explicitly derived in this thesis, rather the author directs the reader to Jianming Jin's comprehensive text on the subject (Jin and Jin, 2002). Throughout this thesis, all FEM calculations were carried out using the commercial software COMSOL Multiphysics (ver. 3.5a), specifically the built-in 2D RF Module. The COMSOL software package allows for PML coordinate systems including Cartesian, cylindrical, or spherical; of which the user must choose correctly depending on the nature of the simulation.

### 3.3 Finite Difference Time Domain Modeling

Finite Difference Time Domain (FDTD) is another common numerical technique used in the modeling electromagnetic systems. The method is based in the time-domain as its name suggests, allowing for wide range of frequencies in single run; hence it is typically the method of choice for broadband simulations (Tavlove and Hagness, 1995). The technique directly approximates the differential operators in Maxwell's equations on a grid staggered in space and time, first introduced by Kane Yee (Yee, 1966).

In the finite difference approximation, the derivative of a smooth function with respect to a variable is approximated by a two-point finite difference over the sufficiently discretized variable. The technique allows for the quick computation of fields at several points in space and time. The one dimensional finite difference equation is:

$$f'(x) = \frac{df}{dx} \approx \frac{f(x + \Delta x) - f(x - \Delta x)}{2\Delta x} \quad (3.28)$$

From Eq. (3.28) it is clear that the accuracy of the approximation increases with decreasing spatial grid size  $\Delta x$ . As mentioned previously, the work by Kane Yee established what is known today as the Yee cell (2D representation shown in Figure 3.4), which is the building block for calculations of Maxwell's equation in the FDTD method.

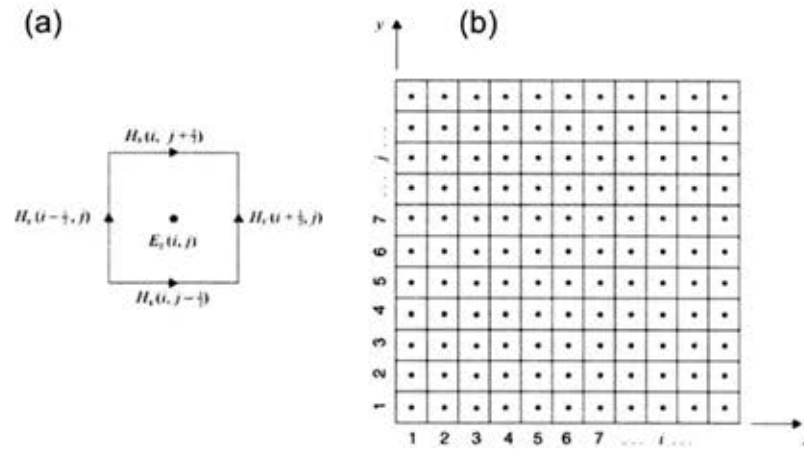


**Figure 3.4:** (a) The demonstration of the Two-dimensional Yee cell, the basis of the FDTD algorithm. The cell edges are set to be the Magnetic field whereas the center of the cell is set to represent the Electric field. (b) Finite difference mesh for Yee ' s FDTD algorithm. Modified figure from (Jin, 2011).

As noted in Figure 3.4, the electric and magnetic fields are spatially staggered and solved at specific points along the grid of Yee cells. Maxwell's equations in the time domain can be expressed as the following scalar equations in a rectangular coordinate system:

$$\frac{\partial E_x}{\partial t} = \frac{1}{\epsilon} \left( \frac{\partial H_z}{\partial y} - \frac{\partial H_y}{\partial z} - \sigma E_x \right) \quad (3.29)$$

$$\frac{\partial E_y}{\partial t} = \frac{1}{\epsilon} \left( \frac{\partial H_x}{\partial z} - \frac{\partial H_z}{\partial x} - \sigma E_y \right) \quad (3.30)$$

$$\frac{\partial E_z}{\partial t} = \frac{1}{\varepsilon} \left( \frac{\partial H_y}{\partial x} - \frac{\partial H_x}{\partial y} - \sigma E_z \right) \quad (3.31)$$

$$\frac{\partial H_x}{\partial t} = \frac{-1}{\mu} \left( \frac{\partial E_z}{\partial y} - \frac{\partial E_y}{\partial z} \right) \quad (3.32)$$

$$\frac{\partial H_y}{\partial t} = \frac{-1}{\mu} \left( \frac{\partial E_x}{\partial z} - \frac{\partial E_z}{\partial x} \right) \quad (3.33)$$

$$\frac{\partial H_z}{\partial t} = \frac{-1}{\mu} \left( \frac{\partial E_y}{\partial x} - \frac{\partial E_x}{\partial y} \right) \quad (3.34)$$

We then assign the magnetic field components at the center of each edge of the cells and the electric field components at the center of each face cell. Additionally, the electric and magnetic fields can switch places if the entire grid is offset by one-half of a cell in each direction. By using the central differencing scheme, Eq. (3.29)-(3.31) can be rewritten as:

$$\begin{aligned} E_x^{n+1}(i+\frac{1}{2}, j, k) = & \frac{1}{\beta(i+\frac{1}{2}, j, k)} \left\{ \alpha(i+\frac{1}{2}, j, k) E_x^n(i+\frac{1}{2}, j, k) \right. \\ & + \frac{1}{\Delta y} \left[ H_z^{n+1/2}(i+\frac{1}{2}, j+\frac{1}{2}, k) - H_z^{n+1/2}(i+\frac{1}{2}, j-\frac{1}{2}, k) \right] \\ & - \frac{1}{\Delta z} \left[ H_y^{n+1/2}(i+\frac{1}{2}, j, k+\frac{1}{2}) - H_y^{n+1/2}(i+\frac{1}{2}, j, k-\frac{1}{2}) \right] \\ & \left. - J_x^{n+1/2}(i+\frac{1}{2}, j, k) \right\} \end{aligned} \quad (3.35)$$

$$E_y^{n+1}(i, j+\frac{1}{2}, k) = \frac{1}{\beta(i, j+\frac{1}{2}, k)} \left\{ \alpha(i, j+\frac{1}{2}, k) E_y^n(i, j+\frac{1}{2}, k) \right.$$

$$\begin{aligned}
& + \frac{1}{\Delta z} \left[ H_x^{n+1/2} \left( i, j + \frac{1}{2}, k + \frac{1}{2} \right) - H_x^{n+1/2} \left( i, j + \frac{1}{2}, k - \frac{1}{2} \right) \right] \\
& - \frac{1}{\Delta x} \left[ H_z^{n+1/2} \left( i + \frac{1}{2}, j + \frac{1}{2}, k \right) - H_z^{n+1/2} \left( i - \frac{1}{2}, j + \frac{1}{2}, k \right) \right] \\
& \quad - J_y^{n+1/2} \left( i, j + \frac{1}{2}, k \right) \} \tag{3.36}
\end{aligned}$$

$$\begin{aligned}
E_z^{n+1} \left( i, j, k + \frac{1}{2} \right) &= \frac{1}{\beta \left( i, j, k + \frac{1}{2} \right)} \left\{ \alpha \left( i, j, k + \frac{1}{2} \right) E_z^n \left( i, j, k + \frac{1}{2} \right) \right. \\
& + \frac{1}{\Delta x} \left[ H_y^{n+1/2} \left( i + \frac{1}{2}, j, k + \frac{1}{2} \right) - H_y^{n+1/2} \left( i - \frac{1}{2}, j, k + \frac{1}{2} \right) \right] \\
& - \frac{1}{\Delta y} \left[ H_x^{n+1/2} \left( i, j + \frac{1}{2}, k + \frac{1}{2} \right) - H_x^{n+1/2} \left( i, j - \frac{1}{2}, k + \frac{1}{2} \right) \right] \\
& \quad \left. - J_z^{n+1/2} \left( i, j, k + \frac{1}{2} \right) \right\} \tag{3.37}
\end{aligned}$$

where  $J_x$ ,  $J_y$ , and  $J_z$  are the source components and  $\alpha$  and  $\beta$  are defined as:

$$\begin{aligned}
\alpha &= \frac{\varepsilon}{\Delta t} - \frac{\sigma}{2} \\
\beta &= \frac{\varepsilon}{\Delta t} + \frac{\sigma}{2}
\end{aligned} \tag{3.38}$$

Similarly the  $H_x^{n+1/2}$ ,  $H_y^{n+1/2}$  and  $H_z^{n+1/2}$  components can be defined, however for brevity they are not shown here.

The user defined source pulse with central frequency and duration is initiated at time  $t = 0$ . At time steps  $\Delta t$  the electric and magnetic fields are calculated at each Yee cell using the finite difference equation for the scalar Maxwell's equations. From

Maxwell's differential equations we know that the electric field in time is dependent on the change in the magnetic field across space. This time stepping relation in FDTD calculates an updated electric field in time that is dependent on the stored value of the electric field and the numerical curl of the local distribution of the magnetic field in space (Yee, 1966). This implies that on the  $n^{\text{th}}$  iteration, the electric fields are evaluated at  $t = n\Delta t$  and the magnetic fields at a "half-time" step  $t = (n+1/2)\Delta t$ . As with all numerical techniques, the accuracy of the solution is directly tied to spatial grid sizes and in the case of FDTD  $\Delta t$  as well. The time step criterion for a realistic solution is defined as

$$\Delta t \leq \frac{1}{c \sqrt{\frac{1}{(\Delta x)^2} + \frac{1}{(\Delta y)^2} + \frac{1}{(\Delta z)^2}}}. \quad (3.39)$$

As a good rule of thumb, if the highest frequency of interest is  $f$  so that  $\lambda = c/f$ , and the temporal periodic is  $T = 1/f$ , the gridding should at a minimum satisfy  $\Delta t < T/20$  and  $(\Delta x, \Delta y, \Delta z) < \lambda/20$  (Jin, 2011).

One of the major challenges in the use of FDTD is working within a finite simulation window, when in the experimental world electromagnetic fields are unbounded. Typically the use of a mathematical boundary condition and the use of fictitious absorbing material layers are used to truncate the infinite space to a finite computational domain. Additionally, there are several other types of finite boundary conditions that can be utilized, including periodic, perfectly reflecting, Bloch, symmetric, and asymmetric boundary conditions. The most commonly used boundaries are again

PML, as was the case in FEM computations. In all simulations performed in this thesis PML boundary conditions were used and will thus only be discussed here.

First let us consider the reflection of a plane wave by an interface (coinciding with the  $xy$ -plane) between two half-spaces in the stretched coordinate system shown in Figure

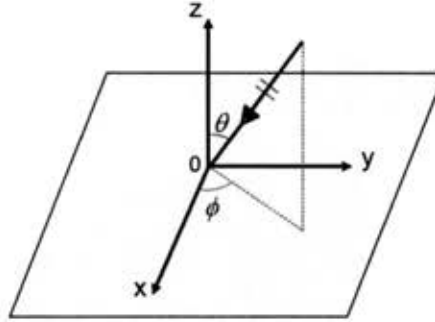


**Figure 3.5:** A plane wave incident on the interface between the upper and lower half-spaces.

For the  $TE_z$  case, the incident, reflected and transmitted fields can be written as

$$\mathbf{E}^i = \mathbf{E}_0 e^{-jk^i \cdot \mathbf{r}} \quad (3.40)$$

$$\mathbf{E}^r = R_{TE} \mathbf{E}_0 e^{-jk^r \cdot \mathbf{r}} \quad (3.41)$$

$$\mathbf{E}^t = T_{TE} \mathbf{E}_0 e^{-jk^t \cdot \mathbf{r}} \quad (3.42)$$

where  $\mathbf{E}_0$  is a constant vector perpendicular to  $\hat{z}$ , and  $R_{TE}$  and  $T_{TE}$  are the reflection and transmission coefficients, respectively. Next, using tangential continuity conditions and phase-matching for  $\mathbf{E}$  and  $\mathbf{H}$ , we obtain the TE reflection coefficient

$$R_{TE} = \frac{k_{1z} s_{2z} \mu_2 - k_{2z} s_{1z} \mu_1}{k_{1z} s_{2z} \mu_2 + k_{2z} s_{1z} \mu_1} \quad (3.43)$$

and the similarly the TM reflection coefficient can be written as

$$R_{TM} = \frac{k_{1z}s_{2z}\epsilon_2 - k_{2z}s_{1z}\epsilon_1}{k_{1z}s_{2z}\epsilon_2 + k_{2z}s_{1z}\epsilon_1} \quad (3.44)$$

where the subscript 1 denotes parameters in the upper half-space and subscript 2 denotes those in the lower half-space and the parameter  $s$  is a stretching factor described in detail in (Jin, 2011). The reflection coefficients can then be forced to 0 when the parameters are chosen correctly, namely  $\epsilon_1 = \epsilon_2$ ,  $\mu_1 = \mu_2$ ,  $s_{1x} = s_{2x}$ ,  $s_{1y} = s_{2y}$ ,  $\theta_1 = \theta_2$  and  $\phi_1 = \phi_2$ . The result remains true regardless of the choice of  $s_{1x}$  and  $s_{2x}$ , the angle of incidence and the frequency and hence the interface is referred to as a perfectly matched interface. If we choose  $s_{2z} = s' - js''$ , where  $s'$  and  $s''$  are real numbers with  $s' \geq 1$  and  $s'' \geq 0$ , then  $k_{2z} = k_2(s' - js'') \cos \theta$ . The result implies the transmitted wave will be attenuated exponentially by the factor  $\exp(k_2 s'' z \cos \theta)$  in the  $-\hat{z}$  direction. Finally, by assigning a finite thickness (thickness =  $L$ ) to medium 2 and placing a conducting surface at its back, the magnitude of the reflection coefficient can be written as

$$|R(\theta)| = e^{-2k_2 \int_0^L s'(x) dz \cos \theta} \quad (3.45)$$

From this result it is clear that the reflection is a minimum for normal incidence plane waves and maximum at grazing incidences.



## Chapter 4

### 4 Nanofabrication Methods

This chapter details the various nanofabrication techniques utilized to fabricate both metallic and dielectric nanostructures. Additionally, process flows for a silicon-based photo-detectors will be discussed.

#### 4.1 Fabrication of Nanoplasmonic Structures

The fabrication of metallic nanostructures is first discussed as it serves as the initial steps in fabricating dielectric nanopillars. Figure 4.1 shows the electron beam lithography (EBL) based process flow for the fabrication of metallic nanostructures on an insulating substrate such as fused silica or quartz. Figure 4.2 shows the process flow for conductive substrates such as Si or a metallic film.

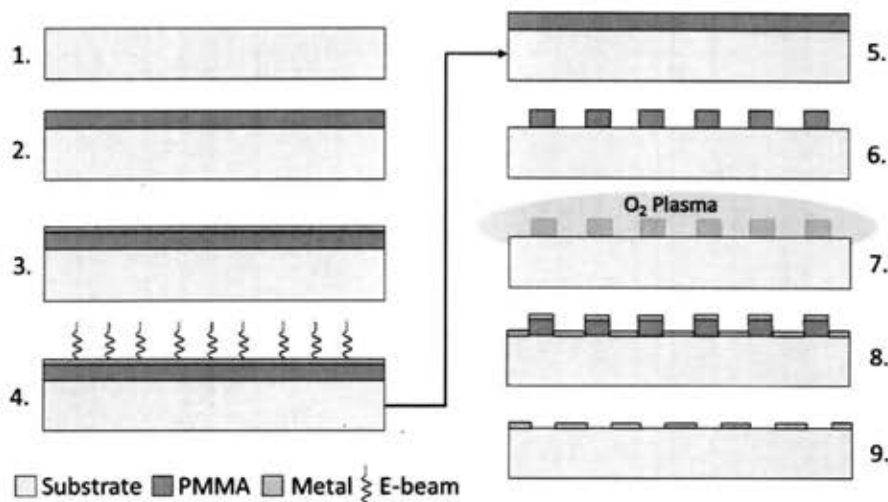


**Figure 4.1:** The general process flow of EBL used for the fabrication of metallic nanostructures that are on an insulating substrate (i.e. quartz or fused silica).

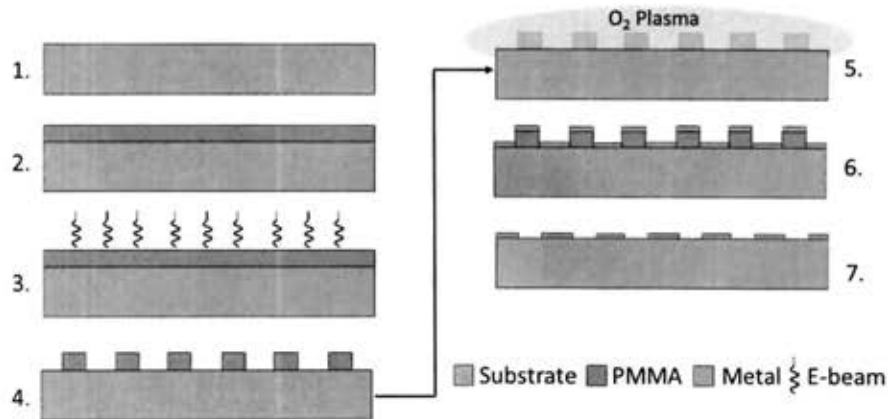


**Figure 4.2:** The general process flow of EBL used for the fabrication of metallic nanostructures that are on a conductive substrate (i.e. Si, SiN, or metal surfaces).

The starting substrate is typically diced from a 4" wafer of Si, fused silica or quartz, using a fully automated dicing saw (Disco DAD 3220) configured with a 2" hubbed resin bonded blade (CA-006-325-XXX-H). Substrates are typically cut to 10x10 mm<sup>2</sup> pieces; however samples larger or smaller were also utilized for particular applications.

#### 4.1.1 Sample Cleaning and Spin-coating

Prior to any lithography steps, each substrate must be cleaned of impurities that may exist due to general handling, shipping or dicing (step 1 in both Figures 4.1 and 4.2). Substrates are first sonicated in de-ionized (DI) water for 5 minutes to remove any small particles that have accumulated on the surfaces. The substrates are then subjected to semiconductor industry standard RCA cleaning, developed by Werner Kern in 1965 while at the Radio Corporation of America. The RCA process begins the removal of organic contaminants (SC-1, where SC stands for standard clean) using a 5:1:1 volume mixture of de-ionized (DI) water, hydrogen peroxide (H<sub>2</sub>O<sub>2</sub>, 30% by wt.), and ammonium

hydroxide ( $\text{NH}_4\text{OH}$ , 33% by wt.) at a temperature of  $75^\circ\text{C}$  for 10 minutes. The chip is then rinsed in DI water removing any residual SC-1 solution. An optional step in the RCA process, only used on bare Si substrates, is the removal of the thin native oxide layer by short immersion in a buffered oxide etch (BOE) at room temperature. Typically 15 seconds is more than enough to remove the  $\sim 1$  nm-thick  $\text{SiO}_2$  layer. Subsequently, the chip is thoroughly rinsed in DI water to remove all residual BOE. The final step of the RCA process involves the removal of ionic contamination (SC-2) via a 5:1:1 volume solution of DI water,  $\text{H}_2\text{O}_2$  and hydrochloric acid (HCL) at  $75^\circ\text{C}$  for 10 minutes. A thorough DI water and isopropanol (IPA) rinse are followed by drying the sample with forced nitrogen ( $\text{N}_2$ ) and bake out at  $120^\circ\text{C}$  for 5 minutes to dehydrate the surface.

The cleaned substrates are now spin-coated with PMMA 950 (Poly-Methyl MethAcrylate, 4% by wt.) at 2000 rpm for 45 seconds, immediately followed by a hot-plate bake at  $180^\circ\text{C}$  for 2 minutes (step 2 in both Figures 4.1 and 4.2). The resulting PMMA measures approximately 180 nm-thick; however thinner or thicker layers can be achieved by adjusting the spin speeds according to spin speed verse thickness curves provide by MicroChem Corporation.

#### 4.1.2 Electron-Beam Lithography and Development

Since electrons are charged particles, they tend to charge the substrate negatively, unless they can quickly be dissipated through a path to ground. For a high-energy beam incident on a conductive Si wafer, virtually all the electrons stop in the wafer where they are immediately passed to ground through the substrate. However, for an insulating

substrate such as quartz or fused silica, the embedded electrons will take a much longer time to move to ground without a conductive path. This effect is known as "charging" in E-beam imaging and lithography. The build of negative charge can deflect the beam of electrons away from the intended target area making imaging and repeatable EBL results virtually impossible. To resolve this issue for insulating substrates, an ultra-thin layer of Au (~5 nm-thick) is sputtered onto the PMMA coated insulating substrate (step 3 in Figure 4.1). The Au layer serves to dissipate the built up charge through the conductive film and eventually to ground through the metal sample holder. Conductive substrates do not require the ultra-thin Au layer, so this step is omitted in Figure 4.2.

Nanopatterns are written using a Zeiss SUPRA 40VP SEM equipped with Raith beam blanker and NPGS software for nanopatterning. Patterns are generated by Matlab code, creating files with positions and radii of each particle in the array. A second Matlab code is then implemented to convert the position file into the format (.dc2 file extension) required by the NPGS software. The e-beam exposure occurs at a working distance of 6 mm, a beam voltage of 30-keV and at an aperture size of 10  $\mu\text{m}$ . Pattern sizes range from 25x25  $\mu\text{m}^2$  to 300x300  $\mu\text{m}^2$ , depending on the application of the structures. The current is measured using a Faraday cup, typically measuring between 35-45 pA. The line-to-line spacing of the e-beam is set at 5 nm to maximize the writing resolution and a line dosage of 250-450  $\mu\text{C}/\text{cm}^2$  is used, depending on the array density and substrate material. It is necessary in the case of new geometries and substrates to run a dosage test matrix to identify the ideal exposure conditions to realize the designed geometries. Array patterns are spaced between 200 and 300  $\mu\text{m}$  apart to avoid undesirable cross-talk between arrays.

Additionally, large triangular or cross shaped markers ( $\sim 200 \times 200 \mu\text{m}^2$  in size) are written near the arrays as a means to globally locate the arrays on the chip when conducting experiments.

After e-beam exposure, the conductive Au layer must be removed from the insulating substrates (step 5 in Figure 4.1). The Au layer is selectively removed by Gold Etchant TFA (8 wt% Iodine, 21 wt% Potassium Iodide, 71 wt% water), without harming the underlying PMMA layer. The Au etch step requires only a 15 seconds emersion in solution, followed by thorough rinsing in DI water and blown dry with a  $\text{N}_2$  gun. At step 6 of Figure 4.1 (insulating substrate) and at step 4 of Figure 4.2 (conductive substrate), the process moves to development of the e-beam resist. The development is carried out in a 3:1 solution of IPA:MIBK (isopropanol : methylisobutyle ketone) for 70 seconds, while gently agitating the solution to improve feature resolution (Vieu et al., 2000). The samples are then rinsed in IPA and blown dry with a  $\text{N}_2$  gun.

#### 4.1.3 Metal Deposition and Lift-off

Prior to metal deposition the newly developed films are treated with oxygen ( $\text{O}_2$ ) plasma in a PVA TePla America M4L plasma asher (step 7 in Figure 4.1 and step 5 in Figure 4.2). The  $\text{O}_2$  plasma removes any possible residual PMMA and solvent contamination remaining in the patterned arrays from the development process. The plasma ash is carried out with 200 sccm of  $\text{O}_2$  flow and 200 W RF power for 30 seconds.

The next step in the nanofabrication process flow is the deposition of the metallic film via e-beam evaporation (step 8 in Figure 4.1 and step 6 in Figure 4.2). E-beam

evaporation is a process similar to thermal evaporation, i.e. a source material is heated above its boiling/sublimation temperature and evaporated to form a film on the substrate. In the case of e-beam evaporation, the heating is done by rastering an e-beam across the metal. This evaporation method is highly directional which results in poor step coverage. This feature is in fact desirable and enabling of the proceeding lift-off processes. One major advantage of e-beam evaporation over thermal evaporation is the possibility to add a larger amount of energy into the source material, resulting in higher density films and increased adhesion to the substrate.

The e-beam evaporation is implemented using a CHA Solution evaporator, controlled by a Sycon STC-2000A deposition rate controller. At this point in the process several metals can be deposited, depending on the application of the device. The discussion will now follow the metal choice of Au as it is the most commonly used plasmonic material (along with Ag) and is the metal most utilized in this thesis. In targeting a final particle thickness of 30 nm, a 2 nm-thick titanium (Ti) or chromium (Cr) adhesion layer is first deposited, followed by a 28 nm-thick Au layer. The deposition takes place under high vacuum (pressure  $< 3 \times 10^{-6}$  torr) while the samples are rotated to ensure uniform coverage across the planar surface of the samples. Au films are evaporated at 0.1 nm/sec, while the adhesion layer is typically evaporated at 0.05 nm/sec.

The last step in both process flows concludes with the lift-off procedure. During the lift-off, the PMMA under the film is removed with a solvent, taking the film with it, and leaving only the parts of the film that were deposited directly on the substrate. The

solvent used is acetone heated to 70°C. The sample is soaked in the heated solvent for 5 minutes or until the metal film displays significant wrinkling across the chip. At this time the film is briefly sonicated (10-30 seconds) to remove the remaining PMMA/metal. The sample is then sprayed with a stream of acetone to remove any of the lifted-off metal film that may be adhered to the substrate. This step is critical as it prevents any re-deposition of excess metal particulates. The sample is then rinsed thoroughly with IPA and dried by blowing with a N<sub>2</sub> gun. Figure 4.3 shows SEM micrographs of representative arrays of Au nanocylinders (30 nm height).

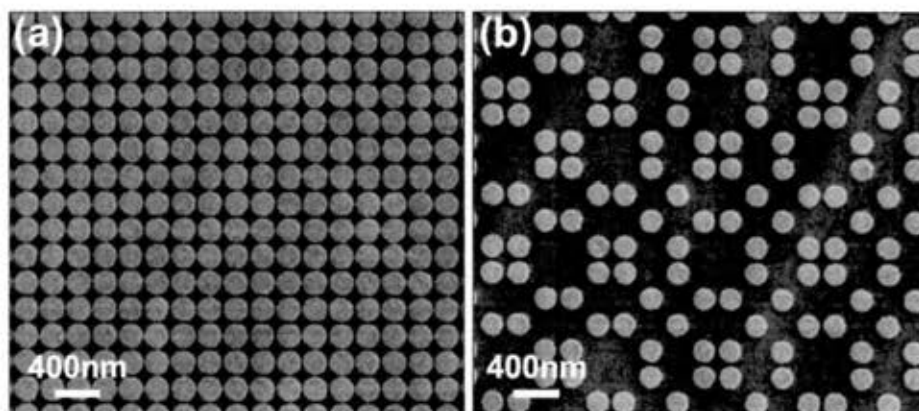


**Figure 4.3:** SEM micrographs of Au nanocylinders arrays (30 nm height). (a) Periodic array with particle diameter 215nm and edge-to-edge separation 15nm. (b) Thue-Morse array with particle diameter 195nm and minimum edge-to-edge separation of 30 nm.

With the process flow described above, edge-to-edge interparticle separations of 15 nm are readily achievable as well as particle arrangements of any complex geometry. The e-beam lithography process is highly accurate in producing features with rounded edges; however limitations exist when attempting to fabricate features with sharp edges such as triangles.

## 4.2 Fabrication of Dielectric Nanopillar Arrays

Recent developments in nanofabrication methods allow us to construct 3D dielectric nanopillars, which reach aspect ratios that approximate 2D arrays. Numerous studies on the photonic band gaps displayed by 2D arrays of Si pillars have been conducted (Poborchii, Tada and Kanayama, 2002). The band gaps allow their effective use as waveguides (De Dood et al., 2002), optical switches (Sharkawy et al., 2002), beam splitters (Ao et al., 2006), and wavelength multiplexers (Sharkawy, Shi and Prather, 2001). In this section the fabrication of nanopillars of various dielectric materials will be discussed.

The vast majority of top-down fabricated nanopillar research has been conducted on crystalline Si-based (c-Si) nanopillars etched from Si wafers; however the ability fabricate nanopillar arrays from active materials, optically transparent materials and on transparent substrates opens the door to several new photonic device applications. Here, this is achieved through radio frequency (RF) reactive sputtering of dielectric materials onto transparent fused silica substrates and subsequent nanofabrication processing steps, ending in nanopillar array formation. The complete process flow is shown in Figure 4.4.



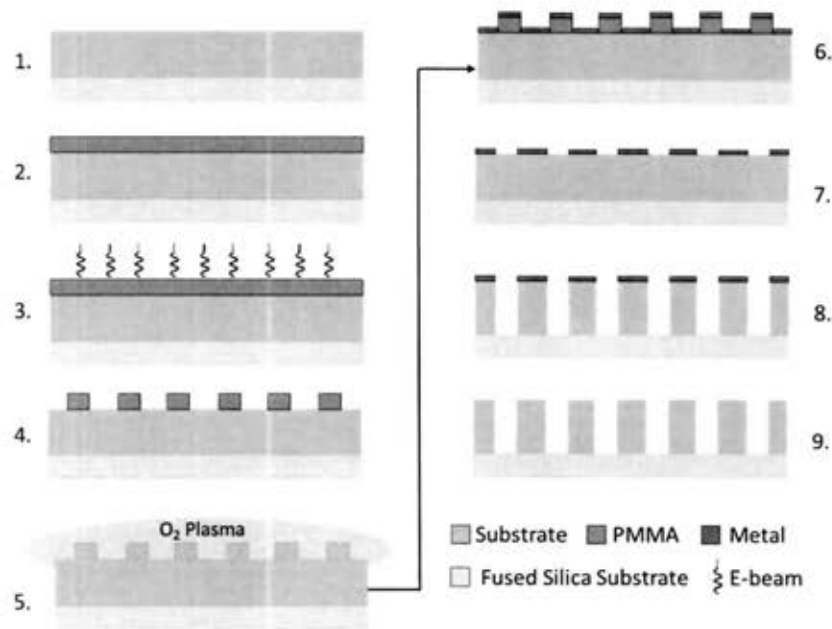


**Figure 4.4:** The complete nanofabrication process flow used in the fabrication of dielectric nanopillar arrays on a transparent glass.

#### 4.2.1 RF Sputter Deposition of Nanopillar Materials

The process begins with the selection of the nanopillar material appropriate for the device application. In this thesis, a nanopillar fabrication process was developed and demonstrated for several different dielectric materials, including c-Si, stoichiometric silicon nitride (SiN), erbium doped silicon nitride (Er:SiN<sub>x</sub>) and hydrogenated amorphous Si (a-Si:H). All pillar material utilized in this thesis was deposited by radio frequency (RF) magnetron sputtering, using a Denton Discovery 18 confocal-target sputtering system. Sputtering is a highly employed vacuum deposition technique used by manufacturers of semiconductors, CDs, disk drives, optical devices and several other industries (Kelly and Arnell, 2000).

Magnetrons are a class of cold cathode discharge devices used generally in a diode mode. The plasma is initiated between the cathode and the anode at low pressures by the application of a high voltage that is in this case RF. The plasma is sustained by the ionization caused by secondary electrons emitted from the cathode due to ion bombardment, which are accelerated into the plasma across the cathode sheath. These collisions create a momentum transfer that ejects atomic size particles from the target. These particles traverse the chamber and are deposited as a thin film onto the surface of the substrates. In reactive sputtering, the sputtering of the elemental target in the presence of a gas reacts with the target material to form a new compound.

Sputter depositions occur at a base pressure  $\sim 10^{-7}$  mbars and with RF generator operating at 13.56 MHz. A detailed description of the sputter configuration and process development can be found in the following reference (Yerci, 2011). Additionally, the  $\text{SiN}_x$  and  $\text{Er:SiN}_x$  film recipes utilized in this thesis have been optimized previously by Dr. Selcuk Yerci and Dr. Rui Li while at Boston University, using the same Denton sputter (Yerci et al., 2009; Li, Yerci and Dal Negro, 2009). Likewise, a more detailed description of a-Si:H deposition process will be discussed in later chapters.

As previously described in section 4.2, substrates are first cleaned using the standard RCA process prior to any fabrication steps. For fused silica substrates the middle BOE step is omitted. Step 1 of Figure 4.4 shows the deposition of the dielectric film on the clean glass substrate. Deposition parameters for a-Si:H, SiN and Er:SiN<sub>x</sub> films are shown in Table 4.1. The thickness of the film will determine the final pillar

height, which can be targeted using timed depositions and known deposition rates shown in Table 4.1.

Film	Gas 1 / Gas 2	Flow Rate 1 / Flow Rate 2 (sccm)	Cathode Power (W)	Base Pressure (kPa)	Deposition Rate (nm/min)
a-Si:H	H / Ar	0.7 / 10.3	350 (Si)	6.20E-07	10.4
SiN	N <sub>2</sub> / Ar	2.6 / 9.8	350 (Si)	6.00E-07	11.3
Er:SiN <sub>x</sub>	N <sub>2</sub> / Ar	2.2 / 10.2	350 (Si) 10 (Er)	6.80E-07	17.0

**Table 4.1:** Sputter deposition parameters for a-Si:H, SiN and Er:SiN<sub>x</sub> films.

For nanopillar fabrication in this thesis, film thickness range from 750 nm to 1.0  $\mu\text{m}$ . This equates to approximate deposition times between 1 and 1.5 hours. With films requiring depositions of such length, the maximum continuous deposition time was restricted to 20 minutes at which time the cathode power was turned off and the chamber was allow to cool down. For times longer than 20 minutes, the increased temperature results in deviations in film composition over the thickness of the film, as well as a significant decrease in deposition rate. Additionally, it is important to note that if the depositions greater than 1.5 hours are needed, the author suggests that a chamber clean is performed prior to further depositions. Over time, significant material build up occurs on the shutter and chamber walls. Soon thereafter debris begins to flake off and become possible contamination and particle sources for the sample.

#### 4.2.2 Pillar Metal Mask Fabrication

The next steps in the process flow are represented in Figure 4.4 by steps 2 thru 7. These steps are identical to and detailed in the previous section (4.2). In review, a

combination of EBL, metallization and lift-off are used to fabricate metal nanostructures onto the surface of the dielectric film. The difference now is found in the choice of metal and the thickness, selection of which is dependent on subsequent etching steps. These metal films will be used as an etch mask during a subsequent reactive ion etch (RIE) which defines the pillar geometry. Described in more detail in the next section, SiN based films were etched using a standard RIE system located at Boston University while Si based films are etched using a inductively coupled plasma RIE (ICP-RIE) at Harvard University. For SiN based films, the metal utilized was a 40 nm-thick Cr layer. For Si based films etched by ICP-RIE, a 30 nm-thick aluminum (Al) layer was used. The choice of different metals for different RIE tools will be detailed in the next section.

#### 4.2.3 Pillar Etching and Metal Removal

Plasma etching has two fundamental steps, the generation of ions and then imparting the ions with momentum to direct them at their target. Once the ions reach their target, the ions can either mechanically or chemically remove atoms from the substrate. Two etchant tools were utilized in this thesis. The first, here on referred to as the *RIE*, is located in the Boston University Optical Processing Facility (BU OPF) and is a capacitive coupled plasma (CCP) etcher (Plasma-Therm 790). The second, here referred to as the *ICP RIE*, is located at the Harvard University Center for Nanoscale Research (HU CNS) and is an inductively coupled plasma (ICP) etcher (Surface Technology Systems ICP RIE). In a CCP process, energy is supplied as a voltage between an anode and a cathode plate at a RF frequency. In an ICP process, the excitation is again using a

time-varying RF source, but is instead delivered inductively, via a coil wrapped around the RIE plasma discharge region, resulting in a changing magnetic field. The ICP configuration allows for more control of the ion density without significantly perturbing the incident energy of the ions. With higher plasma densities, very efficient and highly directional etching is possible, more so than in a standalone CCP configuration. Table 4.2 shows the etch recipes for a SiN based film using RIE as well as etch recipes for Si films using the ICP RIE.

An additional advantage to the ICP RIE system at CNS is found in the control of the sample chuck temperature, which is maintained at 45°C. At this temperature, a base pressure of 0.5 mTorr, and using a SF<sub>6</sub> based etch, Al has an etch rate of almost 0, while Cr will be etched at approximately 0.7 nm/min (Williams, Gupta and Wasilik, 2003). For this reason, engineers at HU CNS require Al to be used as the metal mask, ensuring a reduction in metal contamination of the chamber. Additionally, the temperature controlled etch conditions make for a more uniform and consistent etch profile. Under the SiN etch conditions in the BU RIE, Cr consistently displayed a slightly better etch selectivity than Al, so it was used in all pillar etching of these films.

Etch Type	Gas 1 (sccm)	Gas 2 (sccm)	Power (W)	Pressure (mTorr)	Etch Rate (nm/min)
SiN (RIE)	CHF <sub>3</sub> (100)	O <sub>2</sub> (1.5)	150	30	50
Si (ICP RIE)	SF <sub>6</sub> (65)	C <sub>4</sub> F <sub>8</sub> (160)	1200	0.5	75

**Table 4.2:** Etch recipes for SiN based films using RIE and Si films using an ICP RIE.

The final step of the nanopillar fabrication (step 9 in Figure 4.4) is the removal of the remaining metal mask layer. For Cr mas removal the sample is submerged in heated

(50°C) Chromium Etchant 1020 (Transene, Inc.) for 10 minutes. For an Al mask, the sample is submerged in a heated (50°C) Aluminum Etchant Type A (Transene, Inc.) for 2 minutes. Samples are then thoroughly rinsed in DI water and dried with a N<sub>2</sub> gun. Figure 4.5 shows SEM micrographs of nanopillars fabricated from c-Si, a-Si:h and SiN.

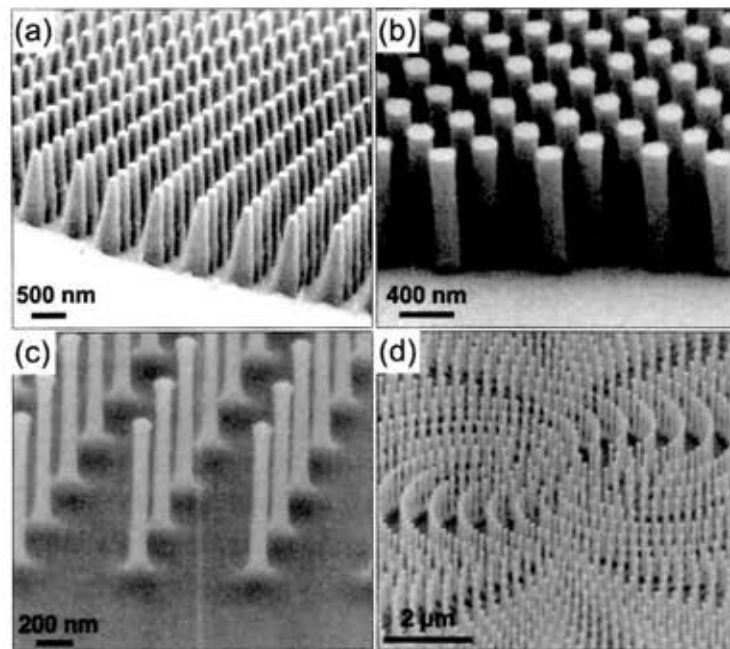


**Figure 4.5:** SEM micrographs of fabricated nanopillar arrays. (a) 750 nm-tall SiN pillars with 150 nm top diameter (b) 1  $\mu\text{m}$ -tall a-Si:H nanopillars with 100nm diameters, (c) 1  $\mu\text{m}$ -tall c-Si nanopillars with 100nm diameters (d) c-Si aperiodic nanopillar spiral array with pillars 1  $\mu\text{m}$ -tall and 100nm diameters.

Figure 4.5a shows an SEM micrograph of SiN pillars etched using the RIE system. The nanopillars were designed to have 150 nm diameters, be 750 nm-tall, and have a cylindrical profile. It is evident from the SEMs that the etch profile of SiN is non-ideal, becoming less directional as the function of depth and resulting in a conical shaped pillar. For pillars with such an aspect ratio (5), an optimized SiN recipe to solve this tapering was not developed. Lawrence *et al.* found the recipe to work sufficiently well for

low aspect ratio pillars ( $\sim 1.5$ ) for the engineering of radiation from aperiodic arrays of active nanopillars (Lawrence, Trevino and Dal Negro, 2012).

Figure 4.5b and 4.5c show SEM micrographs of 1  $\mu\text{m}$ -tall nanopillars with 100 nm diameters (aspect ratio of 10) made from a-Si:H and c-Si respectively. The etch profile is highly anisotropic and smooth, making for ideal photonic structures for several applications. Figure 4.5c displays the ability to make arbitrarily complex and large patterns of nanopillars without loss of pillar profile quality.

### 4.3 Photo-detector Device Fabrication

The following section details the fabrication of a Si based Schottky photo-detector integrated with plasmonic nanoparticles. Motivation and experimental details will be discussed in subsequent chapters. Figure 4.6 shows the process flow for the photo-detector fabrication, beginning with a purchased SIMGUI Silicon on Oxide (SOI) wafer in step 1. The SOI wafer has a 50 nm-thick ( $\pm 1.2$  nm) c-Si (p-type doped, 1-20 ohm-cm resistivity) top layer, with a 156 nm-thick buried oxide layer on top of a 525  $\mu\text{m}$ -thick c-Si wafer (p-type doped). Step 2 utilizes the process flow described previously (Section 4.1) to fabricate 30 nm-tall Au nanoparticle arrays by EBL, metallization and lift-off. Details of the array geometries and particle sizes will be discussed in Chapter 8.

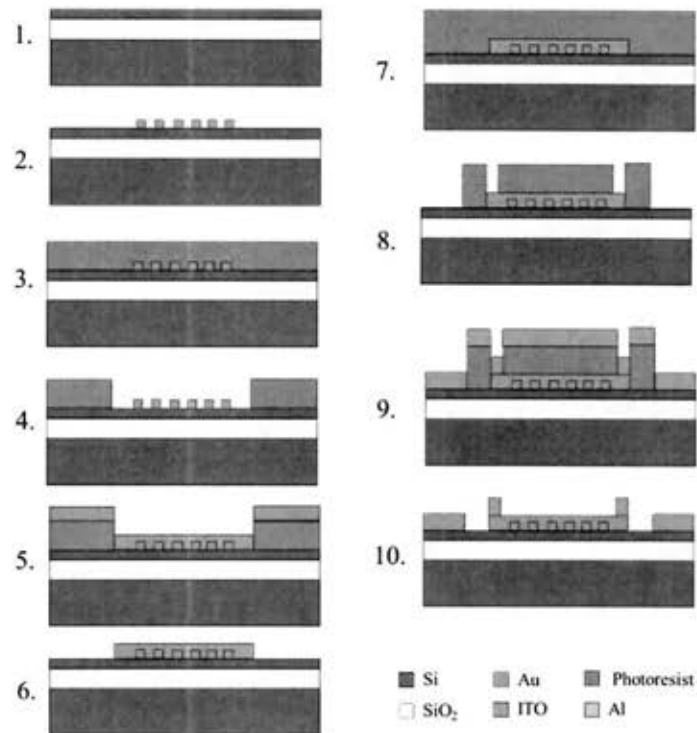


**Figure 4.6:** Si based Schottky photo-detector fabrication process flow.

After the arrays of Au nanoparticles have been fabricated onto the top surface of SOI, a photolithographic process is used to define a window around the arrays. Here after, this process will be known as *standard photolithography* (steps 3 and 4). The standard photolithography process begins with the spin coating of AZ 5214E photoresist at 4000 rpm for 45 sec (500 rpm/sec ramp up and down), followed by a 100°C hotplate bake for 45 sec. The resulting film thickness is  $\sim 1.4 \mu\text{m}$ . The chip is then aligned to photo-mask and exposed for 11 seconds in hard contact mode using a Karl Suss MA6 mask aligner. The mask contains the desired pattern, which selectively allows for the exposure of the area over the arrays. The chip is then developed for 17 seconds in AZ 400k and rinsed in DI water. The resulting cross section is shown in step 4 of Figure 4.6.



Post development, a 40 nm-thick conductive and optically transparent indium tin oxide (ITO) film is deposited via the Denton RF magnetron sputter (step 5). The sputter parameters for the ITO deposition are 100 W RF power, Ar flow rate of 11 sccm at a base pressure of  $5 \times 10^{-7}$  kPa, with a deposition rate of 10 nm/min. The chip is then soaked in heated acetone (70°C) for 5 minutes, lifting off the unwanted resist/metal stack. Occasionally, an additional 2-minute sonication is required to remove any remaining resist/metal. The resulting cross-section is shown in step 6 of Figure 4.6. Next, the standard photolithography process is carried out again to define windows for metallic contacts (steps 7 and 8). E-beam evaporation is then used to deposit a 300 nm-thick Al film (step 9). Another heated acetone lift-off is preformed, resulting in the final structure shown in step 10. The defined Al pads separately contact the top Si layer as well as the ITO layer. A 3D representation is shown in Figure 4.7 with exaggerated features to better visualize the device configuration.

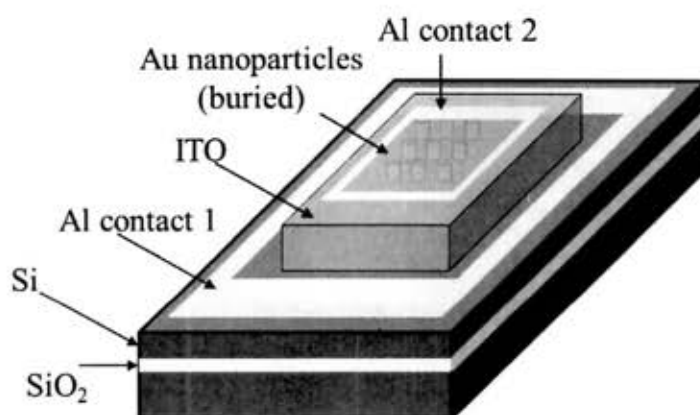


**Figure 4.7:** SEM micrographs of fabricated nanopillar arrays. (a) 750 nm-tall SiN pillars with 150 nm top diameter.

### 4.3.1 Fabrication of Optical Absorption Quantification Chip

The fabrication of a chip integrated with Au nanoparticles used for optical absorption measurements will now be discussed. The details regarding the experimental techniques and array parameters will be discussed fully in Chapter 8 and the reader can find the published results in the following reference (Trevino, Forestiere, et al., 2012) . The device process flow can be seen in Figure 4.8.

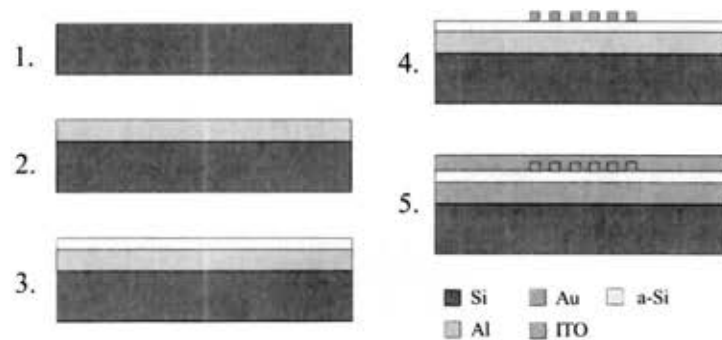


**Figure 4.8:** Fabrication process flow for optical absorption quantification chip.

Step 1 begins with the standard RCA clean of a Si (p-type) chip. A 300 nm-thick reflecting Al film is then deposited by e-beam evaporation (step 2). A 50 nm-thick absorbing a-Si layer is then deposited by RF magnetron sputtering (step 3). The a-Si film was sputtered using 10 sccm of Ar, 0.5 sccm of H<sub>2</sub>, 200 W RF power, and a base pressure of  $1 \times 10^{-6}$ . The deposition rate under these conditions is  $\sim 15$  nm/min. Step 4 utilizes the process flow described previously in Section 4.1 to fabricate Au nanoparticle arrays by EBL, metallization and lift-off. The metallic particles are cylindrical in shape with a circular diameter of 100 nm and thickness of 30 nm. All arrays are fabricated within a circular frame region with identical diameter of 100  $\mu$ m. Finally, a 40nm-thick ITO film

is deposited via RF magnetron sputtering, with the same deposition parameters described in Section 4.3.

## Chapter 5

### 5 Deterministic Aperiodic Order

Aperiodic optical media generated by deterministic mathematical rules have recently attracted significant attention in the photonics community due to their ability to leverage varying degrees of spatial complexity while maintaining simplicity in design and generation (Dal Negro and Boriskina, 2012; Maciá, 2006; Steurer and Sutter-Widmer, 2007; Macia, 2009). Several foundational studies in aperiodic systems were conducted on 1D systems, stimulating broader theoretical and experimental studies on photonic and plasmonic structures that utilize aperiodicity as a strategy to enable optical devices and novel functionalities (Kohmoto, Kadanoff and Tang, 1983; Kohmoto, Sutherland and Iguchi, 1987; Vasconcelos and Albuquerque, 1999; Dulea, Severin and Riklund, 1990). In this chapter, the conceptual framework of 2D aperiodic order for the manipulation of optical fields will be briefly discussed. Specifically, deterministic aperiodic nanostructures (DANS) will be introduced as their classification based on Fourier spectral properties.

#### 5.1 Periodic and Quasi-Periodic Order

Historically, both crystallographic and optical media were simply classified as either periodic or non-periodic in nature, without further distinctions. The non-periodic classification however held a broad range of concepts that described structural

correlations, ranging from random or amorphous structures to more ordered systems such as quasiperiodic structures. It wasn't till Dan Shechtman *et al.*'s landmark discovery in 1984 of sharp diffraction peaks arranged with icosahedral point group symmetry in certain metallic alloys (Shechtman et al., 1984) that the scientific community moved toward defining a new class of structures known as aperiodic crystals or quasicrystals (Levine and Steinhardt, 1984). An event so revolutionary for the field that Dr. Shechtman was eventually awarded the 2011 Nobel Prize in Chemistry for the discovery of quasicrystals.

The discovery of quasicrystals boosted the investigation of the "large phase-space" between periodic and disordered systems. Additionally, the studies spawned several new questions regarding the classification of non-periodic geometries. The most common ways to categorize periodic and non-periodic structures is by the nature of their Fourier and energy spectra, which correspond to mathematical measures (Barber, 2008). In optics and in crystallography, these spectral measures are frequency identified with the characteristics of the diffraction patterns. Additionally, one should also consider the optical mode spectra or Local Density of States (LDOS) in a photonic geometry, as this will be discussed in further in Section 5.3. For example, Figure 5.1 displays a 2D periodic square lattice, a periodic lattice that has had randomly selected particles removed, a Penrose lattice, as well as their corresponding reciprocal space as calculated by their Fourier transform amplitudes.

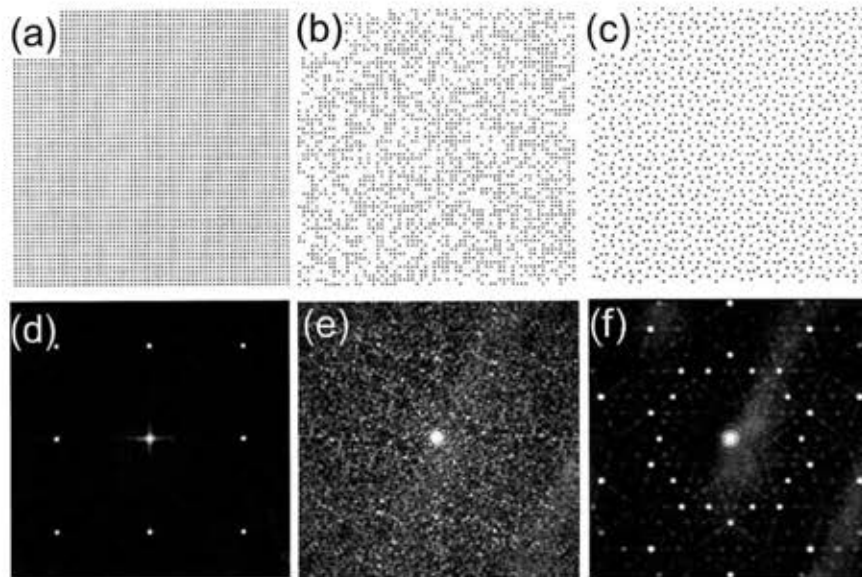


**Figure 5.1:** (a) Periodic array; (b) random array on periodic lattice; (c) Penrose array; (d) periodic array reciprocal space; (e) random array reciprocal space; (f) Penrose array reciprocal space.

A fundamental feature of the diffraction patterns of all types of periodic and quasi-periodic lattices is the presence of well-defined and sharp (i.e.,  $\delta$ -like) peaks, corresponding to the presence of long-range order. Moreover, the reciprocal Fourier space of periodic and multi-periodic lattices is discrete (i.e., pure-point), with Bragg peaks positioned at rational multiples of primitive reciprocal vectors. In contrast, the sharp ( $\delta$ -like) Bragg peaks of quasi-periodic structure are incommensurate and densely fill the reciprocal space. In the case of the random structure, the lack of any long-range order results in a diffuse Fourier spectrum with constant amplitude. The Penrose array, shown in Figure 5.1c, was first described by Roger Penrose in 1974 who found the existence of two simple polygonal shapes capable of tiling the infinite Euclidean plane without spatial periodicity (Penrose, 1947). The point array is obtained by positing particles at the vertices of the Penrose tiling. As seen in Figure 5.1f, the Penrose Fourier

spectra possess sharp diffraction peaks, as found in periodic lattices; however now with incommensurate spacings. Moreover, the interior Bragg peaks display ten-fold rotational symmetry, a feature impossible for periodic arrangements to reproduce.

According to the Lebesgue's decomposition theorem (Kolmogorov, Fomin and Fomin, 1999), any measure can be uniquely decomposed in terms of three primitive spectral components (or into a mixture of them), namely: pure-point ( $\mu_p$ ), singular continuous ( $\mu_{sc}$ ), and absolutely continuous spectral components ( $\mu_{ac}$ ), with:  $\mu = \mu_p \cup \mu_{sc} \cup \mu_{ac}$  (Dal Negro and Boriskina, 2011). The periodic and Penrose Fourier spectra, shown in Figure 5.1d and 5.1f, represent a pure-point spectra with no other contributions. At the other extreme, the random Fourier spectra shown in Figure 5.1e represent an absolutely continuous case. Such definitions are useful in categorizing aperiodic arrays, which spectra comprise of various combinations of the three types.

Recently, Enrique Macia Barber has proposed a classification scheme of aperiodic systems based on the nature of their lattice Fourier transform and transport properties (as determined by the main features of the energy spectrum and nature of eigenstates) (Maciá, 2006). According to this classification, the rigid dichotomy between periodic and amorphous structures is surpassed by a matrix with nine different entries, corresponding to all the combinations of the possible types of spectral measures, as shown in Figure 5.2.

ENERGY SPECTRUM	$\beta_{sc}$	USUAL CRYSTALLINE MATTER		SPIRAL LATTICE?
	$\beta_{sc}$	FIBONACCI PERIOD- DOUBLING	THUE-MORSE	RUDIN- SHAPIRO?
	$\beta_p$	IDEAL QUASICRYSTAL?		AMORPHOUS MATTER
		$\beta_p$	$\beta_{sc}$	$\beta_{ac}$
	LATTICE FOURIER TRANSFORM			

**Figure 5.2:** (a) Classification of aperiodic systems according to the spectral measures of their Fourier transform and their Hamiltonian energy spectrum. Reprinted from (Maciá, 2006).

Here we have a periodic lattice in the top-left corner, with a pure point Fourier spectra and an absolutely continuous energy spectrum (Bloch-like wavefunctions in allowed bands). At the other corner, we have an amorphous or randomized structure, exhibiting an absolutely continuous Fourier spectrum (flat or diffuse) and a pure point energy spectrum (exponentially localized wave-functions). In between, we have Fibonacci and Thue-Morse arrays (described in the next section) both of which have a purely singular continuous energy spectrum, but differing Fourier transform spectra. Further discussions regarding these and other aperiodic arrays will be discussed, including proposed changes to the Barber matrix based on findings of this dissertation.



## 5.2 Beyond Quasicrystals: Aperiodic Order and Substitutions

In optics and electronics, a very efficient algorithmic approach to generate aperiodic structures with controlled Fourier spectral properties is provided by symbolic substitutions (Queffélec, 1987; Lind, 1995; Barber, 2008; Dal Negro, Feng and Gopinath, 2008). In physical realizations, each letter in the alphabet can be associated to a different type of building block (e.g. nanoparticle or dielectric layer). These simple mathematical rules or substitutions can be iteratively applied on a set of abstract symbols to increase (inflate) the size of the system. For example, the Fibonacci sequence is obtained by combining two different symbols A and B according to the inflation rule  $A \rightarrow AB$  and  $B \rightarrow A$ . The first iterations of this rule then generates the strings A, AB, ABA, ABAAB, etc.. The three classic examples of substitutional aperiodic sequences are shown in Table 5.1 below.

Sequence	Substitution Rules	Spectral Classification (reciprocal space)
Fibonacci	$A \rightarrow AB; B \rightarrow A$	pure-point
Thue-Morse	$A \rightarrow AB; B \rightarrow BA$	singular-continuous
Rudin-Shapiro	$AA \rightarrow AAAB; BA \rightarrow BBA$ $AB \rightarrow AABA; BA \rightarrow BBAB$	absolutely continuous

**Table 5.1:** Substitution rules and reciprocal space spectral classification for Fibonacci, Thue-Morse and Rudin-Shapiro sequences.

2D representations of aperiodic sequences can be formed by applying two complementary substitution rules along the horizontal and the vertical directions (Dal

Negro, Feng and Gopinath, 2008). Figure 5.3 plots the Fibonacci, Thue-Morse and Rudin-Shapiro substitutional sequences as 2D arrays, as well as their calculated Fourier space.

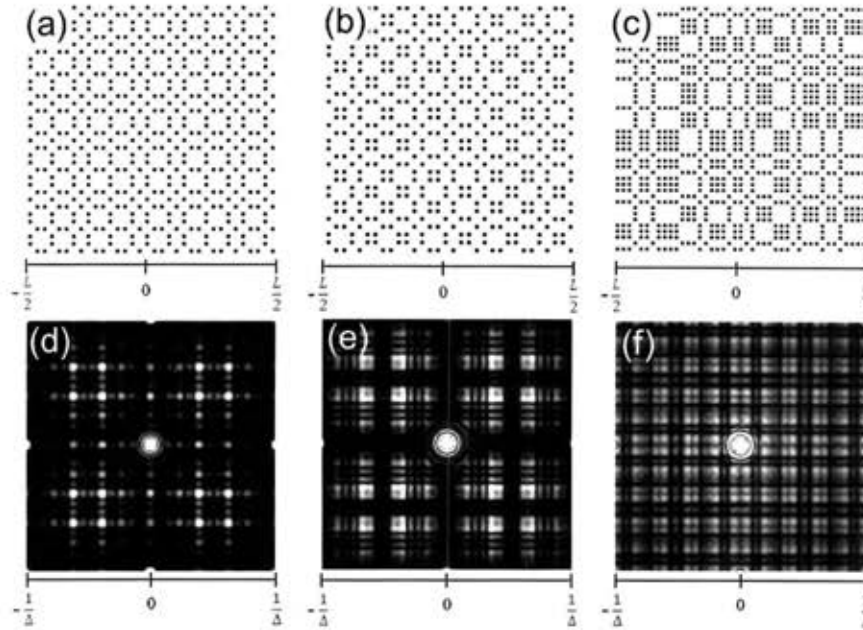


**Figure 5.3:** (a) Fibonacci array,  $L = 13.4\mu\text{m}$ , generation 7 (b) Thue-Morse array,  $L = 12.6\mu\text{m}$ ; (c) Rudin-Shapiro array,  $L = 16.4\mu\text{m}$ , generation 6; (d) Fibonacci reciprocal space; (e) Thue-Morse reciprocal space; (f) Rudin-Shapiro reciprocal space. In all cases  $\Delta = 400\text{ nm}$  is the minimum center-to-center particle distance.

It is important to note here that differently from periodic structures, Brillouin zones cannot be defined for aperiodic arrays. As a result, when displaying the diffraction spectra of aperiodic systems, we restrict the Fourier space vectors to spatial frequencies within the interval  $\pm 1/\Delta$ , where  $\Delta$  is the minimum center-to-center interparticle separation represented in the array, termed the first "pseudo-Brillouin zone". The Fibonacci, Thue-Morse and Rudin-Shapiro arrays are chief examples of deterministic aperiodic structures with pure-point, singular-continuous, and absolutely continuous reciprocal space spectra,

respectively. Recently, these three arrays have been realized in metallic nanoparticle arrays and shown to have unique scattering resonances and field localization properties ideal for enhanced light matter interactions on the surface of photonic devices (Gopinath et al., 2008; Gopinath, Boriskina, Premasiri, et al., 2009; Gopinath, Boriskina, Reinhard, et al., 2009).

Additionally, several other aperiodic arrays exist beyond those generated with substitutional rules, each having a mix of the Lebesgue's three spectral components. For example, 2D DANS arrays can be generated based on Gaussian prime number properties of integers and generalizations to Galois fields in the complex domain (Schroeder, 2009; Walsh, 2013; Dal Negro and Boriskina, 2011; Lee, Walsh and Dal Negro, 2013). 2D Galois arrays display diffraction spectra with high density of spatial frequencies, reaching a theoretically flat measure for an infinite-sized array (Dal Negro and Boriskina, 2011). Furthermore, 2D arrays based on a prime numbers (prime number array and Ulam spiral array) and co-prime numbers (co-prime array) have been investigated in the context of plasmon scattering and optical sensing (Carlo Forestiere, Gary F Walsh, et al., 2009; Boriskina et al., 2010; Lee et al., 2010).

### 5.2.1 Rotational Symmetry in Aperiodic Arrays

A key feature of aperiodic arrays is the ability to encode forbidden rotational symmetries in their diffraction diagrams as displayed in their Fourier spectra (Janot, 1997; De Graef and McHenry, 2007). As shown previously, the Penrose array displays 10-fold rotational symmetry in the Fourier space. An example of an aperiodic array with

Fourier space rotational symmetries and with mixed spectral components is the Danzer array (shown in Figure 5.4), possessing seven-fold symmetry (Danzer, 1989). In fact, it is possible to design an array with an arbitrary degree of rotational symmetry using an algebraic approach (De Bruijn, 1981). Additionally, deterministic tilings with infinite rotational symmetry or circular symmetry in the Fourier space have been constructed in what is known as the Pinwheel tiling (Rudin, 1994). The Pinwheel tiling is created by iteratively, decomposing a triangle into five congruent copies. The resulting tiling has triangular elements which appear in infinitely many orientations. Figure 5.4 plots a representative Pinwheel tiling and its corresponding Fourier space.

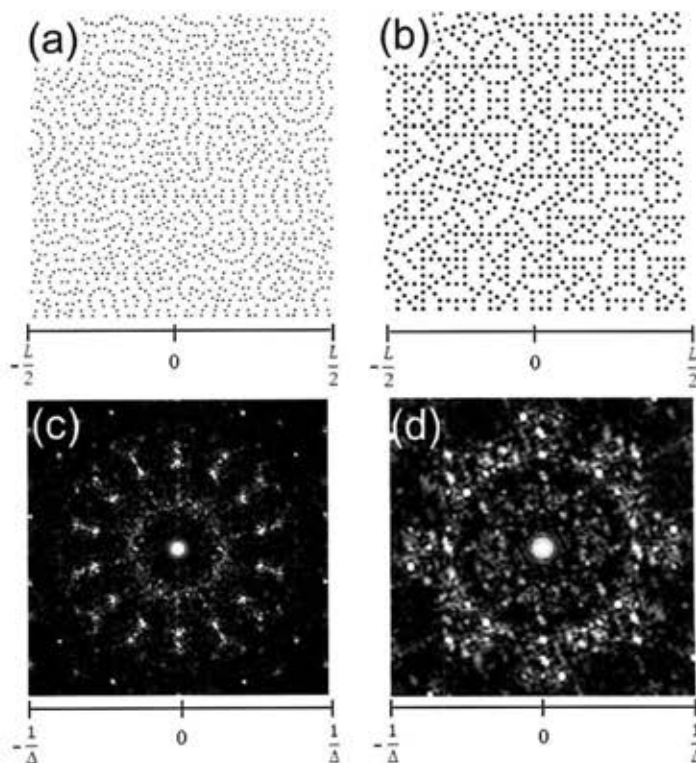


**Figure 5.4:** (a) Danzer array,  $L = 26.6 \mu\text{m}$ , generation 4 (b) Pinwheel array,  $L = 16.1 \mu\text{m}$ ; (c) Danzer array reciprocal space; (e) Pinwheel array reciprocal space. In all cases  $\Delta = 400 \text{ nm}$  is the minimum center-to-center particle distance.

It is clear that the rotational symmetry falls short of being continuous in the limit of a finite sized array. In Chapter 6 we will introduce a special class of finite-sized particle arrays with full rotational symmetry in the Fourier space, known as Vogel spirals.

### 5.3 Classification of Aperiodic Structures

A key question in the theory of aperiodic systems regards the relationship between their atomic topological order, determined by a given aperiodic density function, and the physical properties stemming from their structure (Barber, 2008). Of particular interest is the *gap-labeling theorem*, which provides a relationship between reciprocal space (Fourier) spectra and Hamiltonian energy spectra. In fact, this theorem relates the position of a number of gaps in the energy spectra of elementary excitations to the singularities of the Fourier transform of the substrate lattice (Ghosh and Karmakar, 1999; Iguchi, 1994).

It is then convenient to focus on the nature of the measure associated with the lattice Fourier transform, which is related to the main features of the diffraction pattern through the expression

$$I_N(q) = |F_N(q)|^2, \quad (5.1)$$

where  $I_N$  is the intensity of the diffraction peaks,  $N$  measures the system size,  $q$  denotes the scattering vector, and  $F_N$  is the Fourier transform of the lattice. The diffraction spectra can then be described in terms of the integrated intensity counting function in reciprocal space defined as

$$H(q) = \lim_{N \rightarrow \infty} \int_0^q \frac{I_N(q')}{N} dq'. \quad (5.2)$$

This function represents the normal distribution of the diffracted intensity peaks up to a given point ( $q$ ) in the reciprocal space. In the case of both periodic and quasiperiodic crystals there are intervals along a given  $q$  axis where the intensity vanishes, so that  $H(q)$  remains constant. These intervals are separated by Bragg peaks, where  $H(q)$  has finite jumps. This is seen in Figure 5.5a where the  $H(q)$  for the first 3 Brillouin zones of a periodic array is plotted. Figure 5.5b

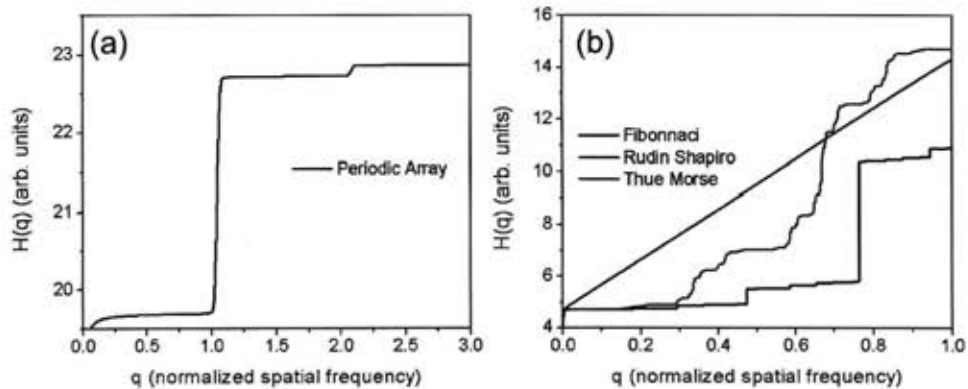


**Figure 5.5:** (a)  $H(q)$  plot for periodic array, plotting the first 3 Brillouin zones. (b)  $H(q)$  plots for Fibonacci, Rudin-Shapiro and Thue-Morse arrays, plotting the first pseudo Brillouin zone.

Figure 5.5b plots the  $H(q)$  for the first pseudo Brillouin zone of the Fibonacci, Rudin-Shapiro and Thue-Morse arrays. Recalling that Fibonacci Fourier space has a pure point measure, we notice it's  $H(q)$  resembles that of a periodic array with a countable set of sharp rises with periods of flatness in-between. On the other hand, the Thue-Morse array Fourier transform is no longer composed of a countable set of points separated by well-defined intervals. More precisely, it is singular continuous, possessing a Fourier

spectrum that can be covered by an ensemble of open intervals with arbitrary small total length (Barber, 2008). The Rudin-Shapiro possesses a purely absolutely continuous Fourier transform. In this case, we have a diffuse spectrum, where the contribution to  $H(q)$  of any interval on a given  $q$  axis is roughly proportional to its length, making the  $H(q)$  plot appear linear. By making these intervals arbitrarily small it can be proved that any single point in the spectrum has zero weight and  $H(q)$  is both continuous and derivable (Barber, 2008).

## 5.4 Conclusion

With the means of classification introduced in this chapter, the aperiodic spiral lattice will be investigated thoroughly. Of interest to note, is the tentative placement of the spiral lattice in the upper right corner of Barber's classification matrix in Figure 5.2. The spiral lattice is a unique array which is perfectly ordered without any translational or orientational symmetry. The array's Fourier transform possess no well-defined peaks, but rather diffuse rings similar to amorphous materials, making it absolutely continuous in nature. When Macia Barber created the matrix, the energy spectrum of elementary excitations propagating through spiral lattices had yet to be reported.

Chapter 6 will introduce the spiral array and provide detailed commentary on its distinctive geometrical and photonic properties. Several proceeding chapters will provide examples of device applications enabled by spiral's unique photonic properties. After comprehensively studying the aperiodic spiral's Fourier space and energy spectra

properties, remarks on the placement of these spiral arrays on Barber's matrix will be made.



## Chapter 6

### 6 Engineering Aperiodic Spiral Order

The spiral pattern is found extensively in nature; encoded into plants, animals, humans, the earth and even the galaxies around us. Figure 6.1 shows a sampling of the more well-known spiral examples.

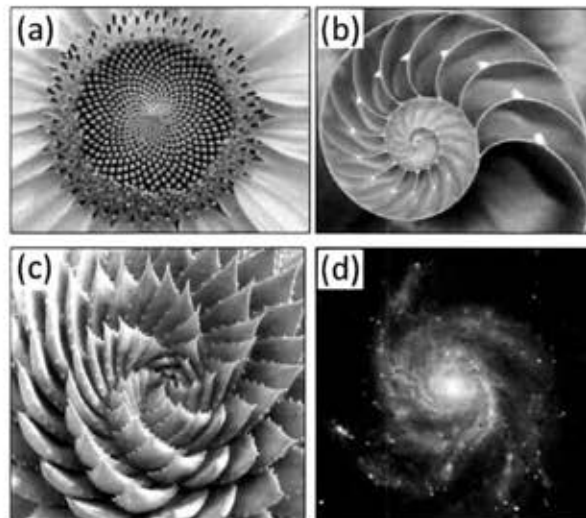


**Figure 6.1:** Examples of spirals in nature: (a) seeds on the head of a sunflower (Morrow, 2010), (b) nautilus shell (Wolff, 2012), (c) cactus leaves (Wolff, 2012), and (d) spiral galaxy (NASA, 2013).

The peculiar arrangement has for centuries drawn botanists, mathematicians and physicist to study the geometry, its origin and physical implications. More recently, the photonic properties of such arrangements have been of high interest (Trevino, Cao and Dal Negro, 2011; Pollard and Parker, 2009; Agrawal et al., 2008). The following chapter will introduce aperiodic Vogel spirals as a powerful and diverse platform for engineering light-matter interactions in planer surfaces.

Segments of this Chapter have been adapted from the 2011 Nano Letters publication *Circularly Symmetric Light Scattering from Nanoplasmonic Spirals* and the Optics Express publication *Analytical Light Scattering and Orbital Angular Momentum Spectra of Arbitrary Vogel Spirals* which can be found here (Trevino, Cao and Dal Negro, 2011) and (Dal Negro, Lawrence and Trevino, 2012), respectively.

## 6.1 Spiral Geometry

Vogel spirals can be considered a subset of the more general class of Fermat's spirals. First proposed by Helmut Vogel to approximate the complex arrangement of florets in the sunflower head in two spatial dimensions (Vogel, 1979; Mitchison, 1977; Naylor, 2002), these arrays are obtained by a simple generation rule expressed in polar coordinates  $r$  and  $\theta$  as:

$$r = a\sqrt{n} \quad (6.1)$$

$$\theta = n\alpha \quad (6.2)$$

where  $n = 0, 1, 2, \dots$  is an integer,  $a$  is a constant scaling factor,  $\alpha \approx 137.508^\circ$  is an irrational number known as the "golden angle". The golden angle can be expressed as  $\alpha = 360/\varphi^2$ , where  $\varphi = (1 + \sqrt{5})/2 \approx 1.618$  is the golden number, which can be approximated by the ratio of consecutive Fibonacci numbers. Rational approximations to the golden angle can be obtained by the formula  $\alpha^\circ = 360 \times (1 + p/q)^{-1}$  where  $p$  and  $q < p$  are consecutive Fibonacci numbers. The angle  $\alpha$  gives the constant aperture between adjacent position vectors  $r(n)$  and  $r(n+1)$  of particles in the "sunflower

spiral”, also called the “golden angle spiral”, and here referred to as the GA-spiral shown in Figure 6.2a. Two other Vogel spirals often studied are known as “nearly golden spirals” and are obtained by the following choice of divergence angles:  $137.3^\circ$  (i.e.,  $\alpha_1$ -spiral) and  $137.6^\circ$  (i.e.,  $\beta_4$ -spiral), shown in Figure 6.2b and Figure 6.2c, respectively (Naylor, 2002). The nomenclature used in naming the  $\alpha_1$ -spiral and  $\beta_4$ -spiral will become more evident in later sections of this chapter.

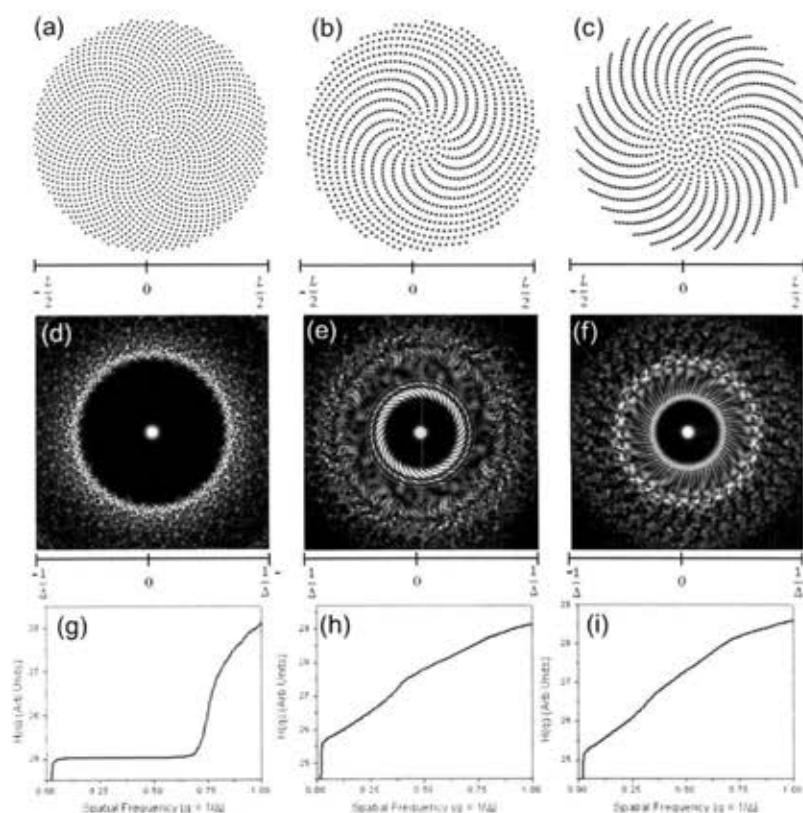


**Figure 6.2:** Representations of the first 1000 particles plotted in the (a) GA-spiral ( $\alpha \approx 137.5077^\circ$ ), (b)  $\alpha_1$ -spiral ( $\alpha = 137.3^\circ$ ), and (c)  $\beta_4$ -spiral ( $\alpha = 137.6^\circ$ ). The calculated discrete Fourier transform of the (d) GA-spiral, (e)  $\alpha_1$ -spiral, and (f)  $\beta_4$ -spiral, where the plotted region is restricted to the first pseudo-Brillion zone.  $H(q)$  plots for the (g) GA-spiral, (h)  $\alpha_1$ -spiral, and (i)  $\beta_4$ -spiral.

The structure of a GA spiral can be decomposed into an equal number of clockwise and counterclockwise spiral families originating from its center, known as

*parastichies*. The number of spirals in each family is found to be a Fibonacci number. In the case of the nearly golden spirals, their families of parastichies are considerably fewer. It is the case that when the divergence angle is slightly less than the GA, as for the  $\alpha_1$ -spiral, gaps appear in the center head of the spiral, and only the clockwise family of spiral arms can be seen. Gaps appear again if the divergence angle is slightly larger than the GA, as for the  $\beta_4$ -spiral, but this time only the counterclockwise family of spiral arms can be appreciated (Adam, 2009). The GA-spiral is the only structure where the two spiral families are uniformly interlocked and the particles pack closely together without gaps.

Since the golden angle is an irrational number, the GA-spiral lacks both translational and rotational symmetry. Accordingly, its spatial Fourier spectrum does not exhibit well-defined Bragg peaks, as for standard photonic crystals (PhC) and quasicrystals, but shows diffuse circular rings. The calculated pseudo-Brillouin zones of the three types of spirals are shown in Figure 6.2(d-f). It is noted that the DC component of the Fourier transform has been artificially removed to better visualize the scattering properties of the Vogel spirals. Diffuse spectra (i.e., absence of Bragg peaks) with rotational symmetry (i.e., scattering rings) are clearly observed for all the spirals in Figure 6.2. While the GA-spiral features a broad and central scattering ring (Figure 6.2d), the more inhomogeneous structure of the  $\alpha_2$ - (Figure 6.2b,e) and the  $\beta_4$ - (Figure 6.2c,f) spirals is reflected by the presence of multiple scattering rings embedded in a diffuse background of weaker intensity. Figure 6.2(g-i) plots the reciprocal space counting function  $H(q)$  for the three Vogel spirals, introduced in the previous chapter. The function remains zero until reaching the first scattering rings of each spiral, followed by a smooth

rise over the course of the remaining Fourier space. Notice the two nearly GA spirals have an almost linear slope similar to the Rudin-Shapiro investigated in the previous chapter. This correlates to a more diffuse Fourier space, a result of the arrays increased disorder and a topic, which will be further discussed in subsequent chapters. All three spirals display  $H(q)$  functions representative of absolute continuous Fourier space and thus Barber's placement of the spiral lattice in his classification matrix (Figure 5.2) appears correct for now.

The rotational symmetry of the reciprocal space of aperiodic spirals has direct implications on their diffractive properties. This can already be appreciated within standard Fourier optics, neglecting near-field (quasi-static) interactions among neighboring particles. Under these conditions, well-satisfied by the choice of samples parameters, normal incidence radiation of wavelength  $\lambda$  is diffracted into the plane of the arrays when its longitudinal wavevector component vanishes, i.e.,  $k_z = 0$ . This requirement is equivalent to the well-known Rayleigh cut-off condition that determines the propagation of the first diffractive order of a periodic grating on its planar surface (Fano, 1941). The Rayleigh condition depends on wavelength  $\lambda$  and on the transverse spatial frequencies  $\nu_x$  and  $\nu_y$  of the diffracting element, according to

$$k_z = 2\pi\sqrt{(1/\lambda)^2 - \nu_x^2 - \nu_y^2} = 0 \quad (6.3)$$

Equation (6.3) is satisfied on a circle of radius  $1/\lambda$  in reciprocal space, and therefore structures with circularly-symmetric Fourier space satisfy the Rayleigh cut-off condition irrespective of the polarization of the incident field, strongly diffracting normal incident

radiation into evanescent grating modes. It can be said that the resonant condition expressed by Equation (6.3) induces “planar diffraction”. It is important to note that, differently from periodic crystals and quasicrystals with finite-order rotational symmetries, aperiodic spirals satisfy the condition for planar diffraction over a range of wavelengths uniquely determined by the number and the width of the scattering rings in their reciprocal space. The multi-band/broadband polarization-insensitive planar diffraction of Vogel spirals is therefore a highly desirable property for the engineering of a variety of device applications that require increasing photonic-plasmonic coupling on planar optical chips.

It is important to note that simple linear scaling laws determine the frequency of planar diffraction in Vogel spirals. In Figure 6.3a, the calculated spectral position (i.e., in units of inverse spatial frequency) of the center of the first scattering ring in Fourier space is plotted for each type of spiral as a function of the average interparticle separation.

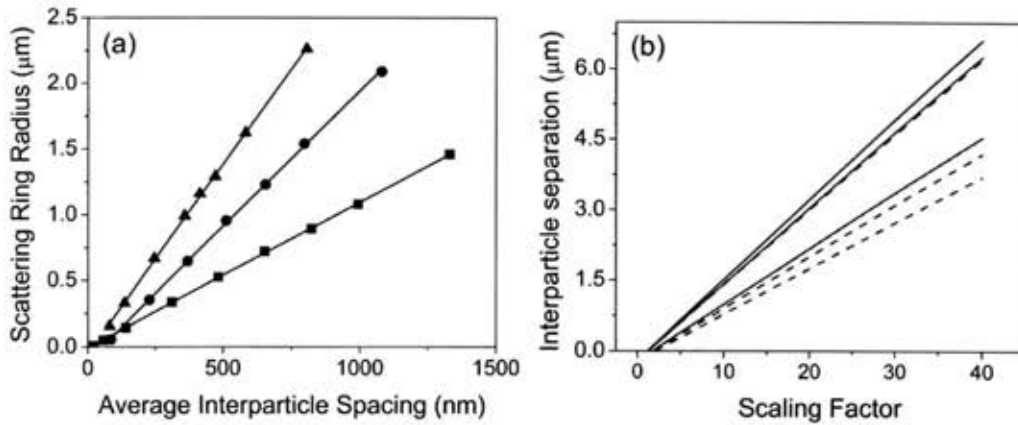


**Figure 6.3:** (a) Inverse of the scattering ring radius  $v$  in the reciprocal space as a function of the average interparticle spacing for a GA-spiral (black),  $\alpha_1$ -spiral (blue) and  $\beta_4$ -spiral (red). (b) Calculated average (solid lines) and minimum (dotted lines) edge-to-edge interparticle separation as a function of the scaling factor for the g-spiral (black),  $\alpha_1$ -spiral (blue) and  $\beta_4$ -spiral (red). All the arrays considered in this analysis contain 8000 particles (Trevino, Cao and Dal Negro, 2011).

We notice in Figure 6.3a that the scattering ring position of the GA-spiral scales nearly one to one with the average interparticle separation (slope approximately equal to 1), a result which is in agreement with what reported by Pollard *et al* (Pollard and Parker, 2009) for dielectric spirals. On the other hand, for the  $\alpha_1$ - and  $\beta_4$ -spirals the scattering ring positions scale more rapidly with the interparticle separations, according to linear relations with increasing slopes (i.e., equal to approximately 2.05 and 2.89, respectively). In Figure 6.3b the simple linear relations that connect the average interparticle separation in the spirals with the corresponding scaling factors are shown. The relations shown in Figure 6.3 enable the engineering of planar diffraction effects in rotationally-symmetric Vogel spirals.

### 6.1.1 Irrational Spirals and Rational Approximations

Vogel spirals are not limited to the golden angle  $\phi$  and numbers near it. In fact, any value of  $\alpha$  can be used to generate a spiral. For example, Figure 6.4a plots the first 9 points of Vogel spiral formed with  $\alpha = 45^\circ$ , equivalent to  $1/8$  of a complete rotation. The first point is located at a distance  $\sqrt{1}$  and an angle of  $45^\circ$ , following the generation equations (6.1) and (6.2). This process continues, as noted in Figure 6.4a, when at the ninth point the position falls on the same line as point 1. Figure 6.4b now plots the first 100 points, displaying a spiral pattern near the center, but quickly converging to eight prominent radial arms. As a second example, now consider a spiral generated with  $\alpha = 172.8^\circ$ , equivalent to  $12/25$  of a complete rotation. Figure 6.4c plots the first 100 points of this spiral. Notice the middle section of the pattern maintains its spiral nature longer than the spiral generated with  $\alpha = 45^\circ$ , however eventually converging into 25 prominent arms.

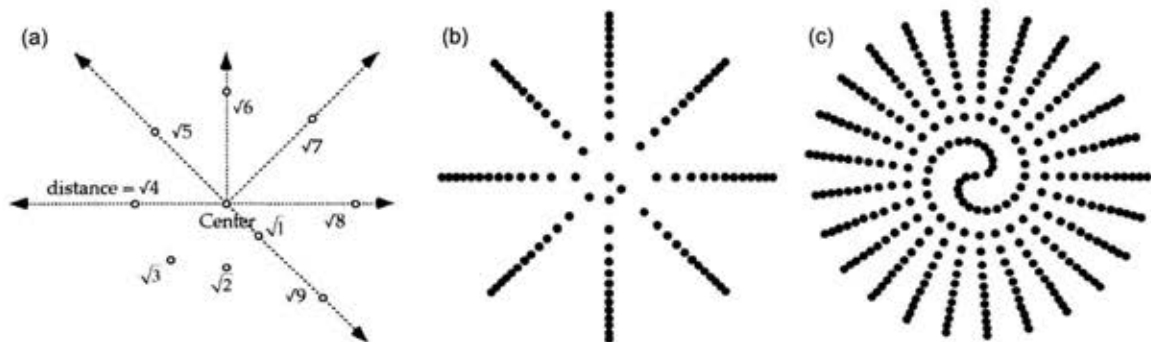


**Figure 6.4:** (a) The first 9 points of a Vogel spiral generated with  $\alpha = 45^\circ$ . (b) First 100 points of Vogel spiral generated with  $\alpha = 45^\circ$  (c) First 100 points of Vogel spiral generated with  $\alpha = 172.8^\circ$  (Naylor, 2002).



Clearly, if the angle is any rational fraction of one revolution, say  $a/b$ , seed  $b$  will fall on the  $0^\circ$  line, since the angle  $ab/b$  is an integral number of complete rotations. In such a case, the pattern eventually repeats and the radial arms are formed. In order to guarantee that no point will fall on the same line as any other seed, the ideal choice becomes an irrational angle.

As seen with the golden angle, any irrational number can be constructed into an irrational angle. This opens the door to a vast number of interesting generation angle options for creating irrational spirals. In mathematics, there exists several well-known irrational numbers, including square roots of numbers like  $\sqrt{2}$  and  $\sqrt{3}$ , as well as the transcendental numbers,  $\pi$ ,  $e$ , Euler's constant and Hilbert's number, for example. It is now appropriate to introduce a few concepts regarding irrational numbers, namely continued fractions and Hurwitz's irrational number theorem.

A continued fraction is an expression obtained through an iterative process of representing a number as the sum of its integer part and the reciprocal of another number, then writing this other number as the sum of its integer part and another reciprocal, and so on. The continued fraction representation of a number  $x$  is given by

$$x = [a_0; a_1, a_2, a_3, \dots] = a_0 + \frac{1}{a_1 + \frac{1}{a_2 + \frac{1}{a_3 + \frac{1}{a_4 + \dots}}}}, \quad (6.4)$$

where  $a_0, a_1, a_2, \dots$  are integers and  $a_1, a_2, \dots > 0$ . An infinite continued fraction representation of an irrational number is very useful because its initial segments provide excellent rational approximations to that number. The rational approximations (i.e., fractions) are called the convergents of the continued fraction, and it can be shown that even-numbered convergents are smaller than the original number  $x$  while odd-numbered ones are bigger (Schroeder, 2009; Hardy and Wright, 2008). Once the continued fraction expansion of  $x$  has been obtained, well-defined recursion rules exist to quickly generate the successive convergents. In fact, each convergent can be expressed explicitly in terms of the continued fraction as the ratio of certain multivariate polynomials called continuants (Schroeder, 2009; Hardy and Wright, 2008). If two convergents are found, with numerators  $p_1, p_2, \dots$  and denominators  $q_1, q_2, \dots$  then the successive convergents are given by the formula

$$\frac{p_n}{q_n} = \frac{a_n p_{n-1} + p_{n-2}}{a_n q_{n-1} + q_{n-2}} \quad (6.5)$$

To generate new terms into a rational approximation only the two previous convergents are necessary. The initial values required for the evaluation of the first two terms are  $(0,1)$  and  $(1,0)$  for  $(p_{-2}, p_{-1})$  and  $(q_{-2}, q_{-1})$ , respectively.

Hurwitz's irrational number theorem states that for every irrational number  $\xi$  there are infinitely many rationals  $p, q$  such that

$$\left| \xi - \frac{p}{q} \right| < \frac{1}{\sqrt{5}q^2}, \quad (6.6)$$

(Havil, 2012). The parameter  $E/M$  is defined as the ratio of the approximation error  $E$  to the Hurwitz's bound  $M = 1/\sqrt{5}q^2$ . The parameter is bounded from 0 to 1 and is a measure of the "difficulty" to approximate the irrational number using rationals, with 1 being the most difficult and values near 0 implying the fraction very well approximates the irrational number. As an example, the golden ratio's continued fraction expansion is

$$\varphi = [1; 1, 1, 1, \dots] = 1 + \frac{1}{1 + \frac{1}{1 + \frac{1}{1 + \frac{1}{1 + \dots}}}} \quad (6.7)$$

The first twelve convergents of these continued fractions are then

$$\frac{1}{1}, \frac{2}{1}, \frac{3}{2}, \frac{5}{3}, \frac{8}{5}, \frac{13}{8}, \frac{21}{13}, \frac{34}{21}, \frac{55}{34}, \frac{89}{55}, \frac{144}{89}, \frac{233}{144}, \dots$$

It is important to note that these fractions are ratios of successive Fibonacci numbers; a fact that will be relevant in the proceeding section. At  $q = 144$ , the resulting  $E/M$  value for the golden ratio is 0.99999. The result implies the ratio 233/144 is still a poor approximation for the golden ratio. Indeed, the golden ratio is the most irrational number of all irrational numbers, as evident by the fact there are no numbers greater than 1 in the continued fraction. This means that it will take longer to find a rational number as close as you like to  $\varphi$  by this method than it does for any other irrational number.

As any number of additional irrational numbers would be of interest to study, we now focus on Vogel spirals generated with a subset of irrational numbers known as the *metallic means* (also called the *silver means*) and  $\pi$ . In addition these arrays, several other

irrational spirals were investigated, including those generated with the irrational numbers  $e$ ,  $i$ , and others, but are not shown in this thesis. The metallic means are irrational numbers generated with the continued fraction

$$\varphi = [n; n, n, n, \dots] = n + \frac{1}{n + \frac{1}{n + \frac{1}{n + \frac{1}{n + \dots}}}}, \quad (6.8)$$

and equivalently

$$\frac{1}{2}(n + \sqrt{n^2 + 4}), \quad (6.9)$$

where  $n$  is a positive integer greater than or equal to 1. The case of  $n = 1$  yields the golden ratio. For  $n = 2$  the value is  $(2 + \sqrt{8})/2$ , known as the silver ratio. Additionally, for other integers the names of various metals have been assigned, hence the designation *metallic means*.

Table 6.1 lists four different Vogel spirals generated by the irrational numbers  $\varphi = (1 + \sqrt{5})/2$ ,  $\tau = (2 + \sqrt{8})/2$ ,  $\mu = (5 + \sqrt{29})/2$ , the mathematical constant  $\pi$  and their corresponding aperture angles ( $\alpha^\circ$ ) listed. The table also shows their rational approximations and, in its last column, the parameter E/M. Figure 6.5 plots the first 2000 points of the GA-spiral,  $\tau$ -spiral,  $\mu$ -spiral, and the  $\pi$ -spiral.

Irrational Number	Aperture Angle ( $\alpha^\circ$ )	Rational Approximations (p/q)	E/M (q)
$\Phi$	137.51...	$\frac{1}{1}, \frac{2}{1}, \frac{3}{2}, \frac{5}{3}, \frac{8}{5}, \frac{13}{8}, \frac{21}{13}, \frac{34}{21}, \frac{55}{34}, \frac{89}{55}, \frac{144}{89}, \frac{233}{144}$	0.99999 (144)
T	210.88...	$\frac{1}{1}, \frac{5}{2}, \frac{12}{5}, \frac{29}{12}, \frac{70}{29}, \frac{169}{70}, \frac{408}{169}$	0.79057 (169)
$\mu$	290.67...	$\frac{5}{1}, \frac{26}{5}, \frac{135}{26}, \frac{701}{135}, \frac{3640}{701}$	0.41523 (135)
$\Pi$	309.03...	$\frac{3}{1}, \frac{22}{7}, \frac{355}{113}$	0.00762 (113)

**Table 6.1:** The Listing of irrational angles as well as their corresponding rational approximations ( $p/q$ ).  $E/M$  is a measure of the difficulty to approximate the irrational number with a given a set of rational approximates, where  $E$  is the absolute difference from the irrational value for a given  $p/q$  and  $M$  is the Hurwitz bound.

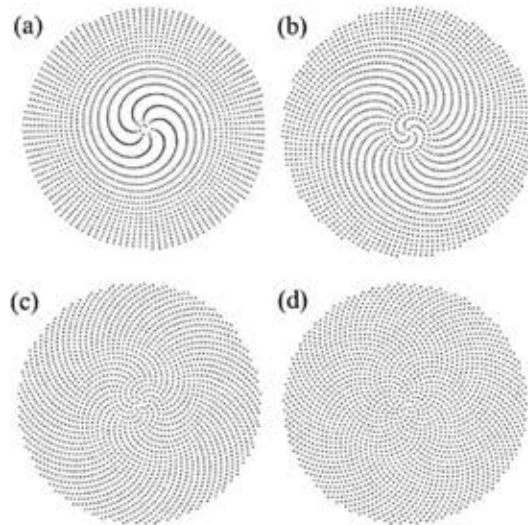


**Figure 6.5:** The first 2000 points of the (a)  $\pi$ -spiral, (b)  $\mu$ -spiral, (c)  $\tau$ -spiral, and (d) GA-spiral.

Given the discussion to this point, one would be inclined to expect all irrational spirals to have relatively even distributions of particles, with non-converging lines. However, from Figure 6.5, it is evident this is not the case, most clearly contrasted by the

$\pi$ -spiral. The  $\pi$ -spiral displays 7 dominate arms in the center of the pattern, transitioning to 113 arms with very little curvature. In fact, a new set of spiral arms would not appear until approximately 1 million points had been plotted. An important observation in designing Vogel spirals is that these numbers match the denominators of the rational approximates shown in Table 6.1. The reason these families of arms are so predominant is that  $22/7$  and  $355/113$  are already very good approximations of  $\pi$ , as evident by the very low  $E/M$  value. The same phenomenon is observed in the  $\mu$ -spiral. Here we notice three regions of predominate arms, numbering 5, 26, and 135. Again, these values correspond to the denominators of the rational approximates. As  $\alpha$  becomes more irrational (higher  $E/M$  value), the families of arms become more frequent and overlap with each other, as seen in the  $\tau$ -spiral. Indeed, for the most irrational spiral (the GA-spiral) the spiral arms are completely intertwined as each rational approximate is only marginally better than the next.

To explore the optical properties of these arrays, we now examine the calculated Fourier space for each array in Figure 6.6.

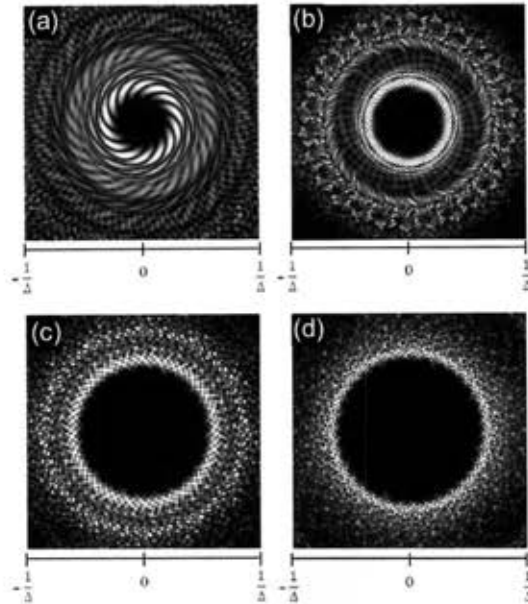


**Figure 6.6:** The calculated Fourier space for the (a)  $\pi$ -spiral, (b)  $\mu$ -spiral, (c)  $\tau$ -spiral, and (d) GA-spiral, shown in Figure 6.5.

We notice the degree of rotational symmetry and the complexity of the azimuthal structure of the Fourier space decreases for arrays generated with less irrational angles, as determined by the  $E/M$  ratio. In fact, the GA and  $\tau$  spirals feature an almost continuous rotational symmetry in their far-field patterns, while less defined azimuthal structure is evident for the other two spiral structures. Therefore, “the degree of irrationality” of Vogel spirals is a key parameter that determines the azimuthal complexity of the scattered far fields. In fact, to analyze the consequences of irrationality on the geometry and the scattering properties, we must now introduce a new technique known as Fourier Hankel decomposition (FHD).

### 6.1.2 Fourier Hankel Decomposition

In order to better understand the structural complexity of Vogel spirals, a Fourier

Hankel spatial analysis is completed. The Fourier Hankel transform decomposes the density function associated with the spiral structure in a series of Bessel functions of the first kind. The transform is given by

$$f(m, k_r) = \frac{1}{2\pi} \int_0^\infty \int_0^{2\pi} r dr d\theta \rho(r, \theta) J_m(k_r r) e^{im\theta}, \quad (6.10)$$

where the density function  $\rho(r, \theta)$  represents the particle array, the azimuthal number  $m$  is an integer, and  $k_r$  represents a spatial frequency in the radial direction. Integrating over the radial frequency  $k_r$ , we can then obtain

$$F(m) = \int |f(m, k_r)|^2 k_r dk_r. \quad (6.11)$$

The frequency range of integration is  $[\pi/d_o, 3\pi/d_o]$ , centered on the dominant spatial frequency  $2\pi/d_o$ , where  $d_o$  is the most probable nearest neighbor distance (details regarding the calculation  $d_o$  are in the next section). The function  $F(m)$  provides a measure of the azimuthal components in an array, which is plotted in Figure 6.7 for the four irrational angles discussed. Each peak is labeled with its corresponding  $m$  value for clarity.



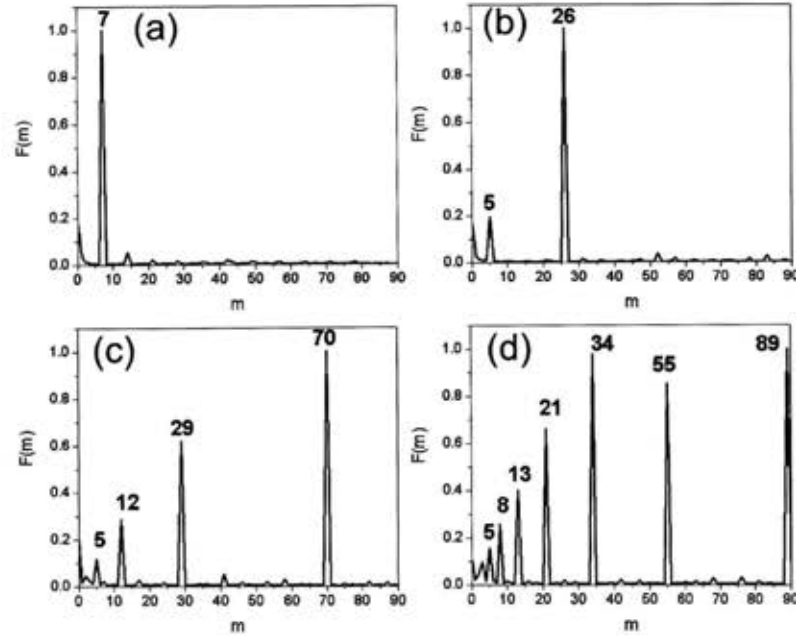


**Figure 6.7:**  $F(m)$  values calculated by the Fourier Hankel transform of the spiral geometry for the (a)  $\pi$ -spiral, (b)  $\mu$ -spiral, (c)  $\tau$ -spiral, and (d) GA-spiral, shown in Figure 6.5.

We notice interestingly the dominant  $m$  values for each array represent the number of arms in each family, also corresponding to the denominators of the rational approximates. We will now discuss the consequences and the usefulness of having these  $m$  values encoded into the structure of the spirals.

## 6.2 Orbital Angular Momentum in Scattered Radiation

Singular optics is a branch of modern physical optics that involves a wide class of effects associated with the phase singularities in wave fields and with the topology of wavefronts. Optical singularities (optical vortices) exhibit some fundamental features absent in the "usual" fields with smooth wavefronts. Namely, optical vortices possess orbital angular momentum (OAM), topological charge for helical wavefront of beams

with well-defined direction of propagation. Rotation of the field around the axis produces the vortex, and the combination of the field circulation and of the longitudinal propagation of the wave results in the helicoidal wavefront structure, shown in Figure 6.8. These helical modes are characterized by an integer number  $m$ , which can be positive or negative. In the case of  $m = 0$ , the field represents a plane wave. If  $m = +/- 1$  the phase around the central vortex passes through a full rotation from 0 to  $2\pi$ . Likewise, when  $m = 2$ , the phase rotates through two full 0 to  $2\pi$  rotations.

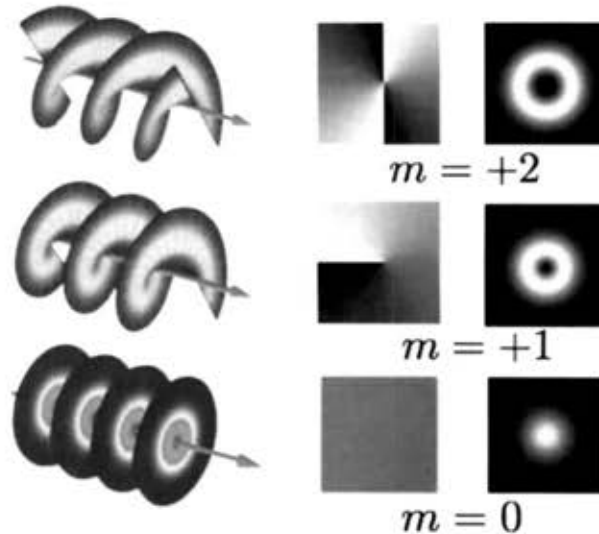


**Figure 6.8:** Different columns show the beam helical structures, phase fronts, and corresponding intensity distributions (Wikipedia, 2013).

Optical beams carrying OAM are of great interest to the optical communications community. The ability to engineering high  $m$  values in propagating beams opens the possibility for transferring unprecedented quantities of data through optical fibers. Recent research suggests that OAM could provide an additional degree of freedom for data

multiplexing in future fiber networks, pushing data rates into the terabit per second range (Bozinovic et al., 2013).

The generation of OAM can be achieved by converting Gaussian laser modes to Laguerre–Gaussian modes, which have explicit azimuthal phase dependence. This can be accomplished using a system of cylindrical lenses (Padgett, Courtial and Allen, 2004) or spatial light modulators (Heckenberg et al., 1992). Additionally, optical vortices frequently occur in reflection from or propagation through random, turbulent, and chaotic media. A simple representation of such a random field is shown in Figure 6.9, where there are at least as many completely dark points as there are bright speckles (Dennis, O’Holleran and Padgett, 2009). In this section, the generation of OAM from planar Vogel spiral geometries will be discussed.

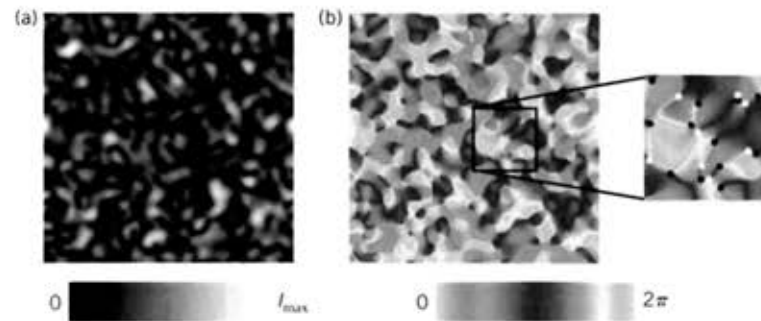


**Figure 6.9:** A simulated random optical field (speckle field), computed as a superposition of 729 plane waves with random phases and amplitudes. (a) Intensity; (b) phase, with inset showing singularities (strength +1 black, -1 white) (Dennis, O’Holleran and Padgett, 2009).

The Hankel decomposition analysis introduced in the previous section is now performed on the far-field radiation patterns generated by the same four irrational spirals shown in Figure 6.5. To do so, we have developed a more rigorous and general analytical

model for light scattering by arbitrary Vogel spiral arrays of circular apertures illuminated at normal incidence. The model is described in detail in the following reference (Dal Negro, Lawrence and Trevino, 2012) and will only be briefly introduced in this text.

A spiral array of point scatterers is represented by the following density function:

$$\rho(r, \theta) = \sum_{n=1}^N \frac{1}{r} \delta(r - \sqrt{n}a_0) \delta(\theta - n\alpha) \quad (6.12)$$

where  $N$  is the total number of scatterers in the spiral array and the  $1/r$  factor comes from the definition of the Delta function in cylindrical coordinates. If a plane wave is normally incident on the array, the field at the plane of the array ( $z = 0$ ) is given by,

$$E_{z=0}(r, \theta) = \frac{E_0}{r} \sum_{n=1}^N \delta(r - \sqrt{n}a_0) \delta(\theta - n\alpha) \quad (6.13)$$

Within the validity limits of scalar diffraction theory, the Fraunhofer far-field of a general Vogel spiral density function can be obtained by the evaluation of its cylindrical Fourier transform (i.e., Fourier-Hankel transform). Through the use of the sampling property of the Dirac delta function and identities of Bessel functions (i.e., cylindrical wave expansion of a plane wave), we can arrive at the closed form analytical solution for the Fraunhofer far field pattern of a point pattern with an arbitrary Vogel spiral geometry:

$$E_{\infty}(v_r, v_{\theta}) = E_0 \sum_{n=1}^N e^{j2\pi\sqrt{n}a_0 v_r \cos(v_{\theta} - n\alpha)}. \quad (6.14)$$

To account for the circular apertures of radius  $a$ , instead of points, the Fraunhofer diffraction pattern becomes:

$$E_{\infty}(v_r, v_{\theta}) = E_0 \left[ (a/v_r) J_1(2\pi v_r a) \right] \sum_{n=1}^N e^{j2\pi \sqrt{n} a_0 v_r \cos(v_{\theta} - n\alpha)}, \quad (6.15)$$

where the square brackets in Equation (13) contains an Airy factor, which is the Fourier transform of the circular function  $circ(r/a)$  that represents the individual circular apertures. Now applying the previous definition of the Fourier Hankel transform shown previously in equation (6.10) we arrive at final result of the analytical Fourier Hankel decomposition of the Fraunhofer diffraction pattern of an arbitrary Vogel spiral:

$$f(m, k_r) = \frac{1}{2\pi} \sum_{n=1}^N J_m(k_r a_0 \sqrt{n}) e^{inm\alpha}. \quad (6.16)$$

The analytical Fourier Hankel decomposition (FHD) is now performed summed over the radial wavenumber  $k_r$  on the Fraunhofer diffraction pattern for the four irrational spirals and is plotted in Figure 6.10.

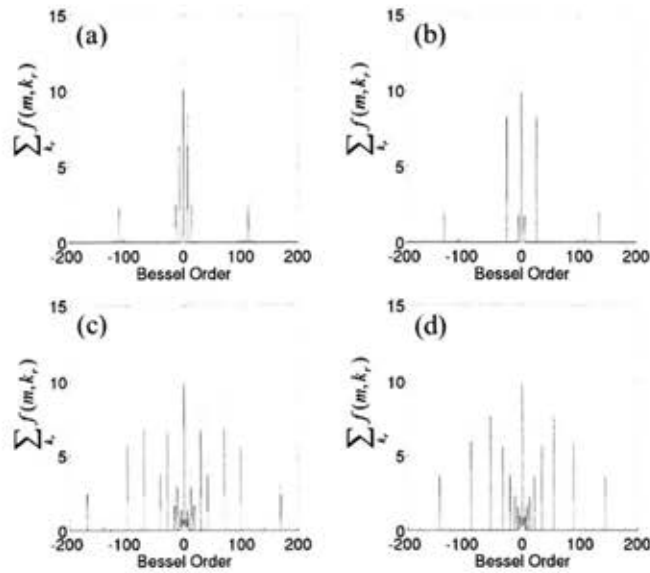


**Figure 6.10:** Fourier-Hankel decomposition of far-field scattered radiation from the (a)  $\pi$ -spiral, (b)  $\mu$ -spiral, (c)  $\tau$ -spiral, and (d) GA-spiral, shown in Figure 6.5.

It is clear from Figure 6.10 that the far-field radiation has well defined azimuthal components, implying that Vogel spiral arrays are able to generate fields carrying OAM through scattering. In fact, upon closer evaluation of the  $m$  values, one notices that they are once again the same integers embedded into the geometry by the generating irrational angles. For example, in the GA-spiral the FHD peaks are 2, 3, 5, 8, 13, 21, 34, 55, 89, and 144, the same found from the FHD of the geometry, and the same as the denominators of the rational approximates.

The result can be anticipated by examining Equation (6.16) more closely. In the case of the GA-spiral, the exponential factor  $e^{im\alpha}$  in the summation generates peaks for all the Fibonacci numbers when the azimuthal number  $m$  runs across the integers. Therefore, GA-spirals are defined by a divergence angle  $\alpha = 2\pi[1 - \text{frac}(\varphi)]$  where  $\text{frac}(\varphi)$  is the fractional part of the golden number  $\varphi = (1 + \sqrt{5})/2$ , which can be approximated by rational fractions that are consecutive Fibonacci numbers:  $\varphi \approx F_{n+1} / F_n$ . In fact, the product  $m\alpha$  in the exponential sum of Equation (6.16) will contribute strongly to the sum when  $m = F_n$ , which is a Fibonacci number. Under this condition, the exponents are approximately all integer multiples of  $2\pi$  (i.e., in-phase phasors) and the Fourier Hankel decomposition will feature strong peaks (Dal Negro, Lawrence and Trevino, 2012). Further studies regarding the effects of aperture angle and number of particles have been conducted and can be found in the following reference (Dal Negro, Lawrence and Trevino, 2012). Additionally, the model has been extended to the analytical calculation of the scattered field in the near and intermediate zones using the

general angular spectrum approach in the same reference.

The ability to engineer Vogel spirals with known rational approximates which impart coded OAM values into their far-field radiation is of great interest to several emerging fields, including singular optics, secure communication, and optical cryptography. In fact, in collaboration with Alexander Sergienko's research group at Boston University, we have proposed an approach to high-capacity, high-efficiency quantum key distribution protocol, utilizing Vogel spirals as a novel source of entangled Fibonacci-valued OAM states. Details regarding this study can be found in the following reference (Simon et al., 2013).

### 6.3 Conclusions

In this chapter, the aperiodic Vogel spiral array was introduced as a highly engineerable optical platform with several unique mathematical and photonic properties. Vogel spirals were shown to possess diffuse Fourier space spectra with rotational symmetry, leading to the possibility of engineered polarization-insensitive planar diffraction. It was shown that known sequences of numbers, based on rational approximates of the divergence angle, are encoded into the geometry of the array. Moreover, it was demonstrated that these sequences can be encoded into discrete OAM values in the scattered radiation from Vogel spiral arrays. The unique diffractive properties of Vogel spiral arrays make it an ideal platform for engineering polarization insensitive planer light-matter coupling, omnidirectional extraction, novel polarization devices, and several OAM applications such as optical cryptography and singular optics.

## Chapter 7

### 7 Optical Properties of Dielectric Spirals

Until this point, all discussions of Vogel spirals have been independent of material properties, based in the context of Fourier optics. The potential of aperiodic Vogel spirals in a dielectric medium will now be explored. Segments of this chapter have been adapted from the 2012 Optics Express publication *Geometrical Structure, Multifractal Spectra and Localized Optical Modes of Aperiodic Vogel Spirals* and the 2011 Optics Express publication *Localized Photonic Band Edge Modes and Orbital Angular Momenta of Light in a Golden-Angle Spiral*, which can be found (Trevino, Liew, et al., 2012) and (S.F. Liew et al., 2011), respectively.

#### 7.1 Engineering Band Gaps and Band Edge Modes

Photonic bandgap structures have received significant attention in recent years (Joannopoulos et al., 2008). The ability to engineer spectral gaps in the electromagnetic wave spectrum and create highly localized modes opens the door to numerous exciting applications including, high-Q cavities (Meade et al., 1994), PBG novel optical waveguides (Mekis et al., 1996), enhanced light-emitting diodes (LEDs) (Krauss et al., 1998) and lasing structures (Notomi et al., 2004). Many of these applications rely on photonic crystals that possess a complete photonic bandgap (PBG), which is readily achieved in quasiperiodic lattices with a higher degree of rotational symmetry (Chan,



Chan and Liu, 1998). However, while photonic quasicrystals have been mostly investigated for the engineering of isotropic PBGs, the more general study of two-dimensional (2D) structures with deterministic aperiodic order offers additional opportunities to manipulate light transport by engineering a broader spectrum of optical modes with distinctive localization properties (Dal Negro and Boriskina, 2012).

In this section, a systematic study of the structural properties, photonic gaps, and bandedge modes of 2D Vogel spiral arrays of dielectric cylinders in air will be presented. Specifically, a number of Vogel spiral arrays generated by the gradual structural perturbation of the GA-spiral will be studied. The divergence angle is varied in an equispaced fashion between  $\alpha_1$  ( $137.3^\circ$ ) and the golden angle, and also between the golden angle and  $\beta_4$  ( $137.6^\circ$ ), as summarized in Table 7.1.

Divergence Angle	Labeling	Divergence Angle	Labeling
137.300000	$\alpha_1$	137.507764	GA
137.369255	$\alpha_2$	137.523137	$\beta_1$
137.403882	$\alpha_3$	137.553882	$\beta_2$
137.473137	$\alpha_4$	137.569255	$\beta_3$
137.507764	GA	137.600000	$\beta_4$

**Table 7.1:** Divergence angle structural perturbations of GA-spiral.

These structures can be considered as one-parameter ( $\alpha$ ) structural perturbations of the GA-spiral, and possess fascinating geometrical features, which are responsible for unique mode localization properties and optical spectra, as it will be discussed from section 7.1.4. The nine Vogel spirals are plotted in Figure 7.1, each consisting of 1000 particles.

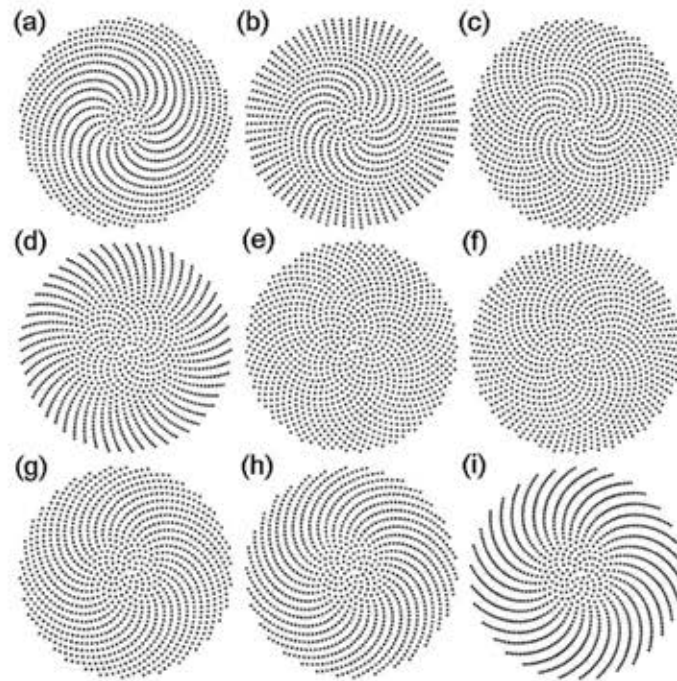


**Figure 7.1:** Vogel spiral array consisting of 1000 particles, created with a divergence angle of (a)  $137.3^\circ$  ( $\alpha_1$ ), (b)  $137.3692546^\circ$  ( $\alpha_2$ ), (c)  $137.4038819^\circ$  ( $\alpha_3$ ), (d)  $137.4731367^\circ$  ( $\alpha_4$ ), (e)  $137.5077641^\circ$  (GA), (f)  $137.5231367^\circ$  ( $\beta_1$ ), (g)  $137.553882^\circ$  ( $\beta_2$ ), (h)  $137.5692547^\circ$  ( $\beta_3$ ), (i)  $137.6^\circ$  ( $\beta_4$ ).

As previously mentioned, the GA-spiral has several spiral arms, or parastichies, that can be found in both clockwise (CW) and counter-clockwise (CCW) directions (Adam, 2009). The numbers of parastichies are consecutive numbers in the Fibonacci series, the ratio of which approximates the golden ratio. As the divergence angle is varied either above (supra-GA or  $\beta$ -series) or below the golden angle (sub-GA or  $\alpha$ -series), the center region of the spiral where both sets of parastichies (CW and CCW) exist shrinks to a point. The outer regions are left with parastichies that rotate only CW for divergence angles greater than the golden angle and CCW for those below. For the spirals with larger deviation from the golden angle ( $\alpha_1$  and  $\beta_4$  in Figure 7.1), gaps appear in the center head of the spirals and the resulting point patterns mostly consist of either CW or CCW

spiraling arms. Stronger structural perturbations (i.e., further increase in the diverge angle) eventually lead to less interesting spiral structures containing only radially diverging parastichies, as the angle becomes less close to an irrational value.

To better understand the consequences of the divergence angle perturbation on the optical properties of Vogel spiral arrays, their Fourier spectra, or reciprocal space vectors are investigated. Figure 7.2 displays the 2D spatial Fourier spectra obtained by calculating the amplitude of the discrete Fourier transform (DFT) of the spiral arrays shown in Figure 7.1. Again, since the spiral arrays are non-periodic, periodic Brillouin zones cannot be rigorously defined. The reciprocal space structure is instead restricted to spatial frequencies in the compact interval  $\pm 1/\Delta$ , with  $\Delta$  being the average center-to-center inter-particle separation (Janot, 1997; Carlo Forestiere, Giovanni Miano, et al., 2009). The Fourier spectra for all the Vogel spirals explored in this paper lack Bragg peaks, and feature diffuse circular rings (Figure 7.2a-i). The many spatial frequency components in Vogel spirals give rise to a diffuse background, as for amorphous and random systems. Interestingly, despite the lack of rotational symmetry of Vogel spirals, their Fourier spectra are highly isotropic (approaching circular symmetry), as a consequence of a high degree of statistical isotropy (Trevino, Cao and Dal Negro, 2011; Seng Fatt Liew et al., 2011).

As previously reported (Trevino, Cao and Dal Negro, 2011; Seng Fatt Liew et al., 2011; Pollard and Parker, 2009), the GA-spiral features a well-defined and broad scattering ring in the center of the reciprocal space (Figure 7.2e), which corresponds to

the dominant spatial frequencies of the structure. Perturbing the GA-spiral by varying the divergence angle from the golden angle creates more inhomogeneous Vogel spirals and results in the formation of multiple scattering rings, associated with additional characteristic length scales, embedded in a diffuse background of fluctuating spots with weaker intensity. In the perturbed Vogel spirals (i.e., Figures 7.2a,b,d,g-i) patterns of spatial organization at finer scales are clearly discernable in the diffuse background. The onset of these sub-structures in Fourier space reflects the gradual removal of statistical isotropy of the GA-spiral, which “breaks” into less homogeneous sub-structures with some degree of local order. In order to characterize the local order of Vogel spirals we need to abandon standard Fourier space analysis and resort to analytical tools that are more suitable to detect local spatial variations in geometrical structures.

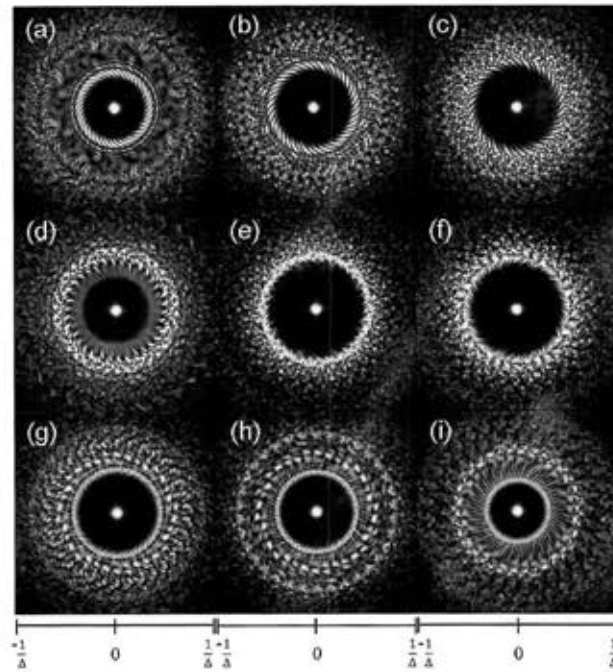


**Figure 7.2:** Calculated spatial Fourier spectrum of the spiral structures show in Figure 7.1. The reciprocal space structure of a (a)  $\alpha_1$ -spiral, (b)  $\alpha_2$ -spiral, (c)  $\alpha_3$ -spiral, (d)  $\alpha_4$ -spiral, (e) g.a.-spiral, (f)  $\beta_1$ -spiral (g)  $\beta_2$ -spiral, (h)  $\beta_3$ -spiral, and (i)  $\beta_4$ -spiral are plotted where  $\Delta$  represents the average edge-to-edge minimum inter-particle separation.

Further analysis moves the discussion to the geometrical structure of Vogel spirals by applying the well-known statistical mechanics technique of correlation functions to investigate the local structural differences of these arrays and discuss their impact on the resulting optical properties. The pair correlation function,  $g(r)$ , also known as the radial density distribution function, is used to characterize the probability of finding two particles separated by a distance  $r$ , measuring the local (correlation) order in the structure. Figure 7.3(a) displays the calculated  $g(r)$  for spiral arrays with divergence angles between  $\alpha_1$  and the golden angle ( $\alpha$  series), while Figure 7.3(b) shows the results of the analysis for arrays generated with divergence angles between the golden angle and  $\beta_4$ . ( $\beta$  series). In order to better capture the geometrical features associated to the

geometrical structure (i.e., array pattern) of Vogel spirals, the  $g(r)$  was calculated directly from the array point patterns (i.e., no form factor associated to finite-size particles) using the library *spatstat* (Baddeley and Turner, 2005) within the R statistical analysis package. The pair correlation function is calculated as:

$$g(r) = \frac{K'(r)}{2\pi r} \quad (7.1)$$

where  $r$  is the radius of the observation window and  $K'(r)$  is the first derivative of the reduced second moment function ("Ripley's K function") (Ripley, 1977).

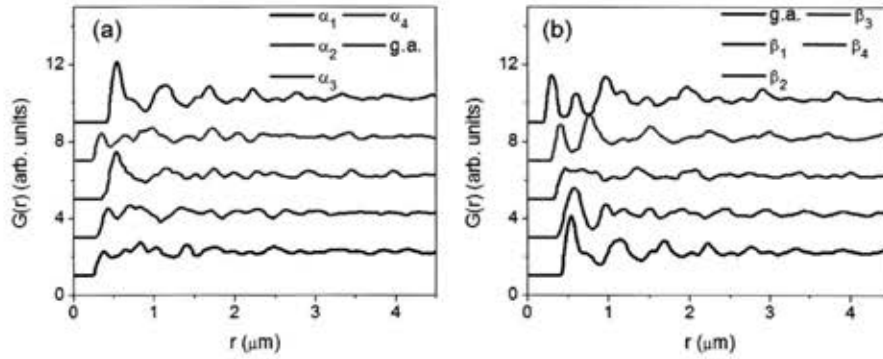


**Figure 7.3:** Pair correlation function  $g(r)$  for spiral arrays with divergence angles between (a)  $\alpha_1$  and the golden angle and (b) between the golden angle and  $\beta_4$ .

The results of the pair correlation analysis shown in Figure 7.3 reveal a fascinating aspect of the geometry of Vogel spirals, namely their structural similarity to gases and liquids. We also notice that in Figure 7.3, the GA-spiral exhibits several oscillating peaks, indicating that for certain radial separations, corresponding to local coordination shells, it is more likely to find particles in the array.

A similar oscillating behavior for  $g(r)$  can be observed when studying the structure of liquids by X-ray scattering (Janot, 1997). We also notice that  $g(r)$  of the most

perturbed (i.e., more disordered) Vogel spiral (Figure 7.3(a),  $\alpha_1$ -spiral) presents strongly damped oscillations on a constant background, similarly to the  $g(r)$  measured for a gas of random particles. Between these two extremes ( $\alpha_2$  to  $\alpha_4$  and  $\beta_1$  to  $\beta_3$ ) a varying degree of local order can be observed. These results demonstrate that the degree of local order in Vogel spiral structures can be deterministically tuned between the correlation properties of photonic amorphous structures (Yang et al., 2011; Torquato and Stillinger, 2003) and uncorrelated random systems by continuously varying the divergence angle  $\alpha$ , which acts as an order parameter.

In further analyzing the complex particle arrangement in Vogel spirals, the spatial distribution of the distance  $d$  between first neighboring particles is calculated by performing a Delaunay triangulation of the spiral array (Pollard and Parker, 2009; Seng Fatt Liew et al., 2011). This technique provides information on the statistical distribution of  $d$ , which measures the spatial uniformity of spatial point patterns (Illian et al., 2008). In Figure 7.4, the calculated statistical distribution is shown, obtained by the Delaunay triangulation, of the parameter  $d$  normalized by  $d_0$ , which is the most probable value (where the distribution is peaked). In all the investigated structures, the most probable value  $d_0$  is generally found to be close in value to the average inter-particle separation.

It is interesting to note that the distributions of neighboring particles shown in Figure 7.4 are distinctively non-Gaussian in nature and display slowly decaying tails, similar to “heavy tails” often encountered in mathematical finance (i.e., extreme value theory), suddenly interrupted by large fluctuations or “spikes” in the particle

arrangement. These characteristic fluctuations are very pronounced for the two series of perturbed GA-spirals, consistently with their reduced degree of spatial homogeneity.

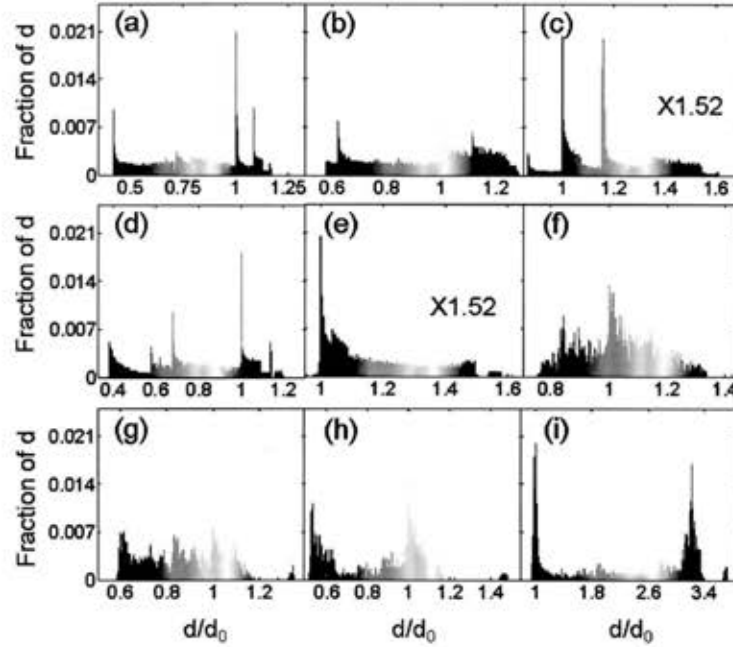


**Figure 7.4:** Statistical distribution of spiral structures shown in Figure 7.1. Values represent the distance between neighboring particles  $d$  normalized to the most probable value  $d_0$ , obtained by Delaunay triangulation (increasing numerical values from blue to red colors). The Y-axis displays the fraction of  $d$  in the total distribution.

All the distributions in Figure 7.4 are broad with varying numbers of sharp peaks corresponding to different correlation lengths, consistent with the features in the Fourier spectra shown in Figure 7.2. Next, a Delaunay triangulation is performed in order to visualize the spatial locations on the spirals where the different correlation lengths (i.e., distribution spikes) appear more frequently. The Delaunay triangulation is a triangulation of the convex hull of the points in a diagram in which every circumcircle of a triangle is an empty circle (Okabe et al., 2009). The Delaunay triangulation provides a useful set of



triangles to use as polygons in the modeling terrains and FEM grids, avoiding narrow triangles (as they have large circumcircles compared to their area)

In Figure 7.5 the spatial map of the first neighbors connectivity of the Vogel spirals, obtained from Delaunay triangulation, is visualized. Each line segment in Figure 7.5 connects two neighboring particles on the spirals, and the connectivity length  $d$  is color coded consistently with the scale of Figure 7.4 (i.e., increasing numerical values from blue to red colors).

The non-uniform color distributions shown in Figure 7.5 graphically represent the unique spatial order of Vogel's spirals. In particular, we notice that distinct circular symmetries are found in the distribution of particles for all the spirals, including the strongly inhomogeneous  $\alpha$  and  $\beta$ -series. Moreover, the color patterns in Figure 7.5 feature well-defined circular regions of markedly different values of  $d$ , thus defining "radial heterostructures" that can trap radiation in regions of different lattice constants, similar in nature to the concentric rings of Omniguide Bragg fibers. The sharp contrast between adjacent rings radially traps radiation by Bragg scattering along different circular loops. The circular regions discovered in the spatial map of local particle coordination in Figure 7.5 well correspond to the scattering rings observed in the Fourier spectra (Figure 7.2), and are at the origin of the recently discovered circular scattering resonances carrying orbital angular momentum in Vogel spirals (Trevino, Cao and Dal Negro, 2011; Seng Fatt Liew et al., 2011). As will be shown in the next sections, the characteristic "circular Bragg scattering" occurring between dielectric rods in Vogel

spirals gives rise to localized resonant modes with well-defined radial and azimuthal numbers like the whispering gallery modes of microdisk resonators.

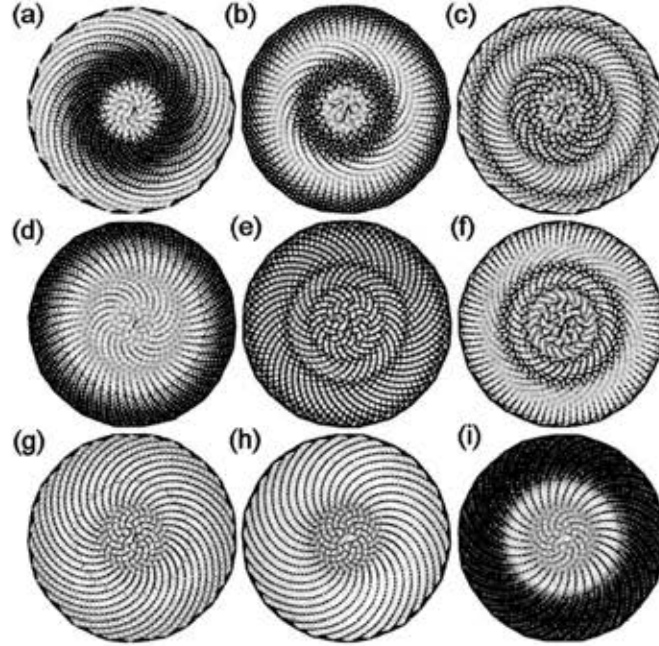


**Figure 7.5:** Delaunay triangulation of spiral structures shown in Figure 7.1. The line segments that connect neighboring circles are color-coded by their lengths  $d$ . The colors are consistent to those in Figure 7.4.

### 7.1.1 Density of States and Optical Modes

The optical properties of Vogel spirals are now investigated by numerically calculating their LDOS across the large wavelength interval from  $0.4\mu\text{m}$  to  $2\mu\text{m}$ . This choice is mostly motivated by the engineering polarization insensitive and localized band-edge modes for applications to broadband solar energy conversion. Calculations were performed for all arrays shown in Figure 7.1, consisting of  $N = 1000$  dielectric cylinders,  $200\text{nm}$  in diameter with a permittivity  $\epsilon = 10.5$  embedded in air, for which TM

PBG are favored. All arrays are generated using a scaling factor,  $\alpha$ , equal to  $3 \times 10^{-7}$ . The LDOS is calculated at the center of the spiral structure using the well-known relation  $g(\mathbf{r}, \omega) = (2\omega/\pi c^2) \text{Im}[G(\mathbf{r}, \mathbf{r}', \omega)]$ , where  $G(\mathbf{r}, \mathbf{r}', \omega)$  is the Green's function for the propagation of the  $E_z$  component from point  $\mathbf{r}$  to  $\mathbf{r}'$ . The numerical calculations are implemented using the Finite Element method within COMSOL Multiphysics (version 3.5a). A perfectly matched layer (PML) is utilized in order to absorb all radiation leaking towards the computational window. In Figs. 7.6(a,b) we display the calculated LDOS for the spiral arrays in the  $\alpha$  and  $\beta$  series as a function of frequency ( $\omega$ ) normalized by the GA-spiral bandgap center frequency ( $\omega_0 = 13.2 \times 10^{14}$  Hz), respectively. For comparison, the LDOS of the GA-spiral is also reported in both panels.

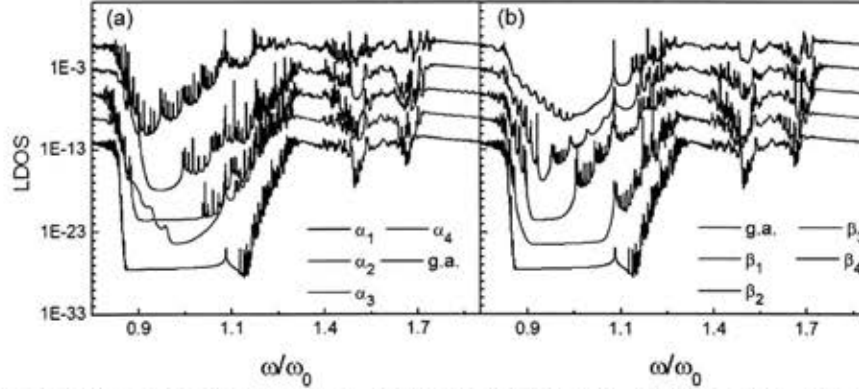


**Figure 7.6:** LDOS calculated at the center of the each spiral array as a function of normalized frequency for spiral arrays with divergence angles between (a)  $\alpha_1$  and the golden angle and (b) between the golden angle and  $\beta_4$ .

The results in Figure 7.6 demonstrate the existence of a central large LDOS bandgap for all the investigated structures, which originates from the Mie-resonances of the individual cylinders, as previously demonstrated by Pollard *et al* for the GA-spiral (Pollard and Parker, 2009). However, it is also observed that the edges of these bandgaps

split into a large number of secondary gap regions of smaller amplitudes (i.e., sub-gaps) separated by narrow resonant states that reach, in different proportions, into the central gap region as the inhomogeneity of the structures is increased from the GA-spiral. The width, shape and the fine resonant structure of these bandedge features are determined by the unique array geometries. A large peak located inside the gap at  $\omega/\omega_0 = 1.122$  (1.273  $\mu\text{m}$ ) represents a defect mode localized at the center of the spiral array where a small air region free of dielectric cylinders acts as a structural defect. Several peaks corresponding to localized modes appear both along the band edges and within the gap. These dense series of photonic bandedge modes have been observed for all types of Vogel spirals and correspond to spatially localized modes due to the inhomogeneous distribution of neighboring particles. A more detailed study of the formation of mechanism of these modes in a GA-spiral is presented in section 7.1.4 and can be found in detail here (Seng Fatt Liew et al., 2011). Here these results are extended to all the investigated Vogel spirals based on the knowledge of their first neighbor connectivity structure, shown in Figure 7.5. In particular, we note that localized bandedge modes are supported when ring shaped regions of similar interparticle separation  $d$  in Figure 7.5 are sandwiched between two other regions of distinctively different values of  $d$ , thus creating a photonic heterostructure that can efficiently localize optical modes. In this picture, the outer regions of the spirals act as “effective barriers” that confine different classes of modes within the middle spirals regions. According to this mode localization mechanism, the reduced number of bandedge modes calculated for spirals  $\alpha_4$  and  $\beta_4$  is attributed to the monotonic decrease (i.e., gradual fading) of interparticle separations when moving away

from the central regions of the spirals, consistent with the corresponding Delaunay triangulation maps in Figures 7.5(i,d). In particular, since these strongly perturbed spiral structures do not display clearly contrasted (i.e., sandwiched) areas of differing interparticle separations, their bandedge LDOS is strongly reduced and circularly symmetric bandedge modes cannot be formed. These observations will be validated by the detailed optical mode analysis presented in proceeding sections for all the different spirals.

Finally, we notice a similarity between the highly singular character of the LDOS at the bandedge of Vogel spirals shown in Figure 7.6 and the fractal-like energy/transmission spectra universally exhibited by a number of different quasiperiodic and deterministic aperiodic electronic/photonic systems (Lai et al., 2007). In the next section it will be demonstrate that geometrical structure of Vogel spirals and the strongly fluctuating character of their photonic LDOS spectra in Figure 7.6 indeed display clear multifractal scaling.

### 7.1.2 Multifractal and scaling properties of Vogel spirals

In this section, we apply multifractal analysis to characterize the inhomogeneous structures of Vogel's spirals arrays as well as their LDOS spectra. Geometrical objects display fractal behavior if they display scale-invariance symmetry, or self-similarity, i.e. a part of the object resembles the whole object (Feder, 1988). Fractal objects are described by non-integer fractal dimensions, and display power-law scaling in their structural (i.e., density-density correlation, structure factor) and dynamical (i.e., density

of modes) properties (Janot, 1997; Gouyet and Mandelbrot, 1996). The fractal dimensions of physical objects can be operatively defined using the box-counting method (Gouyet and Mandelbrot, 1996). In the box-counting approach, the space embedding the fractal object is sub-divided into a hyper-cubic grid of boxes (i.e., cells) of linear size  $\varepsilon$  (i.e., line segments to analyze a one-dimensional object, squares in two dimensions, cubes in three dimensions, and so on). For a given box of size  $\varepsilon$ , the minimum number of boxes  $N(\varepsilon)$  needed to cover all the points of a geometric object is determined. The procedure is then repeated for several box sizes and the (box-counting) fractal dimension  $D_f$  of the geometric object is simply determined from the power-law scaling relation:

$$N(\varepsilon) = \varepsilon^{-D_f} \quad (7.2)$$

The relevance of fractals to physical sciences and other disciplines (i.e., economics) was originally pointed out by the pioneering work of Mandelbrot (Mandelbrot, 1982). However, the complex geometry of physical structures and multi-scale physical phenomena (i.e., turbulence) cannot be entirely captured by homogeneous fractals with single fractal dimension (i.e., mono-fractals). In general, a spectrum of local scaling exponents associated to different spatial regions needs to be determined. For this purpose, the concept of multifractals, or inhomogeneous fractals, has been more recently introduced (Stanley and Meakin, 1988; Mandelbrot, 1988) and a rigorous multifractal formalism has been developed to quantitatively describe local fractal scaling (Frisch, 1980).

In general, when dealing with multifractal objects on which a local measure  $\mu$  is defined (i.e., a mass density, a velocity, an electrical signal, or some other scalar physical parameter defined on the fractal object), the (local) *singularity strength*  $\alpha(x)$  of the multifractal measure  $\mu$  obeys the local scaling law:

$$\mu(B_x(\varepsilon)) \approx \varepsilon^{\alpha(x)}. \quad (7.3)$$

where  $B_x(\varepsilon)$  is a ball (i.e., interval) centered at  $x$  and of size  $\varepsilon$ . The smaller the exponent  $\alpha(x)$ , the more singular will be the measure around  $x$  (i.e., local singularity). The *multifractal spectrum*  $f(\alpha)$ , also known as *singularity spectrum*, characterizes the statistical distribution of the singularity exponent  $\alpha(x)$  of a multifractal measure. If we cover the support of the measure  $\mu$  with balls of size  $\varepsilon$ , the number of balls  $N_\alpha(\varepsilon)$  that, for a given  $\alpha$ , scales like  $\varepsilon^\alpha$ , behaves as:

$$N_\alpha(\varepsilon) \approx \varepsilon^{-f(\alpha)} \quad (7.4)$$

In the limit of vanishingly small  $\varepsilon$ ,  $f(\alpha)$  coincides with the fractal dimension of the set of all points  $x$  with scaling index  $\alpha$  (Gouyet and Mandelbrot, 1996). The spectrum  $f(\alpha)$  was originally introduced by Frisch and Parisi (Frisch, 1980) to investigate the energy dissipation of turbulent fluids. From a physical point of view, the multifractal spectrum is a quantitative measure of structural inhomogeneity. As shown by Arneodo et al (Muzy, Bacry and Arneodo, 1994), the multifractal spectrum is well suited for characterizing complex spatial signals because it can efficiently resolve their local fluctuations. Examples of multifractal structures/phenomena are commonly encountered in dynamical



systems theory (e.g., strange attractors of nonlinear maps), physics (e.g., diffusion-limited aggregates, turbulence), engineering (e.g., random resistive networks, image analysis), geophysics (e.g., rock shapes, creeks), and even in finance (e.g., stock markets fluctuations). In the case of singular measures with a recursive multiplicative structure (i.e., the devil's staircase), the multifractal spectrum can be calculated analytically (Halsey et al., 1986). However, in general multifractal spectra are computed numerically.

In this work, the multifractal spectra of Vogel spirals and of their LDOS spectra are calculated for the first time. The multifractal singularity spectrum of each spiral structure was calculated from the corresponding 600 dpi bitmap image, using the direct Chhabra-Jensen algorithm (Chhabra and Jensen, 1989) implemented in the routine *FracLac* (ver. 2.5) (Karperien) developed for the NIH distributed *Image-J* software package (Rasband). In order to calculate the singularity spectrum  $f(\alpha)$  of a digitized spiral image, *FracLac* generates a partition of the image into a group of covering boxes of size  $\epsilon$  labeled by the index  $i=1,2,\dots, N(\epsilon)$ . The fraction of the mass of the object (i.e., number of pixels) that falls within box  $i$  of radius  $\epsilon$  is indicated by  $P(i)$ , and it is used to define the generalize measure:

$$\mu_i = \frac{P(i)^q}{\sum P(i)^q} \quad (7.5)$$

where  $q$  is an integer and the sum runs over all the  $\epsilon$ -boxes. The quantity in Equation (7.5) represents the  $(q-1)$ -th order moment of the “probability” (i.e., pixel fraction)



$P(i)/N$ , where  $N$  is the total number of pixels of the image. The singularity exponent and singularity spectrum can then be directly obtained as (Chhabra and Jensen, 1989):

$$\alpha = \sum \mu_i \times \ln P(i) / \ln \varepsilon \quad (7.6)$$

$$f(\alpha) = \sum [\mu_i \times \ln \mu_i] / \ln \varepsilon \quad (7.7)$$

Multifractal measures involve singularities of different strengths and their  $f(\alpha)$  spectrum generally displays a single humped shape (i.e., downward concavity) which extends over a compact interval  $[\alpha_{\min}, \alpha_{\max}]$ , where  $\alpha_{\min}$  (respectively  $\alpha_{\max}$ ) correspond to the strongest (respectively the weakest) singularities. The maximum value of  $f(\alpha)$  corresponds to the (average) box-counting dimension of the multifractal object, while the difference  $\Delta\alpha = \alpha_{\max} - \alpha_{\min}$  can be used as a parameter reflecting the fluctuations in the length scales of the intensity measure (Albuquerque and Cottam, 2003).

The calculated multifractal spectra are shown in Figure 7.7(a) and Figure 7.7(b) for the spiral arrays in the  $\alpha$  and  $\beta$  series, respectively. For comparison, the LDOS of the GA-spiral is also reported in both panels. All spirals exhibit clear multifractal behavior with singularity spectra of characteristic downward concavity, demonstrating the multifractal nature of the geometrical structure of Vogel's spirals. We notice in Figures 7.7(a,b) that the GA-spiral features the largest fractal dimensionality ( $D_f = 1.873$ ), which is consistent with its more regular structure. We also notice that the  $\Delta\alpha$  for the GA-spiral is the largest, consistently with the diffuse nature (absolutely continuous) of its Fourier spectrum (Figure 7.2c). On the other hand, the less homogeneous  $\alpha_1$ -spiral structure features the lowest fractal dimensionality ( $D_f = 1.706$ ), consistent with a larger degree of

structural disorder. All other spirals in the  $\alpha$  series were found to vary in between these two extremes. However, the results shown in Figure 7.7(c,d) demonstrate significantly reduced differences in the singularity spectra of the spirals in the  $\beta$  series, due to the much smaller variation of the perturbing divergence angle  $\alpha$  (137.5-137.6) reported in Table 7.1. These results demonstrate that multifractal analysis is suitable to detect the small local structural differences among Vogel spirals obtained by very small variations in the divergence angle  $\alpha$ .

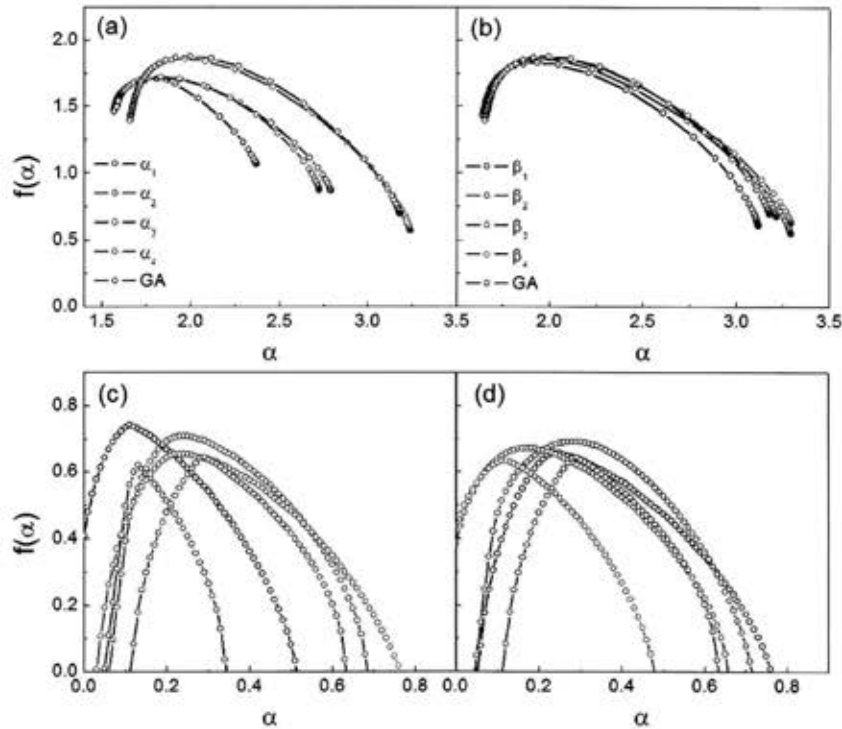


**Figure 7.7:** Multifractal singularity spectra  $f(\alpha)$  of direct space spiral arrays ( $N=1000$ ) with divergence angles between (a)  $\alpha_1$  and the golden angle and (b) between the golden angle and  $\beta_4$ . Multifractal spectra for spiral LDOS with divergence angles between (c)  $\alpha_1$  and the golden angle and (d) between the golden angle and  $\beta_4$ .

Now we turn our attention to the multifractal analysis of the LDOS spectra of Vogel spirals. We notice first that the connection between the multifractality of

geometrical structures and of the corresponding energy or LDOS spectra is not trivial in general. In fact, multifractal energy spectra have been discovered for deterministic quasiperiodic and aperiodic systems that do not display any fractality in their geometry despite the fact that they are generated by fractal recursion rules. Typical examples are Fibonacci optical quasicrystals and Thue-Morse structures (Albuquerque and Cottam, 2003). Optical structures with multifractal eigenmode density (or energy spectra) often display a rich and fascinating behavior leading to the formation of a hierarchy of satellite pseudo-gaps, called “fractal gaps”, and of critically localized eigenmodes when the size of the system is increased (Jiang et al., 2005). Moreover, dynamical excitations in fractals, or fracton modes, have been found to originate from multiple scattering in aperiodic environments with multi-scale local correlations, which are described by multifractal geometry (Mitchison, 1977).

In order to demonstrate the multifractal character of the LDOS spectra of Vogel’s spirals, we performed wavelet-based multifractal analysis (Mallat, 1999). This approach is particularly suited to analyze signals with non-isolated singularities, such as the LDOS spectra shown in Figure 7.6. The wavelet transform of a function  $f$  is a decomposition into elementary *space-scale contributions*, associated to so-called wavelets that are constructed from one single function  $\psi$  by means of translations and dilation operations. The wavelet transform of the function  $f$  is defined as:

$$W_{\psi}[f](b, a) = \frac{1}{a} \int_{-\infty}^{+\infty} \bar{\psi}\left(\frac{x-b}{a}\right) f(x) dx \quad (7.8)$$

where  $a$  is the real scale parameter,  $b$  is the real translation parameter, and  $\bar{\psi}$  is the complex conjugate of  $\psi$ . Usually, the wavelet  $\psi$  is only required to be a zero-average function. However, for the type of singularity tracking required for multifractal analysis, it is additionally required for the wavelet to have a certain number of vanishing moments (Mallat, 1999). Frequently used real-valued analyzing wavelets satisfying this last condition are given by the integer derivatives of the Gaussian function, and the first derivative Gaussian wavelet is used in our multifractal analysis of the LDOS. In the wavelet-based approach, the multifractal spectrum is obtained by the so called wavelet transform modulus maxima method (Mallat, 1999), using the global partition function introduced by Arneodo et al. (Halsey et al., 1986) and defined as:

$$Z(q, a) = \sum_p |W_\psi[f](x, a)|^q, \quad (7.9)$$

where  $q$  is a real number and the sum runs over the local maxima of  $|W_\psi[f](x, a)|$  considered as a function of  $x$ . For each  $q$ , from the scaling behavior of the partition function at fine scales one can obtain the scaling exponent  $\tau(q)$ :

$$Z(q, a) \approx a^{\tau(q)}. \quad (7.10)$$

The singularity (multifractal) spectrum  $f(\alpha)$  is derived from  $\tau(q)$  by a Legendre transform (Mallat, 1999). In order to analyze the LDOS of photonic Vogel's spirals, the aforementioned wavelet transform modulus maxima method within the free library of Matlab wavelet routines WaveLab850 (Buckheit et al., 2005) has been implemented. The

code has been carefully tested against a number of analytical multifractals (i.e., devil's staircase) and found to generate results in excellent agreement with known spectra.

The calculated LDOS singularity spectra are shown in Figure 7.7(c,d) for the  $\alpha$  and  $\beta$  spiral series, respectively. For comparison, the LDOS of the GA-spiral is also reported in both panels. The data shown in Figure 7.7(c,d) demonstrate the multifractal nature of the LDOS spectra of Vogel spirals with singularity spectra of characteristic downward concavity. The average fractal dimensions of the LDOS were found to range in between  $D_f \approx 0.6-0.74$ , with the two extremes belonging to the  $\alpha$ -series (i.e.,  $\alpha_1$  and  $\alpha_2$ , respectively). The strength of the LDOS singularity is measured by the value of  $\alpha_0 = \alpha_{\max}$ , which is the singularity exponent corresponding to the peak of the  $f(\alpha)$  spectrum. In Figure 7.7(c), we notice that the singular character of the LDOS spectra steadily increases from spiral  $\alpha_1$  to the GA-spiral across the  $\alpha$ -series. On the other hand, a more complex behavior is observed across the  $\beta$  series, where the strength of the LDOS singularity increases from  $\beta_2$  to  $\beta_4$  spirals.

### 7.1.3 Optical Mode Analysis of Vogel spirals

The properties of optical modes localized at the higher frequency multifractal bandedge of Vogel spirals are now investigated. Across this bandedge, the field patterns of the modes show the highest intensity in the air regions between the dielectric cylinders and thus are best suitable for sensing and lasing applications where gain materials can easily be embedded between rods (Ling et al., 2001).

The spatial profile of the modal fields and their complex frequencies  $\omega = \omega_r + i\omega_i$  were calculated using eigenmode analysis within COMSOL. Complex mode frequencies naturally arise from radiation leakage through the open boundary of the arrays. The imaginary components of the complex mode frequencies give the leakage rates of the mode, from which the quality factor can be defined as  $Q = \omega_r/2\omega_i$ . The calculated quality factors of the modes are plotted in Figure 7.8(a) for the  $\alpha_1$ -spiral and in Figure 7.8(b) for the GA-spiral and the  $\beta_4$ -spiral as a function of normalized frequency. The analysis is limited to only these three structures since they cover the full perturbation spectrum and are representative of the general behavior of the localized bandedge modes in Vogel spirals. By examining the spatial electric field patterns of the modes across the air bandedge of Vogel spirals we discovered that it is possible to group them into several different classes. The Q factors of modes in the same class depend linearly on frequency, as shown in Figure 7.8. In particular, their quality factors are found to linearly decrease as the modes in each class move further away from the central PBG region. The frequency range spanned by each class of modes depends on the class and the spiral type. For example, the modes in classes A and B (Figure 7.8a) of the  $\alpha_1$ -spiral span the entire air-bandedge, while modes in classes C-F are confined within a narrower region of the bandedge.

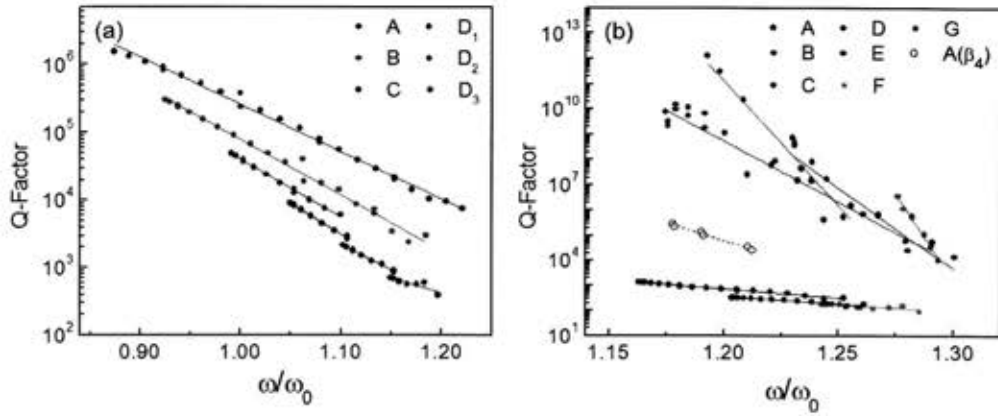


**Figure 7.8:** Quality factors of the air band edge modes for (a)  $\alpha_1$ -spiral and (b) GA-spiral and  $\beta_4$ -spiral versus normalized frequency.

As an example, in Figure 7.9 we show the calculated electric field distribution ( $E_z$  component) for the first three bandedge modes in class B of  $\alpha_1$ -spiral and GA-spiral, as well as the first three bandedge modes in class A of the  $\beta_4$ -spiral. Each spiral bandedge mode is accompanied by a degenerate mode at the same frequency but with complementary spatial pattern, rotated approximately by  $180^\circ$  (not shown here). We notice in Figure 7.9 that modes belonging to each class are (radially) confined within rings of different radii, and display more azimuthal oscillations as the frequency moves away from the center of PBG (i.e., Figure 7.9a-c). A detailed analysis of the mechanism of mode confinement and mode separation into different classes for the GA-spiral is discussed in section 7.1.4 and can be found in the following reference (Seng Fatt Liew et al., 2011). In this study, it has been shown that the unique spatial distribution of neighboring particles in the GA-spiral gives rise to numerous localized resonant modes at different frequencies. Different areas of the spiral hosting particles with similar spacing, evidenced by the similarly colored rings in Figure 7.5, lead to mode confinement at various radial distances from the center, as in circular grating structures of different radii.

In particular, for the GA-spiral the field patterns of bandedge modes originate via Bragg scattering occurring perpendicularly to curved lines of dielectric cylinders called parastichies (Seng Fatt Liew et al., 2011).

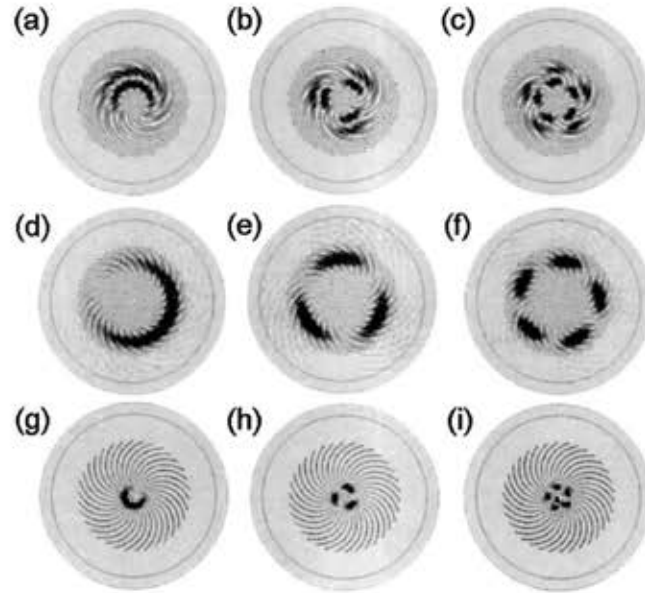


**Figure 7.9:** Spatial distributions of electric field  $E_z$  for the first three band edge modes of (a-c) class B in a  $\alpha_1$ -spiral, (d-f) class A in a g-spiral and (g-i) class A in a  $\beta_4$ -spiral. Spectrally located at  $\omega/\omega_0 =$  (a) 0.9248, (b) 0.9290, (c) 0.9376, (d) 1.1629, (e) 1.1638, (f) 1.1657, (g) 1.1781, (h) 1.1900, and (i) 1.2152.

It is now discovered that the same mechanism occurs for all Vogel spirals examined here, each characterized by a unique configuration of parastichies that reflect into characteristic spatial patterns of the modes. As an example, first analyzing the behavior of the  $\alpha_1$  spiral, and it is discovered that its bandedge modal classes contain modes spatially confined to the red region in Figure 7.5(a), bounded on either side by areas of higher particle density (i.e., shorter interparticle separations). The spatial profiles of the representative class-B modes of the  $\alpha_1$  spiral, shown in Figure 7.9(a), are centered



around this low density circular region (i.e., central red ring in Figure 7.5a) and have the same number of oscillations in the radial field (i.e., radial number 2) while displaying increasing azimuthal oscillations (i.e., increasing azimuthal numbers). On the other hand, for the GA-spiral the modal patterns in class A, shown in Figure 7.9(d-f), are also confined to this spatial region, but have radial number equal to one along the series of increasing azimuthal numbers. Modes in class C also occupy the same spatial region of the spiral, but with a radial number of three (not shown here). This characteristic cascade process of “radial splitting” of the modes continues for classes D, E and F in each spiral. However, as the radial numbers increase, the less confined outer portions of the modes result in a reduced quality factor. It is also relevant to note here that the slopes of the linear trends in Q-factors with frequency are all approximately the same for modes that are confined approximately within the same spatial region.

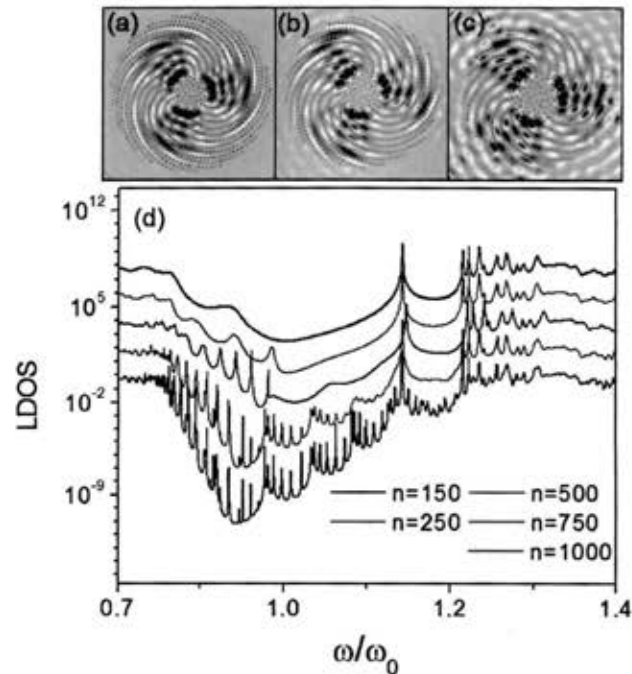


**Figure 7.10:** Spatial distributions of electric field  $E_z$  class  $D_1$  band edge mode ( $\omega/\omega_0 =$

1.053 normalized as described in Section 3) in a  $\alpha_1$ -spiral with (a) 1000 particles, (b) 750 particles and (c) 500 particles. (d) LDOS calculated at the center of  $\alpha_1$ -spirals with varying number of particles between  $n = 150$  and  $n = 1000$ .

The regions of spatial localization of spiral modes can be easily identified in Figure 7.5. For example, the geometrical structure of the GA-spiral, captured in Figure 7.5(e), indicates the presence of multiple circular regions of similar interparticle separations that act as radial heterostructures inducing spatial mode confinement (Seng Fatt Liew et al., 2011). The first three field distributions of class A-modes of the GA-spiral, shown in Figure 7.8(d-f), are all confined to the outermost light blue region evident in Figure 7.5(e). Here again, secondary classes can be confined to the same spatial region with increased radial numbers (i.e., class D with radial number 2, and class F with radial number 3). Classes B and E both occupy the second light blue ring shown in Figure 7.5(e), while classes C and G share the innermost. The trends in Q-factors for the different series can again be seen to depend on the region of mode confinement. Contrary to the behavior of GA and  $\alpha_1$ -spirals, the  $\beta_4$ -spiral supports only one class of modes localized by the disordered arrangement of cylinders at its center, as shown in Figure 7.8(g-i). The lack of radial classes in this spiral can be readily explained by its geometrical structure. In fact, in Figure 7.5(i) we notice that the spirals arms quickly diverge with gradually decreasing interparticle separations, providing no “heterostructure regions” for radial light confinement.

Finally the size scaling of the LDOS and of the bandedge modes for the three most representative spiral structures (GA,  $\alpha_1$ , and  $\beta_4$ ) is investigated. The LDOS is again computed at the center of the array utilizing the same methodology described previously.

In Figures 7.10-7.12 the calculated LDOS for the three spiral types with progressively decreasing number of cylinders from 1000 to 150 is shown. Also included in Figures 7.10-7.12 are representative air-bandedge modes calculated for a spirals with decreasing size (from panels a to c).

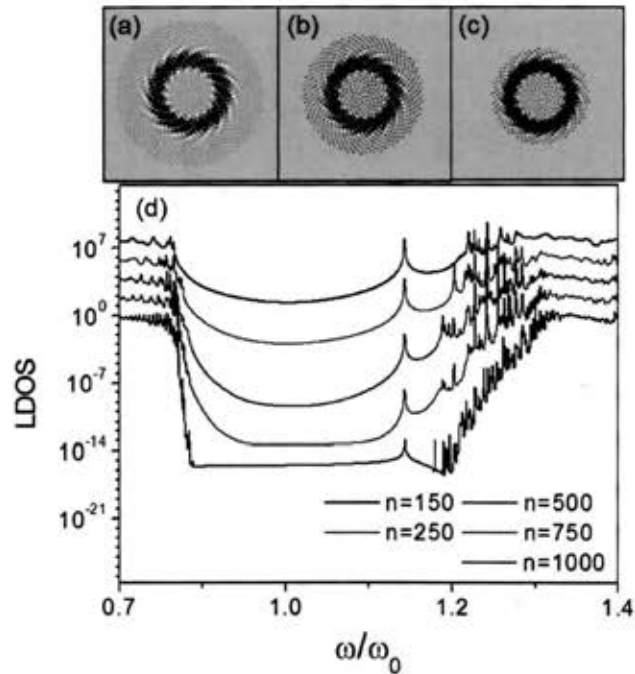


**Figure 7.11** Spatial distributions of electric field  $E_z$  class B band edge mode ( $\omega/\omega_0=1.175$  normalized as described in Section 3) in a GA-spiral with (a) 1000 particles, (b) 750 particles and (c) 500 particles. (d) LDOS calculated at the center of GA-spirals with varying number of particles between  $n = 150$  and  $n = 1000$ .

Examining the size scaling behavior of the LDOS of the spiral arrays shown in Figures 7.10-7.12 certain general characteristics can be noticed. First of all, for each spirals the frequency positions and overall width of the principal TM gaps remain unaffected when scaling the number of particles, but the gaps become deeper as the number of particles is increased. This is consistent with the known fact that the main gaps

supported by arrays of dielectric cylinders are dominated by the single cylinder Mie resonances for TM polarization. Moreover, the frequency position of the most localized resonant mode inside the gap remains almost constant when varying the particles number, while its intensity decreases with the bandgap depth. This implies that this mode is created by the small number of cylinders at the center, which is defined in the first few generated particles. However, the most striking feature of the LDOS scaling, evident in Figures 7.10-7.12, is the generation of a multitude of secondary sub-gaps of smaller intensity as the number of cylinders is increased. As the number of dielectric cylinders is increased, regions with different spatial distributions of cylinders are created in the spirals resulting in many more spatial frequency components. As previously shown, these are key components in creating new classes of modes, leading to the distinctive behavior of fractal bandedge modes.

This phenomenon is most evident in the  $\alpha_1$ -spiral scaling shown in Figure 7.10, which we found to possess the lowest fractal dimension (i.e., or the highest degree of structural inhomogeneity). Below 750 cylinders, the air bandedge region is almost completely depopulated of bandedge modes, which become strongly leaky as shown in Figure 7.10(a-b). This behavior can directly be attributed to the loss of the outermost boundary region (outer blue region in Figure 7.5a) when the number of cylinder is decreased, eliminating the radial heterostructure confinement scheme needed to support localized bandedge modes. On the other hand, the modes in the LDOS whose confinement regions remain intact upon size scaling, such as the ones shown in Figure 7.11(a-c) and Figure 7.12(a-c), exist even when scaling the size of the spiral down to only

a few hundred cylinders. These results demonstrate the localized nature of the air bandedge modes that densely populate the multifractal LDOS spectra of Vogel spirals.

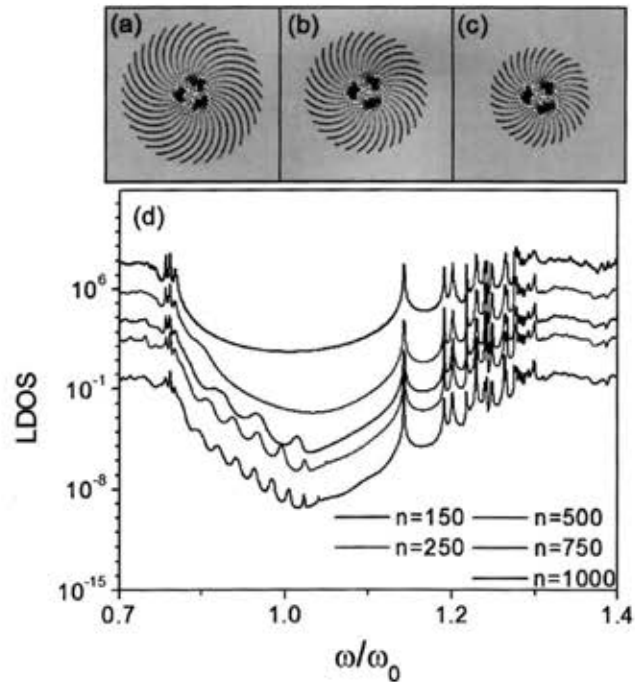


**Figure 7.12:** Spatial distributions of electric field  $E_z$  class A band edge mode ( $\omega/\omega_0=1.190$  normalized as described in Section 3) in a  $\beta_4$ -spiral with (a) 1000 particles, (b) 750 particles and (c) 500 particles. (d) LDOS calculated at the center of  $\beta_4$ -spirals with varying number of particles between  $n=150$  and  $n=1000$ .

#### 7.1.4 Band Edge Mode Formation and OAM

Presented here is a brief summary of a numerical study on photonic bandgap and band edge modes in the GA-spiral array of air cylinders in dielectric media. For a detailed description of the study, the readers are referred to (Seng Fatt Liew et al., 2011). The optical properties are studied for a GA-spiral that consists of  $n = 1000$  air cylinders in a dielectric medium with refractive index  $n = 2.65$ . This structure is the inverse of that in

previous sections and facilitates the formation of a photonic bandgap for TE polarized light with  $(E_r, E_\theta, H_z)$ . Once again, the LDOS has been calculated from the Green's function for the propagation of  $H_z$  from point  $r$  to  $r'$  at the center of the array and is shown in Figure 7.13a.

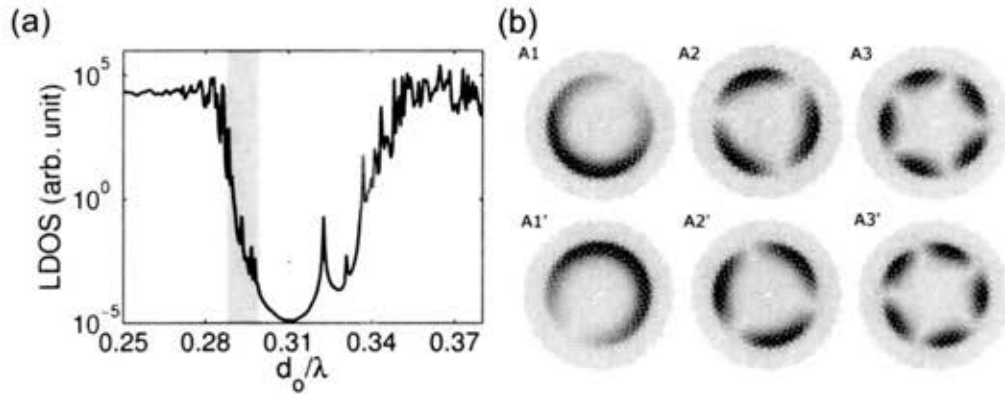


**Figure 7.13:** (a) LDOS calculated at the center of the golden-angle spiral array as a function of the normalized frequency  $d_o/\lambda$ . The regions at the lower and upper band edge where the band edge modes exist are highlighted. (b) Spatial distributions of magnetic field  $H_z$  for the first three pairs of band edge modes of class A (Seng Fatt Liew et al., 2011).

As in the case of the dielectric pillars, a large central gap is formed as well as several peaks corresponding to band edge modes. Additionally, the center defect mode is still present in the gap. Those modes on the higher (lower) frequency edge of the gap are denoted as upper (lower) band edge modes. As in the case of the dielectric cylinders (previous section), from their frequencies and field patterns, several classes of the band edge modes can be identified. Within each class, the modes have similar field patterns at similar radial distances and display monotonic variation of Q-factor. Figure 7.13b shows a sampling from a group of modes labeled class A. A careful inspection of the mode profiles reveals that the class A modes have the magnetic field maxima along the

parastichies that are formed by the air cylinders and twist in the CCW direction. These local standing wave pattern behaviors indicate light is confined in the direction perpendicular to the parastichies via Bragg scattering from the air holes.

To better understand the formation of these modes we again turn to the Delaunay triangulation plot of the GA-spiral, shown in Figure 7.14; however now overlapped with the region that contains 90% of the energy of modes in class A.

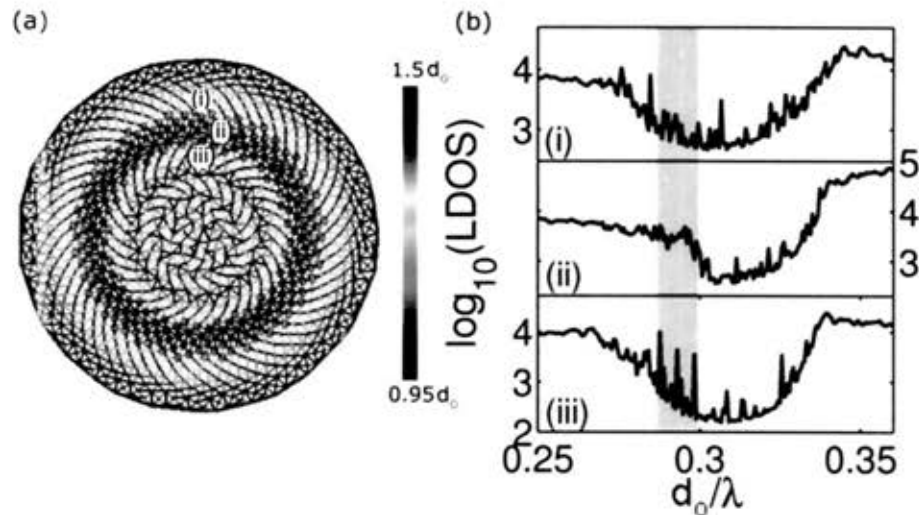


**Figure 7.14:** (a) Overlay of the region where class A modes are localized on the color map of the neighboring particles distance of air cylinders revealing class A modes stay mostly inside a ring labeled (ii) and sandwiched between two other rings (i) and (iii). (b) LDOS in the regions (i), (ii) and (iii) (Seng Fatt Liew et al., 2011).

As observed previously in the case of dielectric cylinders, the modes are confined in region (ii), which is sandwiched by regions (i) and (iii) of different nearest neighbor distributions, leading to a change of PBG. The LDOS is now computed in regions (i), (ii) and (iii) by removing air cylinders outside that region, plotted in Figure 7.14b. The frequency range of class A modes is inside the PBG of region (i) and (iii) but outside the

PBG of region (ii). Consequently, light within this frequency range is allowed to propagate in region (ii) but not in (i) or (iii). Hence, regions (i) and (iii) act like barriers that confine class A modes in region (ii). Thanks to its broad distribution of spacing between neighboring particles  $d$ , the GA-spiral can support numerous modes at different frequencies. The spatial inhomogeneity of holes or particles leads to mode confinement in different parts of the structure.

As mentioned earlier, the standing wave patterns of the photonic band edge modes are formed by distributed feedback from the parastichies that spiral out. One example is presented in Figure 7.15, where the dashed arrows denote two families of parastichies along which the field maxima of mode A1 follow. The magnetic field  $H_z$  oscillates between the positive maxima on one parastichy and the negative maxima on the next one of the same family.

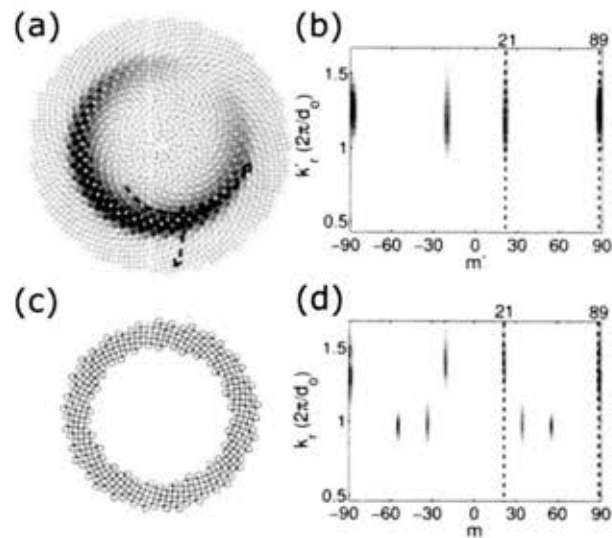


**Figure 7.15:** (a) Magnetic field distribution of mode A1 revealing the field maxima follow a family of 21 parastichies twisting in the CCW direction and another family of 89 parastichies in the CW direction (both are marked by the dashed arrows). (b) FFT of the



field distribution in (a). (c) Region of the spiral array that contains 90% energy of mode A1. (d) FBT of the structure in (c) (Seng Fatt Liew et al., 2011).

The FHD is again utilized to bring to light any azimuthal components that might be present in the field or the structure. Figure 7.15b shows the FHD on the Hz field distribution. A significant observation is that the modes have discrete angular momenta  $m = 21$  and  $m = 89$ , both Fibonacci numbers. To better understand the origin of the discrete OAM, the region where 90% of the mode's energy is located is shown in isolation in Figure 7.15c. The FHD is again performed on this region and is plotted in Figure 7.15d. The result indeed shows  $m = 21$  and  $m = 89$  components with radial frequency  $k_r$  similar to that in the field profile of mode A1. While there are also  $m = 34$  and  $m = 55$  components in the structure, they are at lower  $k_r$ , thus corresponding to modes at lower frequencies and further away from the band edge. Hence, these analysis shows that the angular momenta of the band edge modes are imparted by the underlying structure, more specifically, the parastichies in the GA-spiral.

It is now well established by these studies that spatial inhomogeneity in the distances of neighboring air holes or dielectric cylinders, localize the band edge modes within rings of different radii via Bragg scattering from the parastichies in the spiral structure. Additionally, these modes are wrapped around azimuthally to form circular patterns, which carry the well-defined angular momenta. The band edge modes have discrete angular momenta that originate from different families of the parastichies whose numbers correspond to the Fibonacci numbers in the case of the GA-spiral, but more generally, to known rational approximates of the generating irrational angle.

## 7.2 Dielectric Vogel Spiral Nanopillar Arrays

In this section, dielectric Vogel spiral nanopillar arrays are fabricated and their photonic properties are experimentally investigated. The design and measurement of a photonic band gap in a GA-spiral will be presented with motivation towards realizing lasing in these structures. Additionally, the scattering properties of nanopillar Vogel spiral arrays will be presented.

### 7.2.1 Motivation for Lasing in DANS

Unlike a conventional laser which utilizes mirrors or periodic structures to trap light, a random laser relies on the multiple scattering of light in a disordered gain medium for optical feedback and light confinement, as shown in Figure 7.16a (Wiersma, 2000; Cao et al., 2000; Wiersma, 2008). Coherent laser emission has been generated from various random structures, ranging from semiconductor nanoparticles and nanorods to polymers and organic materials. Additionally, lasing emission from scarred modes of wave-chaotic optical resonators with asymmetric resonant have been demonstrated, as shown in Figure 7.16b (Rex et al., 2002). Over the past decade, random lasers have generated significant interest among researchers because of their unique applications based upon the spectral fingerprint of the random structure, their micron-scale size, low fabrication cost, robustness to surface roughness and shape deformation, and nearly isotropic emission output (Wiersma, 2008; Cao, 2003).

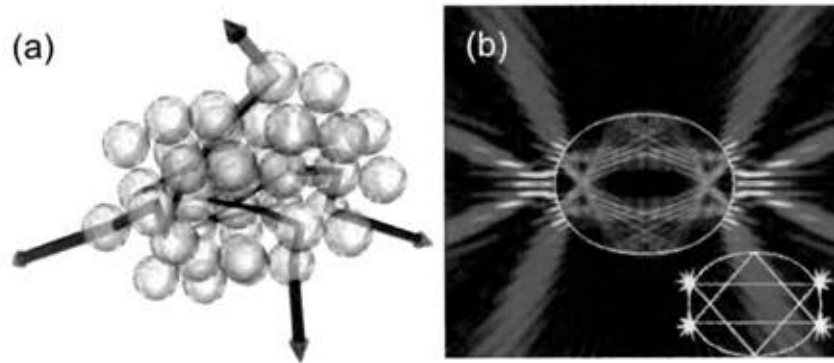


**Figure 7.16:** (a) Multiple light scattering with gain. A random collection of microspheres containing laser dye is excited to obtain population inversion. The propagation of the light waves becomes that of an amplified random walk (Wiersma, 2008). (b) The modulus of the electric field for a calculated quasibound state of  $nkr_0 \approx 129$  ( $n$  is the index of refraction,  $k$  is the real part of the resonant wave vector) and  $\epsilon = 0.12$  which is scarred by the triangular periodic orbits shown in the inset. The four points of low incidence angle which should emit strongly are indicated (Rex et al., 2002).

These characteristics are ideal for identification, encoding, tagging, and optical sensing. However, a major limitation to device applications of random lasers is the lack of control and reproducibility of the lasing modes. Namely, the frequencies and spatial locations of lasing modes are unpredictable, varying randomly from sample to sample. One solution to this problem is the realization of DANS lasers. DANS lasers could combine the advantages of random lasers with the fabrication and design reproducibility required for optoelectronics integration.

Recently, lasing action in localized optical modes of active photonic membranes with pseudo-random deterministic morphologies have been realized (Yang et al., 2010). It has been shown that the lasing modes of pseudo-random structures occur at reproducible spatial locations and frequencies, only slightly affected by structural fluctuations in different samples. The ability to engineer the lasing modes and make them

reproducible is essential to chip-scale photonic applications. Moreover, through tuning the structural aperiodicity, an optimal degree of aperiodicity where light confinement is maximal and lasing is the strongest can be found. The use of DANS in lasing opens a way of controlling lasing characteristic by engineering structural aperiodicity.

### 7.2.2 Band Gaps in GA-spirals

In Section 7.1, it was shown that 2D dielectric Vogel spirals possess large photonic band gaps with several band edge modes populating both the low and the high ends of the gap. In fact, it is well known that GA-spiral array has the ability to create an isotropic photonic bandgap (PBG), inhibiting light propagation in all directions (Pollard and Parker, 2009). The most well-known structures that produce PBGs are photonic crystals (Joannopoulos et al., 2008), but their structural anisotropy leads to spectral mismatch of gaps in different directions. To have complete PBGs, more isotropic structures, e.g. photonic quasicrystals with higher rotational symmetries, are preferred (Chan, Chan and Liu, 1998; Florescu, Torquato and Steinhardt, 2009). However, the photonic quasicrystals still have discrete Fourier spectra and are not fully isotropic. The GA-spiral has better isotropy because its Fourier space is diffuse and rotationally symmetric (Trevino, Cao and Dal Negro, 2011).

To realize an experimental photonic band gap in the GA-spiral geometry, high aspect ratio nanopillars are utilized. The nanopillar material used is a-Si:H with deposition parameters described in Chapter 4. The high density of defects in pure a-Si makes it a lesser material of interest in photonics, which is the reason for the attention on

a hydrogenated material. When hydrogenated, the defect density is greatly reduced by saturation of the several dangling bonds inherently found in a-Si. As a result a-Si:H can be made to be more transparent in the visible range, by adjusting the amount of H incorporated into the film. As an example, the transmission spectra (normalized for film thickness) are plotted in Figure 7.17 for reactive RF magnetron sputtered films deposited with different  $H_2/Ar$  flow ratios. As the ratio increases and more H is incorporated into the film, the transmission is extended to lower wavelengths.

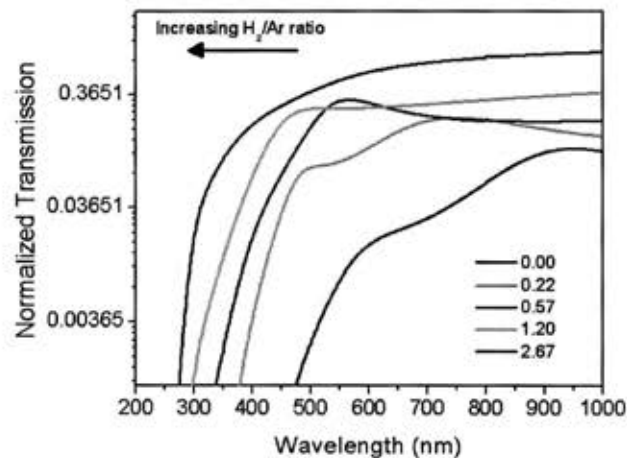


**Figure 7.17:** Normalized transmission spectra for a-Si:H deposited with different  $H_2/Ar$  gas flow ratios.

The advantage of using a-Si:H versus a SiN film or other dielectrics is the materials high index of refraction ( $n > 3$ ), leading to strong scattering. Additionally, nanofabrication techniques are highly developed for Si, as it is still the predominate material used in the CMOS and microelectromechanical systems (MEMS) industries.

In this study, a hexagonal nanopillar lattice is first fabricated and characterized using an ellipsometer (Hung, Lee and Coldren, 2010; Astratov et al., 1999). Reflection

spectra of this photonic crystal (PhC) structure under high incident angles and polarizations are measured for observing its antireflection and optical resonant effect. The optical resonance is mainly due to the existence of PBG inside this material. Analysis of the PhC structure is carried out with the rigorous coupled-wave analysis (RCWA) method, taking the dispersion and absorption of materials into account, which can be used to verify the experimental data (Hung, Lee and Coldren, 2010). Figure 7.18a shows an SEM micrograph of the fabricated Hexagonal lattice nanopillar array on a fused silica substrate. The nanopillars are 125 nm in diameter, 950 nm-tall and have a lattice spacing  $a = 312.5$  nm. The resulting  $r/a$  ratio is then 0.20.

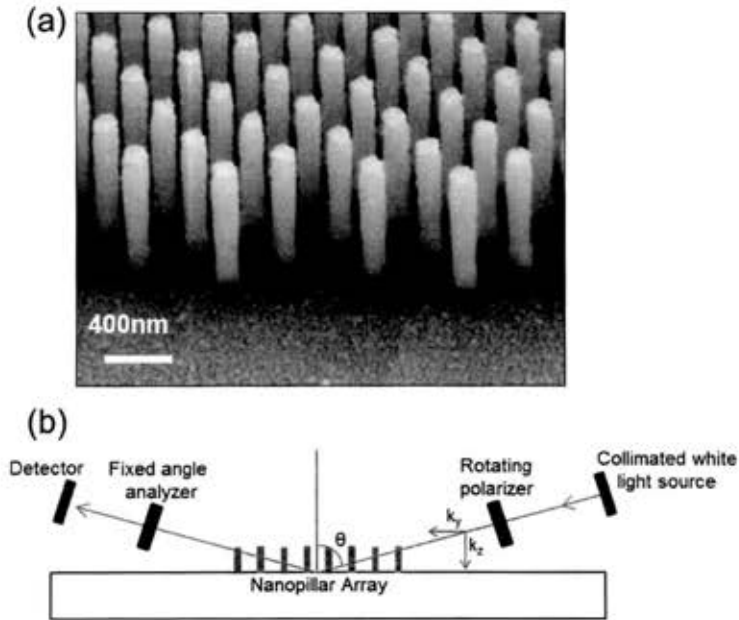


**Figure 7.18:** (a) SEM micrograph of hexagonal array of a-Si:H nanopillars and (b) diagram of ellipsometer reflection measurements taken on nanopillar arrays.

The total array is circular and has a diameter of 300  $\mu\text{m}$  to accommodate the beam spot of the ellipsometer which also approximately 300  $\mu\text{m}$  in diameter.

The use of ellipsometry for characterizing PBG in PhCs has been established in pervious publications (Hung, Lee and Coldren, 2010; Lin et al., 2006). The ellipsometer, shown in Figure 7.18b, measures two of the four Stokes parameters, denoted by  $\psi$  and  $\Delta$ . The polarization state of the light incident upon the sample can be decomposed into a TE and a TM component. The reflection of the TE and TM components are denoted by  $R_{TE}$  and  $R_{TM}$ , respectively. The ellipsometer measures the ratio of the two components as:

$$\rho = \frac{R_{TM}}{R_{TE}} = \tan(\psi)e^{i\Delta}, \quad (7.11)$$

where  $\tan(\psi)$  is the amplitude ratio and  $\cos(\Delta)$  is the phase difference through the material-light interaction (Lin et al., 2006). The parameters are measures along the symmetry points  $\Gamma M$ -direction of the hexagonal lattice. The measured parameters  $\tan(\psi)$  and  $\cos(\Delta)$ , as taken at the oblique angle of  $70^\circ$ , are plotted in Figure 7.19a and 7.19b, respectively.

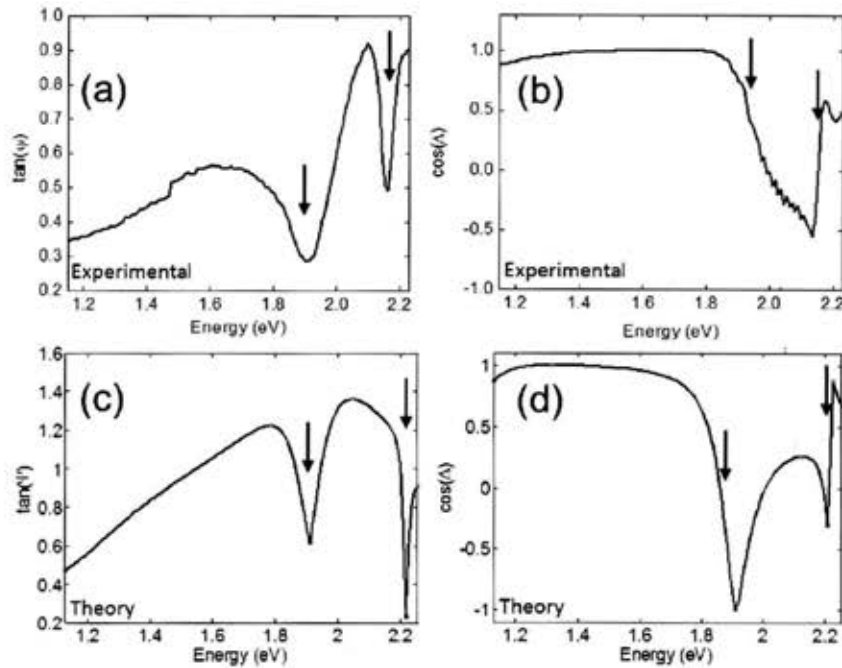


**Figure 7.19:** (a) SEM micrograph of hexagonal array of a-Si:H nanopillars and (b) diagram of ellipsometer reflection measurements taken on nanopillar.

For oblique incidence, the reflection of different polarized light would manifest differently in their corresponding spectra. The  $TE_{phc}$  bandgap leads to higher out-of-plane diffraction for the TM-polarized light (Galli et al., 2002), resulting in lower reflection and thus lower  $\tan(\psi)$  value. Meanwhile, the TM-polarized light would increase its optical paths and corresponding lower  $\cos(\Delta)$  value (Hsieh et al., 2004). A reflection caused by the presence of a  $TE_{phc}$ -mode PBG would then appear as a dip in the  $\tan(\psi)$  and a steep slope in  $\cos(\Delta)$  spectra, respectively (Hsieh et al., 2004).

In Figure 7.19a, two prominent dips in  $\tan(\psi)$  at 1.9 eV ( $\lambda = 653$  nm) and 2.16 eV ( $\lambda = 574$  nm) are seen. These two dips occur at the same energy as two step slopes in the  $\cos(\Delta)$  shown in 7.19b. The spectral features match well with band gap measurements of those published for similar nanopillar arrays of comparable dimensions (Hung, Lee



and Coldren, 2010). To confirm the experimental results, RCWA calculations are performed according to the array parameters and at the same oblique angle of  $70^\circ$ . The calculated  $\tan(\psi)$  and  $\cos(\Delta)$  are plotted in Figures 7.19c and 7.19d, respectively. The spectral dips and steep slopes are found to be in good qualitative agreement with the RCWA simulation.

While the first aim of this research is to measure the presence of a photonic band gap in a GA-spiral array of nanopillars, a second goal is to utilize the unique photonic modes present in the spiral array for lasing. For this to be realized, a material with optical gain must be introduced. The method of choice in this study is the spin coating of a blend of laser dye IR-140 (Exciton, Inc.) and the polymer PMMA. Such a combination has successfully been utilized in other amplified spontaneous emission experiments in the literature (Thompson et al., 2004). Thin films were prepared by dissolving 600 mg of PMMA and 9.38 mg of IR-140 in 6 ml of dichloromethane (DCM), and spin-coating the solution onto the substrate. The sample was then baked on a hot plate at  $180^\circ\text{C}$  for 2 minutes, resulting in a film thickness of  $1.5\ \mu\text{m}$ . The emission spectrum of the film is shown in Figure 7.20a, pumped with a frequency doubled Nd:YAG laser ( $\lambda = 532\text{nm}$ ).

The pillars to be used in subsequent experiments are again  $950\ \text{nm}$ -thick, approximately  $550\ \text{nm}$  shorter than the dye-doped polymer. The process flow used to match the heights of the two materials is shown in Figure 7.20b. In this technique, an  $\text{O}_2$  plasma is used to selectively and controllably etch the polymer down to the height of the nanopillars.

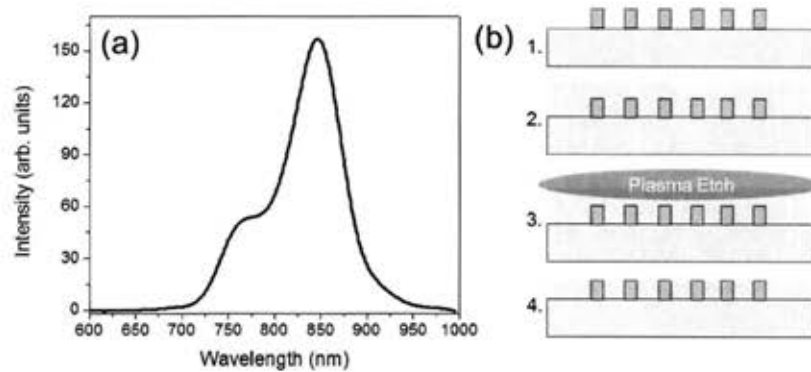


**Figure 7.20:** (a) Emission spectrum of Exciton IR-140 laser dye in PMMA film. (b) Process flow for embedding dye doped PMMA in nanopillar array.

In order to effectively design a band gap overlapping with the emission bandwidth of the laser dye, the open source MIT Photonic-Bands (MPB) software was utilized (Johnson and Joannopoulos, 2001). The MPB program is a highly efficient software package for computing the band structures (dispersion relations) and electromagnetic modes of periodic dielectric structures. A 3D slab model was created using a hexagonal lattice with nanopillar diameter of  $d = 105$  nm, lattice constant  $a = 200$  nm, height of pillar  $h = 950$  nm. Index of refraction values  $n_{\text{pillar}} = 3.1$  for the pillars,  $n_{\text{pol}} = 1.5$  for the polymer layer, and  $n_{\text{sub}} = 1.46$  for the fused silica substrate were used. The resulting band structure is plotted in Figure 7.21a. The parameters simulated result in the desired band gap between 1.4 and 1.5 eV, corresponding to 827 and 886 nm. The key parameter that can be extruded from the simulation is the appropriate filling fraction, equal to 25%. This filling fraction is now used as a guide for generating a GA-spiral with a similar value.

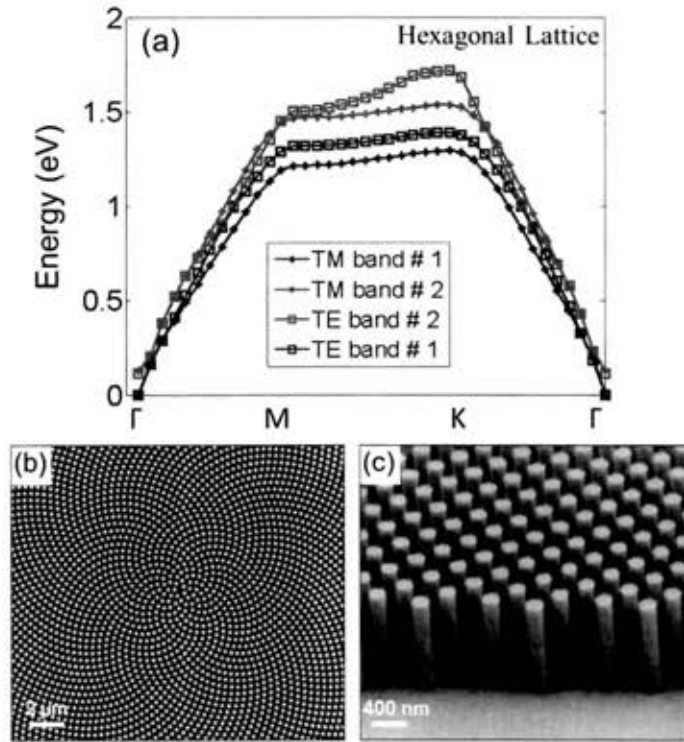


**Figure 7.21:** (a) Calculated band diagram for hexagonal with  $d = 105$  nm and  $a = 200$  nm. (b) Top-down SEM micrograph of fabricated a-Si:H GA-spiral nanopillar array. (c) Angled SEM micrograph of array in (b), displaying pillar sidewall quality.

With guidance from the MPB simulations, a GA-spiral was generated using a scaling factor  $1.9 \times 10^{-7}$  m and pillar diameters of 200 nm, resulting in a filling fraction of 27.3% and  $r/a = 0.308$ . SEM micrographs of the fabricated structure are shown in Figures 7.21b and 7.21c. A final pillar diameter of 200 nm was chosen for its mechanical robustness. For arrays of similar filling fraction and small diameters, pillars often stuck together during proceeding wet processing steps and spin coating.

Figure 7.22a and 7.22b plot the ellipsometer parameters  $\tan(\psi)$  and  $\cos(\Delta)$  as measured in air, respectively. Black arrows highlight the sharp dips in  $\tan(\psi)$  and steep changes in  $\cos(\Delta)$ , associated with the presence of a  $\text{TE}_{\text{phc}}$ -mode PBG.

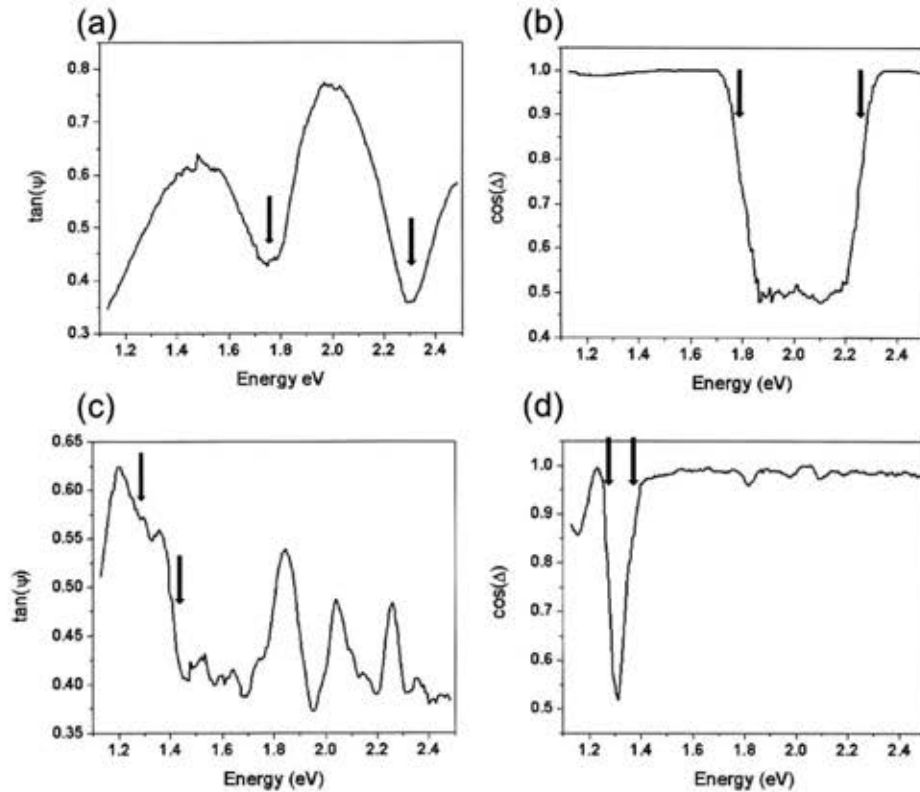


**Figure 7.22:** Measured ellipsometer parameters for a GA-spiral nanopillar array with filling fraction 27.3%: (a)  $\tan(\psi)$  measured in air, (b)  $\cos(\Delta)$  measured in air, (c)  $\tan(\psi)$  measured with PMMA laser dye mixture, and (d)  $\cos(\Delta)$  measured with PMMA laser dye mixture.

The resonant features occur at energies of 2.30 eV ( $\lambda = 537$  nm) and 1.75 eV ( $\lambda = 709$  nm). The band gap is blue shifted from the target range; however the result is expected as the designed structure accounts for the higher index PMMA versus air. After spin-coating the PMMA/laser dye mixture and thinning down to the height of the pillars, the ellipsometer parameters are again measured and plotted in Figure 7.22c,d. In the  $\cos(\Delta)$  plot, we notice the two step features have red shifted to 1.38 eV ( $\lambda = 898$  nm) and 1.26 eV ( $\lambda = 984$  nm) as expected. The  $\tan(\psi)$  data however is not as clear. An observable dip is measured at  $\sim 1.38$  eV, however the second feature at 1.26 eV is less pronounced. Several

factors could attribute to the discrepancy, including induced surface roughness from the PMMA thinning process, as well as non-uniformities in the spun PMMA/laser dye film.

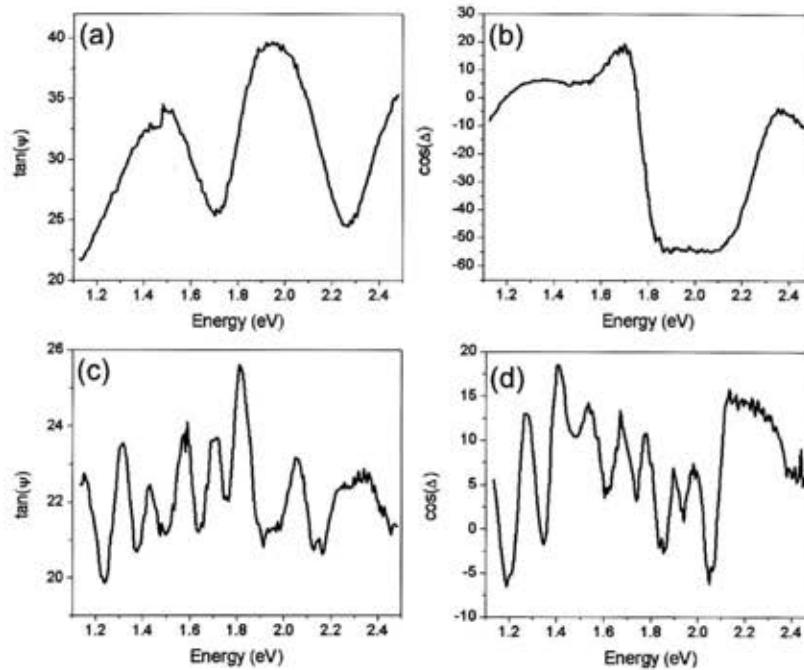


**Figure 7.23:** Measured ellipsometer parameters for a  $\beta_4$ -spiral nanopillar array with filling fraction 27.3%: (a)  $\tan(\psi)$  measured in air, (b)  $\cos(\Delta)$  measured in air, (c)  $\tan(\psi)$  measured with PMMA laser dye mixture, and (d)  $\cos(\Delta)$  measured with PMMA laser dye mixture.

Additionally, a  $\beta_4$ -spiral with the same filling fraction and pillar size parameters was also fabricated. The measured ellipsometer parameters in air and embedded in PMMA are shown in Figure 7.23. The measured  $\tan(\psi)$  and  $\cos(\Delta)$  values feature well pronounced dips and slopes, respectively, at approximately the same energy values as the GA-spiral. However, the measured Stokes parameters in PMMA are observed to have no well-defined spectral features in the shifted energy range that is expected. Again, fluctuations in the PMMA film are expected as the primary factor. Additional work is to be conducted on these samples to solve some of the post PMMA

issues in the measured Stokes parameters, including the further thinning of the PMMA layer to ensure its height remains less than the pillar height.

The current results are promising for prospective lasing in Vogel spirals. The measured band gap is near the edge of the laser dye emission. In fact, the laser dye IR-140 emission can be shifted to a range of 875 nm to 1000 nm, depending on the pump source wavelength as well as the molar concentration of the polymer matrix (from Exciton Inc. data sheets). Lasing experiments are to be carried out at Yale University in the lab of Prof. Hui Cao.

### 7.2.2 Additional Prospects for Lasing in Vogel Spirals

In addition to efforts towards Vogel spiral lasing in the near IR, a collaborative effort is underway to achieve lasing in Vogel spirals in visible wavelengths. In collaboration with Prof. Fiorenzo Omenetto's lab at Tufts University, nanopillar arrays of Vogel spirals have been designed to have strong scattering resonances at 550 nm. Differently from the previous study, the PMMA matrix will be replaced with a dye doped silk film. Silk fibroin, the natural protein produced by the *Bombyx mori* caterpillar, is an attractive material for applications in organic photonics and electronics (Omenetto and Kaplan, 2008). Silk has shown outstanding photonic properties, which include high transparency and easy structuring at the optical wavelengths. Optical components such as microlens arrays, waveguides and diffraction gratings have been demonstrated previously (Omenetto and Kaplan, 2008; Lawrence et al., 2008). In fact, the Omenetto group has previously demonstrated organic lasing from a blue-emitting stilbene doped silk film

spin-coated onto a one-dimensional distributed feedback grating (Toffanin et al., 2012).

In this study, Rhodamine 6G will be used as the laser dye gain medium. In previous studies (Parker et al., 2009), Rhodamine 6G has been successfully incorporated to produce functional silk printed optical waveguides. In this mixture, the Rhodamine 6G/silk film has a peak emission wavelength of 555 nm. 1  $\mu\text{m}$ -tall a-Si:H nanopillar arrays of GA-spirals,  $\alpha_1$ -spirals, and  $\beta_4$ -spirals have been fabricated with pillar diameters of 125nm and varying interparticle separations. Dark-field images of the  $\alpha_1$ -spirals with varying center-to-center separations are shown in Figure 7.24a.

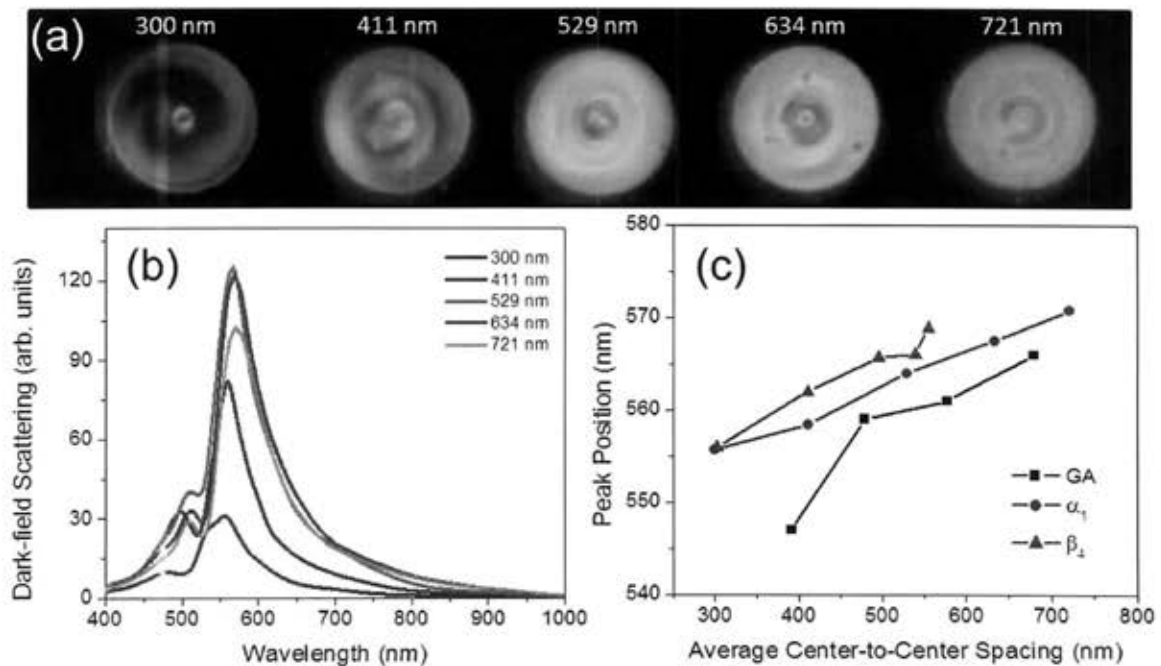


**Figure 7.24:** (a) Dark-field images of  $\alpha_1$ -spirals with increasing average center-to-center separations, labeled above each array. (b) Dark-field scattering spectra for  $\alpha_1$ -spirals shown in (a). (c) The peak scattering wavelength plotted as a function of average center-to-center spacing for the GA-spiral (black),  $\alpha_1$ -spiral (red), and  $\beta_4$ -spiral (blue).

The dark-field scattering spectra for  $\alpha_1$ -spirals shown in (a) are plotted in Figure 7.24b and the spectral peak position is plotted as a function of average center-to-center spacing for the GA-spiral,  $\alpha_1$ -spiral, and  $\beta_4$ -spiral. Notice the scattering resonance can be tuned through photonic coupling, similar to the shifting of a scattering resonance by changing the lattice constant in periodic structure, as shown in Figure 7.24c. The spiral nanopillar arrays scatter strongly in the same wavelength range of the Rhodamine 6G emission band-width. Samples are now being shipped to Tufts University for the spinning of the dye doped silk layer and subsequent lasing experiments.

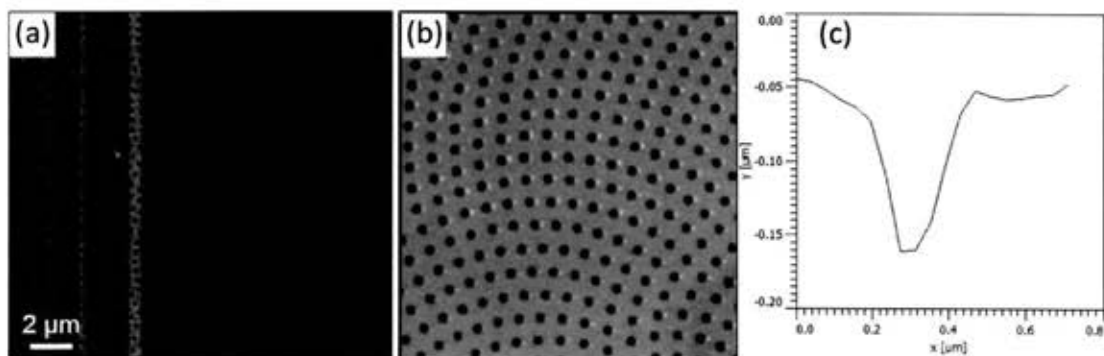


**Figure 7.25:** (a) SEM micrograph of directly EBL written GA-spiral hole array in a 120 nm-thick silk film. (b) AFM image of patterned film in (a). (c) AFM scan of single EBL written and developed hole in (a), showing hole depth through the entire silk film.

Lastly, in continued collaboration with Prof. Omenetto's lab, a process to directly write patterns via EBL has been co-developed with aims once more towards lasing in a silk film patterned with Vogel spiral geometries. Figure 7.25(a) shows a SEM micrograph of a 120 nm-thick film in which a GA-spiral pattern has been directly written into the film. Exposure dosages of  $1000 \mu\text{C}/\text{cm}^2$  are used to change the cross-linkage in the silk film. Subsequent development in DI water for 10 minutes removes the exposed silk.



Figure 7.25(b) plots a 2D AFM scan of the same film, while a 1D cut across hole is shown in 7.25(c). From the AFM image it is clear the holes are fully developed, reaching the depth of the full thickness of the silk film (120 nm). Continued work is ongoing at Tufts to incorporate additives to increase the index of refraction of the silk films, currently at  $n = 1.54$ .

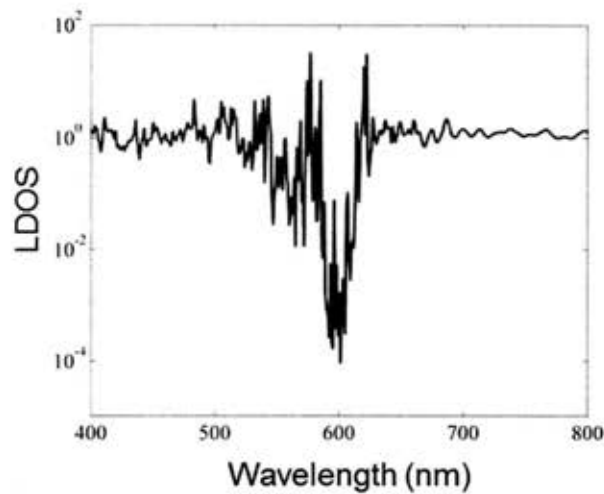


**Figure 7.26:** 2D FEM LDOS calculation at the center of a GA-spiral array with number of holes  $N = 1000$ ,  $r/a = 0.395$ , index of silk  $n_{\text{silk}} = 1.8$  and air holes  $n_{\text{air}} = 1$ .

Through 2D LDOS simulations, it has been determined the minimum index to support a photonic band gap is  $n_{\text{silk}} = 1.80$ . Figure 7.26 plots the 2D FEM LDOS calculation at the center of a GA-spiral array with the number of holes 1000,  $r/a = 0.395$ , index of silk  $n_{\text{silk}} = 1.8$  and air holes  $n_{\text{air}} = 1$ . The center of the gap is position at 600 nm and has several band edge modes on both sides of the gap, ideal for lasing in Rhodamine 6G. In the event the index can be increased beyond 1.80, the gap becomes even more pronounced and can be shifted to the desired wavelength range by adjusting the  $r/a$  ratio or equivalently the filling fraction.

### 7.3 Near-field Coupling and Scattering in Dielectric Vogel Spirals

The following section has been adapted from the 2013 New Journal of Physics publication titled *Near-field distribution and propagation of scattering resonances in Vogel spiral arrays of dielectric nanopillars* which can be referenced here (Intonti et al., 2013).

In this section, scanning near-field optical microscopy (SNOM) and full-vector FDTD simulations are used to investigate the near-field and propagation behavior of the electromagnetic energy scattered at  $1.56\ \mu\text{m}$  by dielectric arrays of SiN nanopillars with  $\alpha_1$ -spiral geometry. In particular, the spatial evolution of scattered radiation is studied and near-field coupling between adjacent nanopillars along the parastichies arms is demonstrated. Moreover, by measuring the spatial distribution of the scattered radiation at different heights from the array plane, a characteristic rotation of the scattered field pattern consistent with net transfer of OAM is demonstrated.

Controlled generation and manipulation of OAM states with large values of azimuthal numbers has been analytically modeled in Chapter 6 (Dal Negro, Lawrence and Trevino, 2012) and has recently demonstrated experimentally using various types of Vogel arrays of metal nanoparticles (Lawrence, Trevino and Negro, 2012), providing opportunities for the generation of complex OAM spectra using planar nanoparticle arrays. More recently, the interaction of optical beams with two-dimensional nanostructures of designed chirality became a topic of great interest from both a

fundamental and a technological standpoint due to the possibility to directly manipulate chiral effects in light-matter coupling by near-field engineering (Gorodetski et al., 2013).

### 7.3.1 Experimental Methods

The spiral nanopillar array fabrication process begins by depositing a 650nm-thick silicon rich nitride layer (SRN) by RF magnetron sputtering onto a silicon dioxide (SiO<sub>2</sub>) substrate. The standard EBL process described in Chapter 4 is used to define an array of 40 nm-thick Cr nanocylinders, to be used as an etch mask. RIE is used to transfer the pattern to the SRN, resulting in 350nm-tall SRN pillars, and leaving a 300nm SRN film beneath. The Cr mask layer is then removed by wet chemical etchant. The study utilizes  $\alpha_1$ -spiral array with diameter of 50  $\mu\text{m}$ , consisting of 1965 pillars each with individual pillar diameter of 520 nm. A scaling factor of 564 nm was used, resulting in an average nearest neighbor center-to-center spacing of 900 nm. The optical behavior of the  $\alpha_1$ -spiral is studied because it is an example of a deterministic chiral structure with an almost constant pair-correlation function, similarly to the case of random gases (Trevino, Liew, et al., 2012). As a result, the  $\alpha_1$ -spiral features a characteristic interplay between structural disorder and the well-defined CCW chirality that could potentially lead to novel wave diffraction and self-imaging phenomena. The A SEM micrograph of the fabricated  $\alpha_1$ -spiral is shown in Figure 7.27a showing that the structure is characterized by 21 parastichies arms.

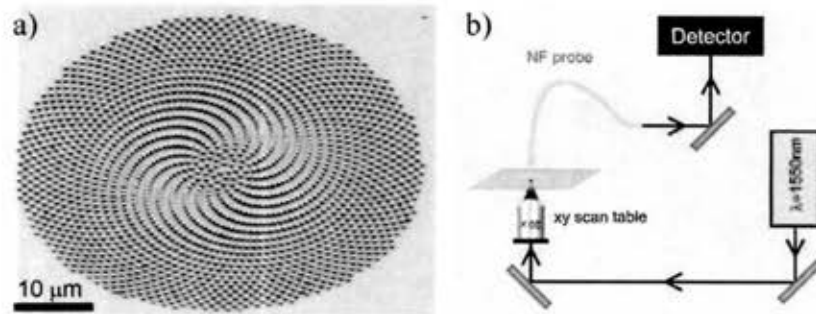


**Figure 7.27:** (a) SEM micrograph of  $\alpha_1$ -spiral nanopillar array with array diameter of 50  $\mu\text{m}$ , pillar diameter of 520 nm, and pillar height of 350 nm. (b) Scanning near-field optical microscope configuration with uncoated near-field probes in transmission geometry, excited with a diode laser ( $\lambda = 1556 \text{ nm}$ ).

Optical field measurements were performed with a commercial SNOM (TwinSNOM, Omicron) equipped with uncoated near-field probes in transmission geometry at the European Laboratory for Non-Linear Spectroscopy (LENS). The light from a diode laser ( $\lambda = 1556 \text{ nm}$ ) is focused on the back side of the sample with a 20x objective ( $\text{NA} = 0.4$ ) and the transmitted light is collected through the near-field probe, as shown in Figure 7.27b. The experiments are performed with two different laser spot dimensions. The first configuration, used for near-field measurements, maintains an optimal focus on the sample surface, resulting in a laser spot with a diameter of few microns. In this configuration, approximately 10 pillars are illuminated at a time. A second configuration used to take far-field measurements, utilizes a defocused laser beam to illuminate the entire spiral pillar array at once. The latter configuration contributes to the enhancement of interference effects in the far-field since each pillar acts as a scattering center and collective effects are more pronounced.

### 7.3.2 Results and Discussion

Using the SNOM setup discussed above, the spatial distribution of the optical intensity scattered by the fabricated  $\alpha_1$ -spiral at  $1.56 \mu\text{m}$  is experimentally investigated. Figure 7.28a displays the overall electric field intensity distribution of the  $\alpha_1$ -spiral with  $50 \mu\text{m}$  diameter obtained by connecting different near-field scans collected on  $20 \times 20 \mu\text{m}^2$  areas. From this image, a typical spatial resolution of  $250 \text{ nm}$  can be extracted. Figure 7.28b shows the spiral geometry extracted from the reassembled topography image, which is acquired simultaneously with the optical data. By comparing the reassembled optical image and the topography, near-field coupling is observed unambiguously between nanopillars along the parastichies arms.

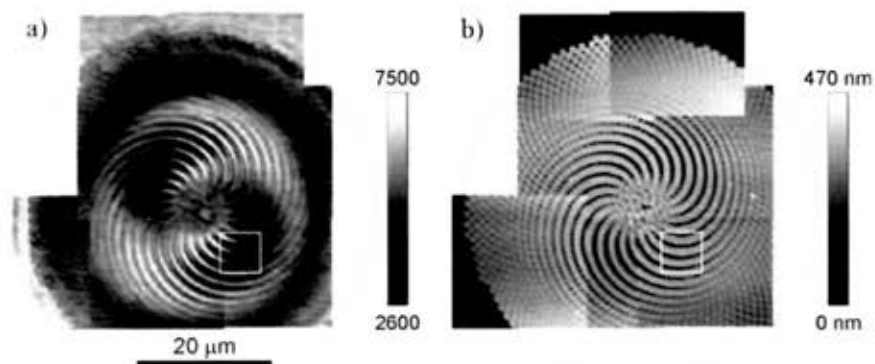


**Figure 7.28:** (a) Near-field optical map of an  $\alpha_1$ -spiral with  $50 \mu\text{m}$  diameter excited at  $\lambda = 1556 \text{ nm}$ , assembled by connecting multiple near-field scans collected on different  $20 \times 20 \mu\text{m}^2$  areas. Outer circle defines the position of outer array edge. (b) Topography map of  $\alpha_1$ -spiral acquired simultaneously with the optical data show in Figure 7.28a.

In order to accurately investigate where the transmitted optical intensity is concentrated, Figure 7.29 magnifies, both for the optical image and for the topography, the  $6 \times 6 \mu\text{m}^2$  region highlighted by the white squares in Figure 7.29. A direct comparison

of the optical distribution with the topographic image reveals that the transmitted signal originates from the top of the pillars forming parastichies arms and from the substrate region between two parastichies arms, highlighted by the corresponding white arrows in Figure 7.29. However, the highest field intensities are recorded near the top of the pillars forming the parastichies arms.

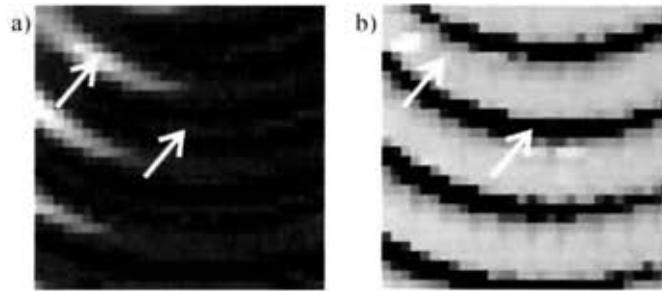


**Figure 7.29:** Magnified image of the (a) optical near-field and the (b) topography of the  $6 \times 6 \mu\text{m}^2$  region highlighted by the white squares in Figs. 7.28(a,b) respectively.

To better understand the near-field coupling effects within the parastichies, 3D FDTD simulations are carried out, using the Lumerical Solutions software package described in Chapter 3. The exact 3D geometry of the device was considered in the simulation. However, due to computational memory limitations, the spiral array was limited to the first 500 pillars. The device is placed on a  $\text{SiO}_2$  substrate and excited from the bottom (through substrate) by a plane wave at 1550 nm to match the experimental conditions as closely as possible. PML boundary conditions are used to terminate the simulation domain. To reduce the presence of the pump beam in the far-field plots the source contribution was subtracted from the simulation immediately above the array, leaving only the contribution of the scattered light.

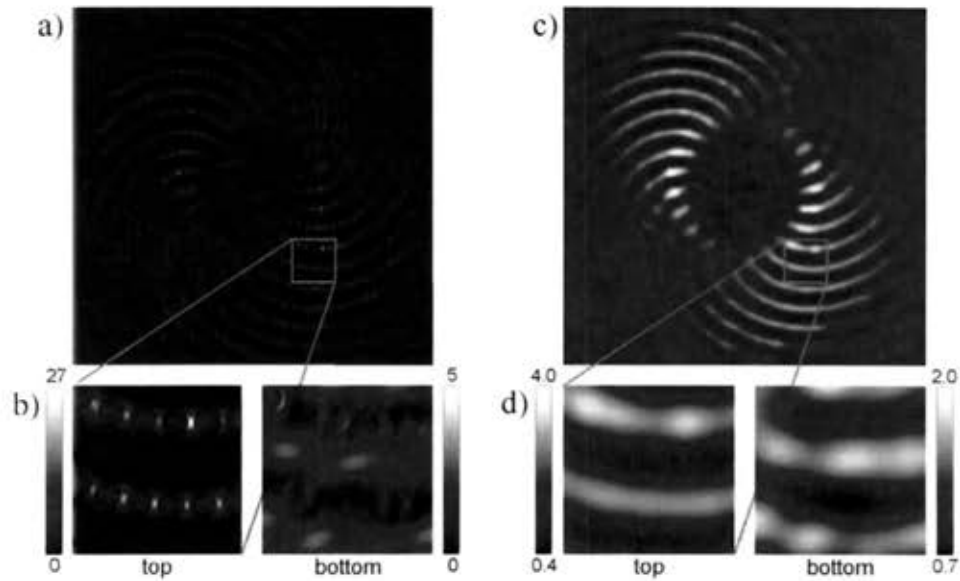


**Figure 7.30:** (a) Simulated (3D FDTD) electric field intensity distribution of the first 500 nanopillars of an  $\alpha_1$ -spiral, excited with a plane wave at  $\lambda = 1550$  nm. The electric field is plotted at the top surface of the nanopillars (b) Magnified plot measuring  $3.6 \times 3.6 \mu\text{m}^2$  of the region highlighted by orange box in Fig. 4a. The electric field distribution is plotted in the top plane (left) and bottom plane (right) of the nanopillars. The same field distributions of (a,b) are convolved with a Gaussian, characterized by a FWHM of 250 nm, and are plotted in (c,d) respectively.

Field monitors were placed in the device to measure the electric field intensity at the top and at the bottom of the nanopillars, as well as at various planes above the array in order to study the evolution of the field structure as it propagates in space away from the pillars plane. The results of the numerical simulations are summarized in Figure 7.30. Figure 7.30a shows the distribution of the electric field intensity sampled in the top plane of the pillars. Figure 7.30b displays a magnified area ( $3.6 \times 3.6 \mu\text{m}^2$ ), encircled by the orange box in Figure 7.30a and approximately corresponding to the central part of the region investigated in Figure 7.29. Both the electric field intensity at the top detector and the bottom detector are plotted in Fig. 7.30b. As observed experimentally in the SNOM measurements, the field intensity measured by the top detector is concentrated between

two subsequent pillars forming the parastichies, while in the bottom detector the signal mostly originates from the substrate plane. In Figures 7.30(c,d) the same field distributions of Figures 7.30(a,b) convolved with a Gaussian function are plotted, characterized by a FWHM of 250 nm, in order to take into account the finite spatial resolution of our experimental setup. It is evident that the main effect of the Gaussian convolution is to blur the images. After convolution, it is no longer possible to distinguish by analyzing the top detector that the signal is localized in the regions between two adjacent pillars. Nevertheless, it is still clear that the optical energy flows along the parastichies. On the contrary, when analyzing the data collected by the bottom detector we observe that the electric field intensity has a maximum on the substrate. It is also remarkable that, as a consequence of the Gaussian convolution, the electric field intensity maxima drop from 27 to 4 in the top detector and from 5 to 2 in the bottom detector, respectively. It follows that the comparison between the experimental and the calculated electric field intensity distributions is quantitatively very good, as it is clear by comparing Figure 7.29a with Figure 7.30d. Here the signal collected by the near-field probe on the parastichies should be associated with the top detector of the simulation, and the signal collected when the near-field probe reaches the substrate should be compared with the bottom detector.



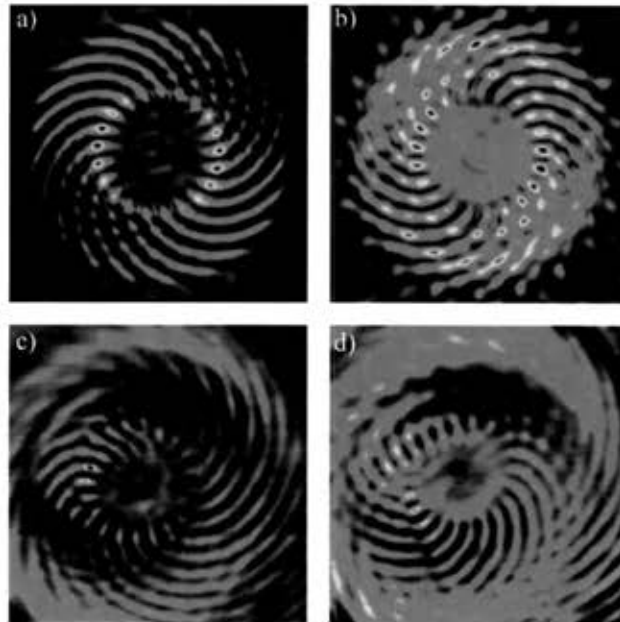


**Figure 7.31:** Numerical 3D FDTD calculations of the electric field intensity calculated with detectors placed at (a) 1  $\mu\text{m}$  and (b) 4  $\mu\text{m}$  above the  $\alpha_1$ -spiral.  $30 \times 30 \mu\text{m}^2$  area SNOM scans collected at a constant height modulus approximately (c) 2  $\mu\text{m}$  and (d) 6  $\mu\text{m}$  away from the sample surface, respectively.

In the following, the wave diffraction properties of the sample are addressed by studying the intensity distribution of the field scattered by the  $\alpha_1$ -spiral at different heights from the pillars array. Figure 7.31(a,b) show the numerical FDTD calculations of the electric field intensity calculated with a field monitor placed 1  $\mu\text{m}$  and 4  $\mu\text{m}$  above the  $\alpha_1$ -spiral, respectively. In Figures 7.31(c,d) the experimentally measured scattered fields are plotted, collected within a  $30 \times 30 \mu\text{m}^2$  region, and probed at a constant height of approximately 2  $\mu\text{m}$  and 6  $\mu\text{m}$  away from the sample surface, respectively. It is observed that at a distance of 1-2  $\mu\text{m}$  from the sample surface the spatial distribution of the electric field is characterized by the 21 curved arms associated with the parastichies that follow a CCW orientation, as seen in both measurements and calculations. However, by increasing the distance from the surface, the 21 curved arms are still unambiguously discernable but

now appear with a CW orientation, demonstrating a remarkable inversion in the optical intensity pattern along its propagation direction in free space. This interesting inversion of the propagating field pattern is observed both in the numerical calculations and in the experimental data. However, minor differences between the experiment and calculations results both from the uncertainty in the experimental determination of the height of the measuring plane and from the fact that the uncoated probe collects signal at slightly different heights. In fact, the SNOM setup used lacks calibration for determining the sample-to-probe distance when the probe is not in feedback.

To further explore the spatial evolution of the scattered field pattern as it propagates away from the pillars array, additional FDTD calculations have been carried out as function of the propagation distance and a video combining all the frames have been. The video can be found in the supplementary section of the following publication (Intonti et al., 2013). The supplementary video illustrates the evolution of the scattered field intensity as it propagates from the top plane of the pillars up to 8  $\mu\text{m}$  above the array plane in approximately 0.1  $\mu\text{m}$  vertical steps. Through the entire progression of vertical planes, the overall field pattern continuously passes from a CCW rotation to a CW rotation, observed unambiguously. The parastichy field components begin with a CCW orientation, exactly following in the near-field zone the geometry of the arms. However, as the plane of observation reaches approximately 3  $\mu\text{m}$ , the parastichies field pattern evolves into a mixture of both CCW and CW arms, slowly transitioning into purely CW arms when propagating in between the 4  $\mu\text{m}$  and the 8  $\mu\text{m}$  observation planes.

The distinct rotation of the scattered field intensity highlights the very rich dynamics of interacting scattered wavelets that transfer net orbital momentum to the overall radiation field in the intermediate Fresnel zone. The data in Figure 7.31 provide the first evidence of net OAM transfer occurring within few micrometers from the object in Vogel spiral arrays of dielectric nanopillars. In fact, while previous studies have focused on the rich spectrum of azimuthal OAM values transferred to the far-field radiation zone by Vogel spirals (Trevino, Cao and Dal Negro, 2011; Lawrence, Trevino and Negro, 2012; Dal Negro, Lawrence and Trevino, 2012), the complex wave diffraction effects that develop in the intermediate Fresnel zone remain to be explored.

In order to investigate the free propagation of the scattered field intensity over a larger range of distances, further studies were carried out; utilizing fractional Fourier transformation method. This approach provides an equivalent formulation of the paraxial wave propagation and Fresnel scalar diffraction theory (Ozaktas, Kutay and Zalevsky, 2001), and considers light propagation as a process of continual fractional transformation of increasing order. The study is not shown here, but can be found in the following reference (Intonti et al., 2013).

In this work, by using SNOM and 3D FDTD, the near-field coupling behavior and the propagation of electromagnetic energy distribution of scattered radiation from SiN based arrays of nanopillars with  $\alpha_1$ -spiral geometry have been investigated. In particular, the spatial distribution of scattered radiation at 1.56  $\mu\text{m}$  has been investigated and found to be in excellent agreement between numerical simulations and SNOM data,

demonstrating near-field coupling of dielectric pillars along the parastichies arms. Moreover, by measuring and computing the spatial structure of the scattered field at different heights from the array plane, the net orbital momentum transfer to the radiation field has been demonstrated.

## 7.4 Conclusions

In conclusion, the structural properties and photonic properties of dielectric based Vogel spiral arrays have been extensively investigated. Specifically, the photonic bandgap and band edge modes in Vogel spiral arrays of air cylinders in dielectric media and dielectric pillars in air. Despite the absence of long-range translational and rotational order, there exists a significant PBG for both TE (air holes in dielectric) and TM (dielectric pillars) polarized light. The upper and lower band edge modes can be categorized into different classes based on the field patterns. Due to spatial inhomogeneity in the spiral arrays, the band edge modes are localized within the rings of different radii via Bragg scattering from the parastichies in the spiral structure, and wrapped around azimuthally to form circular patterns, which carry the well-defined angular momenta. The band edge modes have discrete angular momenta that originate from different families of the parastichies whose numbers correspond to the rational approximates of the generating angle.

Additionally, dielectric nanopillar arrays of Vogel spirals have been successfully designed, fabricated, and experimentally shown to support PBGs near the emission wavelengths of commercial laser dyes. Several avenues are being further explored to

produce lasing action in a Vogel spiral array, including PMMA doped with an NIR laser dye and silk films doped with Rhodamine 6G, coupled to designed spiral arrays. Lastly, the near-field and intermediate field scattered radiation from a Vogel spiral has been investigated numerically and experimentally through FDTD simulations and SNOM. Near-field coupling of dielectric pillars along the parastichies arms and the net orbital momentum transfer to the radiation field have been demonstrated for the first time.

## Chapter 8

### 8 Optical Properties of Plasmonic Spirals

Up until this chapter, all prior studies have been limited to either point pattern or dielectric cylinder Vogel spiral arrays. This chapter will now explore plasmonic Vogel spiral arrays, including device applications. As discussed in Chapter 2, nanoplasmonics is the science of collective oscillations of metal conduction electrons, occurring at metal-dielectric interfaces, metal nanoparticles, or nanoparticles aggregates. Through the use of DANS structures with several spatial frequencies, individual LSPs can strongly couple by near-field quasi-static interactions, as well as by longer range diffractive coupling, giving rise to localized photonic modes. The interplay between these two coupling regimes offers a tunable approach to engineer photonic-plasmonic resonances in DANS, including Vogel spiral arrays (Dal Negro and Boriskina, 2011).

#### 8.1 Plasmonic Vogel Spirals

Segments of the this section have been adapted from the 2011 Nano Letters publication titled *Circularly Symmetric Light Scattering from Nanoplasmonic Spirals* which can be found here (Trevino, Cao and Dal Negro, 2011).

In this section Au nanoplasmonic GA-,  $\alpha_1$ -, and  $\beta_4$ -spiral arrays are explored by experimental dark-field micro-imaging, spectroscopy and rigorous multiple scattering based on the multi-particle GMT calculations. The section will focus on the radiative (i.e., diffractive) coupling regime, which is responsible for the formation of distinctive

structural resonances carrying OAM in the scattered radiation from Vogel spirals. In addition to its fundamental interest, the study of DANS with circular Fourier space provides access to the engineering of nanostructures giving rise to polarization-insensitive planar diffraction effects over large frequency bandwidths, suggesting a number of device applications such as compact circular polarization devices, optical biosensors, and enhanced thin-film solar cells.

As detailed in Chapter 4, the nanoparticle spiral arrays were fabricated using EBL on fused silica substrates. The examples of the three spiral types are shown in the SEM micrographs of Figure 8.1(a-f). All the metal particles are cylindrical in shape with a circular diameter of 200 nm and thickness of 30nm. A set of samples were fabricated with varying minimum interparticle separation (edge-to-edge), ranging between 90 nm and 680 nm and number of particles ranging between 8,000 and 33,058. This effort enabled a systematic study of the influence of the array geometry and dimensionality on the scattering properties. All the arrays were spaced on the chip by approximately 300  $\mu\text{m}$  in order to avoid undesired cross talk.

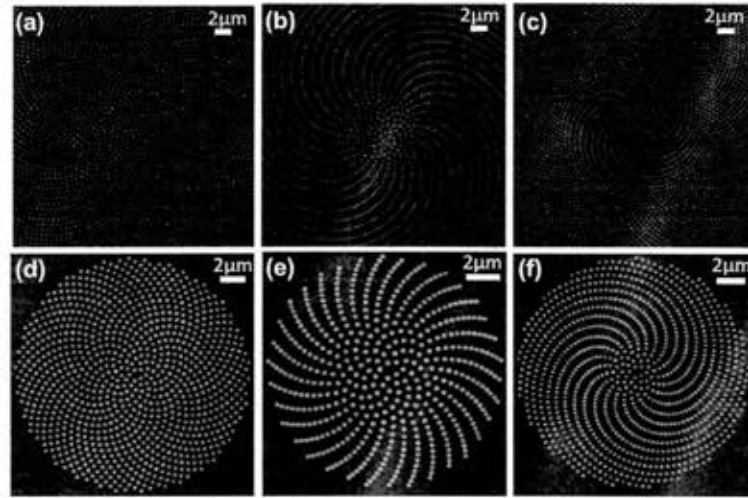


**Figure 8.1:** SEM micrographs of (a) GA-spiral, (b)  $\beta_4$ -spiral, (c)  $\alpha_1$ -spiral Au nanoparticle array. The arrays have 27,778 particles with a diameter of 200nm. SEM micrographs of (d) GA-spiral, (e)  $\beta_4$ -spiral, (f)  $\alpha_1$ -spiral Au nanoparticle arrays containing 1,000 particles with a diameter of 200nm. (g-i).

### 8.1.1 Fourier Space Analysis

As previously discussed in Chapter 6, one of the unique properties of Vogel spirals is their diffuse spectra with rotational symmetry (i.e., scattering rings), as predicted by their calculated Fourier transform (Trevino, Cao and Dal Negro, 2011). Such a Fourier space could enable polarization-insensitive light diffraction across a broad spectral range, providing a novel strategy for enhancing light-matter coupling on planar surfaces.

In order to experimentally demonstrate circular scattering from Vogel spirals, their Fraunhofer far-field intensity (i.e., the diffraction pattern) is directly measured. The results of the measured far-field intensity for the plasmonic GA-,  $\alpha_1$ -, and  $\beta_4$ -spiral arrays are shown in Figure 8.2(a-c).



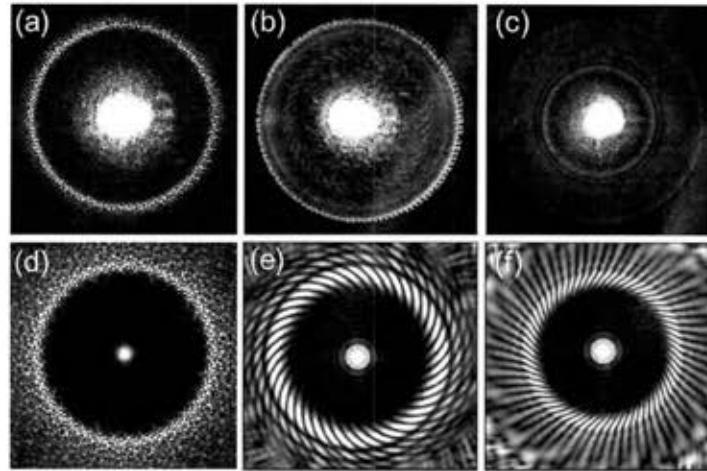


**Figure 8.2:** Measured Fraunhofer far-field intensity for the (a) GA-spiral, (b)  $\alpha_1$ -spiral, (c)  $\beta_4$ -spiral Au nanoparticle array. Calculated DFT of the same arrays, cropped down to the approximate reciprocal space area measured the (d) GA-spiral, (e)  $\alpha_1$ -spiral, (f)  $\beta_4$ -spiral.

The diffraction spectra reported in Figs. 2(a-d) were measured on a GA-spiral with 8000 Au nanoparticles, and generated with scaling factors of  $3 \times 10^{-7}$  m. The diffraction far-field patterns were measured using a HeNe laser ( $\lambda = 633$  nm) source. The transmitted light was collected with a 60x objective (N.A. = 0.85), collimated and focused by lenses with focal lengths of 150 mm and 100 mm respectively onto a CCD camera (Apogee Alta U4000 Camera w/KAI-4022 CCD). The captured far-field is determined by the NA of the objective, wavelength of the excitation, and size and spacing of the Au nanoparticles in the array. While the DC component of the scattered radiation is very intense and thus washes out some of the details of the far-field pattern, the diffuse and circular nature of the arrays is clearly observable. Figure 8.2(d-f) plots the calculated DFT for each array and is cropped down to the approximate reciprocal space area measured for reference. The experimental result confirms the presence of scattering rings in the far-field as predicted by scalar Fourier optics.

To experimentally demonstrate the circular scattering from Vogel spirals is indeed polarization insensitive, the Fraunhofer far-field intensity is measured at varying polarizations of the incident laser. The polarization of the incident beam was controlled by appropriate configurations of quarter and half-wave plates in the beam path. Figure 8.3 shows the measured Fraunhofer far-field of the GA-spiral using (a) Un-polarized, (b) circular polarized, (c) linear polarized ( $0^\circ$ ), (d) linear polarized light ( $60^\circ$ ). We observe that the vertical line common to all the diffraction spectra is an experimental artifact introduced by the CCD camera. We notice regardless of the polarization of the illumination the far-field maintains its structure, demonstrating the robustness of circular scattering to the polarization conditions.

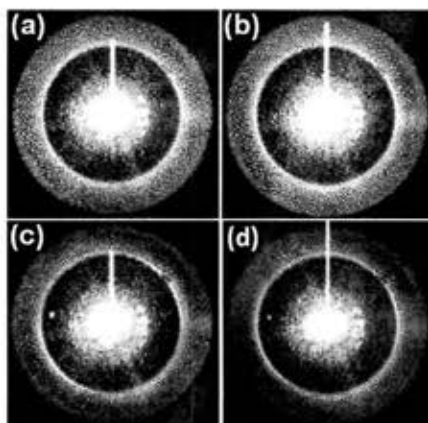


**Figure 8.3:** Experimentally measured far-field diffraction spectra of a g-spiral (8,000 particles) illuminated by a HeNe laser at 633nm, under different conditions: (a) Un-polarized, (b) circular polarized, (c) linear polarized ( $0^\circ$ ), (d) linear polarized light ( $60^\circ$ ). We observe that the vertical line common to all the diffraction spectra is an experimental artifact introduced by the CCD camera.

### 8.1.2 Dark-field Scattering Analysis

Using dark-field microscopy in the visible spectral range, the scattering properties of plasmonic spiral arrays fabricated with different interparticle separations are investigated. For this analysis, the structures consisted of GA-spirals with interparticle separations ranging from 312 nm to 568 nm, and  $\beta_4$ -spirals with separations from 220 nm to 430 nm. The results obtained on  $\alpha_1$ -spirals are very similar to the ones on  $\beta_4$ -spirals, which are therefore not shown here. Transmission scattering measurements were performed under incoherent white-light illumination using a dark-field microscope setup (Olympus, IX71) with a 10x long-working distance objective (NA = 0.3) coupled to a grating spectrometer and CCD detector (Andor, Shamrock 750). The incident angle of illumination was approximately  $15^\circ$  with respect to the normal to the array plane, and spatial filtering at the CCD detector was used for background noise reduction. The dark-field images of the samples were collected in the same microscope configuration by a CCD digital camera (Media Cybernetics Evolution VF). All the scattering spectra were background corrected by subtraction of the scattering signal from an equal-size, unpatterned area adjacent to each spiral. The scattering spectra were additionally corrected by the division with respect to the normalized emission line-shape of the excitation lamp (tungsten halogen bulb). In Figure 8.4(a-b) the corrected dark-field scattering spectra measured on GA-spirals and  $\beta_4$ -spirals are plotted, respectively.

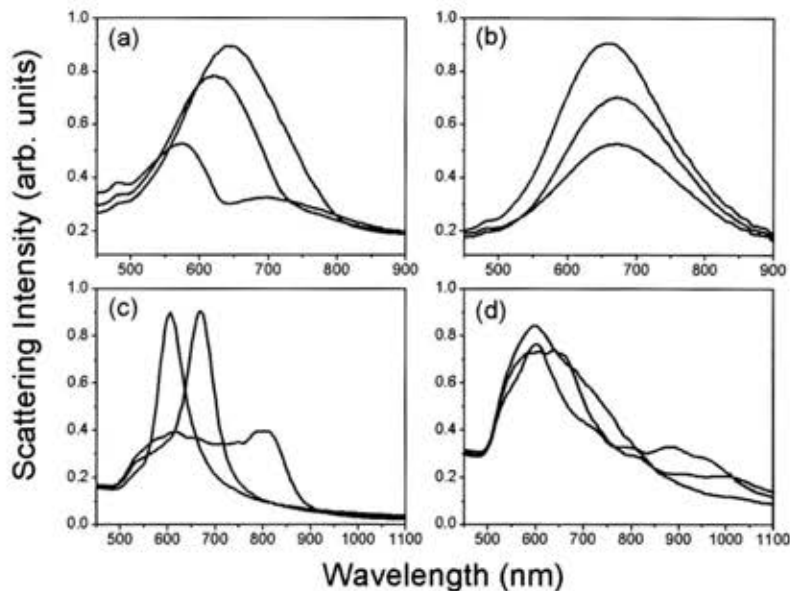


**Figure 8.4:** Measured dark-field scattering spectra of (a) GA-spiral with average interparticle separations  $d$  equal to: 312nm (black, 27,778 particles), 398nm (blue, 20,408 particles), 568nm (red, 12,346 particles). (b)  $\beta_4$ -spiral with average interparticle separations  $d$  equal to: 220nm (black, 27,778 particles), 290nm (blue, 20,408 particles), 430nm (red, 12,346 particles). (c) GMT calculated scattering efficiency of (c) GA-spiral (1,500 particles) and (d)  $\beta_4$ -spiral (1,500 particles) with average interparticle separations matching values in (a) and (b) respectively.

We remark that the GA-spiral, while lacking global periodicity, is “the most regular” among Vogel spirals and the measured scattering bands significantly red-shift with increasing interparticle separation. This behavior is analogous to what observed in the case of periodic plasmonic gratings (Meier, Wokaun and Liao, 1985; Carron et al., 1986), where scattering peaks red-shift due to the coherent contribution of diffraction (i.e., radiative) coupling. However, for all spirals, we found that the scattering spectra are significantly affected by higher order scattering modes developing in the 500 nm - 600 nm spectral range. These modes, which are weakly radiative in regular (i.e., periodic) media, are efficiently enhanced at multiple frequencies in structures with “broken symmetry” such as the aperiodic spirals (Hao et al., 2008; Kim et al., 2010). The red-shift

of the scattering bands is not observed for the more structurally inhomogeneous  $\beta_4$ -spirals because the dipolar modes are mostly outside our experimental range, as evident from the calculated cross sections shown in Figures 8.4(c-d). However, the spectral mixing of dipolar modes with higher order ones makes the  $\beta_4$ -spirals relatively insensitive to increasing interparticle separation (Figure 8.4d). The complex interplay between dipolar and higher order scattering modes has been previously observed in multi-scale aperiodic arrays with diffuse Fourier spectra generated by deterministic inflation rules (Gopinath et al., 2008).

To support the interpretation of the experimental results the rigorous multi-particle GMT is used for the electromagnetic modeling of light scattering. Being formulated in the complex domain, the GMT can be conveniently applied to study plasmonic structures with realistic material losses. In our calculations, the optical dispersion of Au nanoparticles was obtained by a spline interpolation of the Johnson and Christy dispersion data for Au (Johnson and Christy, 1972). Although the validity of the GMT calculation method is limited to clusters of spherical objects, it yields the full analytical solution of multi-particle scattering problems, efficiently providing valuable physical insights into the complex behavior of aperiodic systems (Gopinath et al., 2008; Gopinath, Boriskina, Premasiri, et al., 2009). Figure 8.4(c,d) shows the GMT-calculated scattering efficiencies obtained under linearly-polarized excitation at normal incidence on spiral arrays of 1500 nanospheres, 200 nm in radius. The calculated spectra correspond to GA-spirals and the  $\beta_4$ -spirals, respectively. In order to more clearly visualize the respective contributions of the dipolar versus higher order scattering modes we have

shown the calculated scattering spectra on a slightly larger wavelength range (i.e., from 450 nm - 1100 nm) compared to the corresponding experimental data, which are limited by the detector sensitivity range. These calculations fully confirm the important role played by radiative coupling effects in determining the scattering resonances of the dipolar modes of GA-spirals, which significantly red-shift with increasing interparticle separations. We notice that the calculated dipolar resonances of the GA-spirals are substantially narrower than what experimentally measured (Figure 8.4a). This discrepancy is attributed to the combined effects of the non-collinear nature of the dark-field excitation (limiting frequency resolution) and to the presence of the quartz substrate preventing efficient phase matching at the superstratum (Gopinath et al., 2008). On the other hand, no appreciable shifts and much broader scattering resonances are observed for the more inhomogeneous  $\beta_4$ -spirals (Figure 8.4d) due to the contribution of higher order modes appearing in the visible spectral range, in agreement with the experimental results shown in Figure 8.4(b).

### 8.1.3 Planer Diffraction in Vogel Spirals

A particularly attractive feature of these scattering resonances, which follows from the circular symmetry of the Fourier space, relies on the possibility of polarization-insensitive, planar diffraction of incident radiation at multiple frequencies, thus enhancing light-matter coupling phenomena in thin-film structures. In order to better visualize the effect of planar diffraction originating from the local spatial frequencies on the spirals surface, the fluorescence of a thin dye polymer layer coated on top of the Vogel spirals is directly imaged. For this experiment, a dye polymer solution is prepared

by dissolving common laser dye molecules of 4-Dicyanomethylene-2-methyl-6-p-dimethylaminostyryl-4H-pyran, also known as DCM (Exciton Inc.), in toluene. The dilute solution was then mixed with PMMA, spun onto samples and cured, resulting in 100 nm thick films of laser dye doped PMMA. This particular laser dye has maximum absorption at 480 nm and an emission peak at 640 nm, which overlaps the scattering resonances of  $\beta_4$ -spiral shown in Fig. 8.4(b). The sample was pumped by positioning the laser spot at different locations onto the doped PMMA substrate at normal incidence (focused through a 10x objective) with a laser diode at 480 nm and the emitted light was collected in transmission configuration through the substrate using a lens of 100 mm focal length, and imaged by a CCD camera. In order to capture only the emission patterns, the pump laser light was blocked by a 514 nm high-pass filter. An identically prepared emitting layer was also coated on unpatterned quartz for reference. Figure 8.5 shows the CCD images of the fluorescence collected in transmission through the reference sample when pumped at on its surface (Figure 8.5(a) and through a representative  $\beta_4$ -spiral at different locations (Figure 8.5(b-d)).



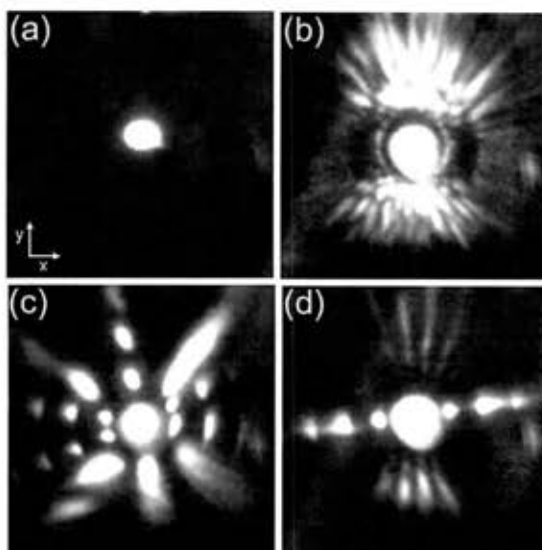


**Figure 8.5:** CCD image of light emission from a DCM dye layer (100 nm-thick) deposited onto: (a) homogeneous quartz substrate (b) dye emission from scattered light of  $\beta$ 4-spiral (27,778 particles) with laser positioned at the center of the spiral. (c) and (d) dye emission from scattered light of  $\beta$ 4-spiral with laser positioned off center of the spiral. The peak emission wavelength was 640 nm and the pump laser wavelength was 480 nm. Samples are pumped with the same power of 30mW.

The data in Figure 8.5(b-d) visibly demonstrate the spreading of the fluorescence signal in the plane of the spiral array, where a significant fraction of the intensity is emitted along multiple directions when the sample is symmetrically pumped through its center (Figure 8.5b). Additionally, we also observed that the angular distribution of the radiation changes dramatically when the position of the laser pumping spot is slightly misplaced (in the x-direction) from the center of the sample by approximately 25  $\mu\text{m}$  in Figure 8.5(c) and 50  $\mu\text{m}$  in Figure 8.5(d). This effect is due to the excitation of different spatial frequencies on the surface of the sample, which translates into vastly different angular spectra. On the other hand, when pumping the dye-doped reference sample (Figure 8.5a), the emission intensity remains well-confined within the pumping spot size of approximately 50  $\mu\text{m}$ . The effect reported in Figure 8.5 is a direct consequence of the



inhomogeneous distribution of local spatial frequencies associated to the surface of aperiodic spirals with circularly-symmetric Fourier space, and will be further analyzed in the next section.

#### 8.1.4 Circular Light Scattering in Vogel Spirals

The scattering resonances of Vogel spirals most strikingly manifest their characteristic circular symmetry when imaged in dark-field mode under white-light illumination. In Figure 8.6 the dark-field scattered intensity is imaged from the three types of Vogel spirals fabricated with three distinct values of scaling factors, corresponding to different interparticle separations. Each spiral is fabricated with a constant array diameter of 100  $\mu\text{m}$  (number of particles ranging between 8,264 and 33,058). In particular, Figures 8.6(a-c) corresponds to GA-spirals, Figures 8.6(d-f) to  $\alpha_1$ -spirals, and Figures 8.6 (g-i) to  $\beta_4$ -spirals of decreasing interparticle separations, from left to right.

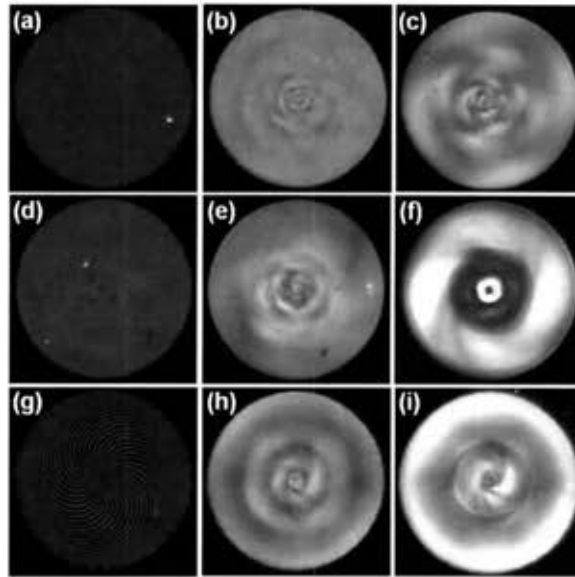


**Figure 8.6:** Dark-field microscopy images of plasmonic spirals on quartz substrates. The samples consist of GA-spirals (a-c),  $\alpha_1$ -spirals (d-f) and  $\beta_4$ -spirals (g-i) of varying (average) interparticle separations, as follows: (a) 1240 nm, (b) 565 nm, (c) 310 nm, (d) 918 nm, (e) 418 nm, (f) 242 nm, (g) 906 nm, (h) 298 nm, (i) 208 nm. All the nanoparticles are Au nanocylinders of 200 nm diameter and 30nm height.

We notice in Figure 8.6 that the dark-field images exhibit highly inhomogeneous spatial distributions of different chromatic components that critically depend on the spiral geometry as well as the minimum interparticle separation. When the interparticle separation is decreased, diffractive coupling effects become more significant and fascinating structural resonances are observed in Figure 8.6. Interestingly, it is observed that the  $\alpha_1$  and  $\beta_4$ -spirals (Figure 8.6f,i) display scattered patterns with a remarkable degree of circular symmetry at the wavelengths matching the local spatial frequencies of the structures. When illuminated by white light, each scattering ring efficiently diffract light of different wavelengths in the array plane, as observed in Figure 8.5. This effect is less pronounced in the GA-spirals due to their higher degree of structural uniformity manifested by the presence of only one broad scattering ring in Fourier space. To further

understand the physical nature of these complex structural resonances, band-pass filters are utilized to collect dark-field scattering images at specific wavelengths, as shown in Figure 8.7(a-c) for the  $\alpha_1$ -spiral. We notice that similar results can be obtained for all the structures (as shown in Figure 8.6), and therefore following analysis is limited to the  $\alpha_1$ -spiral for convenience.

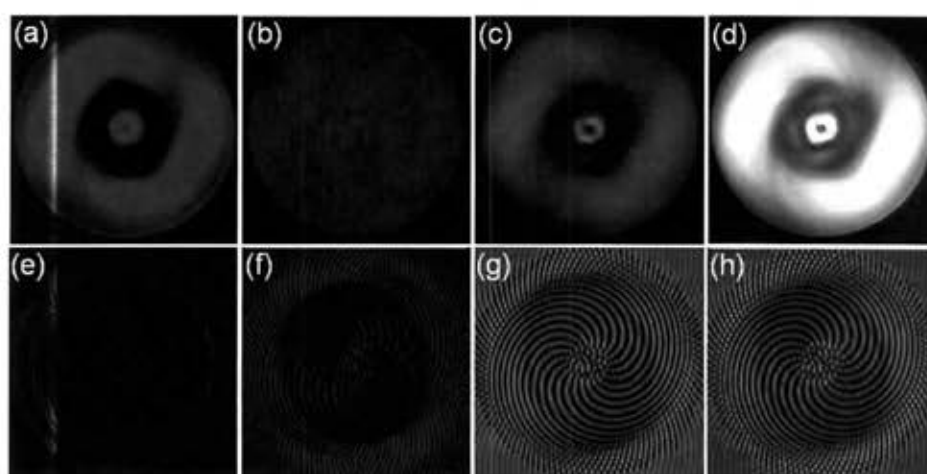


**Figure 8.7:** (a-c) Wavelength filtered (a: 585 nm long pass, (b) 360-460 nm band pass and (c) 490 nm – 560 nm band pass) dark-field images of an  $\alpha_1$ -spiral with particle diameter of 200 nm and average separation of 242 nm. (d) dark-field image under white light illumination and unfiltered detection. (e-g) GMT calculated electric field amplitude at (f) 475 nm, (g) 510 nm, (e) 650 nm (h) incoherent sum (intensity addition) of the three scattering profiles e-g. All simulated arrays have 1,500 particles with a diameter of 200 nm.

The dark-field images of Figure 8.7(a-c) were collected in the same configuration as in Figure 8.6, using red, blue and green band-pass filters in front of the CCD camera. In Figure 8.7(d) the unfiltered dark-field image of the same spiral is shown. We notice that the chromatic components shown in Figures 8.7(a,c) share similar spatial patterns and give rise, when superimposed, to the outer diffraction corona observed in Figure 8.7(d). On the other hand, the more homogeneous intensity distribution of the scattered

component in Figure 8.7(b) is responsible for the formation of the inner diffraction corona observed in Figure 8.7(d). These data experimentally demonstrate that the distinctive structure of spatial frequencies associated to the inhomogeneous particle arrangements of the  $\alpha_1$ - and  $\beta_4$ -spirals diffract incident radiation into a number of circularly-symmetry scattering resonances. All the previous experimental results are consistent with GMT calculations of the near-field intensity distributions, in the plane of the array, for the corresponding spirals. The simulations have been performed under a linearly-polarized plane wave excitation at normal incidence. Figure 8.7(e-g) shows the calculated electric field magnitudes for individual wavelengths of  $\lambda_R = 650$  nm (e),  $\lambda_B = 475$  nm (f),  $\lambda_G = 510$  nm (g), while in Figure 8.7(h) the superposition of the intensity patterns corresponding to the three previous wavelengths is plotted (Gopinath et al., 2008). All the calculations refer to an  $\alpha_1$ -spiral array with 1,500 particles of 200 nm diameter and average interparticle separation of 242 nm. The qualitative agreement between single color and polychromatic scattering data and dark-field images is only limited by computational power that forces a restriction of the simulation area to  $\sim 1/5$  of the experimental array size. However, it should be noted that the GMT simulations well captures the physical picture behind the formation of dark-field scattering images in these large systems, and indicate that these effects are robust with respect to the total number of particles in the spirals.

### 8.1.5 Angular Momentum in Plasmonic Vogel Spirals

It is interesting to note that the dark-field images of Vogel spirals shown in

Figures 8.6 and 8.7 are consistent with the formation of a vortex-like intensity distribution spiraling towards the center of the images. In order to rigorously demonstrate that circularly-symmetric scattering resonances in Vogel spirals can indeed carry orbital angular momentum, a more detailed GMT analysis of the scattered fields is performed. In particular, the spatial distributions of the scattered electric field intensity are calculated at different vertical positions from the array plane. Additionally, the azimuthal components of the electromagnetic linear momentum, which directly conveys information of the angular momentum, are calculated (Andrews, 2008). The analysis is performed on a  $\beta_4$ -spiral with geometric parameters as in Figures. 8.5 and 8.6 (i), as this particular spiral has been previously investigated in relation to planar diffraction. For this reason, the calculations are carried out at 480 nm and 650 nm, previously utilized as pumping and fluorescent wavelengths in the fluorescence diffraction experiment. In what follows, only the results corresponding to the 650 nm excitation will be shown in the interest of conciseness. However, we notice that a similar physical picture also emerged from the simulations performed at 480 nm. In Figures 8.8(a-c) the scattered intensity profiles calculated at 1  $\mu\text{m}$ , 3  $\mu\text{m}$ , and 10  $\mu\text{m}$  from the plane of the array are plotted. In each case, the array was homogeneously excited at normal incidence by a plane-wave.

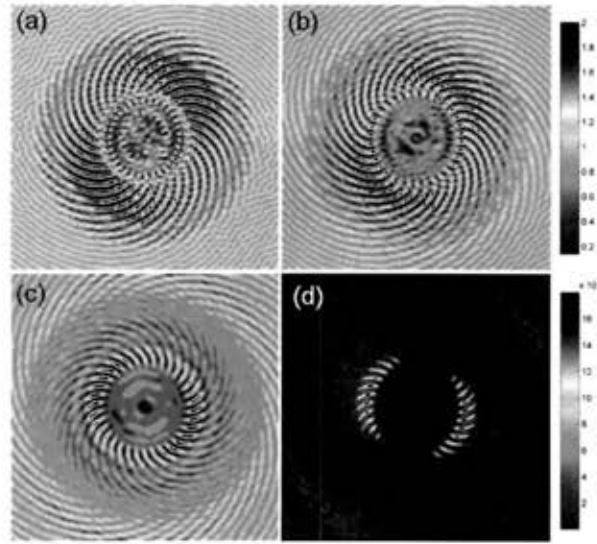


**Figure 8.8:** Analytical GMT simulations of an  $\beta_4$ -spiral. Simulation consists of 1500 Au spheres of diameter 200 nm excited with a plane wave  $\lambda = 650$  nm. Scattered intensity profiles calculated at (a) 1  $\mu\text{m}$ , (b) 3  $\mu\text{m}$ , and (c) 10  $\mu\text{m}$  from the plane of the array. (d) magnitude of the azimuthal-component of the linear momentum density of the scattered electromagnetic field at 10  $\mu\text{m}$  above (time average Poynting vector normalized to  $c^2$ ).

It is evident from Figures 8.8(a-c) that the scattered intensity patterns rotate clockwise as they propagate away from the array plane. The interaction of the incident plane wave with the spiral structures transfers net orbital momentum to the scattered radiation. This effect is demonstrated in Figure 8.8(d) where the azimuthal component  $p_\phi$  of the linear electromagnetic momentum density is plotted. The linear momentum density is obtained by calculating the ratio of the time-averaged Poynting vector  $S$  with the square of the free-space velocity of light (Andrews, 2008). It is known that the  $p_\phi$  component of the linear momentum density is directly related to the angular momentum density of a free beam that propagate along the vertical  $z$  axis (the spiral arrays lie in the horizontal  $x$ - $y$  plane) by the linear relation (Andrews, 2008):

$$J_z = r p_\phi \quad (8.1)$$

where  $r$  is the position vector. The results shown in Figure 8(d) provide a rigorous justification to the angular momentum transfer associated to the excitation of the circularly-symmetric scattering resonances in nanoplasmonic spirals. It is worth mentioning that phase plates with spiral patterns have been previously utilized for the generation of free-space Laguerre Gaussian modes at millimeter-wave frequencies (Turnbull et al., 1996). No prior reports, to the best of our knowledge, of compact plasmonic nanostructures capable of encoding orbital angular momentum at optical frequencies onto a transmitted plane wave have been reported. The engineering of optical vortices in miniature-size chips is another exciting feature of aperiodic nano-spirals that can result in compact polarization devices for on-chip nanoplasmonics and optical trapping applications.

## 8.2 Thin-film Solar Cell Enhancement

In this section, a brief review of photovoltaics will be provided, leading to motivation for the reduction of active absorbing materials used and the need for novel light-trapping schemes. Nanoplasmonic Vogel spiral arrays will be presented as possessing unique scattering properties that make them ideal structures for the broadband performance enhancement of thin-film solar cells. The segments of the following section have been adapted from the 2012 Optics Express publication titled *Plasmonic-photonic arrays with aperiodic spiral order for ultra-thin film solar cells* and can be found here (Trevino, Forestiere, et al., 2012)

### 8.2.1 Photovoltaic Principles

Photovoltaics (PV) is the conversion of incident radiation to an electrical current in a material. PV power generation utilizes a number of solar cells containing these PV materials, fixed together to create large solar panels. Solar cell technology has long been championed as the most feasible route for reduction of nonrenewable power consumption and minimization of the carbon footprint of power generation. Si has long been the most widely used material for PV cells. Over the last half decade, commercial Si PV has reached sunlight to electricity conversion efficiencies of approximately 25% (Kazmerski and Margolis, 2010). However, large-scale implementation is currently not economically feasible because of the high cost as compared to traditional power sources. One of the primary sources of cost for Si PV cells is the starting Si wafer, which requires extensive purification and relatively thick absorbing layers (100 $\mu\text{m}$ -300 $\mu\text{m}$ ) to maintain reasonable performance (Atwater and Polman, 2010). As a result, much effort has recently been made to reduce the material quantity requirements and in parallel, to find alternative PV materials which can be mass produced at a lower cost.

Photovoltaic energy conversion is the production of electrical energy in the form of current and voltage directly from electromagnetic radiation. The term photovoltaics can literally be translated as light-electricity, originating from the Greek word (phōs) for light and volt, referring to the unit of electro-motive force. The first step of PV energy conversion involves the absorption of photons, causing a transition in a material from a ground state to an excited state. The cross section of a simple Si PV cell, Figure 8.9a,



along with its corresponding band diagram in Figure 8.9b is shown to illustrate this process.

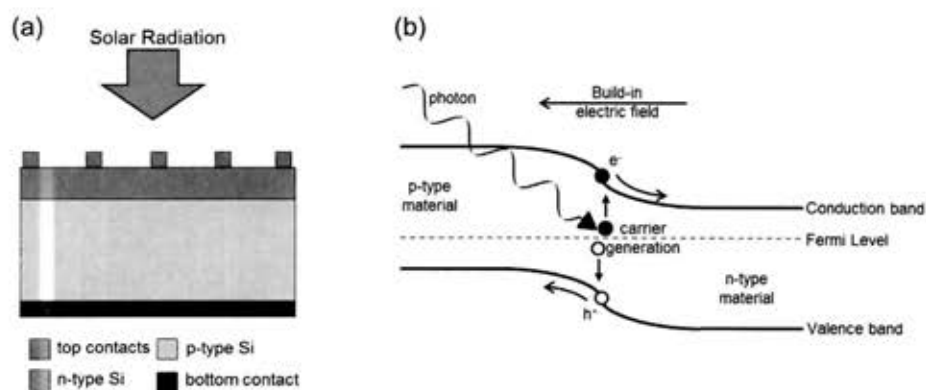


**Figure 8.9:** (a) The basic scheme of a crystalline Si solar cell. (b) Band diagram of the photovoltaic effect in a p-n junction device, where a photon generates a photon-hole pair which is swept out due to the presence of an electric field.

If the photon absorbed possessed sufficient energy, the excited state is converted into a free negative- and positive-charge carrier pair. A discriminating transport mechanism, in this case a p/n junction induced electric field or "built-in" electric field, causes the resulting free negative-charge carriers to move in one direction towards a cathode and the free positive-charge carriers to move in another towards an anode. The negative-charged carriers arrive at the cathode, resulting in electrons that are free to travel through an external electrical circuit. Along the path, their energy can then be used at an electrical load, such as a light bulb or energy storage device. Lastly, they return to the anode where they recombine with positive-charged carriers, thus returning the absorber to the ground state.

At its present state, PV cells can be broken into two categories: crystalline Si (c-Si) and thin-film. The c-Si category is commonly referred to as the first-generation PV,

included monocrystalline and multicrystalline PV cells, which dominate the current PV market. The thin-film, called second generation PV, includes cells consisting of extremely thin layers of semiconductor material such as a-Si, copper gallium indium diselenide ( $\text{Cu(In,Ga)Se}_2$ ) or CIGS, cadmium telluride (CdTe) and Gallium arsenide (GaAs). A third-generation of PV cells has recently gained strong interest from the research and industry communities, consisting of dye-sensitized, organic and quantum dot based materials.

### 8.2.2 Plasmonics for Thin-film Enhancement

As previously mentioned, the current solar cell market is predominantly based on crystalline silicon (c-Si) wafers with absorbing layer thickness in-between  $100\mu\text{m}$ - $300\mu\text{m}$  to guarantee complete light absorption and effective carrier collection. The main disadvantage of this technology is high production costs, resulting from a requirement of large amounts of highly purified silicon feedstock and significant processing costs. To make photovoltaics competitive with fossil-fuel technologies, the cost of traditional solar cells must be reduced by a factor of 2-5 (Atwater and Polman, 2010). These factors have driven recent work in second and third generation solar cell technologies, such as thin-films of non-crystalline Si (amorphous or poly-crystalline) (Nelson and Ratner, 2004; Green, 2003) and nanocrystalline Si (Si-ncs) structures (Song et al., 2008). These materials can be fabricated with strongly reduced thermal budgets, costs and with much larger volumes compared to traditional Si wafers. However, their shorter diffusion lengths (limited by defects and grain boundaries) restrict the active cell thicknesses to a

few hundreds of nanometers, severely decreasing the probability of photon absorption. This has recently motivated the search for advanced photon recycling and light-trapping schemes capable of increasing the optical paths of photons, and therefore the absorption probability, in ultra-thin film solar cells ( $< 200$  nm-thick) (Nelson and Ratner, 2004; Ferry et al., 2009).

Very promising approaches have been developed including the incorporation of metal-dielectric nanostructures into or atop ultra-thin film solar cells for a more efficient coupling of incident solar radiation or to achieve resonant enhancement of absorption cross-sections. Engineered nanostructures for enhanced absorption have recently been investigated in several different configurations, including nanoparticles, nanowires, photonic crystals, and random texturing (Kelzenberg et al., 2010; Ferry et al., 2008; Biswas et al., 2010; Haase and Stiebig, 2007). In particular, recent studies have shown that metal nanostructures can lead to effective light trapping into thin-film solar cells improving the overall efficiency due to the enhancement of optical cross-sections associated to the excitation of LSP modes (Ferry et al., 2010).

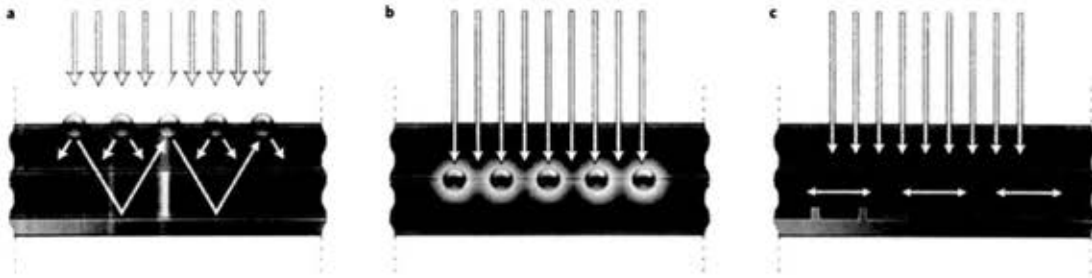


**Figure 8.10:** Plasmonic light-trapping schemes for thin-film solar cells. (a) Light trapping by scattering from metal nanoparticles at the surface of the solar cell. (b) Light trapping by the excitation of localized surface plasmons in metal nanoparticles embedded in the semiconductor. (c) Light trapping by the excitation of surface plasmon polaritons at the metal/semiconductor interface.

Figure 8.10 illustrates the three most common light-trapping techniques utilized in thin-film solar cells as illustrated by Atwater and Polman in a seminal review article (Atwater and Polman, 2010). Figure 8.10a show a configuration where the plasmonic particles are placed at the surface of the solar cell, utilizing multiple and high-angle light scattering preferentially into the semiconductor thin-film and causing an increase in the effective optical path length in the cell (Stuart and Hall, 1998; Beck, Polman and Catchpole, 2009). Second, metallic nanoparticles are used as sub-wavelength antennas in which the plasmonic near-field is coupled to the semiconductor, increasing its effective absorption cross-section (Figure 8.10b). Lastly, shown in Figure 8.10c, a back metallic surface of cell is patterned to couple light into propagating SPP modes supported at the metal/semiconductor interface as well as guided modes in the semiconductor slab.

This plasmonic-enhanced light absorption effect has been demonstrated using periodic arrays of Au or Ag nanoparticles, which give rise to best enhancement in the spectral regions where evanescent diffraction grating orders spectrally overlap the broader LSP resonances characteristic of metallic nanoparticles. However, polarization

sensitivity and the narrow frequency range for effective photonic-plasmonic coupling in periodic grating structures inherently limit these approaches. In order to broaden the spectral region of enhancement, it is crucial to engineer aperiodic nanoparticle arrays with a higher density of spatial frequencies without resorting to uncontrollable random systems, which have only limited engineering appeal. To overcome these limitations, recent studies have proposed to utilize plasmonic arrays with aperiodic quasicrystal structures, such as Penrose lattices, which exhibit non-crystallographic rotational symmetries (Ostfeld and Pacifici, 2011; Ferry et al., 2011). Such arrays, by virtue of their higher degree of rotational symmetry as compared to traditional periodic structures, give rise to enhanced scattering along multiple directions and over a broader wavelength range.

In this study, periodic and GA-spiral arrays of Au nanoparticles are designed and fabricated for the enhancement of an ultra-thin-film Schottky photo-detector. In particular, the spatial frequencies of GA spiral arrays are engineered to obtain large-angle and broadband light scattering and experimentally demonstrate that these novel plasmonic structures produce larger photocurrent enhancement in the 600nm-950nm spectral range compared to optimized nanoparticle gratings. The experimental results are supported by calculations of radiation diagrams based on the CDA and by absorption enhancement numerical analysis based 3D FDTD simulations.

### 8.2.2 Plasmon-enhanced Large-Angle Scattering

As previously shown in Chapters 6, the GA-spiral's distinct scattering ring

corresponds to the dominant spatial frequencies of the structure (Trevino, Cao and Dal Negro, 2011; Pollard and Parker, 2009). Additionally, it has been detailed that the scattering ring in a GA-spiral scales approximately one-to-one with the average center-to-center interparticle separation in the array (Trevino, Cao and Dal Negro, 2011; Pollard and Parker, 2009). This simple linear scaling law is critical to engineering the spectral location of planar omnidirectional diffraction in GA-spirals for increased photonic-plasmonic coupling. A simple scalar Fourier optics picture already suggests that polarization-insensitive large-angle scattering of incident radiation should occur in GA-spiral arrays at frequencies matching the radial position of the scattering ring in reciprocal space (Trevino, Cao and Dal Negro, 2011).

The relation between the spatial Fourier spectrum of GA arrays of Au nanoparticles and the large angular distribution of scattered radiation in the forward scattering hemisphere is now discussed. This will be accomplished by rigorously calculating the angular radiation diagrams within the CDA. In our formulation (C. Forestiere et al., 2009), the numerical method considers the particles of the array as ellipsoidal particles described by a single electric dipole contribution whose polarizability is a function of the ellipsoidal axis. The CDA is particularly suited to efficiently treat large-scale plasmonic systems made of small and well separated nanoparticles, and it has been previously validated against semi-analytical multiple scattering methods (Carlo Forestiere, Giovanni Miano, et al., 2009) used to describe complex nanoparticle arrangements (Carlo Forestiere, Gary F Walsh, et al., 2009). In this study, all calculations are performed assuming Au nanoparticles with metallic dispersion modeled according to

Johnson-Christy data (Johnson and Christy, 1972). All nanoparticles were modeled by oblate spheroids with 100 nm diameter and a height of 30 nm. Moreover, the arrays are embedded in Si and are excited by a linearly polarized plane wave normally incident on the array.

The parameter of interest for the understanding of angular scattering in complex plasmonic arrays is the differential scattering cross section (Bohren and Huffman, 1998; Lee et al., 2011), which describes the angular distribution of electromagnetic power density scattered at a given wavelength within a unit solid angle centered around an angular direction  $(\theta, \phi)$  per unit incident irradiance. In the case of arrays composed of dispersive metal nanoparticles, the power scattered from a particular structure is in general a function of both the geometrical parameters of the array and the wavelength of the incident radiation. Full information on angular scattering is thus captured by calculating the averaged differential scattering cross section, where the average is performed on the azimuthal angle  $\phi$  and the scattered intensity is normalized to the maximum value (i.e., forward scattering peak). By plotting the azimuthally averaged differential scattering cross-section versus the inclination angle, we obtain the radiation diagrams of the arrays. In Figures 8.11(a,b) we show the calculated radiation diagrams for periodic and GA arrays at three different wavelengths  $\lambda_B=480$  nm,  $\lambda_G=550$  nm and  $\lambda_R=610$  nm (i.e corresponding to the blue, green, and red colors), respectively.



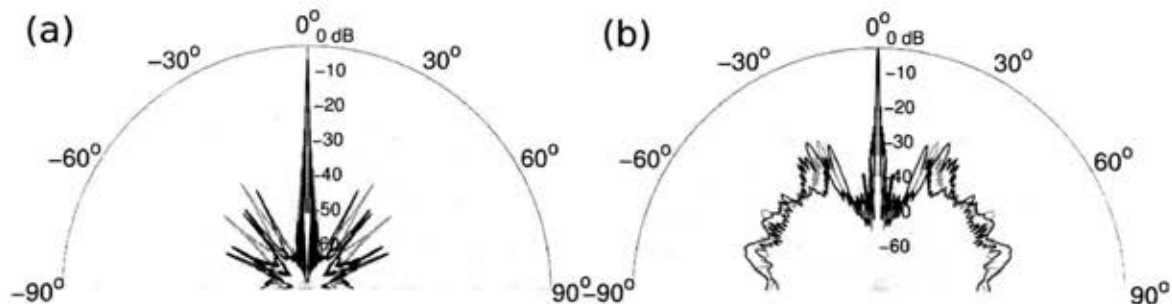


**Figure 8.11:** Calculated radiation diagrams as a function of the inclination angle ( $\theta$ ) for a periodic array with  $N=3505$  (a) and a GA-spiral with  $N=1810$  (b) for three different wavelengths, namely 480 nm (Blue), 520 nm (Green), and 650 nm (Red). The periodic array has a lattice spacing of 300 nm, the GA-spiral features an averaged minimum interparticle separation of 420 nm. (The interparticle separations in both cases results from the experimental optimization performed in 8.2.5)

The radiation diagrams are plotted in dB scale for a periodic array (Figure 8.11a) and a GA-spiral (Figure 8.11b) of the same linear dimension  $D = 20 \mu\text{m}$ . The periodic array contains  $N = 3505$  nanoparticles with 300 nm lattice spacing, while the equivalent-size GA-spiral has  $N = 1810$  with 420 nm averaged minimum inter-particle separation. The results in Figure 8.11(a) illustrate how the radiation diagram of the periodic nanoparticle array is dominated by coherent interactions (Bragg scattering) along certain well-defined scattering directions corresponding to the grating orders of the grating. On the other hand, the angular scattering of GA arrays (Figure 8.11b) is significantly broadened at large angles (i.e.  $>30^\circ$ ) for all the investigated wavelengths, demonstrating the large-angle scattering. We expect that the phenomenon of plasmon-enhanced broadband large-angle scattering demonstrated for GA-spiral arrays should redirect a larger fraction of the incident radiation into the absorbing Si substrate, thus effectively increasing the optical path of photons in the photodetector, and also enhance the coupling



to LSPs in the array plane. This picture will be fully supported by the experimental results discussed in the following sections.

### 8.2.3 Array Parameter Design for Photocurrent Enhancement

In this section, the design of the geometrical parameters of a periodic array of nanocylinders to enhance light absorption inside the Si substrate is presented. Numerical simulations of periodic arrays of nanoparticles were performed in order to estimate the absorption enhancement, using a 3D FDTD method in the LUMERICAL software package. Unfortunately, due to the large amount of nanoparticles involved, a similar analysis for GA-spiral structures cannot be performed due to their lack of translational symmetry. Therefore, GA-spirals have been fabricated and tested with a large range of interparticle separations, including the ones overlapping with the optimized parameters identified here for periodic gratings. Consequently, the better performances experimentally demonstrated for GA-spiral arrays in Section 8.2.5 result from an experimental optimization of array parameters (i.e., interparticle separation) and those results should not be regarded as the theoretical limit of absorption enhancement achievable in Si with GA-spiral arrays.

In the case of periodic arrays, the modeling of the plasmon-enhanced photodetector is obtained by considering the three-dimensional unit cell shown in Figure 8.12(a). This cell is composed of a silicon substrate in air with a cylindrical Au nanoparticle directly on top. Periodic boundary conditions have been imposed on the lateral sides of the simulation box (blue dashed lines) while PML boundary conditions

were used on the top and at the bottom sides (red dashed lines). The nanocylinder dimensions have been optimized with a 100 nm radius and 30 nm thickness, using realistic dispersion data for Au (Palik, 1998). The device is excited from the air side by a linearly polarized plane wave propagating at normal incidence. The absorption of light inside the metallic nanoparticles is obtained by calculating the net power flux through a closed box surrounding the particle in Figure 8.12(a) (Mokkapati et al., 2011). On the other hand, the absorption of light in the Si substrate was determined by the difference between the input and output power flows in a 50 nm-thick absorbing layer (black dashed lines). The net absorption enhancement due to the presence of the metal nanoparticle array is finally calculated by dividing the fraction of absorbed light into the 50nm-thick silicon substrate in the presence of the plasmonic particles and the absorption into the silicon layer in the absence of the plasmonic particles.

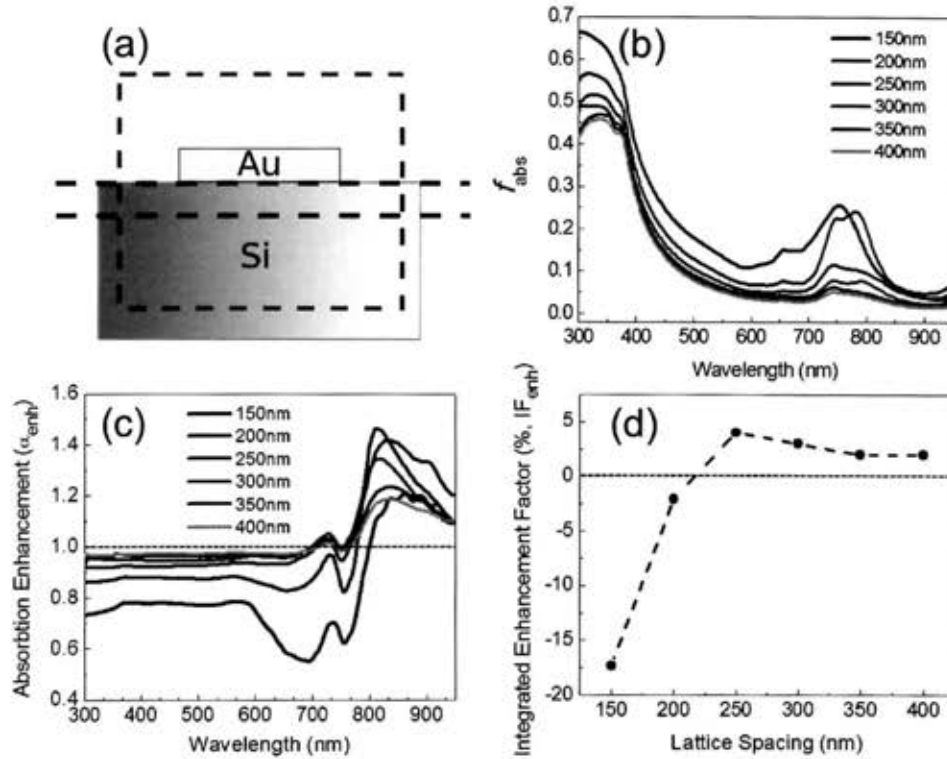


**Figure 8.12:** (a) Schematic cross section (not to scale) of the performed FDTD simulations. The red and blue dashed lines indicate the limits of the simulation box where PML boundary conditions and periodic boundary conditions are enforced, respectively. The black dashed lines are the monitors where power fluxes are calculated. (b) Fraction of the incident power absorbed into a periodic array of gold nanocylinders ( $D=100\text{nm}$ ,  $h=30\text{nm}$ ) and on a  $50\text{nm}$  thick Silicon substrate, calculated with FDTD. Predicted absorption enhancement within a  $50\text{nm}$  thick Si substrate due to a periodic array of gold nanocylinders ( $D=100\text{nm}$ ,  $h=30\text{nm}$ ) with respect to the bare substrate (c) and the correspondent integrated enhancement factor (d).

In Figure 8.12(b) the fraction  $f_{abs}$  of the incident power absorbed, as a function of wavelength, everywhere inside the photodetector (i.e., in the Si layer and inside the metal particles) for several values of lattice spacing is shown. This absorbed power fraction features a distinct resonance in the spectral region around  $\sim 700\text{ nm}$ , which originates from the excitation of LSPs in the arrays of nanocylinders. As we decrease the lattice spacing, we can observe that  $f_{abs}$  increases. In particular, for very short lattice spacings,

i.e. 150, 200, we appreciate a sharp increase in  $f_{\text{abs}}$  due to the significant contribution of metallic absorption losses expected for high-density arrays. Therefore, in order to identify the respective roles of metallic losses versus dielectric absorption, Figure 8.12(c) plots the absorption enhancement  $\alpha_{\text{enh}}$  limited to the 50 nm-thick Si layer calculated in the presence/absence of the periodic array of gold nanocylinders. This enhancement, restricted to the Si absorbing region, is the most relevant parameter for the photodetector design. We can now notice in Figure 8.12(c) that, for any value of lattice spacing, there exist two separate regimes of enhancement. In particular, for wavelengths shorter than the LSP resonance  $\lambda < 700$  nm, the plasmonic nanoparticle array degrades the absorption efficiency compared to the one of a bare Si substrate (i.e., without nanoparticles) due to significant absorption losses inside the metallic particles. On the other hand, for wavelengths that are longer than the LSP resonance, a significant absorption enhancement in the Si layer can be obtained. In particular, at the shortest lattice spacing  $a = 150$  nm, we found a very significant absorption degradation (i.e.,  $\alpha_{\text{enh}}$  less than one) in the short wavelength regime compared to the base Si case, since a large fraction of the incident power is absorbed inside the metal that covers in this case 35% of the Si surface. On the other hand, a small value of  $\alpha_{\text{enh}}$  is achieved for wavelengths longer than the LSP resonance. As we increase the interparticle spacing to  $a = 200$  nm,  $\alpha_{\text{enh}}$  features the highest peak among all the investigated cases. However, since the metal filling fraction is still high (20%), the absorption is still significantly decreased with respect to the bare Si substrate at shorter wavelengths. Therefore, a careful tradeoff between metal losses at short wavelengths and absorption enhancement at longer wavelengths must be obtained.

It was found that the array with  $a = 250\text{nm}$  provides the best solution, which can be appreciate by considering the integrated absorption enhancement factor  $\text{IF}_{\text{enh}}$ , shown in Figure 8.12(d). The  $\text{IF}_{\text{enh}}$  is defined as the average absorption enhancement ratio between  $\lambda_{\text{min}}=300\text{ nm}$  and  $\lambda_{\text{max}}=950\text{nm}$ , namely:

$$\text{IF}_{\text{enh}} = \frac{1}{(\lambda_{\text{max}} - \lambda_{\text{min}})} \int_{\lambda_{\text{min}}}^{\lambda_{\text{max}}} (\alpha_{\text{enh}} - 1) d\lambda \quad (8.2)$$

As the lattice spacing is further increased in the array, we see in Figures 8.12(c,d) that the absorption enhancement converges to one for wavelengths shorter than the LSP resonance, and it steadily decreases for wavelengths longer than the LSP resonance, reducing the corresponding  $\text{IF}_{\text{enh}}$ .

#### 8.2.4 Device Fabrication

To explore the potential of the GA-spiral geometry for enhancing absorption and photocurrent in ultra-thin film solar cells, GA-spirals and periodic Au nanoparticle arrays are fabricated onto a thin-film stack that mimics a solar cell device. Representative SEM of fabricated periodic and GA-spiral Au nanoparticle arrays on Si are shown in Figures 8.13(a,b), respectively.

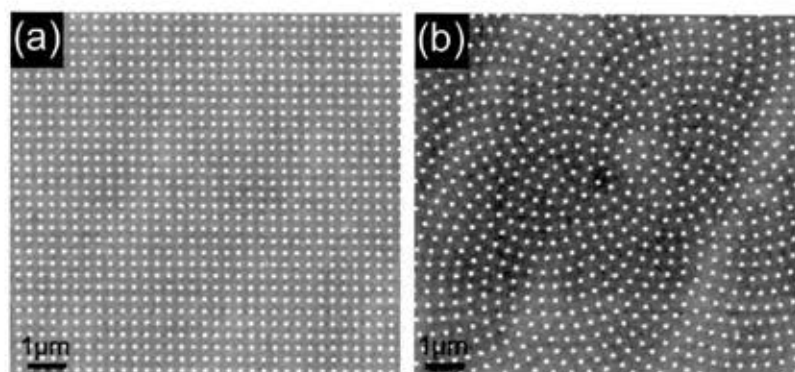


**Figure 8.13:** Representative SEM micrographs of a (a) periodic and (b) GA-Spiral array of Au nanoparticles with lattice spacing 300nm and average center to center spacing of 425nm respectively. The cylindrical particle diameters are 100nm, while the entire array geometry has a 100 $\mu$ m circular diameter.

The light absorption enhancement in the samples is quantified using the reflection-based technique discussed in (Ostfeld and Pacifici, 2011) for the characterization of ultra-thin films organic solar cells. Since this experimental technique requires an optically transparent and highly reflective substrate in order to eliminate transmission losses, we fabricated a specific set of samples for these measurements, with cross sectional geometry shown in Figure 8.14(a). In this case, a 300 nm-thick reflecting aluminum (Al) film is first deposited by electron beam evaporation onto a Si chip. A 50 nm-thick absorbing amorphous Si ( $\alpha$ -Si) layer is then deposited by RF magnetron sputtering and Au nanoparticle arrays are fabricated atop using an EBL and a metallization process detailed in Chapter 4. The metallic particles are cylindrical in shape with a circular diameter of 100 nm and thickness of 30 nm. All arrays are fabricated within a circular frame region with identical diameter of 100  $\mu$ m. Finally, a 40 nm-thick conductive and optically transparent indium tin oxide (ITO) film is deposited via RF magnetron sputtering. Sample reflectance measurements are performed using an un-

polarized broadband light source coupled through an objective with high numerical aperture (50x, NA = 0.5) as shown in Fig. 8.14(b). The reflected light intensity is collected through the same objective and is spatially filtered to guarantee collection only from the area of a single 100nm-diameter spiral/periodic array. The spatially filtered light is then spectrally resolved through a monochromator coupled CCD detector (Ocean Optics QE65000 spectrometer). Spectral reflection measurements are performed on the patterned structure ( $R_{array}(\lambda)$ ), on an unpatterned area of the chip ( $R_{ref}(\lambda)$ ), as well as on a section of the same chip where only the Au reflecting layer is present ( $R_{Au}(\lambda)$ ). The fraction of absorbed energy in the presence ( $A_{array}(\lambda)$ ) and in the absence ( $A_{ref}(\lambda)$ ) of the array is then calculated by the simple equations listed below.

$$\begin{cases} A_{array}(\lambda) = 1 - R_{array}(\lambda)/R_{Au}(\lambda) \\ A_{ref}(\lambda) = 1 - R_{ref}(\lambda)/R_{Au}(\lambda) \\ \alpha_{enh}(\lambda) = A_{array}(\lambda)/A_{ref}(\lambda) \end{cases} \quad (8.3)$$

The absorption enhancement  $\alpha_{enh}(\lambda)$  is then calculated as the ratio of  $A_{array}(\lambda)$  and  $A_{ref}(\lambda)$ , shown in equation (8.3). The experimental configuration assumes all scattered light is collected by the high N.A. objective. To ensure confidence in the measurements, we repeat the experiment under a 20x (N.A. = 0.4) objective and find our results to be consistent.

The set of samples used for photocurrent enhancement characterization were fabricated onto the surface of an SOI Schottky photodetector, as shown in the cross-section of Figure 8.14(c). Device fabrication begins with a p-type silicon on insulator (SOI) substrate, possessing a top Si layer thickness of 50 nm. The Au

nanoparticle arrays are fabricated using the same EBL and metallization process used to produce the samples for absorption quantification and have the same particle and array dimensions. Five 100  $\mu\text{m}$  diameter arrays are fabricated in each active area (400  $\mu\text{m}$  x 400  $\mu\text{m}$ ) of the photodetectors, as shown in the top-down microscopy image of a fabricated structure in Figure 8.14(d). Conductive and optically transparent ITO films (40 nm-thick) are finally deposited via RF magnetron sputtering followed by electron beam evaporation of 300 nm-thick Al contacts. Both ITO and Al layers are defined by a standard photolithography and lift-off processes. A single chip was fabricated containing several periodic and GA-spiral device cells, spanning in lattice spacing a large range between 120 and 680 nm. Adjacent to each device cell, an empty reference cell (i.e., without the particle array) is present to provide direct comparison for the enhancement estimation, as discussed in the next section.



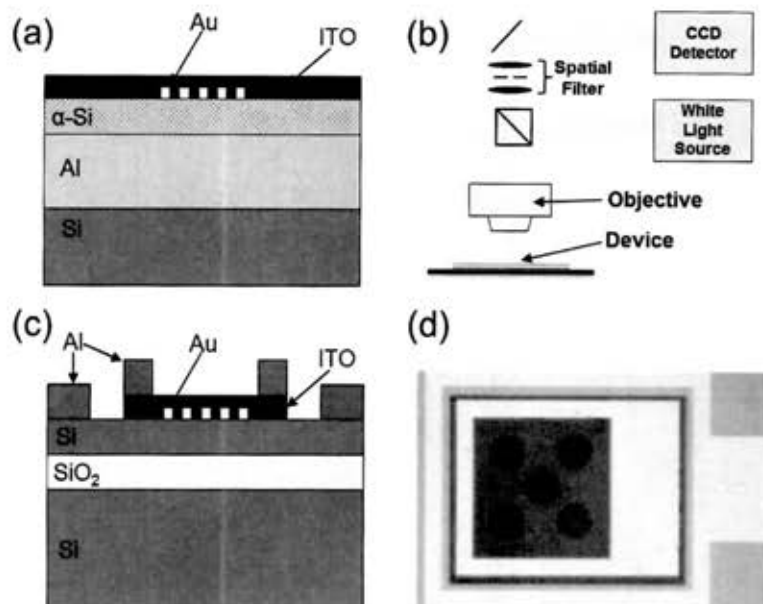


**Figure 8.14:** (a) Device cross-section of stack used to quantify absorption enhancement. (b) Experimental reflection measurement configuration used calculate absorption enhancement. Reflection of a broadband white light source was measured by a CCD detector through excitation and collection of a 50x objective (NA = 0.5). (c) Device cross-section of the SOI Schottky photo-detector with plasmonic arrays integrated onto the absorbing surface. (d) Bright-field microscope image of the device with five 100  $\mu\text{m}$  diameter GA-spirals integrated into the active device area.

A monochromatized broadband xenon lamp source was collimated and focused onto the active device area through a lens ( $f = 100$  mm). Electrical probes contacting the Al pads were biased with 1 V and generated photocurrent was measured with a Keithley 2400-LV SourceMeter controlled by a computer via LabVIEW as a function of wavelength. All enhancement values calculated were derived by dividing the photocurrent spectrum for each device by its nearest neighbor empty reference cell.

### 8.2.5 Absorption and Photocurrent Enhancement Results

In this section, the enhanced absorption and photocurrent spectra for a large number of periodic and GA-spiral devices with varying interparticle separations are

characterized. First the experimental results on light absorption enhancement are discussed. To this regard, it is important to notice that the previously discussed reflection-based technique does not allow for distinction between the two absorption contributions originating from Si on one hand, and the metallic nanocylinders on the other hand. In Figure 8.15(a) a few representative examples of experimentally measured absorption enhancement spectra obtained for a GA-spirals (solid lines) and for periodic arrays (dashed lines) are plotted with varying interparticle separations (reported in the legend) ranging from 120 nm to 680 nm. The presence of a plasmon-enhanced resonance around 700 nm separating two separate enhancement regimes (for  $\lambda < 700$  nm or  $\lambda > 700$  nm, respectively) is clearly visible in Figure 8.15(a), as predicted based on the numerical simulations shown in Fig. 8.12(b). The absorption enhancement spectra in Fig. 8.15(a) are influenced by both the light absorbed in the  $\alpha$ -Si thin film as well as the one absorbed inside the metallic nanoparticles. Therefore, as previously discussed in relation to Figures 8.12(b,c), the metallic losses will dominate the total absorption at wavelengths shorter than the LSP resonance, while for longer wavelengths the absorption in the  $\alpha$ -Si thin film can be enhanced. The total absorption enhancement spectral data shown in Figure 8.15(a) follow closely the trends with respect to interparticle separations predicted by the numerical simulations shown in Figure 8.12(b) for periodic array.

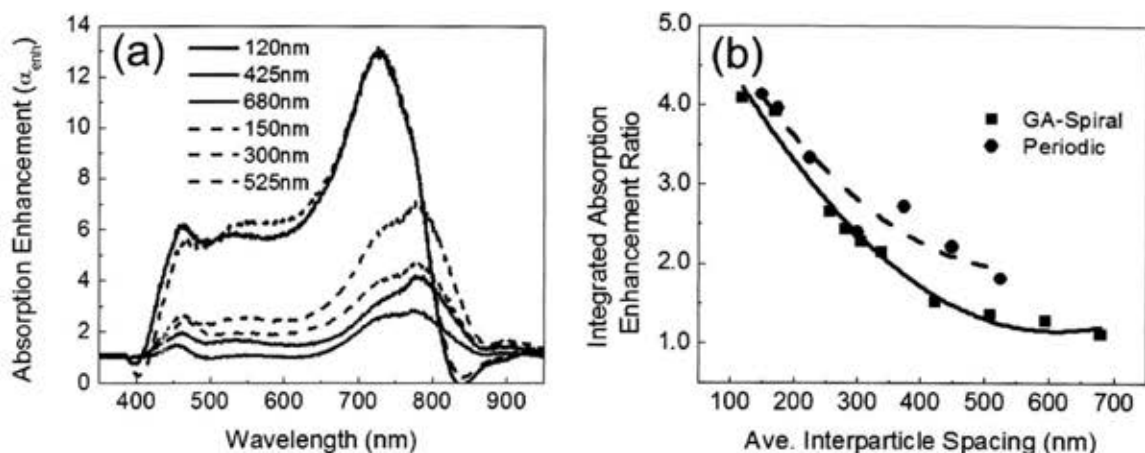


**Figure 8.15:** (a) Experimental absorption enhancement for GA-spirals (solid lines) with average center to center spacing of 120 nm, 425 nm, and 680 nm and periodic arrays (dashed lines) with lattice spacing of 150 nm, 300 nm, and 525 nm. (b) Integrated absorption enhancement ratio for GA-spirals (red, solid) and periodic (black, dashed) arrays of various interparticle spacing. Enhancement ratios are calculated by the ratio of the integrated measure with the nanopatterned device versus the integrated measure without nanopatterning.

In Figure 8.15(b) the integrated absorption ratio is plotted for all the investigated arrays as a function of center-to-center particle spacing. The integrated absorption enhancement ratio is defined as the ratio between the integrated absorption spectra measured on the patterned structure and on a reference unpatterned area of the chip. We notice in Figure 8.15(b) that for arrays with comparable center-to-center spacing, periodic structures always appear to produce larger values of integrated absorption enhancement. However, this result simply reflects the differences in Au nanoparticle densities for devices. In fact, for arrays of the same particle spacing, the GA-spiral structures are approximately 50% less dense in metal nanoparticles than periodic structures. Therefore, as we will also confirm by direct photocurrent measurements, the integrated absorption enhancement data shown in Figure 8.15(b) are dominated by the metallic losses of the more dense periodic arrays.

A definitive picture that demonstrates the full potential of the GA-spiral geometry for enhancing the absorption into thin Si films can be obtained by comparing directly the photocurrent generated in periodic and GA-spiral array Schottky photodetectors as a function of wavelength. Figure 8.16(a) and 8.16(b) show the measured photocurrent spectra for the best performing periodic and GA-spiral photodetectors. The dashed lines are the reference photocurrent spectra measured on the unpatterned devices in the nearest reference cells, respectively. The best results were obtained for periodic arrays with 300 nm particle spacing while the best GA-spiral performances have been measured for 425 nm average interparticle separation.

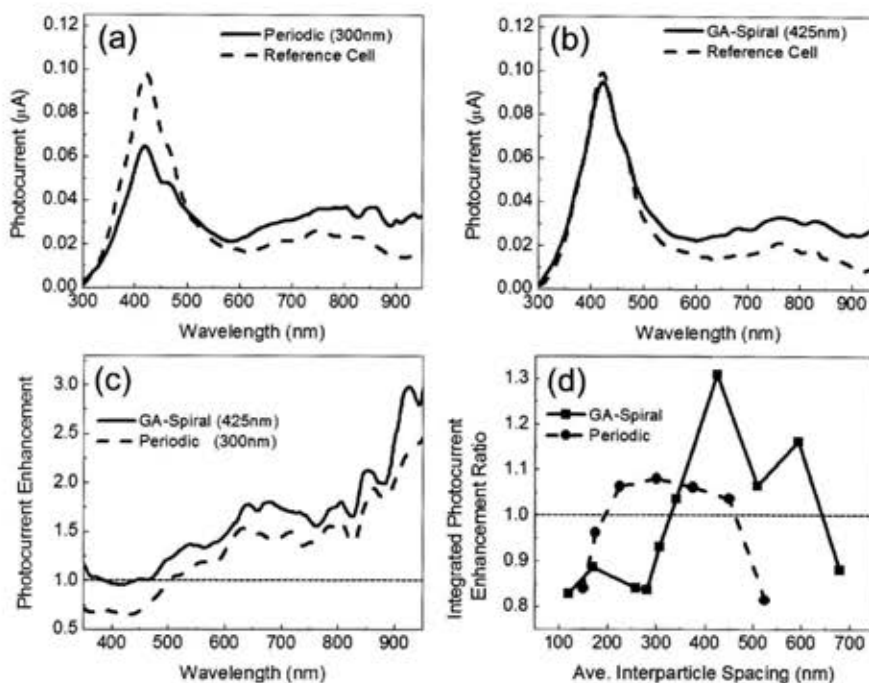


**Figure 8.16:** (a) Periodic array photocurrent spectrum with lattice spacing of 300 nm (solid) and empty neighbor reference cell (dashed). (b) GA-spiral array photocurrent with average center to center spacing of 425 nm (solid) and empty neighbor references cells (dashed). (c) Spectral photocurrent enhancement spectra for GA-spiral arrays (red,  $a = 425$  nm) and periodic arrays (black dashed,  $a = 300$  nm). (d) Integrated photocurrent enhancement ratio for GA-spiral (red) and periodic (black dashed) arrays of different center to center particle spacing.

In Figure 8.16(c) the spectral photocurrent enhancement is plotted, obtained by considering the ratio of the array and the corresponding reference measurements. Values below the dotted line of value one in Figure 8.16(c) indicate a global reduction in photocurrent compared to an unpatterned device area. The presence of nanoplasmonic arrays was found to substantially affect the photocurrent measured in the devices across the investigated wavelength spectrum. As observed in the data in Figure 8.16(a-c), the patterned cells show significant photocurrent enhancements for wavelengths in the 600 nm to 950 nm region, which are around or longer than the LSP resonance wavelength

measured in Figure 8.15(a). On the other hand, for shorter wavelengths we observe a clear decrease in absorption compared to the reference Si cell for the periodic arrays (Figure 8.16(c)), consistently with the predictions based on our numerical modeling (Figure 8.12(c)). We also notice from Figure 8.16(c) that the GA-spiral arrays do not deteriorate the absorption in Si but introduce only negligible metallic losses due to the 50% reduction in array filling fraction. Since the GA-spiral diffracts a larger fraction of light into high angles directions (Figure 8.11) than periodic arrays, less metal particles are required to obtain comparable scattered power into the Si substrate. The maximum photocurrent enhancement of approximately a factor of 3 is measured for the GA-spiral at 950 nm. This increased photocurrent results from the interplay of plasmonic-photonic effects in GA-spirals, which contribute to the overall enhancement as follows: by providing better coupling of incident radiation into the thin Si layer due to photonic large angle scattering (Figure 8.11); by enhancing the intensity of the nanoparticle near-fields at the Si interface owing to better LSP coupling in the plane of the array as compared to periodic structures (Ferry et al., 2010; Mokkaapati et al., 2011).

Additionally, it is important to note that, in varying degrees, all structures with incorporated nanoplasmonic particles feature a reduced photocurrent in the blue part of the solar spectrum below the LSP resonance, as predicted by simulations in Figure 8.12. This reduction is caused by both the onset of metallic losses in the nanoparticles near the LSP resonance as well as by destructive Fano interference induced by plasmonic scattering below the surface plasmon resonances (Beck, Polman and Catchpole, 2009; Nakayama, Tanabe and Atwater, 2008).

In Figure 8.16(d) the integrated photocurrent enhancement ratio is plotted, calculated by the ratio of the integrated photocurrent spectrum of the device with and without the plasmonic arrays. The ratios falling below the dotted line indicate devices with overall reduced performance when compared against their neighboring empty reference cells. We see in Figure 8.16(d) that both GA-spiral and periodic arrays exhibit an optimization trend with respect to the interparticle spacing, yielding maximum integrated enhancements of 8% and 31% over reference cells, respectively. The periodic array with highest integrated enhancement corresponds to a lattice spacing of 300 nm, which is in good agreement with the predicted performance shown in Figure 8.12(d) based on calculated absorption enhancement. The increased enhancement observed for GA-spirals follows from their circular Fourier space inducing the large-angle scattering effect discussed and modeled in Fig. 8.11.

Finally, it is noted that the observed 31% integrated enhancement measured for GA-spiral arrays has been demonstrated with only 25% of the active photodetector device area covered by spiral arrays (Figure 8.14d). This highlights the potential for even greater enhancement in the limit of complete device area coverage using GA-spirals. While this study has focused on enhancing thin-film Si Schottky photodetectors, the unique plasmonic-photonic behavior of GA-spiral arrays presented here are generally scalable to other solar cell material platforms and wavelength regimes. Moreover, a large class of deterministic aperiodic spiral arrays with divergence angles different from the GA remains to be explored, promising even more flexibility in Fourier space while

maintaining almost ideal circular symmetry in multiple scattering rings (Trevino, Cao and Dal Negro, 2011).

### 8.3 Nonlinear Properties of Plasmonic Vogel Spirals

In this section, the near-field and second harmonic generation (SHG) properties of plasmonic Vogel spiral arrays will be investigated. The results will be compared against plasmonic periodic and Fibonacci arrays of comparable densities.

#### 8.3.1 Enhanced 2<sup>nd</sup> Harmonic Generation with Vogel Spiral Arrays

The following section has been adapted from the 2012 Optics Express publication titled *Multipolar second harmonic generation from planar arrays of Au nanoparticles* and can be found here (Capretti et al., 2012).

In this section, multipolar SHG from tightly spaced periodic, Fibonacci, and GA-spiral arrays of Au nanocylinders is investigated. In order to investigate the respective roles of near-field plasmonic and long-range photonic coupling, the interparticle separations are varied systematically in these arrays from 60 nm to distances comparable to the pump wavelength. Moreover, it is shown that the SHG is maximized by arranging Au nanoparticles in GA-spiral arrays. The possibility of engineering multipolar SHG in planar arrays of metallic nanoparticles paves the way to the development of novel optical elements for nanophotonics, such as nonlinear optical sensors.

Recently, a number of studies have examined the origins of SHG from metal nanoparticles (Butet et al., 2010; Bachelier et al., 2010). It has been shown that SHG



from nanoparticles comes from independent contributions from the local surface and the non-local bulk nonlinear source. For noble metals, the local bulk source is absent due to the material's centrosymmetry, leaving only the surface contribution (Walsh, 2013). The local surface contribution to the SHG is due to symmetry breaking at the particle's interface with the embedding medium (Agarwal and Jha, 1982; Dadap et al., 1999). The relative magnitudes of the non-local bulk and local surface SHG contributions depend generally on the shape of the nanoparticles and on the optical properties of the metal at the fundamental and SHG wavelengths (Guyot-Sionnest, Chen and Shen, 1986; Guyot-Sionnest and Shen, 1987).

The SHG is investigated from periodic, Fibonacci and GA-spiral arrays of Au nanocylinders 30 nm in height with a diameter of 200 nm. The arrays are fabricated by the standard EBL, metal evaporation and liftoff process on a fused silica substrate described in Chapter 4. Using single particle T-matrix calculations, the size of the nanocylinders was designed to maximize linear scattering at the pump wavelength (i.e., 780 nm) in the absence of interparticle coupling (Capretti et al., 2012). In order to explore both the short-range plasmonic and long-range photonic coupling regimes we consider arrays with edge-to-edge interparticle separations  $L$  ranging from 60 nm to 650 nm. For periodic and Fibonacci arrays, the interparticle separation is defined as the minimum edge-to-edge particle separation, while for the GA-spirals it is defined as the average nearest neighbor edge-to-edge separation. Figure 8.17 shows SEM micrographs of representative (a) periodic, (b) Fibonacci, and (c) GA-spiral arrays with interparticle separations of 60 nm.

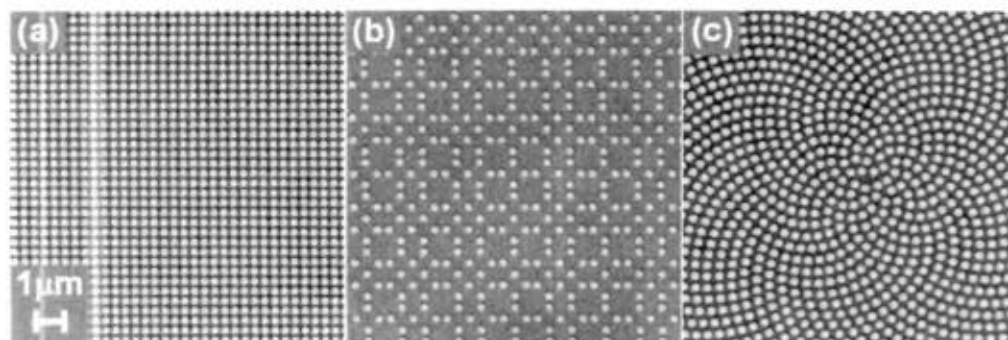


**Figure 8.17:** SEM micrographs of periodic (a), Fibonacci (b) and GA-spiral (c) arrays of 200nm-diameter cylindrical gold nanoparticles with a particle separation of 60 nm.

The SHG from the three array geometries is characterized by excitation at 780 nm with an ultrafast Ti:Sapphire laser (Mai Tai HP, Spectra Physics), with a pulse width of 100 fs and repetition rate of 80 MHz, which is reduced to 10 MHz by an electro-optic pulse picker (Conoptics 360-801). The excitation beam is steered with ultrafast mirrors (Newport) preserving its temporal width. Utilizing a specular reflection configuration, the excitation is obliquely incident on the sample surface at an angle  $\varphi = 45^\circ$  and the reflected SHG signal is collected. The beam is focused onto the array by an 85 mm focal length spherical lens. The time average power prior to the lens is 40 mW. Full experimental details can be found in the following references (Walsh, 2013; Capretti et al., 2012).

The intensity of the SHG signal is plotted as a function of the interparticle separation  $L$  for all the arrays in Figure 8.18(a). A clear dependence of the SHG signal on the interparticle distance is observed, and the largest  $L$  produces the weakest SHG response for each array geometry. Moreover, we notice that GA-spirals give rise to the strongest SHG signals for all the investigated values of interparticle separations. On the other hand, for Fibonacci arrays, the SHG is the lowest for all separations. This can be

attributed to the lower particle-filling fraction of Fibonacci arrays. The variation in the particle-filling fraction of all the arrays as a function of the interparticle separation is shown in the inset of Figure 8.18(a). Furthermore, we notice that the superior performances of GA-spirals over periodic arrays cannot simply be explained by the difference in particle filling fractions, as these are comparable across the investigated range of separations. Therefore, the enhanced SHG is attributed to the asymmetric spatial near-field distribution in the GA-spiral array, which is a consequence of their distinctive aperiodic order. The importance of the near-field intensity distribution at the pump wavelength for the SHG optimization was already pointed out by Canfield *et al* in the case of asymmetric metal nanoparticles (Canfield *et al.*, 2007).

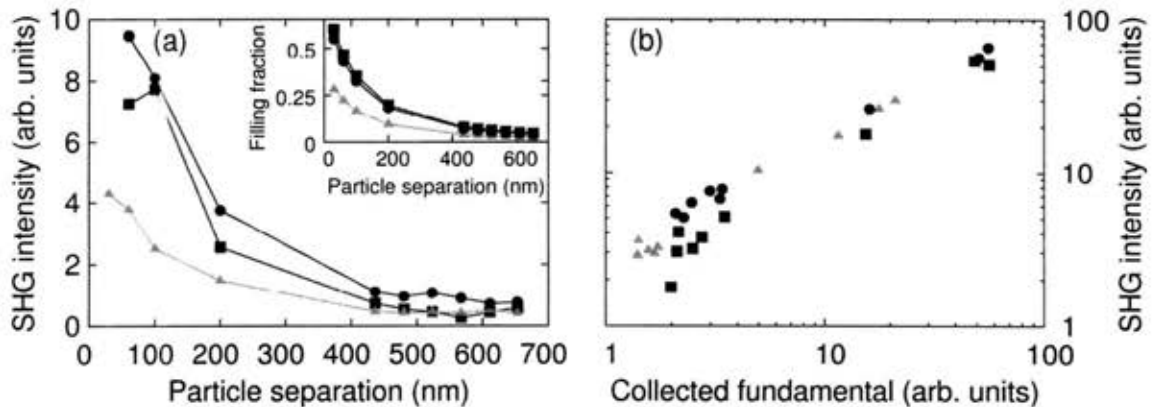


**Figure 8.18:** (a) Intensity of the collected SHG as a function of interparticle separation for periodic (red squares), Fibonacci (green triangles) and GA-spiral (blue circles) arrays; (a inset) Filling fraction of Au for the arrays following the same coloring scheme. (b) Correlation diagram between SHG and pump collected signals.

In Figure 8.18(b) the correlation between the intensities of the SHG signal and of the scattered pump at 780 nm is plotted. A direct dependence of SHG signal on the fundamental is demonstrated, showing that the SHG is mainly driven by the optical

behavior of the NP arrays at the pump frequency. In general, the SHG process depends also on the NP array field distribution at the harmonic frequency, but in this case the strong absorption of Au at the SHG frequency makes this dependence negligible. In order to better understand the role of the asymmetry of the spatial distributions of the pump field over the NPs, the calculated near-field patterns at 780 nm is plotted in Figure 8.19, obtained by GMT (Xu, 1995). The pump fields are calculated in the plane of the arrays for all the array geometries and for two particle separations (60 nm, 611 nm) characteristic of plasmonic near-field coupling and photonic coupling, respectively.

Figure 8.19(a) and 8.19(c) show that periodic arrays display a very regular distribution of near-field around each NP, and the local field intensity is reduced as the NPs are separated. Moreover, we notice that the field is strongly oriented along the direction of polarization of the pump beam. The highly symmetric nature of the near-field pump distribution in periodic plasmonic arrays reduces the SHG signal due to destructive interference (Boyd, Yu and Shen, 1986; Lamprecht, Leitner and Aussenegg, 1999). In Figure 8.19(b) and 8.19(d), the near-field distributions in GA-spiral arrays are plotted for the photonic and plasmonic coupling regimes, respectively. The GA-spiral geometry couples all the particles in the array but, differently from periodic structures, a very asymmetric near-field distribution results from the distinctive aperiodic order. This asymmetry of the pump fields in the GA-spirals prevents destructive interference effects in the SHG for all interparticle separations, resulting in a stronger SHG signal, as experimentally demonstrated over a large range of particle separations.

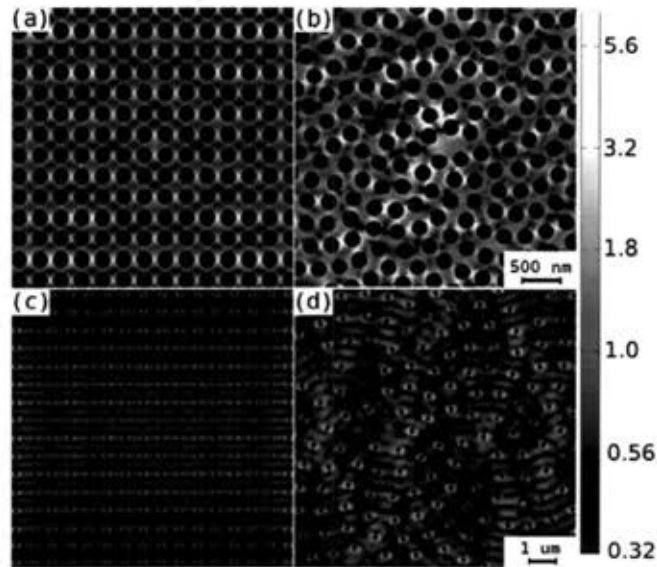


**Figure 8.19:** Near-field distribution at the pump frequency over periodic (a) and GA-spiral (b) arrays with interparticle separation  $L = 60$  nm. Near-field distribution at the fundamental frequency over periodic (c) and GA-spiral (d) arrays with interparticle separation  $L = 611$  nm. All the near-field maps are plotted in logscale.

In this Section, the role of the aperiodic array geometry on the SHG from Au nanoparticles has been investigated. The SHG in the GA-spiral geometry was found to be more efficiently produced when compared to the periodic one, and over a large range of particle separations. The behavior is explained by the asymmetric near-field distribution of the GA-spiral at the pump wavelength. These results are important for the development of novel optical elements for nonlinear nanophotonics applications, such as switchers, frequency converters and nonlinear optical sensors on a planar chip. For more details and further characterization of the SHG from these arrays, the author suggests reviewing the following publication (Capretti et al., 2012).

## 8.4 Conclusions

In conclusion, the scattering properties of the three main types of Vogel spiral arrays of Au nanoparticles have been investigated by experimental dark-field scattering, imaging, and fluorescence spectroscopy in partnership with rigorous electrodynamics calculations. The presence of a diffuse and rotationally symmetric Fourier space has been experimentally measured in plasmonic Vogel spirals, as well as a demonstration of polarization-insensitive planar diffraction. Moreover, it was shown that far-field diffractive coupling in these structures leads to the formation of circular symmetric scattering resonances and scattered fields carrying OAM.

Additionally, ultra-thin SOI Schottky photo-detector cells coupled to GA-spiral and periodic Au nanoparticle arrays were experimentally explored for efficient light trapping. Photo-detector devices coupled to optimized GA-spiral geometries were shown to enhance the spectrally integrated photocurrent by 31%, as compared to only 8% observed in periodic arrays. The resulting enhancement has been related to the distinctive properties of GA-spirals, which give rise to strong photonic high-angle scattering behavior, increasing the coupling into the thin-film absorbing Si layer. Furthermore, localized plasmonic resonances atop the absorbing region occur at significantly reduced metallic particles densities compared to periodic array.

Lastly, the multipolar SHG from tightly spaced periodic, Fibonacci, and GA-spiral arrays of Au nanocylinders were investigated. A more intense SHG signal from GA-spiral arrays was measured, as compared to periodic and Fibonacci arrays over a large range of particle separations. The behavior was found to be a result of the

asymmetric near-field distribution of the GA-spiral at the pump wavelength. The engineering of plasmonic nanoparticle arrays with aperiodic spiral geometry can lead to the fabrication of novel optical devices that benefit from polarization insensitive, enhanced light-matter coupling on planar surfaces, such as thin-film solar cells, plasmonic photodetectors, optical biosensors, and novel polarization devices.

## Chapter 9

### 9 Radiation-enhanced Plasmonic Coupling

Sections of this chapter have been adapted from articles submitted for publication entitled *Photonic-Plasmonic coupled Nanoantennas for Polarization-controlled Multispectral Nanofocusing* and *Photonic-Plasmonic Coupling of GaAs Single Nanowires with Nanoantenna Arrays*, referenced (Trevino, Walsh, et al., 2013) and (Trevino, Alberto, et al., 2013) respectively.

Plasmonics has become a mature technology for nanoimaging and bio(chemical) sensing, and holds high promise for implementation of chip-scale information processing networks (Biagioni, Huang and Hecht, 2012). Recently, plasmonic nanoantennas have been shown to concentrate incident light to length scales much smaller than the diffraction limit at optical frequencies (Bharadwaj, Deutsch and Novotny, 2009). Additionally, optical nanoantennas have been utilized for the enhancement of molecular fluorescence (Bakker et al., 2008), nonlinear optical processes (Navarro-Cia and Maier, 2012), optical bio sensing (Anker et al., 2008; Adato et al., 2009), and photovoltaics (Atwater and Polman, 2010).

#### 9.1 Nanoantennas for Multispectral Nanoscale Focusing

In this section, a polarization-controlled photonic-plasmonic nanoantenna array, which concentrates near-IR radiation to a single subwavelength spot at multiple wavelengths, is designed and demonstrated. The design concept builds on the previous



work by Boriskina *et al* (Boriskina and Dal Negro, 2010), where multiple-periodic plasmon grating structures were shown to efficiently funnel optical radiation into a nanoparticle dimer by the de-radiative coupling of surrounding metallic nanospheres. In this configuration, the resonant wavelength of the antenna can be switched between two well-defined spectral locations by the incident light polarization. This type of device has potential to be used for multiplexed nonlinear sensing, near-field imaging, and to resonantly enhance both the pumping and the emission efficiency of sources (e.g., fluorescence, Raman, broadband nonlinear processes).

Independently two different periodic chains of Au nanocylinders are designed to diffractively couple the incident field into a centrally located double bow-tie antenna (DBA), as shown in Figure 9.1(a,b). The DBA supports a broadband plasmonic resonance, while the linear particle gratings provide frequency selective diffractive coupling through narrow-band photonic resonances. In order to strongly enhance the intensity of the plasmonic near-fields as well as to accurately control their frequency spectrum, we designed the nanoparticle chains to produce strong Fano-type photonic-coupling at the designed wavelengths (i.e., spectral overlap of photonic and plasmonic resonances). The particle sizes  $a_{1,2}$  and particle diameters  $d_{1,2}$  in the chains were optimized using three dimensional finite difference time domain (3D FDTD, Lumerical Solutions, Inc.) to produce the maximum near-field enhancement at the DBA central location when excited with a normally incident plane wave at 780 nm and 860 nm with the polarization direction indicated in Figure 9.1(a,b). The Au nanoparticles, which are situated on a fused silica substrate, are 30 nm-tall and are designed using experimentally

measured material dispersion (Johnson and Christy, 1972). The tips of triangles in the DBA have been rounded in the FDTD simulation to better describe the experimental situation, which is limited by the resolution of our nanofabrication process. The calculated electric near-field distributions of the grating-coupled plasmon resonances are visualized within the marked dashed regions of in Figure 9.1 (a) and (b) for an excitation wavelength of 780 nm and 860 nm, respectively. Figure 9.1(c) shows the calculated maximum near-field enhancement spectra of the antennas probed at the center of the DBA region for three different situations: (i) when an isolated DBA is excited (black); (ii) when the DBA is coupled to the chains designed to resonate at 780 nm (blue); (iii) when the DBA is coupled to the chains designed to resonate at 860 nm (red). The chains are excited with the polarizations indicated by the arrows in the figure. It is well known that diffractive coupling between nanoparticles in linear gratings is maximized when both polarization and wave vector of the incident plane wave are perpendicular to the grating axis (Zou and Schatz, 2004).

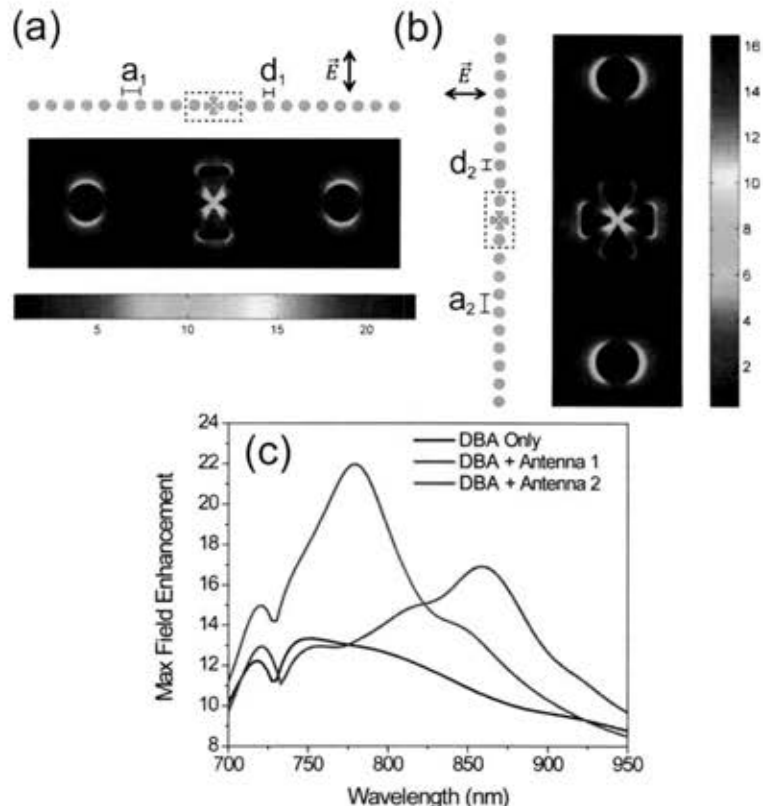


**Figure 9.1:** (a) Antenna chain designed for near-field enhancement at 780 nm and near-field calculation of the electric field distribution in the dashed area at that wavelength. (b) Antenna chain designed for near-field enhancement at 860 nm and near-field calculation of the electric field distribution in the dashed area at that wavelength. (c) Maximum near-field enhancement spectra in the DBA region for (black) DBA only, (blue) DBA and linear grating optimized for 780 nm (configuration 9.1a), and (red) DBA and linear grating optimized for 860 nm (configuration 9.1b).

As can be observed in the near-field plots in Figure 9.1, the single Au cylinders of the chains support dipolar resonances that are designed to spectrally overlap the DBA plasmon resonance, thus enhancing its nanoscale near-field intensity response in a tunable fashion (Zhang et al., 2009).

Based on the described concept, the two linear chains of Au nanoparticles are combined to produce a single multi-wavelength nanoantenna device shown in Figure

9.2(a). The optimized lattice constants and particle diameters for the chain oriented at  $0^\circ$  are  $a_1 = 540$  nm,  $d_1 = 160$  nm, and for the chain oriented at  $90^\circ$  they are  $a_2 = 600$  nm,  $d_2 = 185$  nm. Figure 9.2(b) shows the DBA dimensions used, optimized for broadband near-field enhancement over the wavelengths of interest. An SEM of the fabricated antenna arrays on a fused silica substrate is shown in Figure 9.2(c) and a close-up of the DBA is visible in Figure 9.2(d), matching the dimensions used in the FDTD simulations. The Au nanoparticles were fabricated using an EBL process, described previously in Chapter 4. An array of periodically spaced multi-wavelength nanoantennas was fabricated, covering an area  $100 \mu\text{m}$  by  $100 \mu\text{m}$ . The antennas were spaced sufficiently far apart (lattice constant =  $16 \mu\text{m}$ ) to avoid diffractive coupling of adjacent devices.

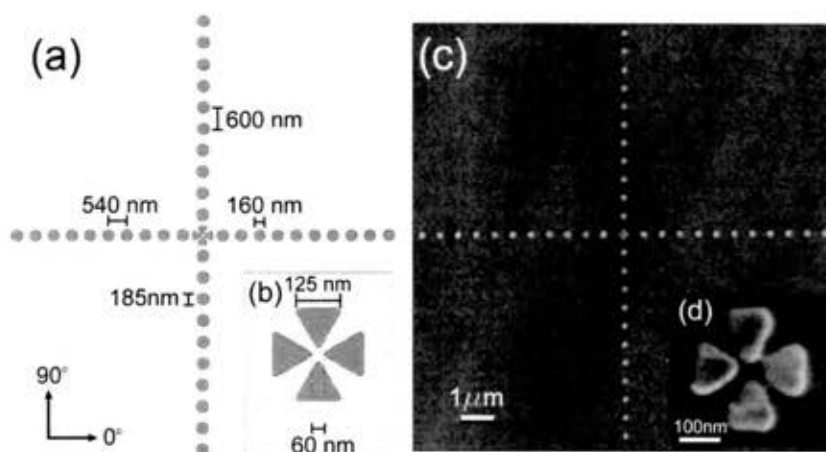


**Figure 9.2:** (a) Optimized multi-wavelength nanoantenna array geometry. (b) Double bow-tie antenna (DBA) at center of antenna array. (c) SEM micrograph of EBL fabricated gold nanoantenna array. (d) Close up SEM micrograph of DBA.

In order to characterize the near-field resonant properties of the fabricated structure, we performed second harmonic excitation (SH-E) spectroscopy. The technique has recently been shown to be an effective probe of photonic-plasmonic Fano coupling in

arrays of metallic nanoparticles by Walsh et al (Walsh and Dal Negro, 2013). The generation of enhanced electromagnetic fields by excited plasmon resonances drives nonlinear harmonic generation from the metal nanoparticles (Chen, DeCastro and Shen, 1981). SHG, as described in Chapter 2, is a nonlinear process where a medium is excited by two photons at a fundamental frequency  $\omega_0$  and emits a single photon at twice that frequency  $2\omega_0$ .

The experimental setup utilized for the SH-E characterization of the antenna arrays is sketched in the inset of Figure 9(a). Laser pulses are generated by a tunable mode locked Ti-Sapphire laser with 150 fs pulse duration and 82 MHz repetition rate. The excitation beam is focused on the array by a 20x microscope objective. A 700 nm long pass filter located before to the sample removes any SH signal produced by the optical components. The SHG is then collected in transmission with a 50x, 0.5 NA objective. The signal is detected with a photon multiplier tube (PMT) coupled to a lock-in amplifier after passing through a monochromator. The excitation beam is removed with a 670 nm short pass filter prior to the monochromator. The sample is aligned with an imaging system consisting of a reflection microscope with a CCD camera, as shown. A removable mirror is placed in front of the camera to direct the SHG signal to the detector. The time averaged excitation power is kept constant at 20 mW. The pump polarization is controlled by a half-wave liquid crystal variable retarder (Thorlabs LCC1111-B).

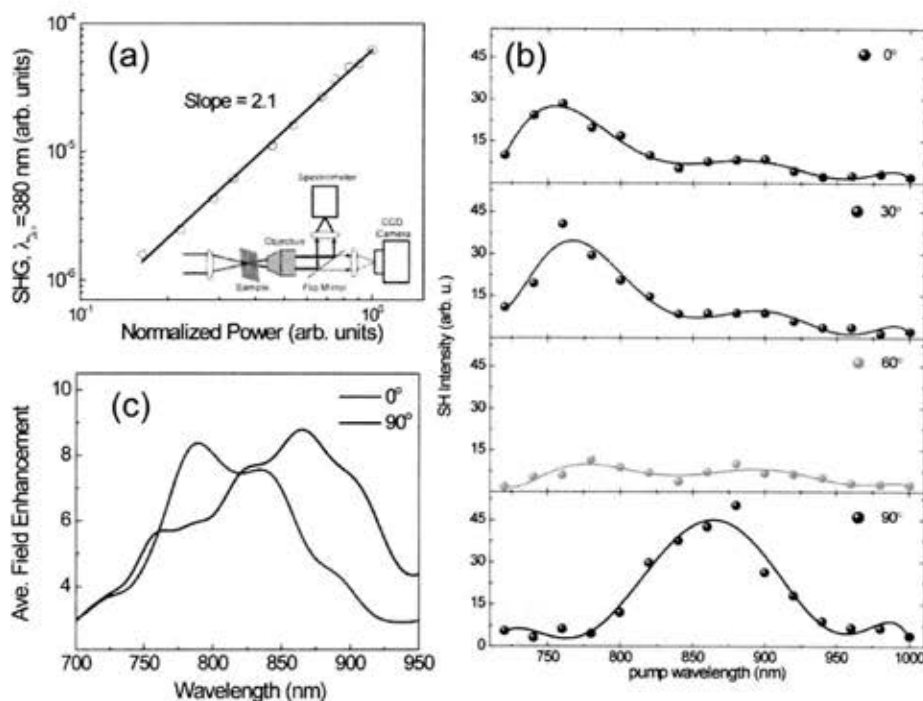


**Figure 9.3:** (a) Pump ( $\lambda_{\omega} = 760$  nm) power dependence of SH signal ( $\lambda_{2\omega} = 380$  nm) from representative array. (Inset) Diagram of SH-E experimental setup. (b) Experimentally measured SH-E spectra of the antenna arrays as a function of the polarization angle. (c) FDTD calculation of the spatially averaged near-field enhancement of the nanoantenna arrays for plane wave excitation with a polarization angle of  $0^\circ$  (red) and  $90^\circ$  (black).

In Figure 9.3(a) the pump power dependence of the SHG signal is shown, detected at 380 nm for a representative array excited at 760 nm. The slope of the log-log plot demonstrates almost quadratic scaling ( $m = 2.1$ ) of the signal with the incident intensity, consistent with the SHG process.

Figure 9.3(c) shows the spatially averaged field enhancement in the DBA antenna feedgap calculated using 3D FDTD. To ensure the reproducibility of the simulated spectra, the area over which the field is spatially averaged was varied, resulting in no spectral changes, but only modifications in relative magnitude were observed. The

antennas were excited with two orthogonal polarization states ( $0^\circ$  and  $90^\circ$ ). Notice that the resonance wavelength is controlled solely by the incident polarization. The experimentally measured SH-E spectra of the antenna as a function of the polarization state are reported in Figure 9.3(b). Data are normalized for the system response and for the pumping photon flux. Note that when the antenna is excited using a polarization angle of  $0^\circ$  (top panel), the SH-E spectrum peaks between 740 to 800 nm. A much weaker peak is detectable at longer wavelengths (850 – 950 nm). As the polarization direction is changed, the relative intensity of the two peaks becomes comparable. At a polarization angle of  $90^\circ$  (bottom panel), the first peak almost disappears, while the resonance on the right side of the spectrum is dominant. These results are consistent with the simulated average near-field enhancement and match the designed resonance wavelength for each polarization. We notice that in the experimental situation the arrays are excited using a focused laser beam, which has a range of k-vector components not present in the numerical calculations. Therefore, despite the agreement with FDTD calculations can only be considered qualitatively, our data demonstrate polarization control over the spectral position of local field enhancement of radiatively-coupled plasmon nanoantennas, as directly probed by their nonlinear SHG properties. These results could be further extended to longer wavelengths as demonstrated in the IR by Blanchard *et. al* (Blanchard et al., 2011).

In summary, a grating-assisted nanoantenna geometry has been demonstrated that is polarization selective and allows for multi-wavelength focusing into a subwavelength spot, in good agreement with full-vector FDTD simulations. The selective spectral

response of such nanoantennas has been experimentally demonstrated using SH-E spectroscopy. These structures could potentially open new paths for molecular linear and nonlinear spectroscopy, Raman spectroscopy, and near-field optical lithography with polarization controlled and spectral selectivity of hot spots.

## 9.2 Coupling of GaAs Nanowires with Nanoantenna Arrays

The optical properties of semiconductor nanowires (NWs) and plasmonic structures are currently at the center of an intense research effort due to their potential applications in a number of nanoscale optoelectronic devices, such as tunable and enhanced light sources (Shegai et al., 2011), solar cells and photodetectors (Muskens et al., 2008; Tsakalacos et al., 2007; Rosfjord et al., 2006), optical switches (Kind et al., 2002), non-linear devices and modulators (Nakayama et al., 2007).

NWs with engineered composition, size and morphology offer the possibility to control the electronic structure and the linear and non-linear optical properties of semiconductor materials. Recently, the engineering of metal-dielectric NWs that support structural resonances, such as the ones predicted by the classical Mie theory, has been proven as a convenient pathway to enhance light matter coupling (Wang and Leu, 2012). Moreover, resonant metallic nanostructures supporting travelling or localized SPPs have been thoroughly investigated as a powerful approach to manipulate optical radiation at the sub-wavelength scale (Maier, 2007). Plasmonic nanoparticle arrays and nanoantennas have shown the ability to strongly concentrate and increase the intensity of local electromagnetic fields over engineered nanoscale spatial domains and spectral



bandwidths (Bharadwaj, Deutsch and Novotny, 2009). However, while a significant amount of work has been devoted to understand and manipulate the optical responses of semiconductor NWs and plasmon systems independently, little is currently known about their optical coupling regime and synergistic properties.

Recently, hybrid optical waveguides consisting of dielectric nanowires coupled to plasmonic structures has been proposed as a novel way to approach truly nanoscale semiconductor-based plasmonics and photonics (Oulton et al., 2008). The combination of the mature semiconductor NW platform with the emerging nanoplasmonics technology could enable applications that leverage strongly confined optical fields for the engineering of optical cross-sections of resonant semiconductor nanostructures. In particular, the study of semiconductor NWs optically coupled to plasmonic nanoantennas with lithographically defined morphologies may result in the basic building-blocks for future high-efficiency solar cells, ultrafast optical switches and modulators with dramatically reduced energy consumption (Muskens et al., 2008; Nakayama et al., 2007).

In this section, by combining Gallium Arsenide (GaAs) NW growth with EBL nanofabrication, we demonstrate plasmonic arrays of Au nanoantennas optically coupled to individual GaAs NWs. The optical resonances of these coupled nanostructures are modeled using 3D FDTD and experimentally probed using SH-E spectroscopy (Walsh and Dal Negro, 2013).

### 9.2.1 Fabrication and design of antenna coupled GaAs NWs

Thanks to the recent advancements in semiconductor NW growth and processing

technologies, large arrays of semiconductor NWs can be fabricated with excellent control of the morphology and doping concentration (Dufouleur et al., 2010; Casadei et al., 2013). In this study, all NW growth and nanofabrication was carried out at École Polytechnique Fédérale de Lausanne (EPFL) in collaboration with the group of Prof. Anna Fontcuberta i Morral. The synthesis of GaAs NWs was carried out on Si(111) undoped substrates (Russo-Averchi et al., 2012) by the Ga-assisted method in a DCA P600 solid source MBE system. The NWs were grown under a rotation of 7 rpm, a flux of Ga equivalent to a planar growth rate of 0.3 Å/s, a substrate temperature of 640°C and a V/III beam equivalent pressure ratio of 50, leading to a NW diameter of ~ 50 nm and a length of 12 μm. After the growth of the NW core, 4 nm Al<sub>x</sub>Ga<sub>1-x</sub>As and 3 nm intrinsic GaAs shells are grown via vapor-solid-solid deposition, leading to an overall NW diameter of ~ 65 to 70 nm. The concentration of Al(x) in the AlGaAs shell is around 30%. This passivation layer avoids the detrimental effect of non-radiative surface trap states on the GaAs NW, offering opportunities to investigate the intrinsic properties of the material (Casadei et al., 2013).

After the synthesis, the NWs were removed from the substrate by placing the sample in isopropanol and a 1 minute of ultrasound bath. A few drops of this NW filled solution were released onto a fused silica substrate where a detailed pattern map has been previously realized with optical photolithography. An optical microscope was utilized to locate the NW position on the wafer. The nanoantennas have been designed around the NWs using custom-made fitting software. The pattern encodes the relative position on the wafer and uses circular shapes for deep sub-micron alignment. The position is determined

via shape recognition algorithms leading to an accuracy of approximately 50 nm. EBL was then used to position the nanoantennas in close proximity to the NW surface along its axis. Before the exposure, a methyl methacrylate (MMA) and PMMA resist layers were spin coated on the substrate, followed by an evaporation of 40 nm of Cr to reduce charging effects during the EBL process. The Cr was then wet etched away and the resist was developed. Finally, 5 nm of Ti and 30 nm of Au were evaporated, followed by a lift-off procedure to remove excess metal.

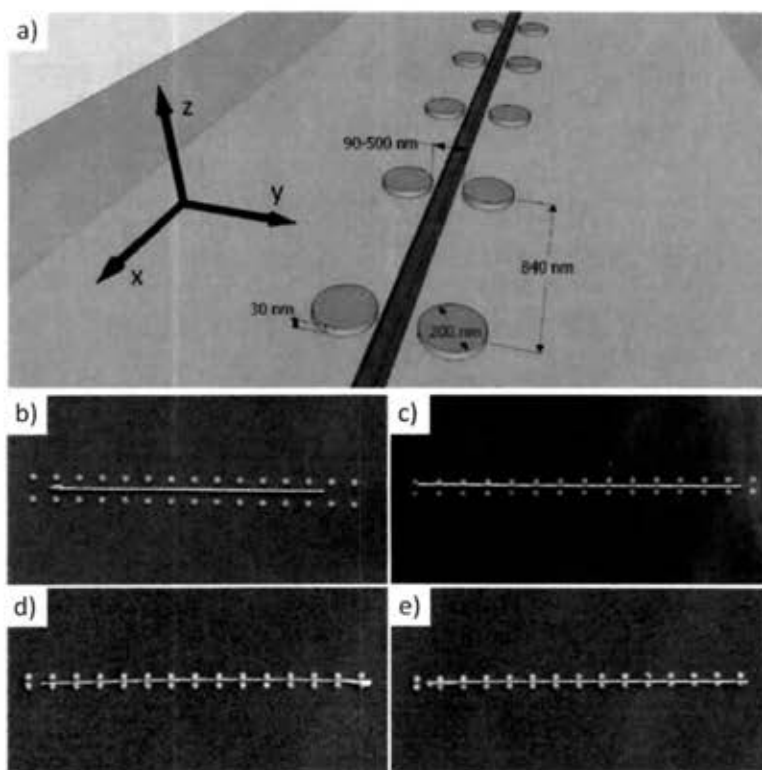


**Figure 9.4:** (a) Schematic of GaAs nanowire coupled to nanoantenna. SEM micrographs of NW coupled nanoantennas with lattice spacing  $a = 840$  nm and nanocylinder edge to NW edge distance  $d$  of (b) 215 nm, (c) 65 nm, (d) 15 nm, (e) 10 nm.

Figure 9.4a displays a schematic of the plasmonic antenna-coupled NW configuration investigated in this study. The individual nanoantennas consist of dimers of

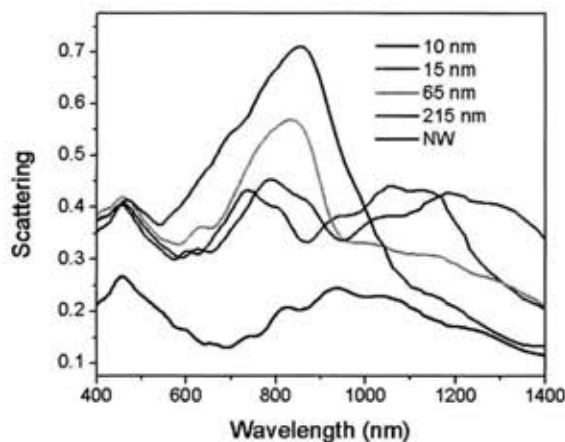
Au cylindrical nanocylinders with 210 nm diameter and 30 nm height. The edge-to-edge separation of the nanocylinders (i.e. the nanoantenna feed-gap region) contains the individual NWs. The spacing of the dimer nanoantennas along the length of the NWs (i.e., the array grating constant,  $a$ ) is kept fixed at 840 nm, designed for maximum radiative field coupling among the nanoantennas. The radiative coupled field arising from the grating is designed to optimize near-field intensity concentration within their respective feed-gap regions.

In order to demonstrate the near-field coupling of plasmonic nanoantennas with GaAs NWs, the study is focused of the optical response of coupled systems that consist of Au nanodimers with feed-gap regions of 90, 100, 200 and 500 nm, resulting in antenna-NW separations  $d$  of approximately 10, 15, 65, and 245 nm, respectively. SEM micrographs of the fabricated antenna coupled NWs are show in Figures 9.4(b-e).

### 9.2.2 Modeling of antenna coupled GaAs NWs

To model the antenna-coupled NW structures, 3D FDTD analysis is carried out using the commercial software package Lumerical FDTD Solutions. The material dispersion parameters of Au nanocylinders are modeled using data from Johnson and Christy (Johnson and Christy, 1972) while the optical dispersion parameters of the GaAs NWs and the fused silica substrate are derived from Palik (Palik, 1998). The simulation grid size surrounding the Au nanoparticles and the NW is 2 nm in all three dimensions. Plane wave excitation at normal incidence was used with the electric field oriented perpendicular to the nanowire axis (i.e., x-direction, as labeled in Figure 9.4a). PML

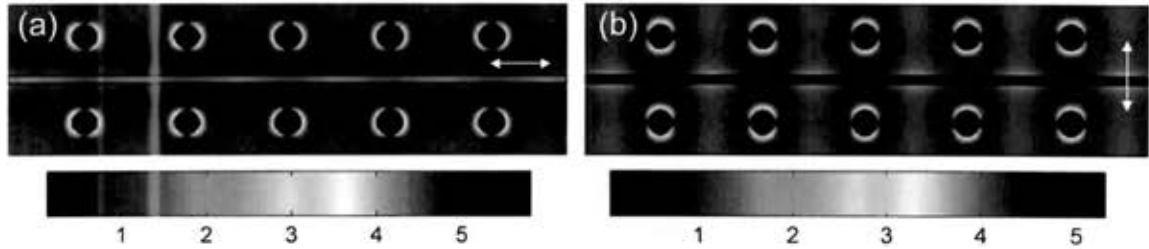
boundary conditions were used to ensure perfect absorption of electromagnetic radiation at the simulation boundaries.



**Figure 9.5:** 3D FDTD calculated scattering cross-section for isolated NW and antenna coupled NWs, as labeled in the figure.

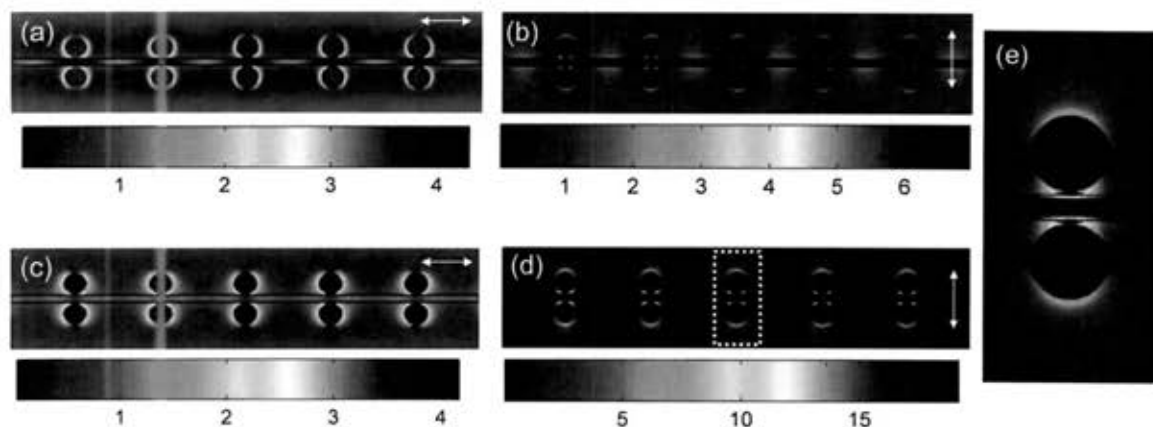
In Figure 9.5 the FDTD calculated scattering cross-sections are plotted for the isolated NW, as well as the antenna coupled NWs. Each cross-section plotted is the summed product of two calculations carried out with incident light longitudinally and transversely polarized with respect to the nanowire to give the total scattering response. We notice in Figure 9.5 that in the case of an isolated NW, two resonances are present around  $\lambda = 450$  nm and  $\lambda = 950$  nm. The resonance at 450 nm corresponds to the excitation of strongly scattering Mie resonances of NWs, as previously discussed in the literature (Wang and Leu, 2012; Muskens et al., 2009; Muskens et al., 2008), while the second peak is attributed to longitudinal resonances of the wire. Upon coupling the nanoantennas to the NW, additional resonances become evident in the scattering spectrum. In the case of  $d = 215$  nm, we notice a dominant peak at  $\lambda = 855$  nm. To better understand the origin of this resonance, the electric near-field distribution in the

horizontal plane of the array is plotted in Figure 9.6 for the case of  $d = 215$  nm at  $\lambda = 855$ . The field is plotted for (a) longitudinal and (b) transverse polarization with respect to the wire, as labeled in the figure by the white arrows.



**Figure 9.6:** Calculated electric near-field distribution of the nanoantenna coupled NW system with  $d = 215$  nm, plotted in the horizontal plane of the array (half-way up the cylinder in the  $z$ -dir) at  $\lambda = 855$  nm. The field is plotted for (a) longitudinal and (b) transverse polarization with respect to the wire, as labeled in the figure by the white arrows.

In both the longitudinal and transverse case, we notice field is weakly quasi-statically coupled to the NW. At a distance of 215 nm, strong quasi-static coupling is not possible. However, as evident in both polarizations, the antenna is still capable of radiatively funneling light to wire. The scattering resonance at  $\lambda = 855$  nm is dominated by the plasmonic response of the antennas, only slightly perturbed by the presence of the nanowire. To examine the resonances observed for the case of  $d = 10$  nm, the electric near-field distribution in the horizontal plane of the array are plotted in Figure 9.7.



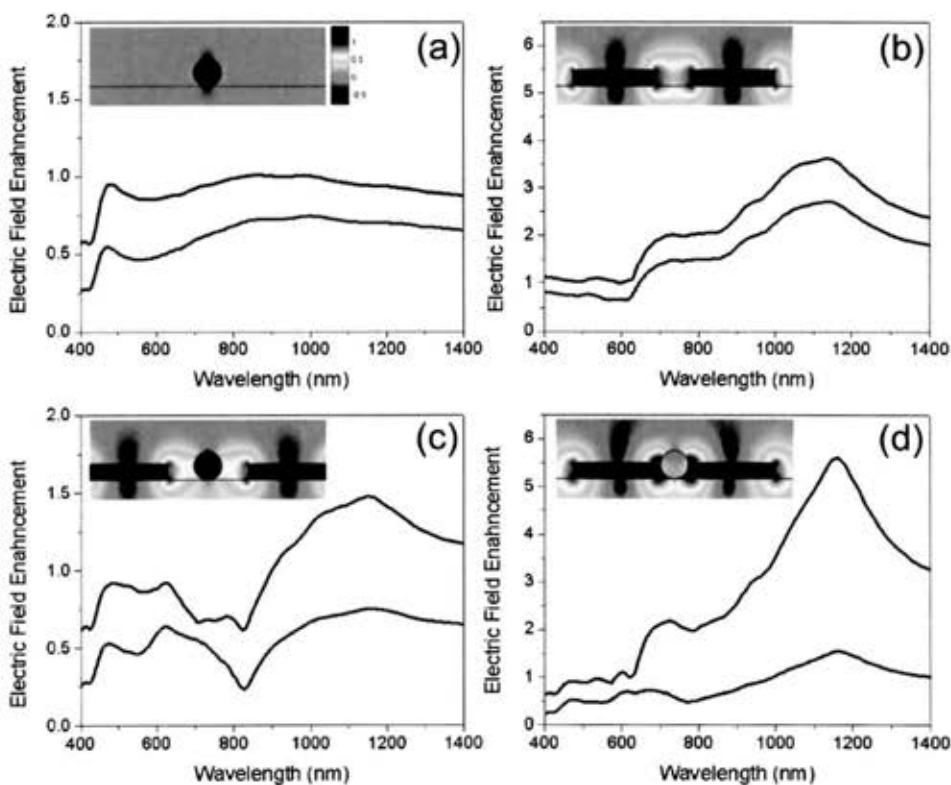
**Figure 9.7:** Calculated electric near-field distribution of the nanoantenna coupled NW system with  $d = 90$  nm, plotted in the horizontal plane of the array (half-way up the cylinder in the  $z$ -dir). The field is plotted at  $\lambda = 735$  nm for (a) longitudinal and (b) transverse excitation and at  $\lambda = 1150$  nm for (c) longitudinal and (d) transverse excitation. The magnified region denoted by the dashed box in panel (d) is plotted in panel (e).

Figure 9.7(a,b) plots the near-field distribution ( $d = 10$  nm) at the first scattering resonance located at  $\lambda = 735$  nm for both polarizations. The electric field profile now demonstrates strong near-field coupling of the NW resonance with the Au nanoantennas. The increased coupling serves to reduce the nanoantenna scattering as more energy is lost to the high field concentrations in the Au nanocylinders and resulting absorption. This phenomenon is clearly observable in the scattering spectra plotted in Figure 9.5. As the dimer gap is closed, the resonance peak attributed to the antenna scattering is seen to decrease and blue-shift as the coupling increases.

The second peak, located in the near-IR, arises from even more intense quasi-static coupling. Figure 9.8(c,d) plot the near-field distribution located at  $\lambda = 1150$  nm for both polarizations. We notice the maximum field amplitude between the nanocylinder and NW is enhanced approximately 19 times for the transvers polarization in Figure 9.8(d). Figure 9.8(e) plots a magnified view of the region denoted by the dashed box in

Figure 9.8(d) for clarity. Additionally, we note that the NIR resonance is only present for the separations of 10 nm and 15 nm, supporting the theory that the origin of the resonance is founded in strong quasi-static coupling.

To further examine the near-field properties of the nanoantenna coupled NWs, the cross-sectional ( $z$ - $y$  plane) spatially averaged and maximum electric field enhancement values inside the region of the NW is plotted versus wavelength in Figure 9.8.



**Figure 9.8:** Cross-sectional average (red) and maximum (black) electric field enhancement values inside the region of the NW are plotted for the case of (a) isolated NW, (b) isolated dimer pair with  $d = 10$  nm, (c) antenna coupled NW with  $d = 215$  nm, and (d) antenna coupled NW with  $d = 10$  nm. Insets are electric field cross-sections, plotted at 1165 nm in log-scale for each configuration.



For the case of the isolated NW (Figure 9.8a), both the averaged and maximum field values inside the NW are lower than the pump fields, as expected, given the high index of refraction of GaAS ( $n \approx 3.4$  in the NIR). For the weakly coupled system (Figure 9.8c), we notice the average field is still lower than the pump fields; however small enhancements on the order of 50% are observed near the surface of the NW. In the case of the strongly coupled system (Figure 9.8d), the maximum field inside the NW rises to almost 6 times that of the pump fields. For qualitative comparisons, Figure 9.8b plots the isolated dimer pair with the same spacing in Figure 9.8d. While direct comparisons are not possible due to the index differences with and without the NW, it is important to note that coupling is not only between the dimer pairs, but between the NW and the nanocylinders. Even in the presence of a higher index medium, the antenna coupled system is able to produce a higher maximum enhancement than that of the isolated dimer pair.

These results demonstrate that the designed nanostructures offer the possibility to flexibly tailor the electromagnetic coupling between NWs and the confined modes of plasmonic nanoantennas, resulting in nanoscale regions with controllable and strongly enhanced near-field intensity.

### 9.2.3 SH-E Spectroscopy of Antenna Coupled GaAs NWs

To experimentally support the predicted near-field coupling of NWs and dimer plasmon antennas, SH-E spectroscopy is performed. This technique, introduced in section 9.1, provides a powerful tool to experimentally probe and analyze the near-field

resonances in metallic nanoparticles (Walsh and Dal Negro, 2013). In the SH-E experiment, ultrafast laser pulses are generated by a tunable mode locked Ti-Sapphire laser with a pulse duration of 100 fs and a duty cycle of 82 MHz. The beam is modulated at 67 Hz by a mechanical chopper with a 50% duty cycle and is steered with Ag mirrors. A 700 nm long pass filter prior to the sample removes any SHG signal produced by the optical components. Additionally, the linearly polarized beam is passed through a quarter-wave plate, creating a circularly polarized beam to allow for consistent pumping conditions regardless of the nanowire's orientation on the substrate. The excitation beam is then focused on the nanostructure to a spot size of approximately 5  $\mu\text{m}$  by a 50x objective (NA 0.5) from the backside of the sample. The SHG is then collected in transmission mode with a 100x objective (NA 0.8) and is detected with a photon multiplier tube (PMT) and a lock-in amplifier (Oriel Merlin) after passing through a monochromator (Cornerstone 260 1/4 m, 1200 lines/mm, 500 nm blaze). This defines an acceptance angle of  $\pm 30^\circ$ , which enables the collection of intense SHG signal in our experimental configuration (Walsh and Dal Negro, 2013). The excitation beam is removed with a 670 nm short pass filter prior to the monochromator. A CCD coupled to a reflection microscope is used for alignment. A removable mirror is placed in front of the camera to direct the SHG signal to the detector. The time averaged excitation power is kept constant at 5 mW for all measurements.

Figure 9.9 illustrates a schematic of the experimental setup utilized for the SH-E analysis. The second harmonic spectra are collected for varying pumping wavelengths and are shown in Figure 9.9b for the case of the antenna coupled NW with  $d = 10$  as an

example. In Figure 9.9c the peak wavelengths of the measured SHG spectra are plotted as a function of the pump wavelength. The linear fit to these data features a slope of exactly 0.5, as expected for the SHG process.

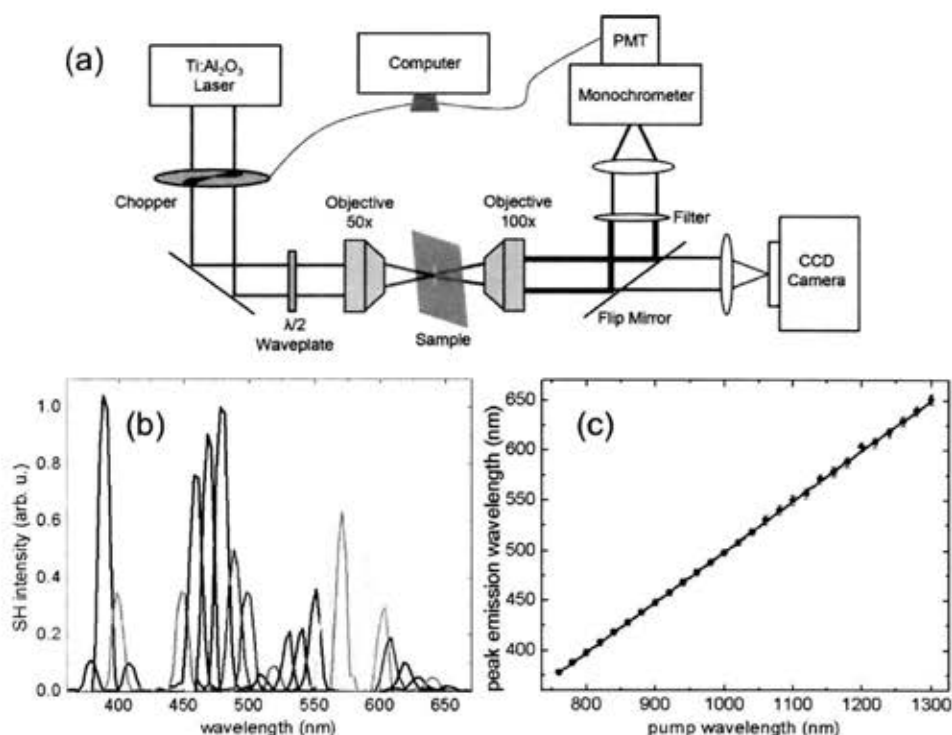


**Figure 9.9:** (a) Diagram of SH-E experimental setup. (b) Pump ( $\lambda_{\omega} = 760$  nm) power dependence of SH signal ( $\lambda_{2\omega} = 380$  nm) from representative array ( $d = 10$  nm). (c) The peak wavelengths of the measured SHG spectra are plotted as a function of pump wavelength, resulting in a slope of 0.5.

The SH-E spectra measured for the investigated samples are plotted in Figure 9.10. Notice that the SH-E spectrum of the isolated nanowire features a prominent peak around 880 nm. The measured resonance arises from the transverse Mie resonance supported by the NW, which spectrally overlaps with the SHG resonance. In fact, previous studies have reported SHG signal from GaAs NWs of comparable sizes,

supported by Mie resonances in the same spectral region as our study (Grange et al., 2012).

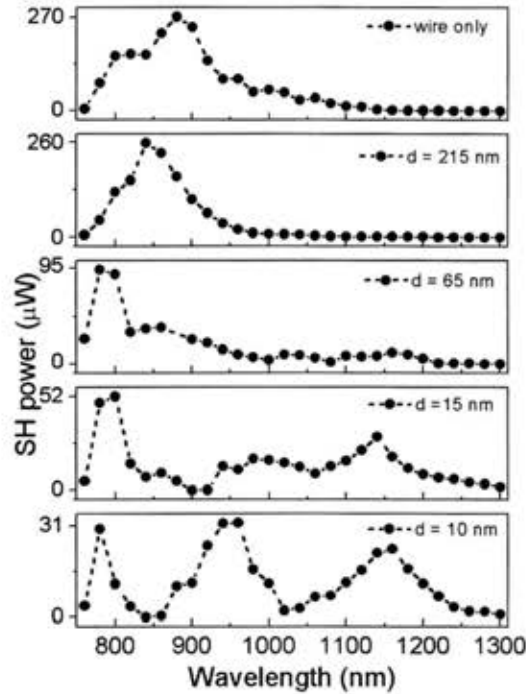


**Figure 9.10:** Experimentally measured SH-E spectra from NW only and NW-coupled antennas with  $d = 215$  nm,  $d = 65$  nm,  $d = 15$  nm and  $d = 10$  nm, as labeled in the figure.

As the weakly coupled antennas ( $d = 215$  nm and 65 nm) are probed by SH-E spectroscopy, we notice a slight blue-shift of the NW resonance, which is attributed to the Mie resonances of the cylinder being perturbed by the increasing presence of the nanocylinders. Moving to the strongly coupled regime ( $d = 15$  and 10 nm), new spectral features arise in the NIR. FDTD near-field simulations of Figure 9.8 predict high near-field concentrations on the surface and inside of the GaAs NW, peaked at 1165 nm for the case of  $d = 10$  nm. This strong enhancement of the fields directly coincides with the SH-E peak measured on the same array, demonstrating the ability to couple near-fields to

NWs through nanoplasmonic arrays.

In examining the absolute intensities of the SH signal, we notice a global decrease as the antennas become strongly coupled (see y-axis scales for each device). The current study is still ongoing as open questions still remain about some of the measured phenomenon. The decrease in SH absolute intensities can possibly be explained by a reduction of scattering through enhanced near-fields and thus increased metallic absorption. While this could account for some of the reduced intensity, further studies are potentially still needed for confirmation. Additionally, a complete understanding of a third peak in the SH-E spectra ( $\lambda = 950$ ) for the strongly coupled case is still outstanding. These resonances could be potentially induced by surface defects in the NW. Currently, further characterization of the NW quality and dispersion is ongoing at EPFL. While these few questions remain open, the results are still significant. The study has successfully demonstrated the near-field coupling of plasmonic nanoantenna arrays to NWs through SH-E spectra for the first time.

### 9.3 Conclusion

In this chapter, a polarization selective, grating-assisted nanoantenna has been designed and experimentally demonstrated, that allows for multi-wavelength focusing into a subwavelength spot. These structures potentially open new paths for molecular linear and nonlinear spectroscopy, Raman spectroscopy, and near-field optical lithography. Additionally, by combining the bottom-up fabrication of NWs with the top-down fabrication of plasmonic nanoantennas, arrays of Au nanocylinders have been

optically coupled to individual GaAs NWs. The optical resonances of these coupled nanostructures have been investigated experimentally by SH-E spectroscopy and found to be in good qualitative agreement with 3D FDTD simulations. These studies have advanced the possibility of engineering novel metal-dielectric resonant nanostructures, which could enable the realization of high-efficiency solar cells, detectors and nonlinear optical devices with dramatically reduced footprints and energy consumption.

## Chapter 10

### 10 Aperiodic SERS Substrates

In this chapter, deterministic aperiodic arrays of metal nanoparticles are utilized in combination with a multilayer dielectric/metallic stack to create reproducible surface enhanced Raman scattering (SERS) substrates. This multilayer structure combines LSPs supported by the nanoparticles with SPPs excited on a buried Au film. Stack and cylinder parameters are optimized using 3D FDTD for maximum field enhancement at the pump wavelength of the Raman experiment. Experimental results will show SERS enhancement factors as high as  $1.1 \times 10^7$  for these engineered substrates.

#### 10.1 Surface Enhanced Raman Scattering

Raman scattering occurs during inelastic collision of photons with molecules (Raman and Krishnan, 1928). In this scattering process, photons will either gain or lose energy from the interacting molecules. The change in photon energy implies a change in frequency  $\Delta\nu = \Delta E/h$ , resulting in scattered photons  $h\nu_s$  with a shifted frequency relative to the excitation photons  $h\nu_L$  by the energy of characteristic molecular vibrations  $h\nu_M$  (Kneipp et al., 1997). Therefore, a Raman spectrum comprising several different Raman peaks generated by scattering from different molecular vibrations provides a vibrational signature or "fingerprint" of a molecule.

The frequency shifts can occur in two ways. The first occurs when the photons interact with a molecule in its vibrational ground state and the photon loses energy upon

scattering. This effect is known as Stokes scattering. The second possibility comes in the form of an anti-Stokes interaction. Here the photons interact with a molecule in an excited state and can gain energy, resulting in a shifted peak on the high-energy side. The Stokes and anti-Stokes frequencies of these Raman bands are then, respectively, represented as:

$$\nu_{aS} = \nu_L + \nu_M \quad (10.1)$$

$$\nu_S = \nu_L - \nu_M \quad (10.2)$$

Generally, the scattering is dominated by the Stokes type due to the fact that only a small fraction of molecules, determined by the Boltzmann population, is in an excited vibrational state and able contribute to anti-Stokes Raman scattering. The scattering signal power  $P_s(\nu_s)$  of a Raman line depends on excitation intensity  $I(\nu_L)$ , the number of Stokes-active scattering centers  $N$  and the Raman cross-section  $\sigma_{RS}$ , where  $\sigma_{RS}$  is determined by the polarizability derivative of the molecular vibration. The relation follows as:

$$P_s(\nu_s) = N\sigma_{RS}I(\nu_L) \quad (10.3)$$

Figure 10.1 depicts the Stokes and anti-Stokes scattering described here, as well as the fluorescence process. The figure displays scattering energy level pictures and representative spectra for each process. Of note, is the shape difference in resulting spectra from the two mechanisms. The fluorescence process has broad spectral features due to non-elastic electron relaxation to the lower edge of the excited level; however



Raman transitions are much sharper (Maier, 2007). These sharp features are what enable the detailed analysis of the molecules under study.

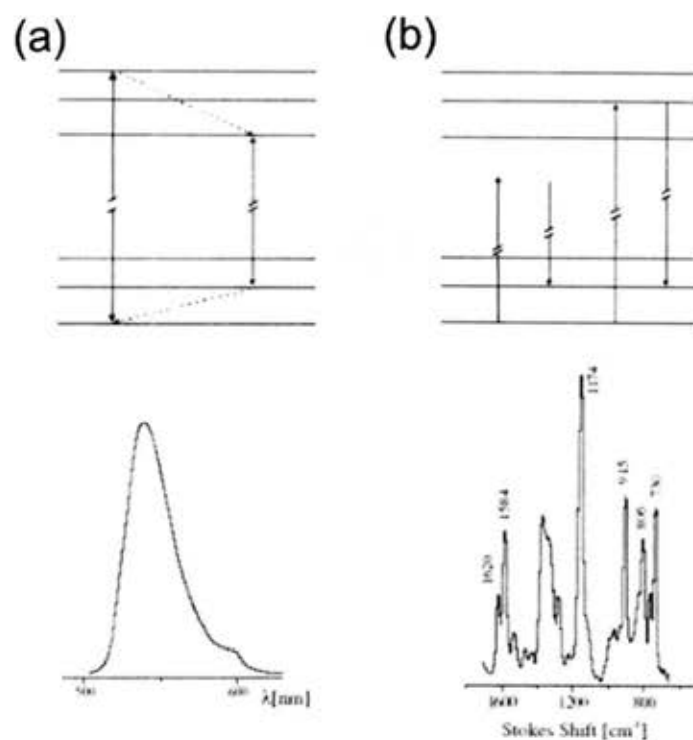


**Figure 10.1:** Schematic depiction of (a) fluorescence and (b) Raman scattering energy level pictures and representative spectra. Image modified from (Kneipp et al., 2002).

Typical Raman scattering cross-sections  $\sigma_{RS}$  are usually more than ten orders of magnitude smaller than those of a fluorescent process, depending on whether the scattering is non-resonant or resonant (Maier, 2007). To enhance the inherently low signal of the Raman scattering, nanoplasmonic structures are employed. When the Raman-active molecule is within the near-field of metallic nanostructures, the response can be greatly enhanced. This process is known as Surface Enhanced Raman Spectroscopy or SERS. The enhancement of the Raman signal  $P_S$  can be driven by two effects. The first, in which the Raman cross-section is increased ( $\sigma_{SERS} > \sigma_{RS}$ ) due to the

change in the local environment of the molecule, is called the chemical or electronic contribution. The theoretical maximum enhancement due to this change in cross-section is of the order of 100 (Maier, 2007).

The second and more dominate possible contribution to the total enhancement, is the increased electromagnetic field due to the excitation of LSPs and the crowding of electric field lines (*lightning rod effect*) at the metal interface (Kerker, Wang and Chew, 1980; Gersten and Nitzan, 1980). These phenomena lead to an enhancement of both the pump and emitted light fields, expressed by

$$L(\nu) = |E_{loc}(\nu)| / |E_0|, \quad (10.4)$$

where  $|E_{loc}|$  the local is field amplitude at the Raman active site and  $L(\nu)$  is the electromagnetic enhancement factor. The total power of the Stokes beam under the SERS condition is then

$$P_S(\nu_S) = N\sigma_{SERS}L(\nu_L)^2L(\nu_S)^2I(\nu_L). \quad (10.5)$$

As the difference in frequency  $\Delta\nu = \nu_L - \nu_S$  between the incoming and scattered photons is generally much smaller than the line-width of a LSP mode, the magnitudes of the two electromagnetic enhancements are approximately equivalent ( $|L(\nu_L)| \approx |L(\nu_S)|$ ) (Maier, 2007). This approximation leads to the key result that the electromagnetic contribution to the total SERS enhancement is proportional to the fourth power of the field enhancement factor or equivalently stated by the commonly used expression for the enhancement of the power of the Stokes beam (Kerker, Wang and Chew, 1980):

$$R = \frac{|E_{loc}|^4}{|E_0|^4}. \quad (10.6)$$

Through the past 20 years, SERS has become a very powerful analytical spectroscopy technique. SERS has been successfully utilized in label-free chemical and biological sensing (Moskovits, 1985; Kneipp et al., 1995; Willets and Van Duyne, 2007), protein binding events (Delfino, Bizzarri and Cannistraro, 2005), tissue imaging (Feng et al., 2009), and other molecular detection down to single molecule sensitivity (Kneipp et al., 1997; Xu et al., 1999; Xu et al., 2000).

Several different approaches to create SERS substrates with large enhancements have been explored. One effective technique is found in *hot spot* engineering, utilizing closely spaced plasmonic particles to enhance local fields between the structures (Gunnarsson et al., 2001; Liu et al., 2008; Talley et al., 2005). Alternatively, LSP resonances of individual metallic nanoparticles on planar substrates can generate high Raman enhancements (Freeman et al., 1995; Oldenburg et al., 1999; Jackson and Halas, 2004). While such techniques prove to be viable, most SERS substrates utilized random “roughening” of metal surfaces for large Raman enhancements. This typically is achieved by etching or by colloidal synthesis of nanoparticles, resulting in aggregates statistically described by fractal morphologies (Shalaev, 2002; Wang et al., 2003). While these roughened surfaces have led to successful applications in single molecule spectroscopy (Kneipp et al., 1998), this technique lacks reproducibility and engineering design rules for deterministic optimization.

To combat the issue of engineerability in complex and disordered systems, Gopinath *et al* proposed and experimentally demonstrated the use of deterministic aperiodic (DA) arrays of Au nanoparticles as a novel approach for the design and implementation of engineered SERS substrates (Gopinath, Boriskina, Reinhard, et al., 2009; Gopinath, Boriskina, Premasiri, et al., 2009). In particular, DANS have been shown to enable the engineering of plasmonic arrays with large spectral flatness and particle filling fractions necessary to achieve a high density of electromagnetic hot spots over a broader frequency range and large area (Carlo Forestiere, Gary F Walsh, et al., 2009). Gopinath *et al*, demonstrated aperiodic arrays of Au nanocylinders with Raman enhancement values of  $\sim 5 \times 10^5$ , and  $\sim 5 \times 10^7$  with the implementation of aperiodic arrays of Au nanotriangles (Gopinath, Boriskina, Reinhard, et al., 2009). Additionally, by adding bottom-up fabrication technique on top of DANS arrays of Au nanocylinders, a hybrid multi-scale aperiodic nanostructure was created, resulted in enhancement factors of  $\sim 10^8$  (Gopinath, Boriskina, Premasiri, et al., 2009).

## 10.2 Coupled SERS System Design

To further build upon the nanoplasmonic aperiodic platform for SERS substrates, this study aims to couple DA arrays of nanocylinders to a Au film buried in a thin layer of SiO<sub>2</sub> (see Figure 10.2). Recent studies have investigated this configuration in the context of coupling between the LSP of Au nanoparticles and SPP supported by the buried Au film (Chu and Crozier, 2009; Chu, Banaee and Crozier, 2010).

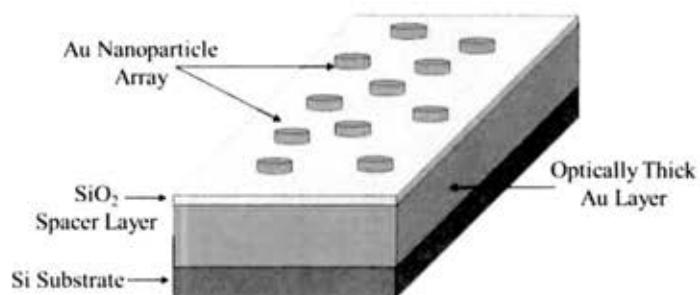


**Figure 10.2:** Schematic of plasmonic double layer coupled SERS substrate. The structure consists of Au nanocylinders arrays fabricated onto a thin SiO<sub>2</sub> spacer on top of a continuous and optically-thick Au film.

Coupling between LSPs and SPPs have been found to enhance the local field intensity, leading to double-resonate features in the extinction spectra of the multiple-layer structures. The SERS enhancement for the double-resonance structure was found to be more than 2 orders of magnitude higher than that of Au nanocylinder arrays on a glass substrate (Chu, Banace and Crozier, 2010). Furthermore, the coupling with a periodic lattice has been modeled as a classical coupled oscillator and the effects of the particle density, the particle size and the SiO<sub>2</sub> spacer thickness on the coupling strength have been investigated (Chu et al., 2011). It has been shown that in tuning the geometrical parameters of the double resonance substrate, the resonance frequencies can be tailored for maximum SERS enhancement.

In this study, 3D FDTD simulations are utilized for optimizing the nanocylinder diameter  $d$  and SiO<sub>2</sub> spacer thickness  $t_{ox}$  for maximum field enhancement on the surface of the nanoparticle. In all simulations the nanocylinder height is kept a constant 30 nm-tall, while dispersion data from Johnson and Christy (Johnson and Christy, 1972) is used for Au and Palik (Palik, 1998) is used for SiO<sub>2</sub>. The simulation grid size surrounding the

Au nanocylinders is 2 nm in all three dimensions. Plane wave excitation at normal incidence to the substrate was used with the electric field oriented parallel to the surface of the substrate. PML boundary conditions were used to ensure perfect absorption of electromagnetic radiation at the simulation boundaries. Field monitors are placed on the surface of the nanocylinders to extract a maximum electric field intensity enhancement value for each simulation.

Prior to investigating the double layer configuration, a series of calculations were performed for the case of a Au nanocylinder on SiO<sub>2</sub> substrate, shown in Figure 10.3a. The cylinder size was varied from 130 nm to 200 nm in order to optimize the resonance of a single nanocylinder at the pump wavelength of  $\lambda_0 = 785$  nm, to be used in proceeding SERS experiments. Figure 10.3a shows the maximum field enhancement occurring at  $d = 175$  nm, confirming the experimental results measured by Gopinath *et al* (Gopinath, Boriskina, Reinhard, et al., 2009).

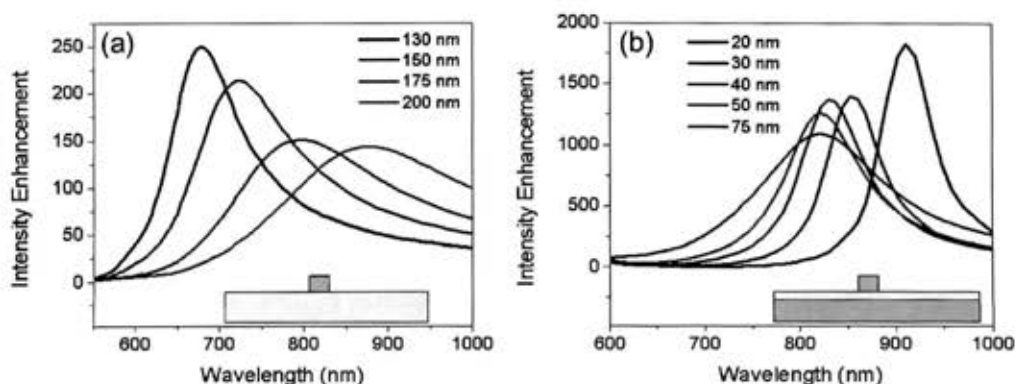


**Figure 10.3:** Maximum intensity enhancement spectra calculated on the surface of a single Au nanocylinder by 3D FDTD. (a) Calculated for a Au cylinder on a SiO<sub>2</sub> substrate with  $d = 130, 150, 175,$  and  $200$  nm. (b) Calculated for a Au cylinder ( $d = 150$  nm) on top of a SiO<sub>2</sub> with varying thickness of  $20, 30, 40, 50,$  and  $70$  nm on top of an optically thick Au layer.

For the case of the double layer configuration, several calculations were made under varying combinations of  $d$  and  $t_{ox}$  to find an optimal configuration at  $\lambda_0$ . Figure 10.3b plots the maximum intensity enhancement for a series of simulations carried out with  $d = 150$  nm and varying  $t_{ox}$ . We notice that as the film thickness is decreased, coupling between the Au cylinder and Au film increases, boosting the maximum intensity enhancement. Additionally, the peak intensity enhancement is observed to red-shift as the coupling increases, shifting further into the near IR for the smallest  $t_{ox}$  values. Results of two additional simulation sweeps are shown in Figure 10.4(a,b). Figure 10.4a plots the maximum intensity enhancement values for varying  $d$  at a constant  $t_{ox} = 10$  nm, while Figure 10.4b plots the same for varying  $d$  at a constant  $t_{ox} = 30$  nm. The two cases presented in Figure 10.4, represent two parameter spaces that yield maximum field enhancement at the desired pump wavelength 785 nm.

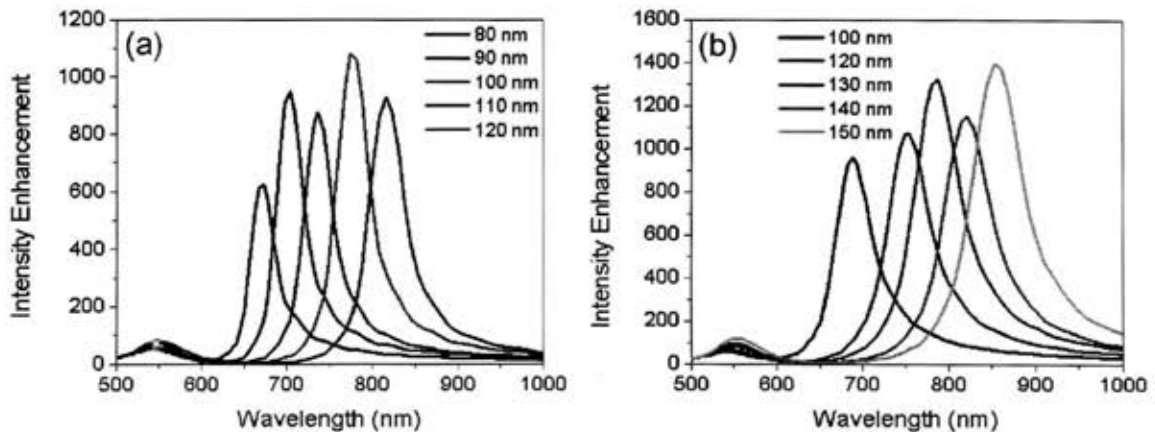


**Figure 10.4:** Maximum intensity enhancement spectra calculated on the surface of a single Au nanocylinder by 3D FDTD. (a) Calculated for a Au cylinder with  $d = 80, 90, 100, 110,$  and  $120$  nm on top of a  $\text{SiO}_2$  layer  $t_{ox} = 10$  nm-thick on top of an optically-thick Au layer. (b) Calculated for a Au cylinder with  $d = 100, 120, 130, 140,$  and  $150$  nm on top of a  $\text{SiO}_2$  layer  $t_{ox} = 30$  nm-thick on top of an optically-thick Au layer.

Figure 10.4 displays that for a given  $t_{ox}$  spacing (within limitations),  $d$  can be used to tune the resonance, as is the case with a glass substrate. In analyzing several combinations of  $d$  and  $t_{ox}$ , the optimal condition was found to be for  $t_{ox} = 30$  nm and  $d = 130$  nm, resulting in a maximum intensity enhancement value of  $\sim 1300$ . The value can further be enhanced by coupling the normally incident pump to SPPs more efficiently in the utilization of diffractive coupling (Chu, Banaee and Crozier, 2010; Chu et al., 2011).

Figure 10.5 plots the calculated cross-sectional electric field plots at  $\lambda_0$  for the optimized Au nanocylinder (a) on quartz with  $d = 175$  nm and (b) on a spacer/Au stack with  $d = 130$  nm and  $t_{ox} = 30$  nm-thick. Figures 10.5a and 10.5b are plotted on the same log-scale shown to the right of the figure. Figure 10.5a displays the well-known dipolar resonance of the single plasmonic nanocylinder, slightly perturbed by the presence of the  $\text{SiO}_2$  film. In the case of the double layer configuration, the field is dramatically enhanced by coupling between the nanocylinder and Au film. We notice enhanced field confined inside the spacer layer, on the surface of the Au nanocylinder, as well as enhanced scattered field radiating outward from the cylinder.

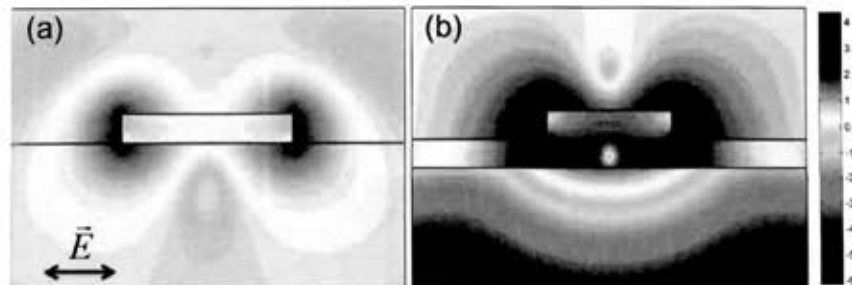


**Figure 10.5:** 3D FDTD calculated cross-sectional field plots (log scale) at  $\lambda = 785$  nm for the optimized Au nanocylinder (a) on quartz ( $d = 175$  nm) and (b) on a spacer/Au stack with  $d = 130$  nm and  $t_{ox} = 30$  nm-thick. Polarization orientation as noted in (a). Cross-sections plotted on the same scale shown to the right of (b).



The simulated results predict significant field enhancement for an engineered double layer plasmonic structure, ideal for SERS enhancement at 785nm. The optimized parameters are now transferred to physical samples for subsequent SERS experiments.

### 10.3 Experimental SERS

The two main components that determine the bandwidth and near-field enhancement of plasmonic arrays are the line-width of the LSP near-field resonance and the availability of spatial frequencies matching the Rayleigh cut-off condition over the entire bandwidth of the LSP quasi-static response (Dal Negro and Boriskina, 2011). By construction, DA arrays of metal nanoparticles offer a high density of spatial frequencies and are ideally suited to feed into multiple LSP resonances (Gopinath et al., 2008). Recently, Gopinath *et al* demonstrated that far-field diffractive coupling is crucial to account for the broad plasmonic bands, originating from photonic-plasmonic scattering resonances in DA arrays (Gopinath et al., 2008). Additionally, it has previously been shown that the engineering of dense arrays, characterized by large values of spectral flatness in the Fourier space, is necessary to achieve a high density of electromagnetic hot spots (Carlo Forestiere, Gary F Walsh, et al., 2009; Dal Negro and Boriskina, 2011).

In this study, four arrays were chosen for their high field enhancement capabilities in combination with their large spectral flatness and filling fractions. These arrays are the Fibonacci, Rudin-Shapiro, co-prime, and Galois (Dal Negro and Boriskina, 2011). In fact, Au nanocylinder arrays on quartz of all four types have previously been shown to be effective SERS substrates with enhancements on the order of  $10^5$  (Gopinath,

Boriskina, Reinhard, et al., 2009; Gopinath, 2010). The Fibonacci and Rudin-Shapiro have previously discussed in Chapter 5 and have been plotted along with their calculated Fourier space in Figures 5.3. The direct and reciprocal Fourier spaces of the Co-prime and Galois arrays are now shown in Figure 10.6(a,c) and 10.6(b,d), respectively.

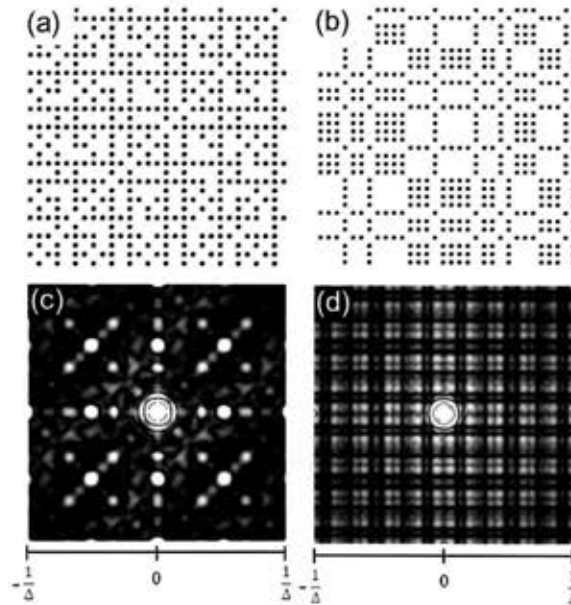


**Figure 10.6:** Direct space representations of (a) co-prime array and (b) Galois array. First pseudo-Brillouin zone plotted, as calculated by DFT, for the (c) Co-prime array and (d) Galois array.

The co-prime array is obtained by positioning metal nanoparticles in correspondence to each co-prime pair of integers in the two-dimensional plane (Carlo Forestiere, Gary F Walsh, et al., 2009). Since the co-prime array is symmetric about the  $45^\circ$  diagonal, so is the Fourier transform. Additionally, since the magnitude of the DFT is plotted, the  $-45^\circ$  diagonal appears as a symmetry axis as well (Carlo Forestiere, Gary F Walsh, et al., 2009). The Galois array is generated from finite Galois fields, producing binary valued periodic sequences with pseudo-random properties (Schroeder, 2009). The

Galois arrays diffraction spectra has a high density of spatial frequencies, theoretically a flat measure for infinite-size arrays (Dal Negro and Boriskina, 2011).

### 10.3.1 SERS Fabrication and Sample Preparation

Two sets of samples were fabricated for SERS experiments. Each set contains  $50\ \mu\text{m} \times 50\ \mu\text{m}$  Au nanocylinder Fibonacci, Rudin-Shapiro, co-prime, and Galois arrays of varying minimum inter-particle separations. The minimum separations tested were 25, 35, 50, 100, 150 and 300 nm. The first sample consists of Au nanocylinders on a quartz substrate, with the optimized  $d = 175$  nm and height of 30 nm. All nanoplasmonic cylinders were fabricated using the standard EBL process detailed in Chapter 4. The second set of plasmonic arrays are fabricated on a  $\text{SiO}_2/\text{Au}$  stack, with the optimized  $d = 130$  nm, cylinder height of 30 nm, and  $t_{\text{ox}} = 30$  nm. Fabrication for the dual layer sample begins with the thermal evaporation of 200 nm-thick Au layer on a Si chip. A 30 nm-thick layer, as measured by ellipsometry, is then deposited via RF magnetron. The  $\text{SiO}_2$  was sputtered from a bulk  $\text{SiO}_2$  target with 450 W, 10 sccm of Ar, and a pressure of 0.45 kPa, resulting in an approximate deposition rate of 15 nm/min. Figure 10.7 plots representative SEM micrographs of the four array types fabricated on quartz. Figure 10.8 plots representative SEM micrographs of the four array types fabricated on the dual layer substrate.

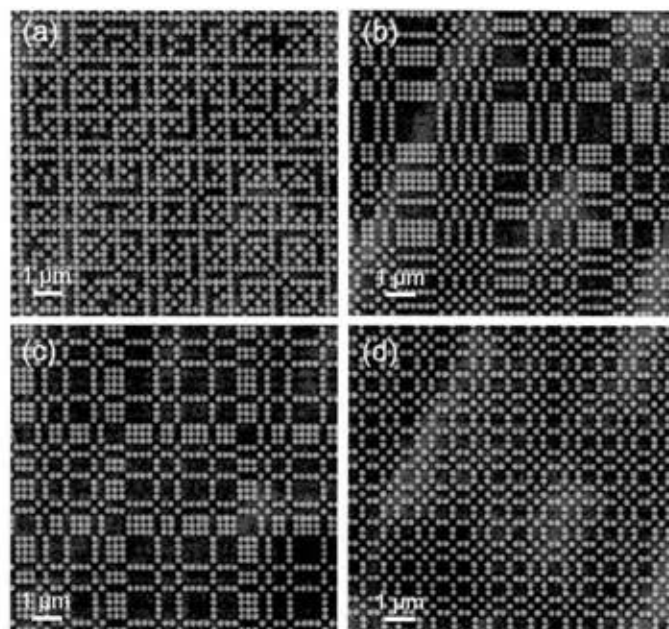


**Figure 10.7:** SEM micrographs of Au nanocylinder ( $d = 175$  nm) fabricated on a quartz substrate in a (a) Co-prime array, (b) Galois array, (c) Rudin-Shapiro array, and (d) Fibonacci array, with minimum edge-to-edge separation of 25 nm for all arrays shown.

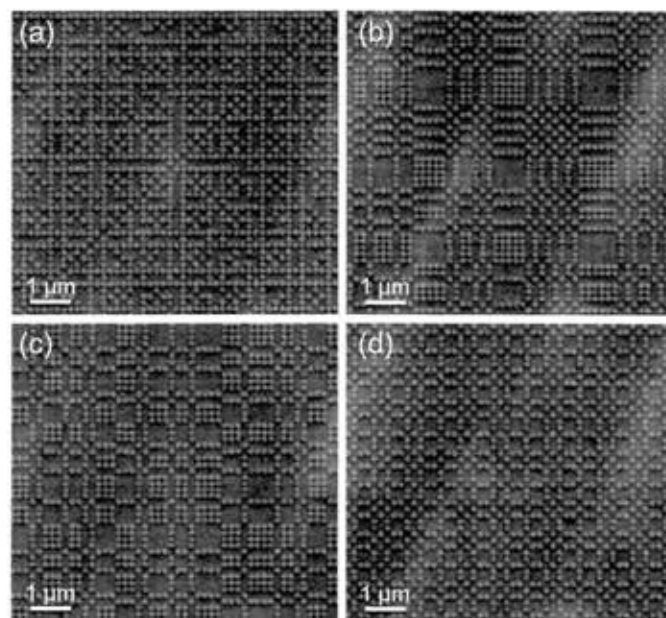


**Figure 10.8:** SEM micrographs of Au nanocylinder ( $d = 130$  nm) fabricated on a  $\text{SiO}_2/\text{Au}$  stack with  $d = 130$  nm and  $t_{\text{ox}} = 30$  nm-thick in a (a) Co-prime array, (b) Galois array, (c) Rudin-Shapiro array, and (d) Fibonacci array, with minimum edge-to-edge separation of 25 nm for all arrays shown.

It is relevant to note the morphology of the two different samples prior to Raman experiments. Figure 10.9 plots a high magnification SEM micrograph of (a) the Au on quartz sample and (b) the Au on SiO<sub>2</sub>/Au. We notice the increased surface roughness in the stacked sample (panel b), which will have an effect on the Raman signal. As mentioned previously, roughened metallic films are ideal for SERS substrates, as these small perturbations in the film will act to enhance local fields along the edges of the roughness.

The source of the roughness is from grain formation during the SiO<sub>2</sub> sputter deposition. The growth kinetics are controlled by the mobility of the impinging atoms on the surface before they condense and become entrapped in the film. This mobility can be enhanced by inputting energy to the system such as increasing deposition temperature or supplying impact energy through ion bombardment (Bhatt and Chandra, 2007). The roughness in the underlying SiO<sub>2</sub> is then transferred to the Au nanocylinders as evident by Figure 10.9b. In this study, the morphology will only boost the SERS signal; however for comparisons between the two samples, this additional roughness should be noted.

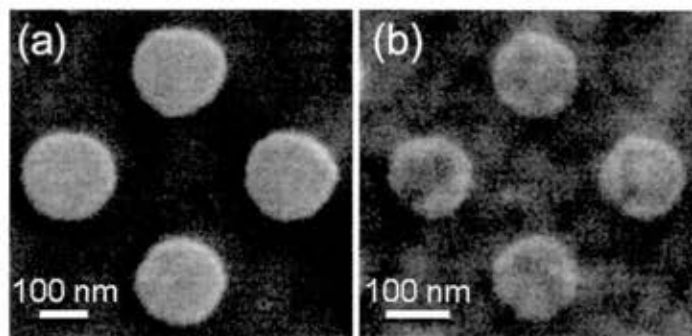


**Figure 10.9:** High magnification SEM micrographs of nanocylinders (a) shown in Figure 10.5d and (b) shown in Figure 10.6d.

Although several analytes exist for Raman spectroscopy, pMA (para-mercaptoaniline) was chosen for this study, which has Stokes modes at 390, 1003, 1077, 1180 and 1590  $\text{cm}^{-1}$  (Jackson and Halas, 2004). SERS samples are first cleaned in a plasma asher for 10 minutes in 300 sccm  $\text{O}_2$  and 300 W RF power. Substrates are then incubated for 12 hours in a 10 mM solution of pMA dissolved in ethanol (200 proof) to form a self-assembled monolayer over the sample surface. The samples are then rinsed in ethanol and dried with  $\text{N}_2$ .

### 10.3.2 Experimental SERS Measurements

The measurement setup utilizes a beam splitter to measure the scattered Raman signal in reflection and is described fully in the following reference (Pasquale, 2012). A CW diode laser is used as a pump ( $\lambda_0 = 785 \text{ nm}$ ) which has a FWHM  $< 0.15 \text{ nm}$ , with a maximum output power of 350 mW. The laser power focused through the objective on all measured samples was 20.0 mW. The backscattered signal is collected by a 40x objective (NA 0.65) and directed to an electrically cooled ( $-75^\circ\text{C}$ ) CCD (Andor DU401-BR-DD) via an Andor Shamrock 303i grating spectrometer. The pump laser is filtered out in reflection using a 785 nm notch filter. The grating used has 600 lines/mm blazed at 750 nm. Spectra were taken from a measured rectangular area of  $8.05 \mu\text{m} \times 64.4 \mu\text{m}$ , determined by the slit size and pixel selection on the CCD detector. The laser spot filled the entire collection area. All spectra are averaged over 5 measurements using a 0.2 second integration time, for background signal reduction. Frequency calibration of the grating is first performed using Si, which has a known Stokes shift of  $520 \text{ cm}^{-1}$ .

Figure 10.10a shows the complete Raman spectra for pMA molecular monolayers deposited on top of the Au nanocylinder Fibonacci arrays on a quartz substrate. Figure 10.10b plots the same for the case of Fibonacci arrays on the dual layer stack. Only the Fibonacci spectra are shown here for brevity; however measurements were taken on all four geometries and are summarized in Figure 10.11. The two dominant Stokes modes ( $1077\text{ cm}^{-1}$ ,  $1590\text{ cm}^{-1}$ ), arising from bending and stretching modes in the benzene rings of the pMA molecule, can clearly be distinguished in all the spectra. The intensity of the background signal varies for different arrays, in accordance with their respective filling fractions. In qualitatively comparing the two results, it is clear the double layer SERS substrate possesses a higher signal-to-noise ratio than the quartz sample.

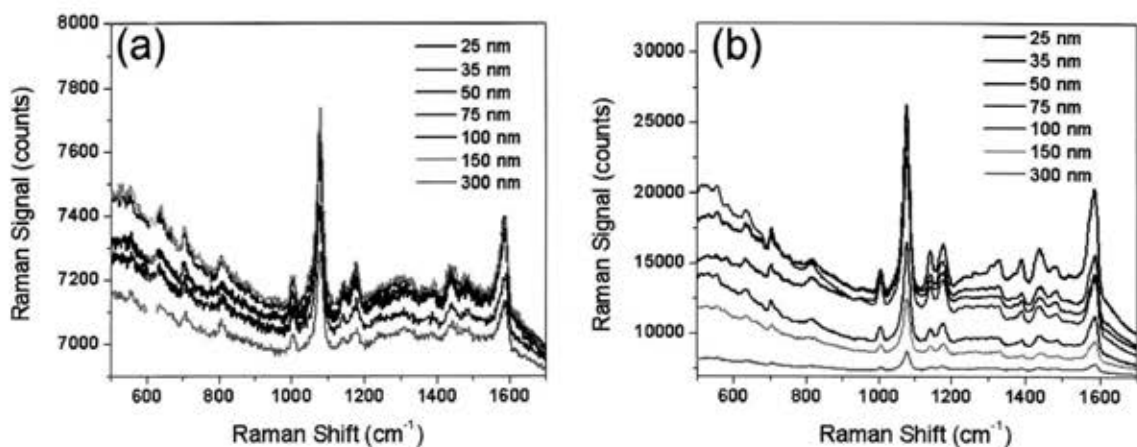


**Figure 10.10:** Experimental Stokes SERS spectra of pMA on (a) Fibonacci array of Au nanocylinders on quartz ( $d = 175\text{ nm}$ ) with minimum inter-particle separations listed in the figure. Experimental Stokes SERS spectra of pMA on (b) Fibonacci array of Au nanocylinders on a spacer/Au stack with  $d = 130\text{ nm}$  and  $t_{ox} = 30\text{ nm}$ -thick and with minimum inter-particle separations listed in the figure.

In order to quantify the SERS enhancement factor for the different arrays and substrates, the Raman peak at  $1077\text{ cm}^{-1}$  of the spectra is monitored. After background



subtraction, the SERS enhancement factor can be estimated from the experimental data by following the procedure discussed in (Jackson and Halas, 2004). Removal of the background contribution is done by using a polynomial fit (4<sup>th</sup> order) of the Raman spectrum. The fit will follow the background of the spectrum with little influence from the sharp Raman peaks. The value of the fit at  $1077\text{ cm}^{-1}$  is subtracted from the measured Raman signal, leaving a background corrected value for the Raman signal.

The experimentally measured SERS enhancement is given by the ratio of Raman signal per molecule measured on the engineered substrates and the reference Raman signal per molecule originating from the pMA bulk crystal (Jackson and Halas, 2004). The SERS enhancement  $G_{SERS}$  is then represented by

$$G_{SERS} = \frac{RS_{En}N_R}{RS_RN_{En}}, \quad (10.7)$$

where  $RS_{En}$  is the measured enhanced Raman signal from the nanocylinder arrays and  $N_{En}$  is the estimated number of molecules on the array which contribute to the measured signal. The number of molecules contributing to the SERS effect  $N_{En}$  can be estimated as the ratio of the total Au surface illuminated by the laser beam and the geometrical cross-section of the individual pMA molecules ( $0.3\text{nm}^2$  per molecule) (Mohri et al., 1998). Additionally, the  $RS_R$  and  $N_R$  are the analogous quantities measured from the reference pMA sample in the absence of the SERS substrate. The latter quantity is calculated using the following formula:



$$N_R = \frac{B_v D_{pMA} A}{M_{pMA}}, \quad (10.8)$$

where  $B_v$  is the optical excitation volume ( $8.05\mu\text{m} \times 64.4\mu\text{m} \times 3.72\mu\text{m}$ ),  $D_{pMA}$  is the density of pMA ( $1.05 \text{ g/cm}^3$ ) in the reference bulk crystal,  $A$  is Avogadro's number, and  $M_{pMA}$  is the molecular weight of pMA (125.19 AMU). The excitation volume is estimated as the product of the laser spot ( $8.05\mu\text{m} \times 64.4\mu\text{m}$ ) and the depth of focus  $D \approx 2\lambda / (NA)^2$ , where  $\lambda = 785 \text{ nm}$ ,  $NA = 0.65$ .

The Raman enhancement factors calculated at  $1077 \text{ cm}^{-1}$  from the experimental spectra by using Equation (10.7) are shown in Figure 10.11 for arrays of different morphologies, inter-particle separations and the two different substrates. The results in Figure 10.7a, for the case of Au nanocylinders on a quartz substrate, display a clear growth of the Raman enhancement with decreasing inter-particle distances in case of all the arrays. This is due to the exponential increase in the near-field coupling between the nanoparticles as they become less separated, which in turn increases the field enhancement and also the associated SERS enhancement factor (Maier, 2007). The values are comparable with those published by Gopinath *et al* for the same geometries (Gopinath, Boriskina, Reinhard, et al., 2009; Gopinath, 2010), validating the measurement techniques.

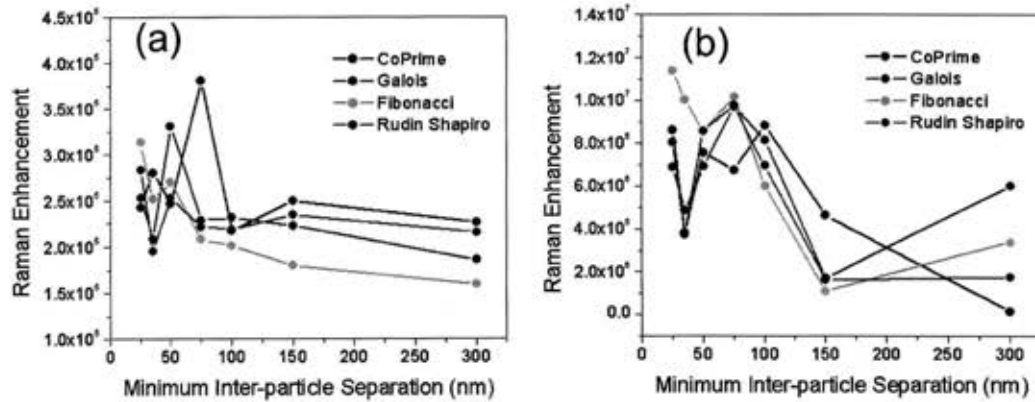


**Figure 10.11:** Enhancement factors calculated from experimental data by using Eq. 2 for aperiodic arrays of Au nanocylinders (a) on quartz ( $d = 175$  nm) and (b) on a  $\text{SiO}_2/\text{Au}$  stack with  $d = 130$  nm and  $t_{ox} = 30$  nm-thick.

For the case of the Au nanocylinders on the  $\text{SiO}_2/\text{Au}$  stack, shown in Figure 10.11b, a strong super linear growth is again measured for decreasing inter-particle separations; however now the Raman enhancement factors reach values on the order of  $10^7$ , almost 2 orders of magnitude greater than the optimized arrays on quartz. Enhancement values of  $10^7$  are evidence to enhanced near-field coupling between the nanocylinder arrays and the  $\text{SiO}_2$  buried Au films predicted by 3D FDTD simulations. It is important to note that these studies only access the spatially average SERS enhancement over the broad distribution of enhancements present within the volume of the SERS-active sample probed by the excitation beam (Gopinath, 2010). The experimental values are therefore considered a lower bound for hot-spot SERS enhancement on these chips (Moskovits, 1985).

## 10.4 Conclusions

By combining 3D FDTD calculations and experimental data, spatially averaged

SERS enhancement values on the order of  $10^7$  have been demonstrated, utilizing DA arrays of Au nanocylinders coupled to a Au film through a thin SiO<sub>2</sub> layer. The incorporation of a double layer moves the field of aperiodic SERS closer to enhancement factors capable of single molecule detection in designed nanostructures. Steps to go beyond enhancement factors of  $10^7$  are within reach with the introduced DA double-layered approach. By combining the double layer approach with other previously investigated DA array schemes, namely the utilization of nanogalaxies (Gopinath, Boriskina, Premasiri, et al., 2009) or by replacing the cylinders with a triangular geometry, even higher orders of magnitude enhancement could be readily achieved.

## Chapter 11

# 11 Conclusions and Future Prospects

## 11.1 Summary of Results

In this thesis, aperiodic Vogel spiral arrays have been presented as a novel platform for engineering enhanced photonic-plasmonic coupling and increased light-matter interaction over broad frequency and angular spectra for planar optical devices. A systematic study of the Vogel spiral's generation and geometric properties reveal the array is highly tunable and diverse in its complexity. The ability to deterministically encode numerical sequences in well-defined azimuthal components has been shown to be a powerful tool in engineering both scattered fields carrying several OAM values, as well as band-edge modes carrying the well-defined angular momenta.

Numerical studies have comprehensively explored the photonic density of states and bandedge modes of dielectric Vogel spiral arrays. It was shown that the rich structural complexity of Vogel spirals results in a multifractal photonic mode density and isotropic bandedge modes with distinctive spatial localization character. Additionally, designed Vogel spiral arrays of dielectric nanopillars were fabricated and characterized, displaying experimentally measured optical properties of a large photonic band gap. Several dielectric structures, including PMMA/laser dye doped films embedded in nanopillar arrays and silk laser dye doped films with air holes, have been fabricated with ongoing experiments towards lasing in Vogel spiral arrays.

The application of the Vogel spiral geometry to nanoplasmonics was also explored in this thesis. The experimental confirmation of a diffuse rotationally symmetric Fourier space was carried out, as well as an experimental demonstration of polarization insensitive planer diffraction. An experimental study of ultra-thin Schottky photo-detector cells coupled to GA-spiral and periodic Au nanoparticle arrays was also detailed. The broad high-angle scattering behavior of GA-spirals, along with their localized plasmonic resonances occurring at significantly reduced particles densities, allowed for a 31% spectrally integrated photocurrent enhancement, as compared to only 8% periodic arrays. Lastly, GA-spiral arrays of tightly spaced nanocylinders were found to generate more intense SHG signal when compared with periodic and Fibonacci arrays over a large range of particle separations. The behavior was attributed to the asymmetric near-field distribution of the GA-spiral at the pump wavelength.

In the latter half of the dissertation, the engineering of radiation-enhanced plasmonic coupling was explored. The design of a plasmonic grating-assisted nanoantenna was implemented, experimentally demonstrating polarization selective, multi-wavelength focusing into subwavelength spots. Additionally, by combining the bottom-up fabrication of NWs with the top-down fabrication of plasmonic nanoantennas, arrays of Au nanocylinders have been optically coupled to individual GaAs NWs. The optical resonances of these coupled nanostructures have been investigated experimentally by SH-E spectroscopy and found to be in good agreement with 3D FDTD simulations. In the final chapter of this thesis, DA arrays of Au nanocylinders were designed for maximum coupling with a SiO<sub>2</sub> buried Au film. Spatially averaged SERS enhancement values on

the order of  $10^7$  have been demonstrated. The results raise the aperiodic SERS platform closer to enhancement factors capable of single molecule detection in designed nanostructures.

## 11.2 Future Prospects

This research presented in this thesis has revealed a number of results and principles that may be applied to future nanophotonic devices and applications. Much of the initial efforts of this thesis focused on linking the dynamic range of structural characteristics of Vogel spirals to their photonic properties for arrays generated with varying angles. Prior to this work, most all studies focused on the photonic properties of the GA-spiral. In fact, upon revisiting Enrique Macia Barber's classification matrix (Figure 5.2), revisions may be necessary based on the LDOS study carried out in Chapter 7. As previously noted, the spectral character of the LDOS spectrum can be dramatically tuned by adjusting the divergence angle. The energy spectrum of the spiral lattice may not solely be limited to absolutely continuous spectral components, as suggested by Barber, but rather dependent upon the choice of divergence angle. Based on the findings of this thesis, I propose the following modification Barber's classification matrix, shown in Figure 11.1. Additionally, fractal structures have been added to the matrix as well as the larger category of aperiodic crystals, which spans the energy spectrum from pure point to singularly continuous.

Energy Spectrum	$\mu_{AC}$	Usual Crystalline Matter				
	$\mu_{SC}$	Aperiodic Crystals	Fractal Structures Fibonacci Period-Doubling	Thue-Morse	Vogel Spirals	Rudin-Shapiro?
	$\mu_P$		Other Quasicrystals			Amorphous Matter
			$\mu_P$	$\mu_{SC}$	$\mu_{AC}$	
Lattice Fourier Transform						

**Figure 11.1:** Proposed modification to the classification of aperiodic systems according to the spectral measures of their Fourier transform and their Hamiltonian energy spectrum (Barber, 2008).

As discussed in Chapter 7, several efforts to produce experimental lasing in a Vogel spiral array are currently in progress. At the time of this thesis, samples have been shipped to Tufts University (lab of Prof. Fiorenzo Omenetto) and Yale University (lab of Prof. Hui Cao). The goal of these experiments is not only to display lasing action in a spiral array, but to couple into one of the several unique band-edge modes predicted by numerical studies in this thesis. Potentially, these lasing modes could carry OAM and, to the best of my knowledge, would be the first demonstration of such a lasing mode generated on-chip. Additionally, further study of the transport mechanisms in Vogel spirals is needed. NSOM studies performed in this thesis showed interesting photonic coupling along parastichies lines, a feature which could be very useful for on-chip optical routing. In fact, within the past month of this thesis being written, our collaborators at

Yale University have shown the control of spatial vectors available for out-of-plane scattering in a spectrometer based on multiple light scattering by utilizing a GA-spiral array (Redding et al., 2013). The work could lead to a new approach to building miniature spectrometers for applications such as lab-on-a-chip spectroscopy

In this thesis, the Vogel spiral has been shown to be an ideal platform for light-trapping in thin-film solar cells. While this has been demonstrated for the case of a simple Schottky photo-detector, the application of the spiral array to a photovoltaic cell has yet to be achieved. Figure 11.2 illustrates a proposed configuration for a plasmonic Vogel spiral integrated into the back reflector of a thin-film p-i-n solar cell.

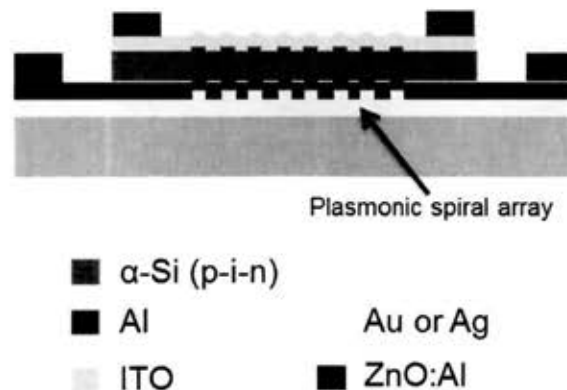


**Figure 11.2:** Proposed thin-film solar cell integrated with plasmonic Vogel spiral back reflector.

Additionally, the metallic spiral could be replaced with a dielectric array to reduce absorptive losses. The ability to fabricate reliable p-i-n junction solar cells and measure their quantum efficiencies at Boston University has limited progress in realizing this design. Through a potential collaboration with a solar cell focused group or time invested at Harvard CNS, this project could potentially be moved forward.



As these structures' diffuse rotationally symmetric Fourier space make them ideal for in-plane coupling, it also makes them a highly efficient geometry for light extraction. Using GA-spiral geometries, we have already demonstrated the enhanced omnidirectional light extraction and coupling of 1.55  $\mu\text{m}$  radiation using optically pumped light emitting materials (Lawrence, Trevino and Dal Negro, 2012). The next logical step in this line of research is to incorporate Vogel spiral arrays (plasmonic or dielectric) into electrically pumped light emitting diodes. The engineerability of the spiral Fourier space allows for this to be possible at wavelengths ranging from the UV to the NIR.

In conclusion, the ability to generate scattered radiation with programmable OAM sequences is a property of Vogel spirals that has a vast application space. With our colleagues in Prof. Sergienko's laboratory here at Boston University, we have proposed the use of Vogel spiral arrays as a unique type of entangled-photon source, as well as a entangled quantum key distribution protocol for efficiently sharing keys (Simon et al., 2013). The experimental demonstration of this protocol should continue to be highly pursued. Additional device applications within the fields of secure optical communication, classical cryptography, and quantum cryptography should also be explored.

## Bibliography

- Adam, J. A. (2009). *A Mathematical Nature Walk*. Princeton University Press.
- Adato, R., Yanik, A. A., Amsden, J. J., Kaplan, D. L., Omenetto, F. G., Hong, M. K., Erramilli, S., and Altug, H. (2009). Ultra-Sensitive Vibrational Spectroscopy of Protein Monolayers with Plasmonic Nanoantenna Arrays. *Proceedings of the National Academy of Sciences of the United States of America*, 106.46: 19227-32.
- Agarwal, G., and Jha, S. (1982). Theory of Second Harmonic Generation at a Metal Surface with Surface Plasmon Excitation. *Solid State Communications*, 41.6: 499-501.
- Agrawal, A., Kejalakshmy, N., Chen, J., Rahman, B., and Grattan, K. (2008). Golden Spiral Photonic Crystal Fiber: Polarization and Dispersion Properties. *Optics Letters*, 33.22: 2716-18.
- Albuquerque, E. L., and Cottam, M. (2003). Theory of Elementary Excitations in Quasiperiodic Structures. *Physics Reports*, 376.4: 225-337.
- Andrews, D. L. (2008). *Structured Light and Its Applications*. Elsevier.
- Anger, P., Bharadwaj, P., and Novotny, L. (2006). Enhancement and Quenching of Single-Molecule Fluorescence. *Physical Review Letters*, 96.11: 113002.
- Anker, J. N., Hall, W. P., Lyandres, O., Shah, N. C., Zhao, J., and Van Duyne, R. P. (2008). Biosensing with Plasmonic Nanosensors. *Nature Materials*, 7.6: 442-53.
- Ao, X., Liu, L., Wosinski, L., and He, S. (2006). Polarization Beam Splitter Based on a Two-Dimensional Photonic Crystal of Pillar Type. *Applied Physics Letters*, 89.17: 171115-15-3.
- Astratov, V., Whittaker, D., Culshaw, I., Stevenson, R., Skolnick, M., Krauss, T., and De La Rue, R. (1999). Photonic Band-Structure Effects in the Reflectivity of Periodically Patterned Waveguides. *Physical Review B*, 60.24: R16255.
- Atwater, H. A., and Polman, A. (2010). Plasmonics for Improved Photovoltaic Devices. *Nature Materials*, 9.3: 205-13.
- Bachelier, G., Butet, J., Russier-Antoine, I., Jonin, C., Benichou, E., and Brevet, P.-F. (2010). Origin of Optical Second-Harmonic Generation in Spherical Gold Nanoparticles: Local Surface and Nonlocal Bulk Contributions. *Physical Review B*, 82.23: 235403.
- Baddeley, A., and Turner, R. (2005). Spatstat: An R Package for Analyzing Spatial Point Patterns. *Journal of Statistical Software*, 12.6: 1-42.

- Bakker, R. M., Yuan, H.-K., Liu, Z., Drachev, V. P., Kildishev, A. V., Shalaev, V. M., Pedersen, R. H., Gresillon, S., and Boltasseva, A. (2008). Enhanced Localized Fluorescence in Plasmonic Nanoantennae. *Applied Physics Letters*, 92.4: 043101-01-3.
- Baldelli, S., Eppler, A. S., Anderson, E., Shen, Y.-R., and Somorjai, G. A. (2000). Surface Enhanced Sum Frequency Generation of Carbon Monoxide Adsorbed on Platinum Nanoparticle Arrays. *Journal of Chemical Physics*, 113: 5432.
- Barber, E. M. (2008). *Aperiodic Structures in Condensed Matter: Fundamentals and Applications*. Taylor & Francis.
- Beck, F., Polman, A., and Catchpole, K. (2009). Tunable Light Trapping for Solar Cells Using Localized Surface Plasmons. *Journal of Applied Physics*, 105.11: 114310-10-7.
- Bharadwaj, P., Deutsch, B., and Novotny, L. (2009). Optical Antennas. *Advances in Optics and Photonics*, 1.3: 438-83.
- Bhatt, V., and Chandra, S. (2007). Silicon Dioxide Films by Rf Sputtering for Microelectronic and Mems Applications. *Journal of Micromechanics and Microengineering*, 17.5: 1066.
- Biagioni, P., Huang, J.-S., and Hecht, B. (2012). Nanoantennas for Visible and Infrared Radiation. *Reports on Progress in Physics*, 75.2: 024402.
- Biswas, R., Bhattacharya, J., Lewis, B., Chakravarty, N., and Dalal, V. (2010). Enhanced Nanocrystalline Silicon Solar Cell with a Photonic Crystal Back-Reflector. *Solar Energy Materials and Solar Cells*, 94.12: 2337-42.
- Blanchard, R., Boriskina, S. V., Genevet, P., Kats, M. A., Tétienne, J.-P., Yu, N., Scully, M. O., Dal Negro, L., and Capasso, F. (2011). Multi-Wavelength Mid-Infrared Plasmonic Antennas with Single Nanoscale Focal Point. *Optics Express*, 19.22: 22113-24.
- Bohren, C. F., and Huffman, D. R. (2008). *Absorption and Scattering of Light by Small Particles*. Wiley-Vch.
- Boriskina, S. V., and Dal Negro, L. (2010). Multiple-Wavelength Plasmonic Nanoantennas. *Optics Letters*, 35.4: 538-40.
- Boriskina, S. V., Lee, S. Y., Amsden, J. J., Omenetto, F. G., and Dal Negro, L. (2010). Formation of Colorimetric Fingerprints on Nano-Patterned Deterministic Aperiodic Surfaces. *Optics Express*, 18: 14568-76.

- Boyd, G., Yu, Z., and Shen, Y. (1986). Photoinduced Luminescence from the Noble Metals and Its Enhancement on Roughened Surfaces. *Physical Review B*, 33.12: 7923.
- Boyd, R. W. (2008). *Nonlinear Optics*. San Diego, Ca. San Diego: Elsevier
- Bozinovic, N., Yue, Y., Ren, Y., Tur, M., Kristensen, P., Huang, H., Willner, A. E., and Ramachandran, S. (2013). Terabit-Scale Orbital Angular Momentum Mode Division Multiplexing in Fibers. *Science*, 340.6140: 1545-48.
- Brongersma, M. L., and Kik, P. G. (2007). *Surface Plasmon Nanophotonics*. Berlin: Springer.
- Buckheit, J., Chen, S., Donoho, D., Johnstone, I., and Scargle, J. "Wavelab850 ". 2005. Stanford University & NASA-Ames Research Center <[www.stat.stanford.edu/~wavelab/](http://www.stat.stanford.edu/~wavelab/)>.
- Butet, J., Bachelier, G., Russier-Antoine, I., Jonin, C., Benichou, E., and Brevet, P.-F. (2010). Interference between Selected Dipoles and Octupoles in the Optical Second-Harmonic Generation from Spherical Gold Nanoparticles. *Physical Review Letters*, 105.7: 077401.
- Canfield, B. K., Husu, H., Laukkanen, J., Bai, B., Kuittinen, M., Turunen, J., and Kauranen, M. (2007). Local Field Asymmetry Drives Second-Harmonic Generation in Noncentrosymmetric Nanodimers. *Nano Letters*, 7.5: 1251-55.
- Cao, H. (2003). Lasing in Disordered Media. *Progress in Optics*, 45: 317-70.
- Cao, H., Xu, J., Zhang, D., Chang, S., Ho, S., Seelig, E., Liu, X., and Chang, R. (2000). Spatial Confinement of Laser Light in Active Random Media. *Physical Review Letters*, 84.24: 5584-87.
- Capretti, A., Walsh, G. F., Minissale, S., Trevino, J., Forestiere, C., Miano, G., and Dal Negro, L. (2012). Multipolar Second Harmonic Generation from Planar Arrays of Au Nanoparticles. *Optics Express*, 20: 15797-806.
- Carron, K. T., Fluhr, W., Meier, M., Wokaun, a., and Lehmann, H. W. (1986). Resonances of Two-Dimensional Particle Gratings in Surface-Enhanced Raman Scattering. *Journal of the Optical Society of America B*, 3: 430.
- Casadei, A., Krogstrup, P., Heiss, M., Rohr, J. A., Colombo, C., Ruelle, T., Upadhyay, S., Sørensen, C. B., Nygard, J., and Fontcuberta i Morral, A. (2013). Doping Incorporation Paths in Catalyst-Free Be-Doped Gaas Nanowires. *Applied Physics Letters*, 102.1: 013117-17-4.

- Chan, Y., Chan, C., and Liu, Z. (1998). Photonic Band Gaps in Two Dimensional Photonic Quasicrystals. *Physical Review Letters*, 80.5: 956-59.
- Chen, C.-Y., Un, I.-W., Tai, N.-H., and Yen, T.-J. (2009). Asymmetric Coupling between Subradiant and Superradiant Plasmonic Resonances and Its Enhanced Sensing Performance. *Optics Express*, 17.17: 15372-80.
- Chen, C., DeCastro, A., and Shen, Y. (1981). Surface Enhanced Second Harmonic Generation. *Physical Review Letters*, 46: 145-48.
- Chhabra, A., and Jensen, R. V. (1989). Direct Determination of the F (A) Singularity Spectrum. *Physical Review Letters*, 62.12: 1327-30.
- Christ, A., Ekinici, Y., Solak, H., Gippius, N., Tikhodeev, S., and Martin, O. (2007). Controlling the Fano Interference in a Plasmonic Lattice. *Physical Review B*, 76.20: 201405.
- Chu, Y., Banaee, M. G., and Crozier, K. B. (2010). Double-Resonance Plasmon Substrates for Surface-Enhanced Raman Scattering with Enhancement at Excitation and Stokes Frequencies. *ACS Nano*, 4.5: 2804-10.
- Chu, Y., and Crozier, K. B. (2009). Experimental Study of the Interaction between Localized and Propagating Surface Plasmons. *Optics Letters*, 34.3: 244-46.
- Chu, Y., Wang, D., Zhu, W., and Crozier, K. B. (2011). Double Resonance Surface Enhanced Raman Scattering Substrates: An Intuitive Coupled Oscillator Model. *Optics Express*, 19.16: 14919-28.
- Dadap, J., Shan, J., Eisenthal, K., and Heinz, T. (1999). Second-Harmonic Rayleigh Scattering from a Sphere of Centrosymmetric Material. *Physical Review Letters*, 83.20: 4045.
- Dal Negro, L., and Boriskina, S. V. (2012). Deterministic Aperiodic Nanostructures for Photonics and Plasmonics Applications. *Laser & Photonics Reviews*, 6: 178-218.
- Dal Negro, L., and Feng, N.-N. (2007). Spectral Gaps and Mode Localization in Fibonacci Chains of Metal Nanoparticles. *Optics Express*, 15: 14396-403.
- Dal Negro, L., Feng, N. N., and Gopinath, A. (2008). Electromagnetic Coupling and Plasmon Localization in Deterministic Aperiodic Arrays. *Journal of Optics A: Pure and Applied Optics*, 10.6: 064013.
- Dal Negro, L., Lawrence, N., and Trevino, J. (2012). Analytical Light Scattering and Orbital Angular Momentum Spectra of Arbitrary Vogel Spirals. *Optics Express*, 20.16: 18209-23

- Danzer, L. (1989). Three-Dimensional Analogs of the Planar Penrose Tilings and Quasicrystals. *Discrete Mathematics*, 76.1: 1-7.
- Davidson, D. B. (2005). *Computational Electromagnetics for Rf and Microwave Engineering*. Cambridge University Press.
- De Bruijn, N. G. (1981). *Proceedings of the Koninklijke Nederlandse Academie van Wetenschappen*, A43.39.
- De Dood, M., Snoeks, E., Moroz, A., and Polman, A. (2002). Design and Optimization of 2d Photonic Crystal Waveguides Based on Silicon. *Optical and Quantum Electronics*, 34.1-3: 145-59.
- De Graef, M., and McHenry, M. E. (2007). *Structure of Materials: An Introduction to Crystallography, Diffraction and Symmetry*. Cambridge University Press.
- Delfino, I., Bizzarri, A. R., and Cannistraro, S. (2005). Single-Molecule Detection of Yeast Cytochrome by Surface-Enhanced Raman Spectroscopy. *Biophysical Chemistry*, 113.1: 41-51.
- Dennis, M. R., O'Holleran, K., and Padgett, M. J. (2009). Singular Optics: Optical Vortices and Polarization Singularities. *Progress in Optics*, 53: 293.
- Ditlbacher, H., Aussenegg, F., Krenn, J., Lamprecht, B., Jakopic, G., and Leising, G. (2006). Organic Diodes as Monolithically Integrated Surface Plasmon Polariton Detectors. *Applied Physics Letters*, 89.16: 161101-01-3.
- Drude, P. (1900). Zur Elektronentheorie Der Metalle. *Annals of Physics*, 306: 566–613.
- Dufouleur, J., Colombo, C., Garma, T., Ketterer, B., Uccelli, E., Nicotra, M., and Fontcuberta i Morral, A. (2010). P-Doping Mechanisms in Catalyst-Free Gallium Arsenide Nanowires. *Nano Letters*, 10.5: 1734-40.
- Dulea, M., Severin, M., and Riklund, R. (1990). Transmission of Light through Deterministic Aperiodic Non-Fibonacci Multilayers. *Physical Review B*, 42.6: 3680.
- Fano, U. (1941). The Theory of Anomalous Diffraction Gratings and of Quasi-Stationary Waves on Metallic Surfaces (Sommerfeld's Waves). *Journal of the Optical Society of America*, 31.3: 213-22.
- Feder, J. (1988). *Fractals*. New York: Plenum Press.
- Féridj, N., Laurent, G., Aubard, J., Lévi, G., Hohenau, A., Krenn, J., and Aussenegg, F. (2005). Grating-Induced Plasmon Mode in Gold Nanoparticle Arrays. *Journal of Chemical Physics*, 123: 221103.



- Feng, S., Lin, J., Cheng, M., Li, Y.-Z., Chen, G., Huang, Z., Yu, Y., Chen, R., and Zeng, H. (2009). Gold Nanoparticle Based Surface-Enhanced Raman Scattering Spectroscopy of Cancerous and Normal Nasopharyngeal Tissues under near-Infrared Laser Excitation. *Applied Spectroscopy*, 63.10: 1089-94.
- Ferry, V. E., Sweatlock, L. A., Pacifici, D., and Atwater, H. A. (2008). Plasmonic Nanostructure Design for Efficient Light Coupling into Solar Cells. *Nano Letters*, 8.12: 4391-97.
- Ferry, V. E., Verschuuren, M. A., Lare, M. C. v., Schropp, R. E., Atwater, H. A., and Polman, A. (2011). Optimized Spatial Correlations for Broadband Light Trapping Nanopatterns in High Efficiency Ultrathin Film a-Si: H Solar Cells. *Nano Letters*, 11.10: 4239-45.
- Ferry, V. E., Verschuuren, M. A., Li, H. B., Schropp, R. E., Atwater, H. A., and Polman, A. (2009). Improved Red-Response in Thin Film a-Si: H Solar Cells with Soft-Imprinted Plasmonic Back Reflectors. *Applied Physics Letters*, 95.18: 183503-03-3.
- Ferry, V. E., Verschuuren, M. A., Li, H. B., Verhagen, E., Walters, R. J., Schropp, R. E., Atwater, H. A., and Polman, A. (2010). Light Trapping in Ultrathin Plasmonic Solar Cells. *Optics Express*, 18.S2: A237-A45.
- Florescu, M., Torquato, S., and Steinhardt, P. J. (2009). Designer Disordered Materials with Large, Complete Photonic Band Gaps. *Proceedings of the National Academy of Sciences of the United States of America*, 106: 20658-63.
- Forestiere, C., Capretti, A., Dal Negro, L., Rubinacci, G., Tamburrino, A., and Miano, G. "Numerical Methods for the Electromagnetic Simulation of Complex Plasmonic Nanostructures." *Plasmonic Nanostructures*. Professional Scholarly Publishing Division, 2013. Print.
- Forestiere, C., Miano, G., Boriskina, S. V., and Dal Negro, L. (2009). The Role of Nanoparticle Shapes and Deterministic Aperiodicity for the Design of Nanoplasmonic Arrays. *Optics Express*, 17.12: 9648-61.
- Forestiere, C., Miano, G., Rubinacci, G., and Dal Negro, L. (2009). Role of Aperiodic Order in the Spectral, Localization, and Scaling Properties of Plasmon Modes for the Design of Nanoparticle Arrays. *Physical Review B*, 79.8: 085404.
- Forestiere, C., Walsh, G. F., Miano, G., and Dal Negro, L. (2009). Nanoplasmonics of Prime Number Arrays. *Optics Express*, 17: 24288-303.
- Freeman, R. G., Grabar, K. C., Allison, K. J., Bright, R. M., Davis, J. A., Guthrie, A. P., Hommer, M. B., Jackson, M. A., Smith, P. C., and Walter, D. G. (1995). Self-

- Assembled Metal Colloid Monolayers: An Approach to Sers Substrates. *Science*, 267.5204: 1629-32.
- Frisch, U. (1980). Fully Developed Turbulence and Intermittency. *Annals of the New York Academy of Sciences*, 357.1: 359-67.
- Galli, M., Agio, M., Andreani, L., Belotti, M., Guizzetti, G., Marabelli, F., Patrini, M., Bettotti, P., Dal Negro, L., and Gaburro, Z. (2002). Spectroscopy of Photonic Bands in Macroporous Silicon Photonic Crystals. *Physical Review B*, 65.11: 113111.
- Garcia-Vidal, F., Martin-Moreno, L., and Pendry, J. (2005). Surfaces with Holes in Them: New Plasmonic Metamaterials. *Journal of Optics A: Pure and Applied Optics*, 7.2: S97.
- Garg, R. (2008). *Analytical and Computational Methods in Electromagnetics*. Artech House.
- Geddes, C. D., Aslan, K., Gryczynski, I., Malicka, J., and Lakowicz, J. R. (2004). Noble-Metal Surfaces for Metal-Enhanced Fluorescence. *Reviews in Fluorescence 2004*: 365-401.
- Gersten, J., and Nitzan, A. (1980). Electromagnetic Theory of Enhanced Raman Scattering by Molecules Adsorbed on Rough Surfaces. *Journal of Chemical Physics*, 73.7: 3023.
- Ghenuche, P., Cherukulappurath, S., Taminiau, T. H., van Hulst, N. F., and Quidant, R. (2008). Spectroscopic Mode Mapping of Resonant Plasmon Nanoantennas. *Physical Review Letters*, 101.11: 116805.
- Ghosh, A., and Karmakar, S. (1999). Existence of Only Delocalized Eigenstates in the Electronic Spectrum of the Thue–Morse Lattice. *Physica A: Statistical Mechanics and its Applications*, 274.3: 555-62.
- Gopinath, A. "Electromagnetic Field Enhancement and Light Localization in Deterministic Aperiodic Nanostructures." Unpublished doctoral dissertation, Boston University, 2010.
- Gopinath, A., Boriskina, S. V., Feng, N.-N., Reinhard, B. M., and Dal Negro, L. (2008). Photonic-Plasmonic Scattering Resonances in Deterministic Aperiodic Structures. *Nano Letters*, 8: 2423-31.
- Gopinath, A., Boriskina, S. V., Premasiri, W. R., Ziegler, L., Reinhard, B. M., and Dal Negro, L. (2009). Plasmonic Nanogalaxies: Multiscale Aperiodic Arrays for Surface-Enhanced Raman Sensing. *Nano Letters*, 9: 3922-9.



- Gopinath, A., Boriskina, S. V., Reinhard, B. M., and Negro, L. D. (2009). Deterministic Aperiodic Arrays of Metal Nanoparticles for Surface-Enhanced Raman Scattering. *Optics Express*, 17: 1102-06.
- Gorodetski, Y., Drezet, A., Genet, C., and Ebbesen, T. W. (2013). Generating Far-Field Orbital Angular Momenta from near-Field Optical Chirality. *Physical Review Letters*, 110.20: 203906
- Gouyet, J. F., and Mandelbrot, B. (1996). *Physics and Fractal Structures*. Masson.
- Grange, R., Brönstrup, G., Kiometzis, M., Sergeev, A., Richter, J., Leiterer, C., Fritzsche, W., Gutsche, C., Lysov, A., and Prost, W. (2012). Far-Field Imaging for Direct Visualization of Light Interferences in Gaas Nanowires. *Nano Letters*, 12.10: 5412-17.
- Green, M. A. (2003). *Third Generation Photovoltaics: Advanced Solar Energy Conversion*. Springer.
- Gunnarsson, L., Bjerneld, E., Xu, H., Petronis, S., Kasemo, B., and Kall, M. (2001). Interparticle Coupling Effects in Nanofabricated Substrates for Surface-Enhanced Raman Scattering. *Applied Physics Letters*, 78.6: 802-04.
- Guyot-Sionnest, P., Chen, W., and Shen, Y. (1986). General Considerations on Optical Second-Harmonic Generation from Surfaces and Interfaces. *Physical Review B*, 33.12: 8254.
- Guyot-Sionnest, P., and Shen, Y. (1987). Local and Nonlocal Surface Nonlinearities for Surface Optical Second-Harmonic Generation. *Physical Review B*, 35.9: 4420.
- Haase, C., and Stiebig, H. (2007). Thin-Film Silicon Solar Cells with Efficient Periodic Light Trapping Texture. *Applied Physics Letters*, 91.6: 061116-16-3.
- Haes, A. J., Haynes, C. L., McFarland, A. D., Schatz, G. C., Van Duyne, R. P., and Zou, S. (2005). Plasmonic Materials for Surface-Enhanced Sensing and Spectroscopy. *MRS Bulletin*, 30.05: 368-75.
- Halsey, T. C., Jensen, M. H., Kadanoff, L. P., Procaccia, I., and Shraiman, B. I. (1986). Fractal Measures and Their Singularities: The Characterization of Strange Sets. *Physical Review A*, 33.2: 1141.
- Hao, F., and Nordlander, P. (2007). Efficient Dielectric Function for FDTD Simulation of the Optical Properties of Silver and Gold Nanoparticles. *Chemical Physics Letters*, 446.1: 115-18.

- Hao, F., Nordlander, P., Sonnefraud, Y., Dorpe, P. V., and Maier, S. A. (2009). Tunability of Subradiant Dipolar and Fano-Type Plasmon Resonances in Metallic Ring/Disk Cavities: Implications for Nanoscale Optical Sensing. *ACS Nano*, 3.3: 643-52.
- Hao, F., Sonnefraud, Y., Van Dorpe, P., Maier, S. a., Halas, N. J., and Nordlander, P. (2008). Symmetry Breaking in Plasmonic Nanocavities: Subradiant Lspr Sensing and a Tunable Fano Resonance. *Nano Letters*, 8: 3983-8.
- Hardy, G. H., and Wright, E. M. (2008). *An Introduction to the Theory of Numbers*. Oxford University Press.
- Havil, J. (2012). *The Irrationals: A Story of the Numbers You Can't Count On*. Princeton University Press.
- Heckenberg, N. R., McDuff, R., Smith, C. P., and White, A. G. (1992). Generation of Optical Phase Singularities by Computer-Generated Holograms. *Optics Letters*, 17: 221.
- Hicks, E. M., Zou, S., Schatz, G. C., Spears, K. G., Van Duyne, R. P., Gunnarsson, L., Rindzevicius, T., Kasemo, B., and Käll, M. (2005). Controlling Plasmon Line Shapes through Diffractive Coupling in Linear Arrays of Cylindrical Nanoparticles Fabricated by Electron Beam Lithography. *Nano Letters*, 5.6: 1065-70.
- Hsieh, C., Chen, H., Chao, W., and Ko, F. (2004). Optical Properties of Two-Dimensional Photonic-Bandgap Crystals Characterized by Spectral Ellipsometry. *Microelectronic Engineering*, 73: 920-26.
- Hung, Y.-J., Lee, S.-L., and Coldren, L. A. (2010). Deep and Tapered Silicon Photonic Crystals for Achieving Anti-Reflection and Enhanced Absorption. *Optics Express*, 18.7: 6841-52.
- Iguchi, K. (1994). Theory of Ternary Quasiperiodic Lattices: Scaling-Group Approach. *Physical Review B*, 49.18: 12633.
- Illian, J., Penttinen, A., Stoyan, H., and Stoyan, D. (2008). *Statistical Analysis and Modeling of Spatial Point Patterns*. Eds. Senn, S. , M. Scott and V. Barnett. West Sussex: John Wiley.
- Intonti, F., Caselli, N., Lawrence, N., Trevino, J., Wiersma, D., and Dal Negro, L. (2013). Near-field Distribution and Propagation of Scattering Resonances in Vogel Spiral Arrays of Dielectric Nanopillars. *New Journal of Physics*, 15.

- Jackson, J. B., and Halas, N. J. (2004). Surface-Enhanced Raman Scattering on Tunable Plasmonic Nanoparticle Substrates. *Proceedings of the National Academy of Sciences of the United States of America*, 101.52: 17930-35.
- Jackson, J. D. (1975). *Classical Electrodynamics*. Wiley.
- Jain, P. K., Huang, W., and El-Sayed, M. A. (2007). On the Universal Scaling Behavior of the Distance Decay of Plasmon Coupling in Metal Nanoparticle Pairs: A Plasmon Ruler Equation. *Nano Letters*, 7.7: 2080-88.
- Jain, P. K., Lee, K. S., El-Sayed, I. H., and El-Sayed, M. A. (2006). Calculated Absorption and Scattering Properties of Gold Nanoparticles of Different Size, Shape, and Composition: Applications in Biological Imaging and Biomedicine. *Journal of Physical Chemistry B*, 110.14: 7238-48.
- Janot, C. (1997). *Quasicrystals: A Primer*. Vol. 50: Oxford University Press, USA.
- Jiang, X., Zhang, Y., Feng, S., Huang, K. C., Yi, Y., and Joannopoulos, J. (2005). Photonic Band Gaps and Localization in the Thue–Morse Structures. *Applied Physics Letters*, 86.20: 201110-10-3.
- Jin, J.-M. (2011). *Theory and Computation of Electromagnetic Fields*. Wiley.
- Jin, J.-M., and Jin, J. (2002). *The Finite Element Method in Electromagnetics*. Wiley.
- Joannopoulos, J. D., Johnson, S. G., Winn, J. N., and Meade, R. D., eds. *Photonic Crystals: Molding the Flow of Light*. Princeton: Princeton University Press, 2008.
- Johnson, P., and Christy, R. "Optical Constants of the Nobel Metals." *Physical Review B*, 1972. Vol. 6.
- Johnson, S. G., and Joannopoulos, J. D. (2001). Block-Iterative Frequency-Domain Methods for Maxwell's Equations in a Planewave Basis. *Optics Express*, 8.3: 173-90.
- Karperien, A. "Fraclac for Imagej Version 2.5". 1999-2007. <<http://rsb.info.nih.gov/ij/plugins/fraclac/FLHelp/Introduction.htm>>.
- Kauranen, M., and Zayats, A. V. (2012). Nonlinear Plasmonics. *Nature Photonics*, 6.11: 737-48.
- Kazmerski, L., and Margolis, R. (2010). Best Research-Cell Efficiencies. *National Renewable Energy Laboratory Annual Review*.
- Kelly, P., and Arnell, R. (2000). Magnetron Sputtering: A Review of Recent Developments and Applications. *Vacuum*, 56.3: 159-72.

- Kelzenberg, M. D., Boettcher, S. W., Petykiewicz, J. A., Turner-Evans, D. B., Putnam, M. C., Warren, E. L., Spurgeon, J. M., Briggs, R. M., Lewis, N. S., and Atwater, H. A. (2010). Enhanced Absorption and Carrier Collection in Si Wire Arrays for Photovoltaic Applications. *Nature Materials*, 9.3: 239-44.
- Kerker, M., Wang, D.-S., and Chew, H. (1980). Surface Enhanced Raman Scattering (Sers) by Molecules Adsorbed at Spherical Particles: Errata. *Applied Optics*, 19.24: 4159-74.
- Kim, H., Park, J., Cho, S.-W., Lee, S.-Y., Kang, M., and Lee, B. (2010). Synthesis and Dynamic Switching of Surface Plasmon Vortices with Plasmonic Vortex Lens. *Nano Letters*, 10: 529-36.
- Kind, H., Yan, H., Messer, B., Law, M., and Yang, P. (2002). Nanowire Ultraviolet Photodetectors and Optical Switches. *Advanced Materials*, 14.2: 158.
- Kneipp, K., Kneipp, H., Itzkan, I., Dasari, R. R., and Feld, M. S. (2002). Surface-Enhanced Raman Scattering and Biophysics. *Journal of Physics: Condensed Matter*, 14.18: R597.
- Kneipp, K., Kneipp, H., Kartha, V. B., Manoharan, R., Deinum, G., Itzkan, I., Dasari, R. R., and Feld, M. S. (1998). Detection and Identification of a Single DNA Base Molecule Using Surface-Enhanced Raman Scattering. *Physical Review E*, 57.6: R6281.
- Kneipp, K., Wang, Y., Dasari, R. R., Feld, M. S., Gilbert, B. D., Janni, J., and Steinfeld, J. I. (1995). Near-Infrared Surface-Enhanced Raman Scattering of Trinitrotoluene on Colloidal Gold and Silver. *Spectrochimica Acta Part A: Molecular and Biomolecular Spectroscopy*, 51.12: 2171-75.
- Kneipp, K., Wang, Y., Kneipp, H., Perelman, L. T., Itzkan, I., Dasari, R. R., and Feld, M. S. (1997). Single Molecule Detection Using Surface-Enhanced Raman Scattering (Sers). *Physical Review Letters*, 78.9: 1667.
- Kohmoto, M., Kadanoff, L. P., and Tang, C. (1983). Localization Problem in One Dimension: Mapping and Escape. *Physical Review Letters*, 50.23: 1870.
- Kohmoto, M., Sutherland, B., and Iguchi, K. (1987). Localization of Optics: Quasiperiodic Media. *Physical Review Letters*, 58.23: 2436.
- Kolmogorov, A. N., Fomin, S. V. e., and Fomin, S. (1999). *Elements of the Theory of Functions and Functional Analysis*. Vol. 1: Courier Dover Publications.
- Krauss, T. F., Labilloy, D., Scherer, A., and De La Rue, R. M. (1998). Photonic Crystals for Light-Emitting Devices. *Proceedings of SPIE*, 3278: 306-13.

- Kravets, V., Schedin, F., and Grigorenko, A. (2008). Extremely Narrow Plasmon Resonances Based on Diffraction Coupling of Localized Plasmons in Arrays of Metallic Nanoparticles. *Physical Review Letters*, 101.8: 087403.
- Kreibig, U., and Vollmer, M. (1995). Optical Properties of Metal Clusters. *Springer Series in Materials Science, Vol. 25*. Berlin; New York: Springer
- Lai, Y., Zhang, Z. Q., Chan, C. H., and Tsang, L. (2007). Anomalous Properties of the Band-Edge States in Large Two-Dimensional Photonic Quasicrystals. *Physical Review B*, 76.16: 165132.
- Lamprecht, B., Leitner, A., and Aussenegg, F. (1999). Shg Studies of Plasmon Dephasing in Nanoparticles. *Applied Physics B: Lasers and Optics*, 68.3: 419-23.
- Lamprecht, B., Schider, G., Lechner, R. T., Ditlbacher, H., Krenn, J. R., Leitner, A., and Aussenegg, F. R. (2000). Metal Nanoparticle Gratings: Influence of Dipolar Particle Interaction on the Plasmon Resonance. *Physical Review Letters*, 84.20: 4721-24.
- Lawrence, B. D., Cronin-Golomb, M., Georgakoudi, I., Kaplan, D. L., and Omenetto, F. G. (2008). Bioactive Silk Protein Biomaterial Systems for Optical Devices. *Biomacromolecules*, 9.4: 1214-20.
- Lawrence, N., Trevino, J., and Dal Negro, L. (2012). Aperiodic Arrays of Active Nanopillars for Radiation Engineering. *Journal of Applied Physics*, 111: 113101.
- Lawrence, N., Trevino, J., and Negro, L. D. (2012). Control of Optical Orbital Angular Momentum by Vogel Spiral Arrays of Metallic Nanoparticles. *Optics Letters*, 37.24: 5076-78.
- Lee, S. Y., Amsden, J. J., Boriskina, S. V., Gopinath, A., Mitropolous, A., Kaplan, D. L., Omenetto, F. G., and Dal Negro, L. (2010). Spatial and Spectral Detection of Protein Monolayers with Deterministic Aperiodic Arrays of Metal Nanoparticles. *Proceedings of the National Academy of Sciences of the United States of America*, 107.27: 12086-90.
- Lee, S. Y., Forestiere, C., Pasquale, A. J., Trevino, J., Walsh, G., Galli, P., Romagnoli, M., and Dal Negro, L. (2011). Plasmon-Enhanced Structural Coloration of Metal Films with Isotropic Pinwheel Nanoparticle Arrays. *Optics Express*, 19.24: 23818-30.
- Lee, S. Y., Walsh, G. F., and Dal Negro, L. (2013). Microfluidics Integration of Aperiodic Plasmonic Arrays for Spatial-Spectral Optical Detection. *Optics Express*, 21.4: 4945-57.

- Levine, D., and Steinhardt, P. J. (1984). Quasicrystals: A New Class of Ordered Structures. *Physical Review Letters*, 53.26: 2477.
- Li, R., Yerci, S., and Dal Negro, L. (2009). Temperature Dependence of the Energy Transfer from Amorphous Silicon Nitride to Er Ions. *Applied Physics Letters*, 95.4: 041111-11-3.
- Liew, S. F., Noh, H., Trevino, J., Negro, L. D., and Cao, H. (2011). Localized Photonic Band Edge Modes and Orbital Angular Momenta of Light in a Golden-Angle Spiral. *Optics Express*, 19.24: 23631-42.
- Lin, C.-H., Chen, H.-L., Chao, W.-C., Hsieh, C.-I., and Chang, W.-H. (2006). Optical Characterization of Two-Dimensional Photonic Crystals Based on Spectroscopic Ellipsometry with Rigorous Coupled-Wave Analysis. *Microelectronic Engineering*, 83.4: 1798-804.
- Lind, D. A. (1995). *An Introduction to Symbolic Dynamics and Coding*. Cambridge University Press.
- Ling, Y., Cao, H., Burin, A., Ratner, M., Liu, X., and Chang, R. (2001). Investigation of Random Lasers with Resonant Feedback. *Physical Review Series A*, 64.6: 63808-08.
- Link, S., Mohamed, M., and El-Sayed, M. (1999). Simulation of the Optical Absorption Spectra of Gold Nanorods as a Function of Their Aspect Ratio and the Effect of the Medium Dielectric Constant. *Journal of Physical Chemistry B*, 103.16: 3073-77.
- Liu, Y.-J., Zhang, Z.-Y., Zhao, Q., and Zhao, Y.-P. (2008). Revisiting the Separation Dependent Surface Enhanced Raman Scattering. *Applied Physics Letters*, 93.17: 173106-06-3.
- Luck, J. M. (1989). Cantor Spectra and Scaling of Gap Widths in Deterministic Aperiodic Systems. *Physical Review B*, 39: 5834-49.
- Luk'yanchuk, B., Zheludev, N. I., Maier, S. A., Halas, N. J., Nordlander, P., Giessen, H., and Chong, C. T. (2010). The Fano Resonance in Plasmonic Nanostructures and Metamaterials. *Nature Materials*, 9.9: 707-15.
- Macia, E. (2009). *Aperiodic Structures in Condensed Matter: Fundamentals and Applications*. Boca Raton: CRC Press Taylor & Francis.
- Maciá, E. (2006). The Role of Aperiodic Order in Science and Technology. *Reports on Progress in Physics*, 69.2: 397.



- Maier, S. A. (2007). *Plasmonics: Fundamentals and Applications*. Springer Science+Business Media, LLC.
- Mallat, S. (1999). *A Wavelet Tour of Signal Processing*. Academic Press.
- Mandelbrot, B. B. (1982). *The Fractal Geometry of Nature*. Times Books.
- Mandelbrot, B. B. (1988). *An Introduction to Multifractal Distribution Functions*. Netherlands: Springer.
- Meade, R. D., Devenyi, A., Joannopoulos, J. D., Alerhand, O. L., Smith, D. A., and Kash, K. (1994). Novel Applications of Photonic Band Gap Materials: Low-Loss Bends and High Q Cavities. *Journal of Applied Physics*, 75.9: 4753-55.
- Meier, M., Wokaun, a., and Liao, P. F. (1985). Enhanced Fields on Rough Surfaces: Dipolar Interactions among Particles of Sizes Exceeding the Rayleigh Limit. *Journal of the Optical Society of America B*, 2: 931.
- Mekis, A., Chen, J., Kurland, I., Fan, S., Villeneuve, P. R., and Joannopoulos, J. (1996). High Transmission through Sharp Bends in Photonic Crystal Waveguides. *Physical Review Letters*, 77.18: 3787-90.
- Mie, G. (1908). Beiträge Zur Optik Trüber Medien, Speziell Kolloidaler Metallösungen. *Annalen der Physik*, 330.3: 377-445.
- Mirin, N. A., Bao, K., and Nordlander, P. (2009). Fano Resonances in Plasmonic Nanoparticle Aggregates†. *Journal of Physical Chemistry A*, 113.16: 4028-34.
- Mitchison, G. (1977). Phyllotaxis and the Fibonacci Series. *Science*, 196.4287: 270-75.
- Mohri, N., Matsushita, S., Inoue, M., and Yoshikawa, K. (1998). Desorption of 4-Aminobenzenethiol Bound to a Gold Surface. *Langmuir*, 14.9: 2343-47.
- Mokkapati, S., Beck, F., De Waele, R., Polman, A., and Catchpole, K. (2011). Resonant Nano-Antennas for Light Trapping in Plasmonic Solar Cells. *Journal of Physics D: Applied Physics*, 44.18: 185101.
- Moran, A. M., Sung, J., Hicks, E. M., Van Duyne, R. P., and Spears, K. G. (2005). Second Harmonic Excitation Spectroscopy of Silver Nanoparticle Arrays. *Journal of Physical Chemistry B*, 109.10: 4501-06.
- Morrow, J. (2010) Untitled Sunflower Image,  
<<http://randomnies.blogspot.com/2010/11/sunflower-fibonacci-sequence-golden.html>>

- Moskovits, M. (1985). Surface-Enhanced Spectroscopy. *Reviews of Modern Physics*, 57.3: 783.
- Muskens, O. L., Diedenhofen, S. L., Kaas, B. C., Algra, R. E., Bakkers, E. P., Gómez Rivas, J., and Lagendijk, A. (2009). Large Photonic Strength of Highly Tunable Resonant Nanowire Materials. *Nano Letters*, 9.3: 930-34.
- Muskens, O. L., Rivas, J. G., Algra, R. E., Bakkers, E. P., and Lagendijk, A. (2008). Design of Light Scattering in Nanowire Materials for Photovoltaic Applications. *Nano Letters*, 8.9: 2638-42.
- Muzy, J. F., Bacry, E., and Arneodo, A. (1994). The Multifractal Formalism Revisited with Wavelets. *International Journal of Bifurcation and Chaos*, 4.02: 245-302.
- Nakayama, K., Tanabe, K., and Atwater, H. A. (2008). Plasmonic Nanoparticle Enhanced Light Absorption in Gaas Solar Cells. *Applied Physics Letters*, 93.12: 121904-04-3.
- Nakayama, Y., Pauzauskie, P. J., Radenovic, A., Onorato, R. M., Saykally, R. J., Liphardt, J., and Yang, P. (2007). Tunable Nanowire Nonlinear Optical Probe. *Nature*, 447.7148: 1098-101.
- NASA. "Messier 101 Galaxy." 2013.
- Navarro-Cia, M., and Maier, S. A. (2012). Broad-Band near-Infrared Plasmonic Nanoantennas for Higher Harmonic Generation. *ACS Nano*, 6.4: 3537-44.
- Naylor, M. (2002). Golden, 2, and II Flowers: A Spiral Story. *Mathematics Magazine*: 163-72.
- Nelson, J., and Ratner, M. (2004). The Physics of Solar Cells. *Physics Today*, 57.12: 71-71.
- Noguez, C. (2007). Surface Plasmons on Metal Nanoparticles: The Influence of Shape and Physical Environment. *Journal of Physical Chemistry C*, 111.10: 3806-19.
- Notomi, M., Suzuki, H., Tamamura, T., and Edagawa, K. (2004). Lasing Action Due to the Two-Dimensional Quasiperiodicity of Photonic Quasicrystals with a Penrose Lattice. *Physical Review Letters*, 92.12: 123906.
- Novotny, L., Bian, R. X., and Xie, X. S. (1997). Theory of Nanometric Optical Tweezers. *Physical Review Letters*, 79.4: 645-48.
- Novotny, L., and Hecht, B. (2011). *Principles of Nano-Optics*. Cambridge University Press.



- Okabe, A., Boots, B., Sugihara, K., and Chiu, S. N. (2009). *Spatial Tessellations: Concepts and Applications of Voronoi Diagrams*. Vol. 501: Wiley.
- Oldenburg, S. J., Westcott, S. L., Averitt, R. D., and Halas, N. J. (1999). Surface Enhanced Raman Scattering in the near Infrared Using Metal Nanoshell Substrates. *Journal of Chemical Physics*, 111: 4729.
- Omenetto, F. G., and Kaplan, D. L. (2008). A New Route for Silk. *Nature Photonics*, 2.11: 641-43.
- Ostfeld, A., and Pacifici, D. (2011). Plasmonic Concentrators for Enhanced Light Absorption in Ultrathin Film Organic Photovoltaics. *Applied Physics Letters*, 98.11: 113112-12-3.
- Oulton, R. F., Sorger, V. J., Genov, D., Pile, D., and Zhang, X. (2008). A Hybrid Plasmonic Waveguide for Subwavelength Confinement and Long-Range Propagation. *Nature Photonics*, 2.8: 496-500.
- Ozaktas, H. M., Kutay, M. A., and Zalevsky, Z. (2001). *The Fractional Fourier Transform with Applications in Optics and Signal Processing*. Wiley New York.
- Padgett, M., Courtial, J., and Allen, L. (2004). Light's Orbital Angular Momentum. *Physics Today*, 57: 35.
- Palik, E. D. (1998). *Handbook of Optical Constants of Solids*. Vol. 3: Access Online via Elsevier.
- Parker, S. T., Domachuk, P., Amsden, J., Bressner, J., Lewis, J. A., Kaplan, D. L., and Omenetto, F. G. (2009). Biocompatible Silk Printed Optical Waveguides. *Advanced Materials*, 21.23: 2411-15.
- Pasquale, A. J. "Engineering Photonic-Plasmonic Devices for Spectroscopy and Sensing Applications." Unpublished doctoral dissertation, Boston University, 2012.
- Penrose, R. (1947). The Role of Aesthetics in Pure and Applied Mathematical Research. *Institute of Mathematics and its Applications*, 10.7.
- Poborchii, V. V., Tada, T., and Kanayama, T. (2002). Photonic-Band-Gap Properties of Two-Dimensional Lattices of Si Nanopillars. *Journal of Applied Physics*, 91.5: 3299-305.
- Pollard, M. E., and Parker, G. J. (2009). Low-Contrast Bandgaps of a Planar Parabolic Spiral Lattice. *Optics Letters*, 34.18: 2805-07.
- Purcell, E. M., and Pennypacker, C. R. (1973). Scattering and Absorption of Light by Nonspherical Dielectric Grains. *Astrophysical Journal*, 186: 705-14.

- Queffélec, M. (1987). *Substitution Dynamical Systems - Spectral Analysis Lecture Notes in Mathematics*. Vol. 1294: Berlin: Springer.
- Raman, C., and Krishnan, K. (1928). A New Type of Secondary Radiation. *Nature*, 121.3048: 501-02.
- Rasband, W. S. "Imagj". Bethesda, MD. U. S. National Institutes of Health 1997-2011. <<http://imagej.nih.gov/ij/>>.
- Redding, B., Liew, S. F., Sarma, R., and Cao, H. (2013). Compact Spectrometer Based on a Disordered Photonic Chip. *Nature Photonics*.
- Rex, N., Tureci, H., Schwefel, H., Chang, R., and Stone, A. D. (2002). Fresnel Filtering in Lasing Emission from Scarred Modes of Wave-Chaotic Optical Resonators. *Physical Review Letters*, 88.9: 094102.
- Ripley, B. D. (1977). Modelling Spatial Patterns. *Journal of the Royal Statistical Society, Series B (methodological)*: 172-212.
- Ritchie, R. (1957). Plasma Losses by Fast Electrons in Thin Films. *Physical Review*, 106.5: 874.
- Rosfjord, K. M., Yang, J. K., Dauler, E. A., Kerman, A. J., Anant, V., Voronov, B. M., Gol'tsman, G. N., and Berggren, K. K. (2006). Nanowire Single-Photon Detector with an Integrated Optical Cavity and Anti-Reflection Coating. *Optics Express*, 14.2: 527-34.
- Rudin, C. (1994). The Pinwheel Tilings of the Plane. *Annals of Mathematics*, 139.3: 661-702.
- Russo-Averchi, E., Heiss, M., Michelet, L., Krogstrup, P., Nygard, J., Magen, C., Morante, J. R., Uccelli, E., Arbiol, J., and i Morral, A. F. (2012). Suppression of Three Dimensional Twinning for a 100% Yield of Vertical Gaas Nanowires on Silicon. *Nanoscale*, 4.5: 1486-90.
- Salerno, M., Krenn, J., Hohenau, A., Ditlbacher, H., Schider, G., Leitner, A., and Aussenegg, F. (2005). The Optical near-Field of Gold Nanoparticle Chains. *Optics Communications*, 248.4: 543-49.
- Schroeder, M. (2009). *Number Theory in Science and Communication*. Vol. 7: Springer.
- Senechal, M. (1996). *Quasicrystals and Geometry* Cambridge University Press.
- Shalaev, V. M. (2002). *Optical Properties of Nanostructured Random Media*. Vol. 82: Springer.

- Sharkawy, A., Shi, S., Prather, D., and Soref, R. (2002). Electro-Optical Switching Using Coupled Photonic Crystal Waveguides. *Optics Express*, 10.20: 1048-59.
- Sharkawy, A., Shi, S., and Prather, D. W. (2001). Multichannel Wavelength Division Multiplexing with Photonic Crystals. *Applied Optics*, 40.14: 2247-52.
- Shechtman, D., Blech, I., Gratias, D., and Cahn, J. W. (1984). Metallic Phase with Long-Range Orientational Order and No Translational Symmetry. *Physical Review Letters*, 53.20: 1951-53.
- Shegai, T., Miljkovic, V. D., Bao, K., Xu, H., Nordlander, P., Johansson, P., and Käll, M. (2011). Unidirectional Broadband Light Emission from Supported Plasmonic Nanowires. *Nano Letters*, 11.2: 706-11.
- Simon, D. S., Lawrence, N., Trevino, J., Dal Negro, L., and Sergienko, A. V. (2013). High-Capacity Quantum Fibonacci Coding for Key Distribution. *Physical Review A*, 87.3: 032312.
- Song, D., Cho, E.-C., Conibeer, G., Flynn, C., Huang, Y., and Green, M. A. (2008). Structural, Electrical and Photovoltaic Characterization of Si Nanocrystals Embedded SiC Matrix and Si Nanocrystals/c-Si Heterojunction Devices. *Solar Energy Materials and Solar Cells*, 92.4: 474-81.
- Stanley, H. E., and Meakin, P. (1988). Multifractal Phenomena in Physics and Chemistry. *Nature*, 335.6189: 405-09.
- Steurer, W., and Sutter-Widmer, D. (2007). Photonic and Phononic Quasicrystals. *Journal of Physics D: Applied Physics*, 40: R229-R47.
- Stuart, H. R., and Hall, D. G. (1998). Island Size Effects in Nanoparticle-Enhanced Photodetectors. *Applied Physics Letters*, 73.26: 3815-17.
- Taflove, A., and Hagness, S. C. (1995). *Computational Electrodynamics: The Finite-Difference Time-Domain Method*. Boston: Artech House.
- Talley, C. E., Jackson, J. B., Oubre, C., Grady, N. K., Hollars, C. W., Lane, S. M., Huser, T. R., Nordlander, P., and Halas, N. J. (2005). Surface-Enhanced Raman Scattering from Individual Au Nanoparticles and Nanoparticle Dimer Substrates. *Nano Letters*, 5.8: 1569-74.
- Thompson, J., Anni, M., Lattante, S., Pisignano, D., Blyth, R., Gigli, G., and Cingolani, R. (2004). Amplified Spontaneous Emission in the near Infrared from a Dye-Doped Polymer Thin Film. *Synthetic Metals*, 143.3: 305-07.

- Toffanin, S., Kim, S., Cavallini, S., Natali, M., Benfenati, V., Amsden, J. J., Kaplan, D. L., Zamboni, R., Muccini, M., and Omenetto, F. G. (2012). Low-Threshold Blue Lasing from Silk Fibroin Thin Films. *Applied Physics Letters*, 101.9: 091110-10-4.
- Torquato, S., and Stillinger, F. H. (2003). Local Density Fluctuations, Hyperuniformity, and Order Metrics. *Physical Review E*, 68.4: 041113.
- Trevino, J., Alberto, C., Pecora, E. F., Forestiere, C., Fontcuberta i Morral, A., and Dal Negro, L. (2013). Photonic-Plasmonic Coupling of Gaas Single Nanowires with Nanoantenna Arrays. *Submitted*.
- Trevino, J., Cao, H., and Dal Negro, L. (2011). Circularly Symmetric Light Scattering from Nanoplasmonic Spirals. *Nano Letters*, 11.5: 2008.
- Trevino, J., Forestiere, C., Di Martino, G., Yerci, S., Priolo, F., and Dal Negro, L. (2012). Plasmonic-Photonic Arrays with Aperiodic Spiral Order for Ultra-Thin Film Solar Cells. *Optics Express*, 20: A418-30.
- Trevino, J., Liew, S. F., Noh, H., Cao, H., and Dal Negro, L. (2012). Geometrical Structure, Multifractal Spectra and Localized Optical Modes of Aperiodic Vogel Spirals. *Optics Express*, 20: 3015-33.
- Trevino, J., Walsh, G., Pecora, E. F., Boriskina, S. V., and Dal Negro, L. (2013). Radiation-Enhanced Plasmonic Nanoantennas for Multispectral Nanoscale Focusing. *Submitted*.
- Tsakalakos, L., Balch, J., Fronheiser, J., Korevaar, B., Sulima, O., and Rand, J. (2007). Silicon Nanowire Solar Cells. *Applied Physics Letters*, 91: 233117.
- Turnbull, G. A., Robertson, D. A., Smith, G. M., Allen, L., and Padgett, M. J. (1996). The Generation of Free-Space Laguerre-Gaussian Modes at Millimetre-Wave Frequencies by Use of a Spiral Phaseplate. *Optics Communications*, 127.4-6: 183-88.
- Vasconcelos, M., and Albuquerque, E. (1998). Plasmon-Polariton Fractal Spectra in Quasiperiodic Multilayers. *Physical Review B*, 57: 2826-33.
- Vasconcelos, M., and Albuquerque, E. (1999). Transmission Fingerprints in Quasiperiodic Dielectric Multilayers. *Physical Review B*, 59.17: 11128.
- Vial, A., Grimault, A.-S., Macías, D., Barchiesi, D., and de La Chapelle, M. L. (2005). Improved Analytical Fit of Gold Dispersion: Application to the Modeling of Extinction Spectra with a Finite-Difference Time-Domain Method. *Physical Review B*, 71.8: 85416.

- Vieu, C., Carcenac, F., Pepin, A., Chen, Y., Mejias, M., Lebib, A., Manin-Ferlazzo, L., Couraud, L., and Launois, H. (2000). Electron Beam Lithography: Resolution Limits and Applications. *Applied Surface Science*, 164.1: 111-17.
- Vogel, H. (1979). A Better Way to Construct the Sunflower Head. *Mathematical Bioscience*, 44.
- Walsh, G. F. "Engineering Optical Nonlinearities in Metal Nanoparticle Arrays." Boston University, 2013.
- Walsh, G. F., and Dal Negro, L. (2013). Enhanced Second Harmonic Generation by Photonic-Plasmonic Fano-Type Coupling in Nanoplasmonic Arrays. *Nano Letters*.
- Wang, B., and Leu, P. W. (2012). Tunable and Selective Resonant Absorption in Vertical Nanowires. *Optics Letters*, 37.18: 3756-58.
- Wang, Z., Pan, S., Krauss, T. D., Du, H., and Rothberg, L. J. (2003). The Structural Basis for Giant Enhancement Enabling Single-Molecule Raman Scattering. *Proceedings of the National Academy of Sciences of the United States of America*, 100.15: 8638-43.
- Wiersma, D. (2000). Laser Physics: The Smallest Random Laser. *Nature*, 406.6792: 132-35.
- Wiersma, D. S. (2008). The Physics and Applications of Random Lasers. *Nature Physics*, 4.5: 359-67.
- Wikipedia. "Helix Oam." 2013.
- Willetts, K. A., and Van Duyne, R. P. (2007). Localized Surface Plasmon Resonance Spectroscopy and Sensing. *Annual Review of Physical Chemistry*, 58: 267-97.
- Williams, K. R., Gupta, K., and Wasilik, M. (2003). Etch Rates for Micromachining Processing-Part II. *Journal of Microelectromechanical Systems*, 12.6: 761-78.
- Wolff, W. (2012) Untitled Nautilus Shell and Cactus Images, <<http://letsgetvisualvisual.wordpress.com/2012/02/21/1-618/>>
- Xu, H., Aizpurua, J., Käll, M., and Apell, P. (2000). Electromagnetic Contributions to Single-Molecule Sensitivity in Surface-Enhanced Raman Scattering. *Physical Review E*, 62.3: 4318.
- Xu, H., Bjerneld, E. J., Käll, M., and Börjesson, L. (1999). Spectroscopy of Single Hemoglobin Molecules by Surface Enhanced Raman Scattering. *Physical Review Letters*, 83.21: 4357.

- Xu, Y. (1995). Electromagnetic Scattering by an Aggregate of Spheres. *Applied Optics*, 34.21: 4573-88.
- Yang, J.-K., Boriskina, S. V., Noh, H., Rooks, M. J., Solomon, G. S., Dal Negro, L., and Cao, H. (2010). Demonstration of Laser Action in a Pseudo-Random Medium. *SPIE NanoScience+ Engineering*: 775602-02-10.
- Yang, J. K., Noh, H., Liew, S. F., Rooks, M. J., Solomon, G. S., and Cao, H. (2011). Lasing Modes in Polycrystalline and Amorphous Photonic Structures. *Physical Review A*, 84.3: 033820.
- Yanik, A. A., Cetin, A. E., Huang, M., Artar, A., Mousavi, S. H., Khanikaev, A., Connor, J. H., Shvets, G., and Altug, H. (2011). Seeing Protein Monolayers with Naked Eye through Plasmonic Fano Resonances. *Proceedings of the National Academy of Sciences of the United States of America*, 108.29: 11784-89.
- Yee, K. (1966). Numerical Solution of Initial Boundary Value Problems Involving Maxwell's Equations in Isotropic Media. *IEEE Transactions on Antennas and Propagation*, 14.3: 302-07.
- Yerci, S. "Erbium-Doped Amorphous Silicon Nitride Light Emitters for on-Chip Photonics Applications." Unpublished doctoral dissertation, Boston University, 2011.
- Yerci, S., Li, R., Kucheyev, S., Van Buuren, T., Basu, S., and Dal Negro, L. (2009). Energy Transfer and 1.54 Mm Emission in Amorphous Silicon Nitride Films. *Applied Physics Letters*, 95: 031107.
- Zhang, Z., Weber-Bargioni, A., Wu, S., Dhuey, S., Cabrini, S., and Schuck, P. J. (2009). Manipulating Nanoscale Light Fields with the Asymmetric Bowtie Nano-Colorsorter. *Nano Letters*, 9.12: 4505-09.
- Zou, S., and Schatz, G. C. (2004). Narrow Plasmonic/Photonic Extinction and Scattering Line Shapes for One and Two Dimensional Silver Nanoparticle Arrays. *The Journal of Chemical Physics*, 121: 12606.



[REDACTED]

[REDACTED]

[REDACTED]

[REDACTED]

[REDACTED]

[REDACTED]

[REDACTED]

[REDACTED]

[REDACTED]

[REDACTED]

[REDACTED]



[REDACTED]

[REDACTED]

[REDACTED]

[REDACTED]

[REDACTED]

[REDACTED]

[REDACTED]

[REDACTED]

[REDACTED]

[REDACTED]

[REDACTED]

[REDACTED]